Comparison of paleoredox signatures from a Mesoarchean oxygen oasis with those of a modern analog environment

Dissertation

der Mathematisch-Naturwissenschaftlichen Fakultät

der Eberhard Karls Universität Tübingen

zur Erlangung des Doktorgrades

der Naturwissenschaften

(Dr. rer. nat.)

vorgelegt von

MSc Gülüm Albut

aus Aydin, Türkei

Tübingen

2018

Tag der mündlichen Prüfung:	18. 01. 2019
Dekan:	Prof. Dr. Wolfgang Rosenstiel
1. Berichterstatter:	Prof. Dr. Ronny Schönberg
2. Berichterstatter:	Prof. Dr. Andreas Kappler

Ich erkläre hiermit, dass ich die zur Promotion eingereichte Arbeit mit dem Titel „Comparison of paleoredox signatures from a Mesoarchean oxygen oasis with those of a modern analog environment“ selbstständig verfasst, nur die angegebenen Quellen und Hilfsmittel benutzt und wörtlich oder inhaltlich übernommene Stellen (alternativ: Zitate) als solche gekennzeichnet habe. Ich erkläre, dass die Richtlinien zur Sicherung guter wissenschafltlicher Praxis der Universität Tübingen (Beschluss des Senats vom 25.05.2000) beachtet wurden. Ich versichere an Eides statt, dass diese Angaben wahr sind und, dass ich nichts verschwiegen habe. Mir ist bekannt, dass die falsche Angabe einer Versicherung an Eides statt mit Freiheitsstrafe bis zu drei Jahren oder mit Geldstrafe bestraft wird.

Ort, Datum Unterschrift

Acknowledgements

I would like to thank Ronny Schönberg for giving me the opportunity to work on this project, and Andreas Kappler and Harald Strauss for designing the Arvadi Project and allowing me to take part in it. I would like to thank the German Research Council (Deutsche Forschungsgemeinschaft DFG) for funding this work.

I am very grateful to Ronny Schönberg for his fair guidance, supervision and support, and most of all for motivating me endlessly during the difficult times throughout my PhD. I would like to further thank him for his patience and availability whenever I had any questions or problems.

I am deeply thankful to Michael Babechuk, who was a great advisor during his time in Isotope Geochemistry group, and contributed very much to this work with his insightful ideas and suggestions. I am also thankful for his motivation and encouragement in difficult moments of my PhD adventure.

Special thanks to Nic Beukes and Albertus Smith, for their help in collection of the samples and their guidance and hospitality during the field campaign of 2016 in South Africa. I am also grateful to the SPP 1833 'Building a Habitable Earth' project coordinators and colleagues for allowing me to take part in the field workshop 2016 in South Africa.

I would like to thank to all current and former members of the Isotope Geochemistry Group, particularly Ilka Schönberg, Martin Wille, Florian Kurzweil, Sümeyya Eroglu, Elmar Reitter, Bernd Steinhilber, Daniel Schöckle, Heinrich Taubald, and Manuela Benger,

as well as Geomicrobiology group members Elif Köksoy, and Andreas Kappler,

and Annika Brüske (Leibniz University of Hannover), Balz Kamber (Trinity College Dublin), Stephanus Kruger (University of Johannesburg), and Harald Strauss (University of Münster),

for their help and contributions in the labwork, and data collection.

The "Schneckes"of the Isotope Geochemistry group are deeply appreciated for making the last year of my PhD amazing: Marie-Laure Pons, Lucile Roué, Luise Wagner, Maria Isabel Varas Reus, Carolina Rosca, Benjamin Eickmann, Stephan König; and the former members Sümeyya Eroglu and Florian Kurzweil for making the first two years more welcoming and fun. Further thanks to Elmar Reitter, Martin Wille, Frantz-Gerard Ossa Ossa, Daniel Schöckle, Timon Kurzawa, Yierpan Aierken, and Yunfeng Wang for their companionship.

I had met great people during my years in Tübingen, who have become dear friends and who made my time here memorable, and for whose friendships, support and solidarity I am deeply thankful for,

particularly Ted Gibbons, Elena Cama, Sergio Latorre, Eva Öhm, Elena Ionesi, Christoph Schäfer, Bilge Sürün, Dee Ann and Bill Gibbons, Sybille von Bremen, and many others.

I would like to further thank my family Ayşen Genç and Semih Albut for their endless love, support, advice and making me the person that I am, as well as my extended family members, particularly Günsel Genç, Selçuk and Sevim Albut, Zeynep Çokuğraş, Göksel and Idil Ebiri, Sevinç Karademir, Sercan and Serpil Abut, Semiha, Ipek and Serhan Nircan, Cansu and Cengiz Korkmaz. Dear friends whom I consider extended family: LSG members Doğa Can Su Öztürk, Yasemin Kalafatoğlu, Gizem Şengör; Zeynep and Furkan Dodurka and ITÜDAK members; as well as Can Elvan, Ulaş Kayır, and Deniz Abuş thank you very much for all your support and friendship despite the long distance.

Finally, I would like to devote this thesis to the dear people I have lost, who are very significant for me, and who had shaped the person that I am, Seyfi Albut, Nadide and Neşe Genç.

Contributions of others

Overall 80 % of the laboratory work and data collection, about 90 % of data evaluation and interpretation, and 80 % of the writing of this thesis were done by myself. The scientific contributions of collaborators were as follows:

1. Project idea

The project idea for the first six chapters of this thesis were developed by Prof. Ronny Schönberg (University of Tübingen). The idea to use the Arvadi Spring in Switzerland as a modern analog for Mesoarchean to Paleoproterozoic Oceans, which is the focus of the 7th chapter of this thesis, results from a collaboration between Prof. Andreas Kappler (University of Tübingen), Prof. Harald Strauss (University of Münster) and Prof. Ronny Schönberg. This work was funded by the Deutsche Forschungsgemeinschaft (DFG) as a joint proposal between Prof. Andreas Kappler and Prof. Ronny Schönberg.

2. Sampling

The DDN-1 and PMH24/L1 drill core samples from the Ijzermijn iron formation (IF), as well as the powdered samples from the WV006 Wolvenkopp drill core of the Scotts Hill IF were provided by Prof. Nicolas Beukes (University of Johannesburg). The outcrop samples of the Ijzermijn IF from the White Mfolozi Inlier in South Africa were sampled by myself with the assistance of Prof. Nicolas Beukes and Dr. Albertus Smith, both from the Department of Geology, University of Johannesburg, during a field campaign in 2016.

The Arvadi water and sediment samples were collected by myself in four consecutive field campaigns, first one in October 2014, which was assisted by members of the Geomicrobiology work group Dr. Elif Köksoy (Bigelow Laboratory for Ocean Sciences), Prof. Andreas Kappler, Dr. Anneli Sundman, and Isotope Geochemistry work group Dr. Sümeyya Eroglu (GEOMAR Helmholtz Center for Ocean Research) and Prof. Ronny Schönberg, second one in April 2015, assisted by Geomicrobiology work group members Dr. Elif Köksoy, Tim Bayer, and Caroline Scholze, third one in April 2017 assisted by Dr. Elif Köksoy and Prof. Ronny Schönberg and last one in June 2018, assisted by Isotope Geochemistry work group members Luise Wagner, Lucile Roué, Dr. Benjamin Eickmann, and Dr. Frantz Ossa Ossa.

3. Analyses and sample collection

Dr. Michel Babechuk (Memorial University of Newfoundland and Labrador) and Bernd Steinhilber (mass spectrometry technician) helped to set up the ThermoFisher Scientific iCAP Qc ICP-MS for the determination of trace element concentrations at the facilities of the Isotope Geochemistry Group of the University of Tübingen. Sample preparation for these measurements, including digestion, dilution and addition of the internal standard solution for instrumental drift corrections were done by myself. Dr. Michael Babechuk and Bernd Steinhilber helped with data reduction and evaluation.

Determination of ($^{234}U/^{238}U$) activity ratios of the Ijzermijn IF samples at Trinity College Dublin (TCD) were conducted by Prof. Balz Kamber (Trinity College Dublin). $^{234}U/^{238}U$ activity and stable $^{238}U/^{235}U$ isotopic ratios of Ijzermijn IF and shale samples determined at the Leibniz University of Hannover (LUH) were conducted by Annika Brüske (Leibniz University of Hannover).

Stephanus Kruger (University of Johannesburg) conducted the XRD analyses of the outcrop samples from Ijzermijn IF at University of Johannesburg.

Major element XRF determinations at the facilities of the Isotope Geochemistry Group of University of Tübingen were conducted by myself with the help of Daniel Schöckle and Dr. Heinrich Taubald. Stable Cr isotopic analyses of part of the samples (Ijzermijn IF drill core samples) were done by Manuela Benger as part of her BSc thesis. I had Dr. Ilka Schönberg´s assistance during the stable Cr isotope measurements, Dr. Martin Wille´s assistance with the stable Mo isotope measurements and Dr. Florian Kurzweil´s assistance with the stable Fe isotope measurements of the Arvadi Spring samples collected at the October 2014 campaign. All these analyses were performed at the facilities of the Isotope Geochemistry Group of the University of Tübingen.

Elmar Reitter assisted me during determination of Fe speciation (i.e. Fe^{2+}/Fe_{tot} ratios) at the facilities of the Isotope Geochemistry Group of University of Tübingen. Per Jeisecke helped with the cutting of the outcrop samples from the Ijzermijn IF at the University of Tübingen for powder and thin section preparation.

4. Text, figures and tables

Prof. Nicolas Beukes edited descriptions of the geological background of the Pongola Basin, South Africa, given in '2. Geological Overview'. Prof. Ronny Schönberg fully and Dr. Michael Babechuk, Dr. Albertus Smith, Prof. Balz Kamber and Annika Brüske partly edited, and reviewed this thesis. Parts of this thesis have been published in a peer-review international journal *(Albut G., Babechuk M. G., Kleinhanns I. C., Benger M., Beukes N. J., Steinhilber B., Smith A. J. B., Kruger S., Schoenberg R. (2018) Modern rather than Mesoarchean oxidative weathering responsible for the heavy stable Cr isotopic signatures of the 2.95 Ga old Ijzermijn iron formation (South Africa). Geochimica et Cosmochimica Acta* ***228****, 157-189.*), and parts of the thesis are under revision (*Albut G., Kamber B. S., Brüske A., Beukes N. J., Smith A. J. B., Schoenberg R. Modern weathering versus ancient paleoredox proxies from a Mesoarchean marine oxygen oasis in Pongola Supergroup, South Africa. Submitted to Geochimica et Cosmochimica Acta).*

All figures and tables were prepared by myself. Dr. Michael Babechuk provided the information on trace element analyses of reference materials, and Dr. Ilka Schönberg provided the information on the stable Cr isotopic analyses of the rock standard IF-G and major element analyses of reference materials, all presented in the Appendices. Prof. Nicolas Beukes provided the logs and correlation of the drill cores DDN-1 and PMH24/L1 as well as the outcrop samples of the Ijzermijn IF.

5. Scientific ideas

Many discussions with and suggestions from Prof. Ronny Schönberg, Dr. Michael Babechuk, Prof. Balz Kamber, Dr. Martin Wille, Prof. Nicolas Beukes, Dr. Albertus Smith and Prof. Andreas Kappler, as well as other members of the Isotope Geochemistry Group and Geomicrobiology Group (University of Tübingen) helped me with the interpretation of the data.

Contents

Acknowledgements **6**

Contributions of others **8**

Abstract **13**

Zussammenfassung **16**

1. Introduction **20**

1.1. Motivation and significance of the study 20

1.2. Scope of the study 22

1.3. Mesoarchean atmospheric and ocean conditions vs. modern weathering effects 23

1.4. Non-traditional stable isotope systematics 27

1.4.1. Principles of mass-dependent stable isotope fractionation 27

1.4.2. Stable Cr isotope systematics 29

1.4.3. Stable Mo isotope systematics 30

1.4.4. Stable Fe isotope systematics 31

1.4.5. Stable U isotope systematics 33

2. Geological/Hydrological Setting and Sampling 34

2.1. Geology of the Pongola Supergroup and sampling of the Ijzermijn Iron Formation 34

2.1.1. Sampling of Ijzermijn IF, Mozaan Group, Pongola Supegroup 36

2.1.2. Sampling of Scotts Hill IF, Mozaan Group, Pongola Supegroup 38

2.2. Hydrology of the Arvadi Spring and sampling 38

3. Analytical methods **41**

3.1. Mozaan Group samples and bulk sample powder preparation 41

3.1.1. Major element analyses of the Mozaan Group samples 41

3.1.1.1. Ijzermijn IF outcrop samples 41

3.1.1.2. Scotts Hill IF and Ijzermijn IF drill core samples 42

3.1.2. Ferrous iron [Fe(II)] content determination of Ijzermijn IF samples 42

3.1.3. Trace elements analysis of the Mozaan Group samples 43

3.1.4. U isotopic analyses of the Mozaan Group samples 45

3.1.4.1. Determination of ($^{234}U/^{238}U$) activity and stable $^{238}U/^{235}U$ isotopic ratios of the Sinqeni Formation samples at the University of Hannover (LUH) 45

3.1.4.2. Determination of ($^{234}U/^{238}U$) activity ratios of the Sinqeni Formation samples at Trinity College Dublin (TCD) 46

3.1.5. Stable Cr isotope analysis of the Mozaan Group samples 46

3.1.6. Stable Mo isotopic analysis of the Mozaan Group samples 47

3.1.7. Stable Fe isotopic analysis of the Mozaan Group samples 49

3.2. Stable Fe isotope analyses of the Arvadi Samples 50

4. Results 51
4.1. The Mozaan Group samples 51
4.1.1. Major element systematics and LOI 51
4.1.2. Detrital component of the Mozaan Group IFs 60
4.1.3. Additional trace element parameters in the Mozaan Group IFs 65
4.1.4. Rare earth elements and yttrium in the Mozaan Group IFs 68
4.1.5. ($^{234}U/^{238}U$) activity ratios and stable $^{238}U/^{235}U$ isotopic compositions of the Sinqeni Formation 72
4.1.6. Stable Cr isotopes of the Mozaan Group samples 73
4.1.7. Stable Mo isotopic compositions and Mo concentrations of the Sinqeni Formation samples… 75
4.1.8. Stable Fe isotopic composition and Fe concentrations of the Sinqeni Formation samples…… ..... .78
4.2. Arvadi Spring samples 80
4.2.1. Stable Fe isotopic composition and Fe concentration of Arvadi Spring samples 80
5. Modern weathering versus Mesoarchean oxidative weathering signatures 85
5.1.1. Trace element indicators for modern aqueous overprinting 85
5.1.2. ($^{234}U/^{238}U$) activity ratios as an indicator for modern weathering-induced alteration on White Mfolozi River outcrop 87
5.1.3. Surface weathering of carbonates 90
5.1.4. Potential origins of the heavy Cr isotopic compositions of Ijzermijn IF outcrop samples 93
5.1.5. Implications for the Cr weathering cycle in the Mesoarchean and the first expression of oxidative weathering 95
5.1.6. Geochemical tracing of the element sources of the Mozaan IFs in outcrop and drill core samples 97
5.1.7. Effects of modern weathering on Mo and Fe concentration and stable isotopic compositions 98
5.2.1. Concluding remarks and outlook 99
6. Implications of the stable Mo and Fe isotopic data for a Mesoarchean oxygen oasis.....100
6.1.1. $\delta^{98/95}Mo_{NIST3134+0.25}$ and $\delta^{56/54}Fe_{IRMM-014}$ values of drill core samples and MnO_2 shuttle in 2.95 Ga Ijzermijn IF 100
6.1.2. Lack of a Ce anomaly 105
7. Arvadi Spring as a modern analog for Archean oxygen oases 106
7.1.1. $Fe(II)_{aq}$ oxidation, Fe(III) reduction and the role of iron metabolizing microorganisms in the Arvadi Spring and implications for the Mesoarchean Ijzermijn IF of the Pongola Basin .. 109
8. Summary and Conclusions 117
Appendices 120
References 135

Abstract

There is growing evidence from redox sensitive elements and stable isotope tracers (i.e. Mn contents, Mo and Fe isotope variations and multiple S isotope systematics) that shallow-water sediments of the 2.95 Ga Mozaan Group (Pongola Supergroup) in South Africa were deposited in a so-called oxygen oasis, i.e. in oxidizing shallow seawater. Moreover, previously reported stable Cr isotopic fractionation in Archean paleosols and iron formations (IF) have been interpreted as a signature of oxidative weathering of Cr(III) to Cr(VI) in soils by free atmospheric oxygen, and delivery of isotopically heavy Cr(VI) into the oceans. The oldest reported isotopically heavy Cr fingerprints of this process were found in the Ijzermijn IF, which is also located within the 2.95 Ga Mozaan Group (Pongola Supergroup) in South Africa. These heavy Cr isotopic signatures thus point to a globally oxygenated atmosphere at the time of the Pongola Supergroup sedimentation rather than the existence of localized oxygen oasis as suggested from Mo and Fe isotope systematics. However, mineralogical, elemental and sulfur isotopic evidence in Mozaan Group sediments is largely in favor of the concurrent atmosphere having remained reducing. Furthermore, fractionated stable Cr isotopic signatures have only been found to date in surface outcrop samples of the Ijzermijn IF from the White Mfolozi Inlier exposed along the White Mfolozi River Gorge. During the course of this thesis, this outcrop was resampled along with two drill cores of the Ijzermijn IF and a drill core of the Scotts Hill IF to represent multiple exposures of Mozaan Group IF with different states of preservation. A detailed geochemical comparison on bulk samples of different units was undertaken using stable Cr, Mo and Fe isotopes as well as ($^{234}U/^{238}U$) activity ratios coupled with trace and major elements. Plausibility of an oxygen oasis during the deposition of the Ijzermijn IF was also investigated and the findings (i.e. the stable Fe isotopic composition) were compared with a ferruginous, oxic modern environment, Arvadi Spring in Engadin, Switzerland, that mimics the depositional conditions during high oxygen intervals before the Great Oxidation Event (GOE).

Drill core samples from the Ijzermijn IF are characterized by high contents in the iron carbonate mineral siderite ($FeCO_3$) and thus reveal large loss on ignition (LOI) and $Fe(II)/Fe_{tot}$ ratios. These samples also have ($^{234}U/^{238}U$) activity ratios that are in secular equilibrium (i.e. value of 1), and have unfractionated $\delta^{53/52}Cr$ values that are within the range of the igneous inventory. Outcrop samples from the White Mfolozi River gorge, on the other hand, have no siderite and thus show low LOI and very low $Fe(II)/Fe_{tot}$ ratios, have disequilibrium ($^{234}U/^{238}U$) activity ratios, unusually high U/Th ratios (up to 12.6), and partly show fractionated $\delta^{53/52}Cr$ values outside of the igneous inventory (up to 0.418 ‰). The outcrop IF and shale samples of the Sinqeni Formation from the White Mfolozi River bed show very strong deviations from the secular equilibrium ($^{234}U/^{238}U$) activity ratio. ($^{234}U/^{238}U$) values for

Ijzermijn IF samples range from 1.05 to 1.77, similar to U dissolved in modern river water. ($^{234}U/^{238}U$) activity in more U-rich, overlying Vlakhoek Member shales range from 0.89 to 0.96, similar to values of actively weathering saprolitic basaltic soil profiles. Outcrop samples also show enrichments of other elements (W, Tl, As, MREE) that far exceeding that observed in correlative drill core units. These data indicate that, modern weathering effects superimposed geochemical fingerprints on the original paleoredox signatures at the White Mfolozi River bed outcrop. Overall rare earth element and yttrium (REE+Y) mixing models agree well with previous studies, confirming that they were minimally disturbed by weathering and are consistent with a high magnitude of continental solutes delivered in a near–shore depositional environment, with a minor contribution of hydrothermally derived fluids that upwelled into shallower depositional setting. Ijzermijn IF outcrop samples tend towards heavier $\delta^{56/54}Fe_{IRMM\text{-}014}$ (- 1.729 to - 0.438 ‰) and $\delta^{98/95}Mo_{NIST3134+0.25}$ (- 0.476 to + 1.160 ‰) values than drill core ones (- 2.522 to - 0.753 ‰ and - 0.546 to + 0.382 ‰, respectively). Neither metal stable isotope system of outcrop samples closely correlates with ($^{234}U/^{238}U$), thus a near-pristine sedimentary origin for these signatures cannot be excluded. Nevertheless, for any interpretation of redox-conditions during the sedimentation of the Mozaan Group in the Pongola basin, Fe and Mo isotopic results of outcrop samples from this and previous studies must be regarded with great caution.

For drill core DDN-1 and PMH24/L1 samples, a moderate positive correlation in $\delta^{56/54}Fe_{IRMM\text{-}014}$ with log [Fe/Mn] and a lack of a negative correlation between $\delta^{56/54}Fe_{IRMM\text{-}014}$ and $\delta^{98/95}Mo_{NIST3134+0.25}$ values are observed. These observations point to preferential adsorption of isotopically light Mo onto MnO_2 particles in surface water, hence oxic surface water conditions in the Pongola Epicontinental Sea, as was already proposed in previous studies. Reduction of the Mn-oxides together with microbial Fe reduction in the reduced sediment pile of the Pongola basin led to the formation of Mn- and Fe-carbonates during early diagenesis storing the observed stable Fe and Mo isotopic signatures. The so-called MnO_2-shuttle first proposed for the Neoarchean 2.46 Ga old Koegas IF is thus extended to late Mesoarchean shallow-marine depositional settings. From the stable Fe isotopic perspective, depositional model for the Ijzermijn IF requires the upwelling and partial oxidation of deep water $Fe(II)_{aq}$ directly by seawater O_2 and MnO_2 particles, leading to the progressive depletion of heavy Fe isotopes in the remaining $Fe(II)_{aq}$ pool at the shallower water depths, following an open system Rayleigh trend.

Iron concentrations and $\delta^{56/54}Fe_{IRMM\text{-}014}$ values of water samples ($Fe(II)_{aq}$) and Fe-precipitates (red flocs; $Fe(III)_{ppt}$) were determined from various sampling locations at the modern analog Arvadi Spring flow system. All results are from samples recovered during two sampling campaigns in October 2014 and June 2018. The source of the Arvadi water has a $\delta^{56/54}Fe_{IRMM\text{-}014}$ value of - 0.359 ‰ and becomes isotopically lighter in the center of the pond and towards the outflowing creek with minimum

$\delta^{56/54}Fe_{IRMM\text{-}014}$ values of - 1.482 ‰ and - 1.598 ‰, respectively. Iron concentrations of Arvadi waters along the flow path correlate with their respective $\delta^{56/54}Fe_{IRMM\text{-}014}$ values (R^2= 0.66) and decrease from 0.436 ppm at the source to 0.082 ppm at the creek and become as low as 0.011 ppm after mixing with the natural forest brook. The iron concentration and $\delta^{56/54}Fe_{IRMM\text{-}014}$ values of red flocs also decrease along the flow path, from the source to the creek, from 32.69 wt % to 1.80 wt % and 0.323 ‰ to - 0.467 ‰, respectively. However, unlike the water samples, the Fe isotopic compositions and Fe concentrations of red flocs lack a strong correlation. The stable Fe isotopic composition of the water and precipitates in Arvadi is a result of abiotic and biotic oxidation of $Fe(II)_{aq}$ to $Fe(III)_{ppt}$ under oxic conditions. The oxidation of $Fe(II)_{aq}$ to $Fe(III)_{ppt}$ follows an open system Rayleigh trend from the source to the creek, leading to progressively lighter Fe isotopic compositions for both, the remaining $Fe(II)_{aq}$ pool and the resulting $Fe(III)_{ppt}$, along the flow path. The ongoing microbial dissimilatory iron reduction in anoxic niches along the flow path of the Arvadi Spring enhances the trend towards lighter Fe isotopic compositions in the $Fe(II)_{aq}$ pool, while causing the remaining $Fe(III)_{ppt}$ pool to become slightly heavier. This combination of abiotic and biotic Fe oxidation in the water and microbial Fe reduction in the sediment causes the observed decoupling of Fe concentrations and $\delta^{56/54}Fe_{IRMM\text{-}014}$ values in the red flocs. As such, the complex mechanism of Fe redox cycling in the Arvadi Spring gives important insight about Fe removal from water to sediment and allowing more accurate models for IF deposition in Mesoarchean to Paleoproterozoic oxygen oasis.

Zussammenfassung

Es gibt zunehmende Beweise von redox-sensitiven Elementen und der Systematik stabiler Isotopensysteme (z.B. Mn-Gehalte, Mo-, Fe- und multiple S-Isotopenvariationen), dass Flachwasserablagerungen der 2.95 Ga Mozaan-Gruppe (Pongola Supergruppe) in Südafrika in einer sogenannte „Sauerstoff Oase“ (in oxidierendem flachem Meerwasser) abgelagert wurden. Darüber hinaus wurde die stabile Cr-Isotopenfraktionierung in archaischen Paläoböden und Eisenformationen (EF) als Signatur der oxidativen Verwitterung von Cr(III) zu Cr(VI) in Böden durch freien Sauerstoff in der Atmosphäre und die daraus resultierende Lieferung von isotopisch schwerem Cr (VI) in die Ozeane interpretiert. Die ältesten isotopisch schweren Cr-Fingerabdrücke dieses Prozesses wurden in der Ijzermijn EF gefunden, welche sich ebenfalls in der 2.95 Ga Mozaan-Gruppe (Sinqeni Formation, Pongola Supergruppe) in Südafrika befindet. Diese schweren Cr-Isotopensignaturen deuten somit auf eine global mit Sauerstoff angereicherte Atmosphäre zum Zeitpunkt der Sedimentation der Pongola-Supergruppe hin und nicht auf lokale Sauerstoffoasen, wie dies bislang anhand der Mo- und Fe-Isotopensystematik nahegelegt wurde. Basierend auf Indizien aus der Mineralogie, der Elementanalyse und stabilen Schwefelisotopen in Sedimenten der Mozaan-Gruppe wurde demnach von einer simultan existierenden anoxischen Atmosphäre ausgegangen. Des Weiteren wurden die fraktionierten stabilen Cr-Isotopensignaturen bisher nur in Oberflächenaufschlussproben der Ijzermijn EF aus dem White Mfolozi Inlier Gebiet gefunden, die entlang des White Mfolozi-Flussbetts exponiert sind. Um mehrere Expositionen der Mozaan Group EF mit unterschiedlichen Erhaltungszuständen darzustellen wurde im Verlauf dieser Dissertation dieser Aufschluss zusammen mit zwei Bohrkernen der Ijzermijn EF und einem Bohrkern der Scotts Hill EF neu beprobt. Ein detaillierter geochemischer Vergleich von sogennanten Gesamtgesteinsproben aus verschiedenen Einheiten wurde unter Verwendung von stabilen Cr-, Mo- und Fe-Isotopen sowie ($^{234}U/^{238}U$)-Aktivitätsverhältnissen in Verbindung mit Spuren und Hauptelementen durchgeführt. Die Plausibilität einer Sauerstoff-Oase während der Ablagerung der Ijzermijn EF wurde ebenfalls untersucht und die Ergebnisse (z.B. die stabile Fe-Isotopenzusammensetzung) wurden mit einer eisenhaltigen, oxischen modernen Umgebung, Arvadi Quelle in Engadin, Schweiz, welche die Ablagerungsbedingungen während hoher Sauerstoffintervalle vor dem Great Oxidation Event (GOE) imitiert, verglichen.

Bohrkernproben aus der Ijzermijn EF zeichnen sich durch hohe Gehalte des Eisencarbonat-Minerals Siderit ($FeCO_3$) aus und weisen somit hohe Glühverluste (engl. Loss on Ignition LOI) und hohe $Fe(II)/Fe_{tot}$-Verhältnisse auf. Diese Proben haben auch Aktivitätsverhältnisse von ($^{234}U/^{238}U$), die sich im säkularen Gleichgewicht (mit einem Wert von 1) befinden, und zeigen unfraktionierte $\delta^{53/52}Cr$-Werte, welche im Bereich des magmatischen Bestandes liegen. Proben aus dem White Mfolozi Flussbett haben dagegen enthalten keinen Siderit und weisen daher niedrigen LOI und sehr niedrige

Fe(II)/Fe_{tot}-Verhältnisse auf. Des Weiteren haben die Aufschlussproben ($^{234}U/^{238}U$)-Aktivitätsverhältnisse welche nicht im Gleichgewicht liegen, ungewöhnlich hohe U/Th Verhältnisse (bis zu 12.6) und sie zeigen teilweise fraktionierte $\delta^{53/52}Cr$ Werte außerhalb des magmatischen Bestandes (bis zu 0.418 ‰) auf. Die Aufschluss-EF- und Schieferproben der Sinqeni-Formation aus dem White Mfolozi-Flussbett zeigen sehr starke Abweichungen vom Aktivitätsverhältnis des säkularen Gleichgewichts in den ($^{234}U/^{238}U$)-Aktivitätsverhältnissen. ($^{234}U/^{238}U$) Werte für Ijzermijn-EF-Proben reichen von 1.05 bis 1.77, ähnlich der Werte gelösten Urans in modernem Flusswasser. Die ($^{234}U/^{238}U$) Aktivität in U-reicheren, überliegenden Vlakhoek Member-Schiefern liegt zwischen 0.89 und 0.96, ähnlich den Werten aktiv verwitternder saprolitischer Basaltbodenprofile. Aufschlussproben zeigen außerdem auch Anreicherungen anderer Elemente (W, Tl, As, MREE), welche die Werte aus in korrelierenden Bohrkern-Proben weit übersteigen. Diese Daten deuten darauf hin, dass geochemische Fingerabdrücke moderner Verwitterungseffekte die ursprünglichen Paleoredox-Signaturen in White Mfolozi River-Aufschlussproben überlagern. Seltene Erden und Yttrium (REE + Y)-Mischungsmodelle stimmen gut mit früheren Studien überein und bestätigen, dass sie durch Witterungseinflüsse minimal gestört wurden. Diese deuten allerdings auf einen hohen Anteil an kontinentalen gelösten Stoffen, welche in einer küstennahen Umgebung abgelagert wurden, sowie auf einen geringen Anteil von hydrothermalen Fluiden, die in das flachere Ablagerungsmilieu aufgestiegend sind, hin. Ijzermijn EF-Aufschlussproben tendieren zu schwereren $\delta^{56/54}Fe_{IRMM-014}$ (- 1.729 bis - 0.438 ‰) und $\delta^{98/95}Mo_{NIST3134+0.25}$ (- 0.476 bis + 1.160 ‰) Werten als Bohrkernproben (- 2.522 bis - 0.753 ‰ und - 0.546 to + 0.382 ‰) hin. Keines der stabilen Isotopensysteme von Übergangsmetallen in Aufschlussproben korreliert mit ($^{234}U/^{238}U$) Aktivitätsverhältnissen. Daher kann ein nahezu ursprünglicher sedimentärer Ursprung für diese Signaturen nicht ausgeschlossen werden. Dennoch sollten alle Interpretationen bezüglich der Redox-Bedingungen während der Sedimentation der Mozaan-Gruppe im Pongola-Becken basierend auf Ergebnissen von stabilen Fe- und Mo-Isotopen von Aufschlussproben aus dieser und früheren Studien mit großer Vorsicht betrachtet werden.

Für Bohrkern DDN-1 und PMH24/L1 Proben sind eine moderate positive Korrelation in $\delta^{56/54}Fe_{IRMM-014}$ mit log[Fe/Mn] und eine negative Korrelation zwischen $\delta^{56/54}Fe_{IRMM-014}$ und $\delta^{98/95}Mo_{NIST3134+0.25}$ Werten zu beobachten. Diese Korrelationen deuten auf eine bevorzugte Adsorption von isotopisch leichtem Mo an MnO_2-Partikel im Oberflächenwasser und damit auf oxische Oberflächenwasserbedingungen im Pongola Epikontinentalen Becken hin, wie dies bereits in früheren Studien vorgeschlagen wurde. Die Reduktion der Mn-Oxide zusammen mit der mikrobiellen Fe-Reduktion im reduzierten Sedimenten des Pongola-Beckens führte während der frühen Diagenese zur Bildung von Mn- und Fe-Carbonaten, wobei die beobachteten stabilen Fe- und Mo-Isotopensignaturen erhalten wurden. Der sogenannte MnO_2-Shuttle, der erstmals für die neoarchaische 2.46 Ga alte

Koegas-EF vorgeschlagen wurde, wird daher auf die späten mesoarchaischen flach-marinen Ablagerungen ausgeweitet. Das Ablagerungsmodell für die Ijzermijn EF beinhaltet partielle Oxidation und Ausfällung von $Fe(II)_{aq}$ durch gelösten Sauerstoff und durch MnO_2 Partikel aus dem Meerwasser, und die daraus resultierende Abnahme der schweren Fe-Isotope im restlichen $Fe(II)_{aq}$-Pool in den flacheren Wassertiefen, welche einem Rayleigh-Trend in einem offenen System folgen.

Eisenkonzentrationen und $\delta^{56/54}Fe_{IRMM-014}$ Werte der Wasserproben ($Fe(II)_{aq}$) und die Eisenpräzipitäte (rote Flocken; $Fe(III)_{pp}$) wurden an Proben verschiedener Probenahmestellen entlang der heutigen Arvadi Quelle (Engadin, Schweiz) und ihres Ausflusses bestimmt. Alle Ergebnisse stammen aus zwei seperaten Probenahmen im Oktober 2014 und im Juni 2018. Die Quelle des Arvadi Wassers hat einen $\delta^{56/54}Fe_{IRMM-014}$ Wert von - 0.359 ‰ und wird in der Mitte des Teichs und in Richtung des ausfließenden Baches isotopisch leichter mit minimalen $\delta^{56/54}Fe_{IRMM-014}$ Werten von - 1.482 ‰ beziehungsweise - 1.598 ‰. Die Eisenkonzentration des Arvadi-Wassers korreliert mit den $\delta^{56/54}Fe_{IRMM-014}$ Werten (R^2 = 0.66) entlang seines Fließweges und sinkt von 0.436 ppm an der Quelle auf 0.082 ppm am Bach und erreicht ein Minimum (0.011 ppm) nach dem Mischen mit einem natürlichen Waldbach. Die Eisenkonzentration und die $\delta^{56/54}Fe_{IRMM-014}$ -Werte der roten Flocken nehmen ebenfalls von 32.69 Gew. % auf 1.80 Gew. % und 0.323 ‰ bis -0.467 ‰ jeweils entlang der Fließstrecke von der Quelle bis zum Bach ab. Die Isotopenzusammensetzung von Fe und die Fe-Konzentration von roten Flocken zeigen jedoch einen Entkopplungstrend und weisen im Gegensatz zu den Wasserproben keine starke Korrelation auf. Die stabile Fe-Isotopenzveränderung des Wassers und der Sedimente der Arvadi-Quelle ist das Ergebnis einer abiotischen und biotischen Oxidation von $Fe(II)_{aq}$ zu $Fe(III)_{ppt}$ unter oxischen Bedingungen. Die Oxidation von $Fe(II)_{aq}$ zu $Fe(III)_{ppt}$ von der Quelle hin zum Bach folgt einem Rayleigh-Trend in einem offenen System, wobei der verbleibende $Fe(II)_{aq}$-Pool und der resultierende $Fe(III)_{ppt}$-Pool allmählich entlang des Flussbetts isotopisch leichter werden. Die fortlaufende mikrobielle dissimilatorische Eisenreduktion in anoxischen Nischen entlang des Fließpfads der Arvadi-Quelle verstärkt den Trend zu leichteren Fe-Isotopenzusammensetzungen im $Fe(II)_{aq}$-Pool, während der $Fe(III)_{ppt}$-Pool etwas schwerer wird. Die Kombination aus abiotischer und biotischer Fe-Oxidation im Wasser und mikrobieller Fe-Reduktion im Sediment bewirkt die beobachtete Entkopplung von Fe-Konzentrationen und $\delta^{56/54}Fe_{IRMM-014}$-Werten in den roten Flocken. Der komplexe Mechanismus des Fe-Redox-Zyklus in der Arvadi-Quelle gibt daher wichtige Einblicke in de Umlagerung von Fe aus dem Wasser in die Sedimente und ermöglicht genauere Modelle für die EF-Ablagerung in mesoarchaischen Sauerstoff-Oasen.

1. Introduction

1.1. Motivation and significance of the study

The appearance of Earth's earliest accumulation of free atmospheric oxygen – widely known as the Great Oxidation Event (GOE) – was dated and constrained between ca. 2.45 and 2.32 Ga based on the disappearance of mass independent fractionation of sulfur isotopes (MIF-S) and observations of redox-changes of surface environments from the sedimentary rock record (e.g. Bekker et al., 2004; Farquhar et al., 2000, 2002; Guo et al., 2009; Hannah et al., 2004; Holland, 1994; 2002; 2006; 2011; Luo et al., 2016; Pavlov and Kasting, 2002; Roscoe, 1973). However, discussions about the exact mode and timing of the appearance of the first free oxygen in the atmosphere and the oceans were re-fuelled due to the suggestion that organisms capable of producing O_2 may already have existed long before the GOE (Figure 1-1) (Haqq-Misra et al., 2011; Hoashi et al., 2009; Kappler et al., 2005; Kasting et al., 1979; Konhauser et al., 2002: Konhauser et al., 2007; Lalonde & Konhauser, 2015; Rasmussen et al., 2008; Towe, 1990).

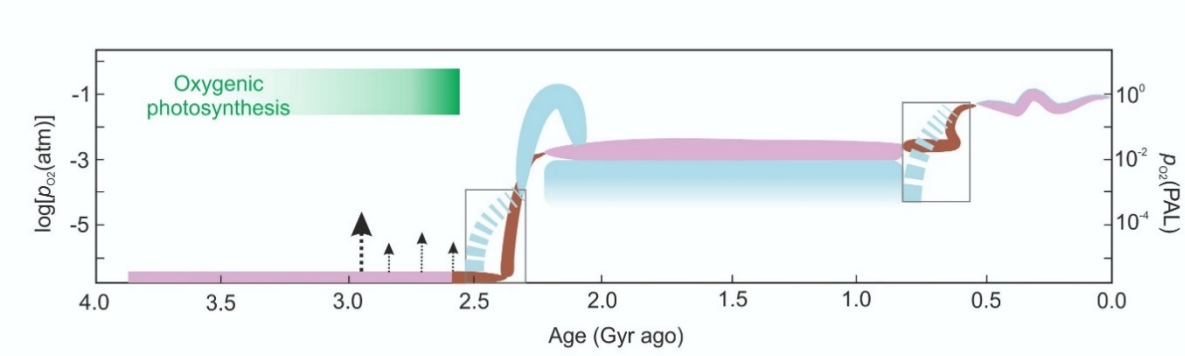

Figure 1-1: Evolution of atmospheric oxygen through time in pink (by Kump, 2008, classical two-step increase of atmospheric oxygen, first step marking the GOE) versus blue (fluctuations in the generally increasing trend of the atmospheric oxygen), along with onset of oxygenic photosynthesis. The black arrows indicate whiffs of oxygen in late Archean. Left axis shows log pO_2 and right axis shows pO_2 relative to the present atmospheric level (PAL). The figure was modified from Lyons et al., (2014).

Deep time elemental systematics and stable isotope variations of the redox-sensitive elements (e.g. Cr, Mo, U and Fe) in marine sedimentary rocks have become very popular tools to investigate the evolution of Earth's atmosphere-hydrosphere system. Nevertheless, reconstructing the exact evolution of redox conditions in the pre – GOE atmosphere and oceans from isotope geochemical signatures of marine sediments remains complex due to local vs. global scales of geochemical signatures, post-depositional effects as well as differences in depositional conditions of the studied sediments. Thus, there is an ongoing debate whether the observed isotope compositions of marine sedimentary rocks depict a globally oxygenated atmosphere in equilibrium with oxygenated surface ocean water or local marine *oxygen oases* (e.g. Fischer, 1965; Kasting et al., 1992; Kendall et al., 2013;

Olson et al., 2013; Pavlov and Kasting, 2002, Reinhard et al., 2013; Riding et al., 2014). "*Oxygen oases*" are restricted shallow marine environments along continental margins, in which a local redox stratified water column develops (Olson et al., 2013; Reinhard et al., 2013). Thereby, oxygen is supplied from photosynthetic activity of microorganisms particularly in the photic zone (Roy, 2000; 2006). According to the *oxygen oasis* model, the reduced compounds in the open ocean (such as CH_4, CO_2, N_2, H_2, SO_2, Fe^{2+}) surrounding the oases prevent oxygen from building up persistently and on a large scale (Gaillard et al., 2011; Kump and Barley 2007; Lyons et al., 2014; Schidlowski, 1983; Swanner et al., 2015).

There is growing evidence from redox sensitive elements and stable isotope tracers (i.e. Mn contents, Mo and Fe isotope variations and multiple S isotope systematics) that shallow-water sediments of the 2.95 Ga Mozaan Group (Pongola Supergroup) in South Africa were deposited in such an oxygen oasis, i.e. in oxidizing shallow seawater, despite the mineralogical, elemental and isotopic evidence for a reducing atmosphere (Crowe et al., 2013; Eickmann et al., 2018; Ossa et al., 2016; Planavsky et al., 2014a). Hence, in this study, 2.95 billion year (Ga) old Ijzermijn Iron Formation (IF), from Mozaan Group was investigated at the outcrop exposed along the White Mfolozi River Gorge, and from two drill cores. A drill core of the Scotts Hill IF was included to represent multiple exposures of Mozaan Group IFs with different states of preservation. Furthermore, an iron-sulfur spring, *Arvadi Spring,* in Bad Alvaneu (Engadin, Switzerland) was included in this study as a modern analog to simulate the depositional environment of a Mesoarchean marine oxygen oasis or the ferro-euxinic, redox-stratified transition zones of late Archean and Proterozoic oceans during high-oxygen intervals.
The main objectives of the study are:

(1) *To test whether the widely cited Cr-stable isotope and redox-sensitive elemental evidence (Crowe et al. 2013) for the late Mesoarchean and Neoarchean oxidative weathering, thus global presence of atmospheric oxygen, is an original fingerprint,*

(2) *The reconstruction of paleoredox conditions in the depositional environment of the Ijzermijn IF as a potential Mesoarchean oxygen oasis,*

(3) *To compare the stable Fe isotopic evidence from a potential Mesoarchean oxygen oasis with a modern analog depositional environment.*

1.2. Scope of the study

In the following 8 chapters of this dissertation, the scientific background is presented in Chapter 1, with a review of the Great Oxidation Event, oxygen oases and atmospheric oxidative weathering during Mesoarchean, original geochemical fingerprints versus modern weathering signatures, and modern habitats mimicking Archean oxygen oases. Principles of the non-traditional isotope systematics including stable Cr, Mo, Fe and U which were used in this study, are also introduced in this chapter. Geological and hydrological overview for the Mesoarchean iron formations and the modern Arvadi Spring are presented in Chapter 2, including detailed descriptions and sampling procedures of drill cores DDN-1, and PMH24L/1, outcrop samples (White Mfolozi Inlier) from the Sinqeni Formation and drill core WV006 from the Thalu Formation, Mozaan Group, South Africa and water and sediment samples from the modern Arvadi Spring, Engadin, Switzerland. Analytical techniques employed during the course of this thesis are described in Chapter 3, and the results are presented in Chapter 4.

Chapter 5 discusses whether oxidative weathering signatures recorded by stable Cr isotopes of the 2.95 Gyr old Ijzermijn iron formation in South Africa, reported in an earlier and this study, are original isotopic signatures or modern weathering overprints. Emphasis of this discussion is also given on ($^{234}U/^{238}U$) activity ratios, trace element and rare earths + yttrium indicators, carbonate content differences between drill cores and the outcrop inferred from ferrous iron contents and the loss on ignition values. Impacts of possible modern weathering effects on the stable Mo, Fe and U isotopic signatures are also evaluated and discussed in this chapter.

Chapter 6 centers on the discussion about the plausibility of a Mesoarchean oxygen oasis on its center using stable Mo and Fe isotopes as a proxy. The importance of MnO_2 shuttling is emphasized with a proposed model for the depositional environment of the Ijzermijn iron formation in Mesoarchean.

Chapter 7 presents an outlook on the modern environments analogous to the Archean oxygen oases, with an example from Arvadi Spring in Switzerland. $Fe(II)_{aq}$ oxidation, Fe(III) reduction and the role of iron metabolizing microorganisms in the Arvadi Spring and implications for the Mesoarchean Ijzermijn iron formation are further discussed in this chapter in detail.

Finally, Chapter 8 provides a summary of the main findings and conclusions of this study and describes a depositional model for the Mesoarchean Ijzermijn iron formation supported by the findings from the modern Arvadi Spring environment.

1.3. Mesoarchean atmospheric and ocean conditions vs. modern weathering effects

Abundances of redox sensitive elements such as Cr, U, Mo, and Fe, and their stable isotopic signatures in ancient marine sedimentary rocks are now widely used to trace paleoredox conditions in Earth´s surface environments. Due to the lack of reliable, direct biomarker tracing of oxygenic photosynthesis (French et al., 2015), these inorganic geochemical paleoredox proxies became the primary tool capable of "fingerprinting" biologically mediated oxygenation of the oceans and atmosphere (Anbar et al., 2007; Crowe et al., 2013; Eroglu et al., 2015; Frei et al., 2009; Frei et al., 2016; Kurzweil et al., 2015; Olson et al., 2013; Reinhard et al., 2009; Riding et al., 2014; Satkoski et al., 2015; Wille et al., 2007). The view that photosynthetic organisms capable of producing O_2 existed since at least the Neoarchean and possibly earlier (Haqq-Misra et al., 2011; Hoashi et al., 2009; Kappler et al., 2005; Kasting et al., 1979; Konhauser et al., 2002; Konhauser et al., 2007; Lalonde & Konhauser, 2015; Rasmussen et al., 2008) is now widely accepted, although molecular clock evidence has been argued for a younger emergence of oxygenic photosynthesis (e.g., Shih et al., 2017) that is close to the timing of the GOE.

Recent studies on Archean sedimentary rocks imply accumulation of oxygen, already several hundred million years before the GOE, at least locally, as "whiffs of oxygen", which led to the oxidative cycling of redox sensitive elements (Anbar et al., 2007) (Figure 1-1). For example, despite lack of authigenic enrichment of Mo in 3.8 to 2.7 Ga deep-sea euxinic black shales and near-igneous rock $\delta^{98/95}$Mo values (see equation 9 in section 3.1.6) indicating absence of free atmospheric O_2 at that time (Anbar et al., 2007; Kendall et al., 2017; Wille et al., 2007; 2013), authigenic enrichment of Mo and increasingly heavy $\delta^{98/95}$Mo values of 2.6 to 2.45 Ga black shales and carbonates were interpreted as rising redox potentials in the atmosphere and oceans and the onset of oxidative Mo weathering some 200 million years before the GOE (Anbar et al., 2007; Eroglu et al., 2015; Kurzweil et al., 2015; 2016, Voegelin et al., 2010; Wille et al., 2007). Similarly, stable isotope variations of chromium, reported as $\delta^{53/52}$Cr values (see equation 8 in section 3.1.5.), emerged as particularly important for being a near-direct reflection of changes in the two major redox states of Cr (+III and +VI), and having a more direct tie to continental oxidative weathering. Unaltered igneous rocks almost exclusively contain trivalent chromium and have a limited range in $\delta^{53/52}$Cr values of - 0.124 ± 0.101 ‰ (2s.d.; Schoenberg et al., 2008) referred to as the "igneous inventory" or "unfractionated" values. The common model for chromium cycling in Earth's surface environments assumes that $\delta^{53/52}$Cr values recorded in soils and marine sedimentary rocks that deviate significantly from this igneous inventory are the result of chromium redox processes on the continents Cr redox cycling is directly linked to the presence of MnO_2, which is known as one of the most favorable oxidants of Cr(III) in modern soils. Thereby, Mn^{2+} liberated from rocks during soil formation is first oxidized by free atmospheric oxygen (and supported

by microbial avtivity) to Mn(IV)-oxide compounds (e.g. birnessite, pyrolusite) and partial oxidation of Cr(III) to Cr(VI) is then catalyzed on the surface of the newly formed MnO_2 minerals (Figure 1-2) (Ball & Izbicki, 2004; Becquer et al., 2003; Bartlett et al., 1979; Cooper, 2002; Eary et al., 1987; Fandeur et al., 2009; Fendorf et al., 1995; Garnier et al., 2013; Mills et al., 2011; Oze et al., 2007). This partial Cr(III)-oxidation results in isotopically heavy Cr(VI), which is transported by river and groundwaters to the oceans to be scavenged and co-precipitated in Fe(III)-Cr(III) oxyhydroxides after quantitative reduction of Cr(VI) by Fe(II) in seawater (Frei et al., 2009; Reinhard et al., 2013) (Figure 1-2). The remaining trivalent chromium in the soil is thereby enriched in the light isotopes with $\delta^{53/52}$Cr values below the range of the igneous inventory (Berger & Frei, 2014; Frei & Polat, 2013; Frei et al., 2014; Døssing et al., 2011).

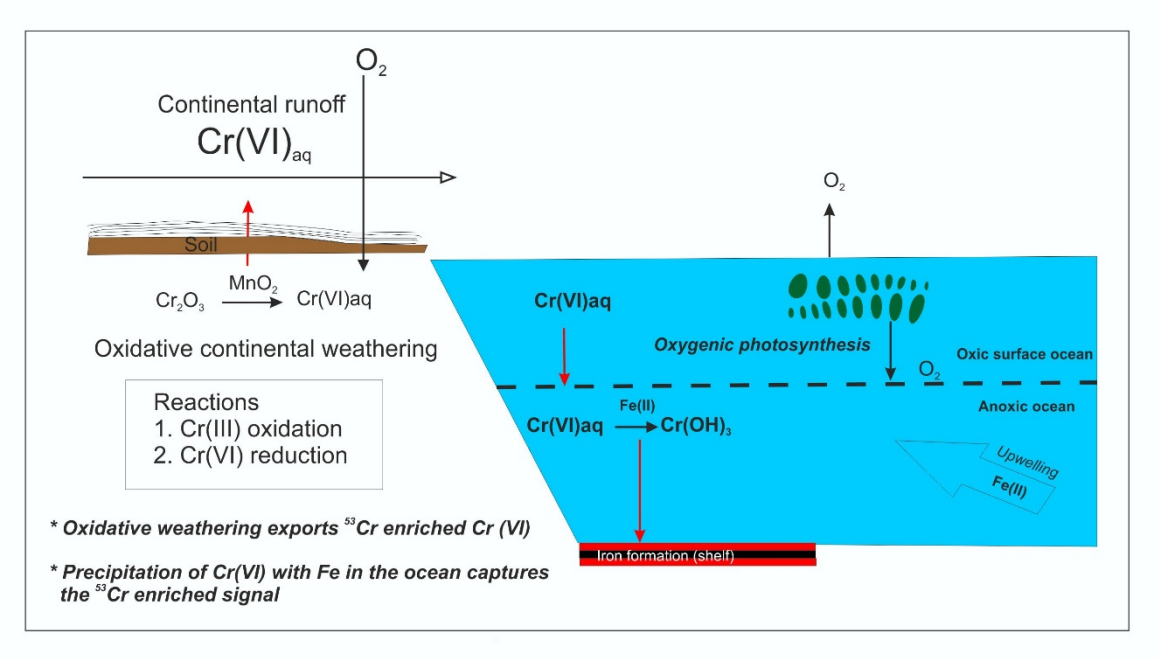

Figure 1-2: The summary of the model by Frei et al. (2009) for oxidative weathering of Cr(III) to Cr(VI) in soils, catalyzed by MnO_2, and consequent delivery of the heavy Cr(VI) into the oceans followed by re-reduction with Fe(II), and co-precipitation with Fe-oxyhydroxides, eventually leading to variations in stable Cr isotopic record, outside of the igneous inventory in marine sedimentary rocks such as iron formations (Schoenberg et al., 2008).

Heavy $\delta^{53/52}$Cr values compared to the igneous Cr isotopic composition have been reported in up to 2.75 Gyr old Banded Iron Formations (BIFs) (Frei et al., 2009), which have been interpreted as evidence for oxidative Cr(VI) delivery from the continents to the oceans at the time of BIF deposition. More recently, Crowe et al., (2013) reported heavy $\delta^{53/52}$Cr values of up to + 0.28 ‰ in outcrop samples from the Ijzermijn IF of the 2.95 Ga old Sinqeni Formation and light $\delta^{53/52}$Cr values down to -0.98 ‰ of drill core samples from the approximately 3.0 Ga Nsuze paleosol of the underlying Nsuze Formation, both belonging to the Pongola Supergroup in South Africa. Taken as evidence for oxidative weathering, the latter study implies that the timing of atmospheric oxygenation occurred 600 million years earlier than recorded in the GOE by MIF-S and mineralogical observations from the rock record (Farquhar,

2002; Holland, 2006; Roscoe, 1973). Most recently, Frei et al. (2016) reported fractionated Cr isotopes relative to the igneous reservoir, and elevated U/Th ratios compared to the modern crust, in 3.8 – 3.7 Ga old BIFs from Isua, Greenland, which they interpreted as a signal for oxidative mobilization of U, and thus presence of reactive oxygen species in the Eoarchean surface environment. However, this interpretation, which would render the usually accepted concept of a reduced Neo- and Mesoarchean atmosphere obsolete, has been received very critically in the scientific community, since the Isua Greenstone Belt has undergone several phases of high-temperature and high-pressure metamorphic overprints (Kamber et al., 2005; Moorbath et al., 1972; 1973; 1975, Moorbath and Kamber, 1998; Whitehouse and Fedo, 2003; 2007; Whitehouse and Kamber, 2005).

Nevertheless, several studies have pointed out complexities in the aforementioned oxidative stable Cr isotope cycle and have resulted in challenges of its direct application to interpreting the reported Cr isotope variations in Archean BIFs and paleosols as an oxidative weathering fingerprint (Konhauser et al., 2011; Planavsky et al., 2014a; Scheiderich et al., 2015; Holmden et al., 2016; Babechuk et al., 2017; Saad et al., 2017; Babechuk et al., 2018). Konhauser et al. (2011), for example, questioned that Cr redox cycling is the only process capable of causing measurable Cr isotopic fractionation and suggested that heavy $\delta^{53/52}$Cr values in Algoma-type BIFs reported by Frei et al. (2009) may be the result of small non-redox dependent Cr isotopic fractionation during rapid precipitation from hydrothermal fluids. Indeed, non-redox dependent Cr isotopic fractionation has been reported as a potential cause of the large variations in $\delta^{53/52}$Cr values determined in highly altered ultramafic rocks (Farkaš et al., 2013) and was recently experimentally proven to occur between co-existing Cr(III)-chloride complexes (Babechuk et al., 2018; Larsen et al., 2016). Babechuk et al. (2017) proposed alternative non-redox Cr isotope fractionation processes, which do not fit the oxidative Cr weathering model due to very heavy $\delta^{53/52}$Cr values in the Cr depleted upper part of the Paleoproterozoic 1.85 Ga old Flin Flon paleosol in Canada. Furthermore, Planavsky et al. (2014b) reported unfractionated $\delta^{53/52}$Cr values for granular iron formations deposited between 1.8 Ga and 0.8 Ga. In particular, Planavsky et al. (2014a) reported unfractionated $\delta^{53/52}$Cr values from drill core and outcrop samples of the Superior-type Ijzermijn IF of the Sinqeni Formation, Pongola Supergroup. These unfractionated $\delta^{53/52}$Cr values are in direct contrast with the previously reported isotopically heavy Cr isotopic data from the Ijzermijn IF outcrop (Crowe et al., 2013), and bring up the possibility for a Cr isotopic overprint from post depositional processes.

Further information regarding redox changes in the atmosphere-hydrosphere system through time were recovered from stable Mo isotope variations of IFs, as important sinks for Mo in Archean oceans (Kurzweil et al., 2015; 2016; Planavsky et al., 2014a). Superior-Type IFs are particularly interesting for the investigation of the atmospheric and marine paleoredox evolutions, since they

formed at passive continental margins in near-shore shelf environments (Gross, 1980; Trendall, 2002). The characteristic rare earth element (REE) pattern largely resembling that of modern seawater can be used to monitor their purity as chemical sediments (Bau, 1993; Bau and Möller, 1993; Bau and Dulski, 1996). Planavsky et al. (2014a) reported significant Mo isotopic variations for Superior–type IFs with a depositional age spanning from 2.95 to 1.8 Ga. The reported variations in $\delta^{98/95}$Mo values positively correlate with Fe/Mn ratios and analyses from other IFs within this time frame as well confirmed this relationship (Kurzweil et al., 2016). Planavsky et al. (2014a) interpreted this correlation as preferential adsorption of isotopically light Mo from dissolved molybdate (MoO_4^{2-}) onto Mn- and Fe-oxide particle surfaces and the consecutive transfer of these signatures from the precursor Mn- and Fe-oxides to the early diagenetic Fe(II)- and Mn(II)-carbonates. As argued by these authors, precursor Mn-oxides would require free O_2 in the ocean water during the time of the deposition of these IFs, which could indicate the existence of oxygenic photosynthesis by 2.95 Ga, 600 million years earlier than the GOE. Furthermore, Ossa Ossa et al. (2016) have given more evidence for the existence of Mn- oxides, and Eickmann et al. (2018) showed that the surface waters were oxidized during that period in the Pongola Basin. However, there is an interesting, clear difference in the correlation between Fe/Mn and Mo isotopic compositions between drill core and outcrop Ijzermijn IF samples reported by Planavsky et al. (2014a), in that outcrop samples showing consistently higher Fe/Mn ratios and $\delta^{98/95}$Mo values (Figure 1-3). This observation can either be explained by different depositional settings for the drill core and outcrop localities in a model for Mn-oxide shuttling along a redox-gradient (Kurzweil et al., 2016) or it might be due to a post-depositional alteration only seen in the outcrop samples of this particular IF.

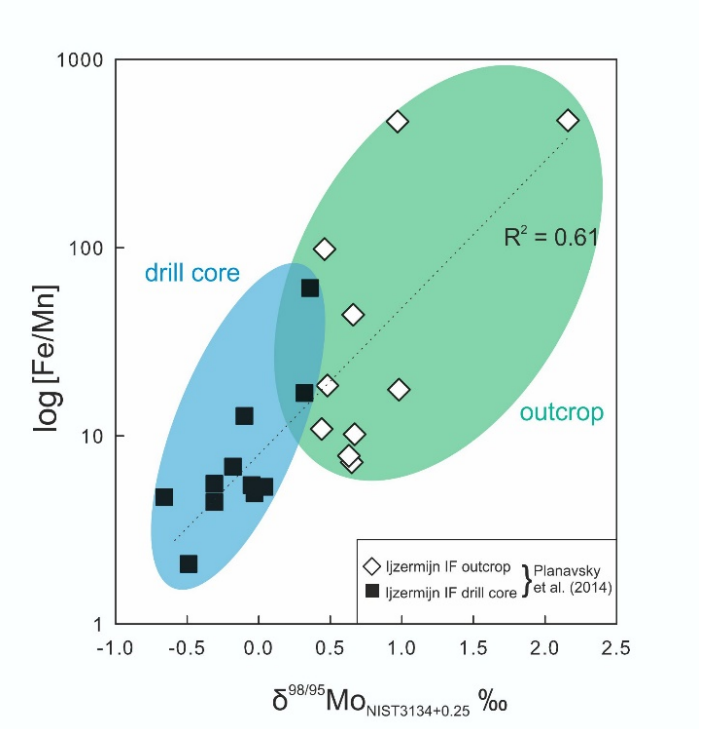

Figure 1-3: Fe/Mn in log scale, plotted against the $\delta^{98/95}Mo_{NIST3134+0.25}$ for the Ijzermijn IF outcrop (green area) and drill core samples (blue area) from Planavsky et al., (2014a) display a positive correlation (R^2 = 0.61). There is a notable cut-off between the drill core and outcrop samples, only the drill core samples showing light $\delta^{98/95}Mo_{NIST3134+0.25}$ values, and only the outcrop samples displaying high Fe/Mn ratios.

1.4. Non-traditional stable isotope systematics

The study of stable isotopes of light elements such as H, C, N, O and S, mainly by gas-source mass spectrometry has been included within the realm of "traditional stable isotope geochemistry" (Valley et al., 1986; Valley and Cole, 2001). The shift to non-traditional stable isotope geochemistry was enabled by the development of multi-collector inductively coupled plasma mass spectrometry (MC-ICPMS) (Halliday et al., 1995; Maréchal et al., 1999), which made it possible to measure isotopes of both light and heavy elements at high precision (e.g. Johnson et al., 2004; Teng et al., 2017). Non-traditional stable isotopes (e.g. Li, Mg, Si, Ca, Cr, Fe, Ni, Cu, Zn, Se, and Mo) differ from the traditional stables isotopes in that many of them are trace elements, with concentrations showing big variations depending on the geological reservoir they originate from. Furthermore, they range from highly volatile to refractory phases, many of them being redox-sensitive and/or biologically active, having differing bonding environments and mainly having high atomic numbers and more than two stable isotopes (Teng et al., 2017). The degree of isotopic fractionation in non-traditional stable isotopes is mainly controlled by:

1) Relative mass difference between isotopes,
2) Oxidation state change
3) Biological sensitivity
4) Volatility

In this study, the non-traditional stable isotopes of Cr, Mo, Fe and U were used as proxies, and are further discussed below. The activity ratio of ($^{234}U/^{238}U$) were used additionally to monitor potential modern weathering effects and is described in detail in section 3.3.1.

1.4.1. Principles of mass-dependent stable isotope fractionation

Under the right conditions *isotopic fractionation* (change in the relative proportions of different isotopes of the same element in various compounds) represents isotope partitioning at thermodynamic equilibrium. The mass dependent isotope fractionation occurs due to quantum chemical effects (Bigeleisen, 1965; Urey, 1947). The masses of the single atoms determine the zero point energy (ZPE) of a molecule, which tends to be lower in molecules with heavier isotopes causing stronger, more stable chemical bonds (e.g. having a higher dissociation energy) (Urey, 1947). The heavier isotope molecules also tend to have a lower vibrational energy which leads to lower translational velocities and result in isotopic fractionations. Thus, isotopic fractionations between molecules can be explained by differences in their zero point energies.

The fractionation resulting from equilibrium exchange reaction between two phases (or substances) A and B can be expressed by the isotope fractionation factor α (alpha):

$$\alpha_{A\text{-}B} = R_A/R_B \quad (1)$$

where *R* is the ratio of the heavy isotope to the lighter isotope in compounds A and B. The isotope difference of a sample is presented relative to a reference standard and is defined as the delta value and expressed in per mil:

$$\delta_{sample}\ (‰) = [(R_{sample}\text{-}R_{standard})/R_{standard}] \times 1000 \quad (2)$$

α is used to describe the isotopic fractionation ε between two compunds A and B, which usually is expressed per mil:

$$\varepsilon_{A\text{-}B}\ (‰) = (\alpha\text{-}1) \times 1000 \quad (3)$$

and the $\Delta_{A\text{-}B}$ value can be calculated according to the approximation:

$$\Delta_{A\text{-}B} = \delta_A - \delta_B \approx 1000 \times \ln\alpha \quad (4)$$

The exchange of isotopes of an element in a closed system between two molecules, until the system reaches equilibrium is called an *equilibrium isotopic fractionation. Kinetic fractionation*, on the other hand, is a unidirectional reaction, in which the isotopes of the product and the reactant cannot be exchanged anymore and cannot reach an equilibrium, due to the difference on reaction rates and/or isolation and lack of further interaction between the product and the reactant phases. The lighter isotopes tend to become preferentially enriched in the product during this process, as they can react faster due to their weaker bonds which can easily break. Mathematically, kinetic fractionation can be expressed with the Rayleigh distillation model, according to the formula:

$$R_A = R_{A0} \times f^{\alpha\text{-}1} \quad (5)$$

where R_A is the ratio of the heavy to the lighter isotope in compound A, and R_{A0} is the initial ratio of heavy to the lighter isotope in compound A, *f* represents the fraction of compound A remaining (A/A_0 = fraction of phase A remaining) and α is the fractionation factor. The δ value of a compound A can be calculated using the Rayleigh formula:

$$\delta_A = ((1000 + \delta_{A0}) \times f^{(\alpha_{A/B}-1)}) - 1000 \quad (6)$$

1.4.2. Stable Cr isotope systematics

Chromium has four stable isotopes (^{50}Cr, ^{52}Cr, ^{53}Cr and ^{54}Cr) with natural abundances of 4.35, 83.79, 9.50 and 2.36 % respectively (Rossman and Taylor, 1998). Chromium is a redox-sensitive element with two valence states in Earth´s surface (Cr^{3+} and Cr^{6+}), Cr^{6+} being found in oxyanion species of chromate (CrO_4^{2-}), chromic acid ($HCrO_4^-$) and dichromate ($Cr_2O_7^{2-}$) which are all highly soluble in water, as opposed to Cr^{3+} which usually forms oxides or oxyhydroxides that are insoluble and immobile in natural pH range. Cr^{3+} in minerals can be oxidized to Cr^{6+} in presence of oxygen which is a process catalyzed by MnO_2 (Fendorf and Zasoski, 1992; Economou-Eliopoulos et al., 2014), and the oxidized Cr^{6+} is delivered to the oceans via riverine transport. Chromium exits as both Cr^{3+} and Cr^{6+} in the modern ocean, the latter being the dominant species (Van der Weijden and Reith, 1982; Frei et al., 2014), and has a residence time of 9000 – 40000 years (Van der Weijden and Reith, 1982; Reinhard et al., 2013) with a mean concentration of 0.05 to 1 ng/g (Jeandel and Minster, 1987; Bonnand et al., 2013; Pereira et al., 2015; Scheiderich et al., 2015). Chromium, being a compatible element and residing mostly in ultramafic and mafic rocks (Faure, 1991), is mainly present as Cr^{3+} in igneous rocks. Cr(II) is present in some meteorites (Berry and O´Neill, 2004; Berry et al., 2006; Bell et al., 2014; Eeckhout et al., 2007), and possibly in deep mantle rocks (Burns, 1975). Earth's core is expected to contain a significant amount of metallic Cr (Moynier et al., 2011). Stable Cr isotopic composition of a set of mantle-derived rocks from different sources, including mantle xenoliths, ultramafic rocks and cumulates, and oceanic and continental basalts revealed a limited $\delta^{53/52}Cr$ range of - 0.211 to - 0.017 ‰, with an average of - 0.124 ± 0.101 ‰, implying a relatively homogeneous mantle source, which is referred to as the igneous inventory range (Schoenberg et al., 2008; 2016).

Chromium can be transported in an atmosphere devoid of oxygen as solid detrital minerals or dissolved Cr^{3+} (Konhauser et al., 2011). Hence, the variations in stable Cr isotopic composition outside of the igneous inventory (Scheonberg et al., 2008) of the ancient marine sedimentary rocks, such as BIFs, might reveal oxidation state of the atmosphere at the time (Frei et al., 2009; Crowe et al., 2013; Planavsky et al., 2014a). BIFs would faithfully record the isotopic signature of the coeval seawater, since the reaction kinetics is fast during Cr^{6+} reduction by Fe^{2+} and consequent co-precipitation with the Fe(III)-oxides, leading to no net Cr isotopic fractionation (Buerge and Hug, 1997; Frei et al., 2009). Once the atmosphere is fully oxygenated Cr isotopic composition of the seawater is mainly controlled by sink fluxes. The seawater Cr inventory becomes lower with higher $\delta^{53/52}Cr$ values, as the reducing conditions start to expand in the ocean, or as a result of changing hydrothermal activity (Holmden et al., 2016; Reinhard et al., 2013; 2014; Wang et al., 2016).

The equilibrium Cr isotopic fractionation factors between coexisting Cr^{3+} and Cr^{6+} species can be as high as 6 ‰ at room temperature (Wang et al., 2015). Complexation with different ligands for the same valence states also generates isotopic fractionation among Cr species, such as Cl-bounded Cr^{3+} being ~4 ‰ lighter than the H_2O bound Cr^{3+} at room temperature, without the need for redox reactions (Babechuk et al., 2018; Schauble et al., 2004; Larsen et al., 2016). Cr isotopic fractionation during oxidation remains poorly understood with a wide range of fractionation values determined in experiments from - 2.5 ‰ to approximately 1 ‰ (Bain and Bullen, 2005; Ellis et al., 2008; Wang et al., 2010; Zink et al., 2010). Reduction of Cr^{6+} to Cr^{3+} leads to the enrichment of lighter Cr isotopes in the reaction product Cr^{3+} following a Rayleigh type fractionation model in a closed system (Schauble et al., 2004). Batch and column Cr reduction experiments yielded ε values ranging from 0.2 to 5 ‰ (Basu and Johnson, 2012; Berna et al., 2010; Døssing et al., 2011; Ellis et al., 2002; Jamieson-Hanes et al., 2012; 2014; Kitchen et al., 2010: Zink et al., 2010). Biotic reduction experiments also yielded a high variation in ε values (Sikora et al., 2008). Fluxes and sinks of Cr in modern ocean environment are summarized in Figure 1-4.

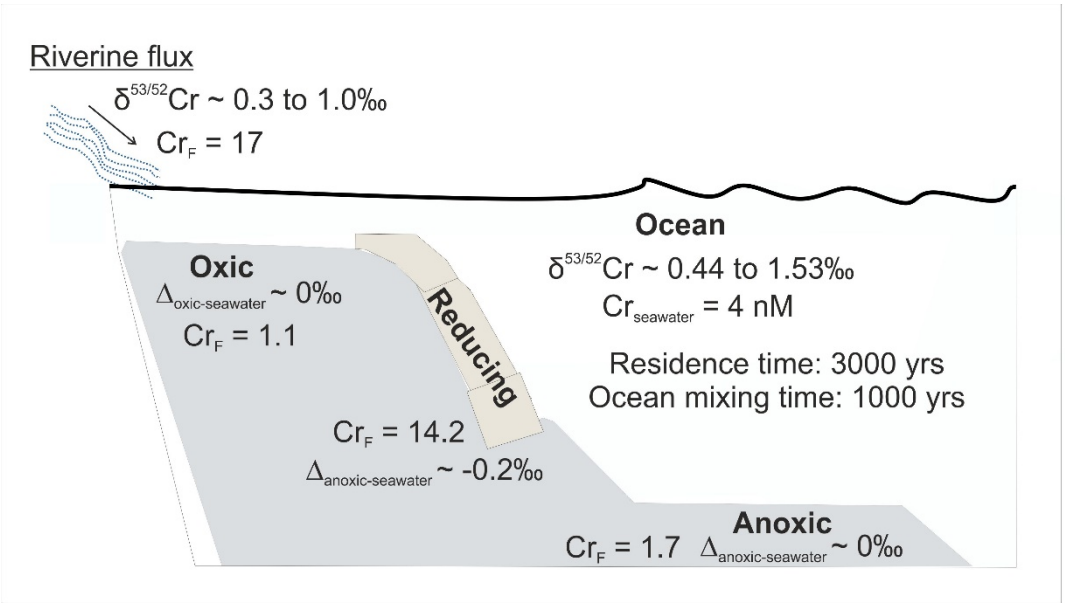

Figure 1-4. The mass balance of Cr fluxes and sinks in modern seawater (after Bonnand et al., 2013; Gueguen et al., 2016; McClain and Maher 2016; Pereira et al., 2015; Reinhard et al., 2013; 2014; Scheiderich et al., 2015; Schoenberg et al., 2008). Cr_F indicates Cr flux as 10^8 mole/yr.

1.4.3. Stable Mo isotope systematics

Molybdenum is a trace constituent in the continental crust with an average concentration of 1.1 µg/g (Rudnick & Gao, 2004). Mo has seven naturally occurring stable isotopes ^{92}Mo, ^{94}Mo, ^{95}Mo, ^{96}Mo, ^{97}Mo, ^{98}Mo, and ^{100}Mo with relative abundances of 14.65, 9.19, 15.87, 16.67, 9.58, 24.29 and 9.74 % of the total, respectively (de Laeter et al., 2003). Molybdenum is present in the modern oxic ocean with a homogeneous distribution in hexavalent state as soluble MoO_4^{2-} oxyanion, with a high

concentration of 105 nM and a residence time of 440 ka (Barling et al., 2001; Greber et al., 2015; Miller et al., 2011; Morford and Emerson, 1999). Preferentially lighter stable isotopes of Mo adsorb onto oxic sediments, and mainly to Fe-Mn crusts and nodules as the Mn-oxides are the most significant sink for Mo in oxic settings, leaving the residual seawater Mo reservoir homogeneous and isotopically heavy, with a $\delta^{98/95}$Mo value of + 2.3 ‰, and a difference for $\Delta^{98/95}Mo_{seawater\text{- }FeMn\ crust}$ of 2.7 to 3.2 ‰ (Barling and Anbar, 2004; Goldberg et al., 2009; McManus et al., 2006; Naegler et al., 2014; Siebert et al., 2001; Siebert et al., 2003; Tossell, 2005). In the presence of pore water or free H_2S in the water column below 11 µM, MoO_4^{2-} is transformed into thiomolybdate, with the light Mo isotope preferentially becoming incorporated, which then adsorbs onto organic matter or forms Fe-sulfides in the sediment (Helz et al., 1996; McManus et al., 2002; Naegler et al., 2011; Tribovillard et al., 2006). As the H_2S concentration in water exceeds 11 µM, the aforementioned transformation to thiomolybdate is very effective and Mo is near-quantitatively scavenged into the reduced sediments. When the removal of Mo from seawater is near quantitative, the isotopic signature of the coeval seawater is preserved in the sedimentary rocks (e.g. black shales) (Arnold et al., 2004; Barling et al., 2001; Erickson and Helz, 2000; Helz et al., 1996; Siebert et al., 2003) (Figure 1-5).

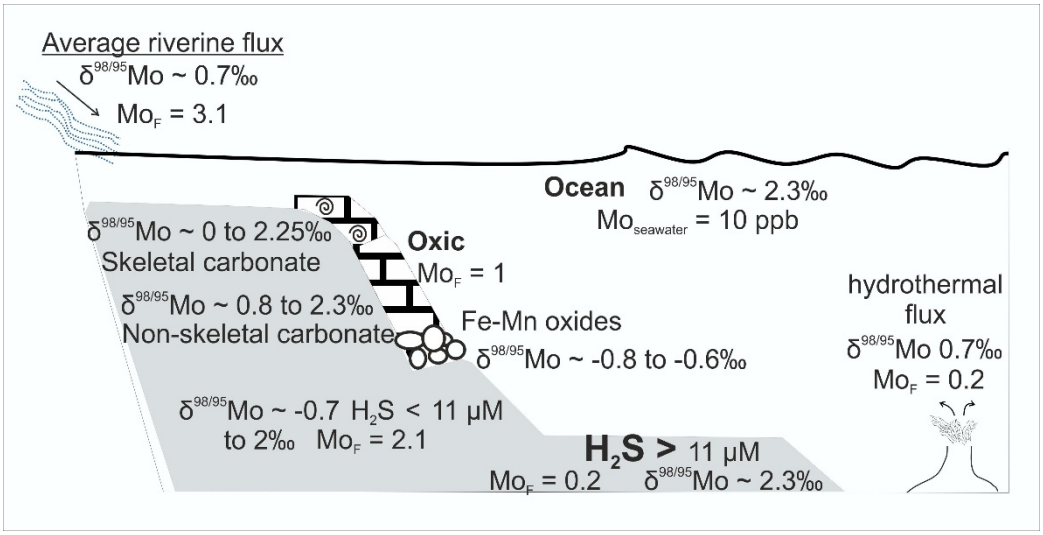

Figure 1-5. The mass balance of Mo fluxes and sinks in modern seawater (e.g. Algeo and Tribovillard, 2009; Archer and Vance, 2008; Arnold et al., 2004; Barling et al., 2001; Barling and Anbar 2004; Dahl et al., 2010; Erickson and Helz 2000; Helz et al., 1996; 2011; Herrmann; 2012; Miller et al., 2011; Nägler et al., 2011; Nakagawa et al., 2012; Noordmann et al., 2015; Neubert et al., 2008 Reinhard et al., 2013; Scholz et al., 2013; Scott et al., 2008; Siebert et al., 2003; Wheat et al., 2002; Vorlicek et al., 2004). Mo_F indicates Mo flux as 10^8 mole/yr.

1.4.4. Stable Fe isotope systematics

Iron is an element with three oxidation states, as metallic iron (Fe^0), ferrous iron (Fe^{2+}) and ferric iron (Fe^{3+}). Metallic iron is partitioned into the core of the Earth, whereas ferrous iron mainly resides in the mantle, and ferric iron is commonly found in oxygenated surface environments and in crustal rocks. Iron has the four stable isotopes ^{54}Fe, ^{56}Fe, ^{57}Fe and ^{58}Fe, with relative abundances of 5.845, 91.754, 2.1191 and 0.2919 % (Berglund and Wieser, 2011). The stable isotopic composition of iron is usually reported as $\delta^{56/54}$Fe, which equals to the deviation in part per mil of the ^{56}Fe/^{54}Fe ratio relative

to the IRMM-014 reference standard (Taylor et al., 1992). The modern oxic ocean is depleted in iron (0.05 to 2 nM) (Baar and de Jong, 2001; Landing and Bruland, 1987; Martin et al., 1990) with a heterogeneous distribution due to the high insolubility of Fe^{3+} (Gordon et al., 1982). Iron is an essential micronutrient for organisms (Martin and Fitzwater, 1988; Moore et al., 2002). The main iron sources to the marine environment are rivers, groundwater, aeolian dust, and hydrothermal fluids (e.g. Anbar and Rouxel, 2007). In reducing environments, iron is very soluble as Fe^{2+}, and thus, Archean oceans were largely ferruginous (enriched with homogeneously distributed Fe^{2+}), in contrast to the modern ocean (Johnson et al., 2008). Despite the anoxic, ferruginous conditions of the Archean ocean, presence of banded iron formations and the oxidation of Fe^{2+} in such an environment are still heavily debated within the scientific community, and abiotic oxidation of Fe^{2+} by UV-light (Cairns-Smith, 1978), or with O_2 generated by oxygenic photosynthesis in the upper water column (Cloud, 1973), and/or biotic oxidation by anoxygenic phototrophic bacteria which use Fe^{2+} as an electron donor (Kappler et al., 2005) were the mechanisms proposed to explain this conundrum.

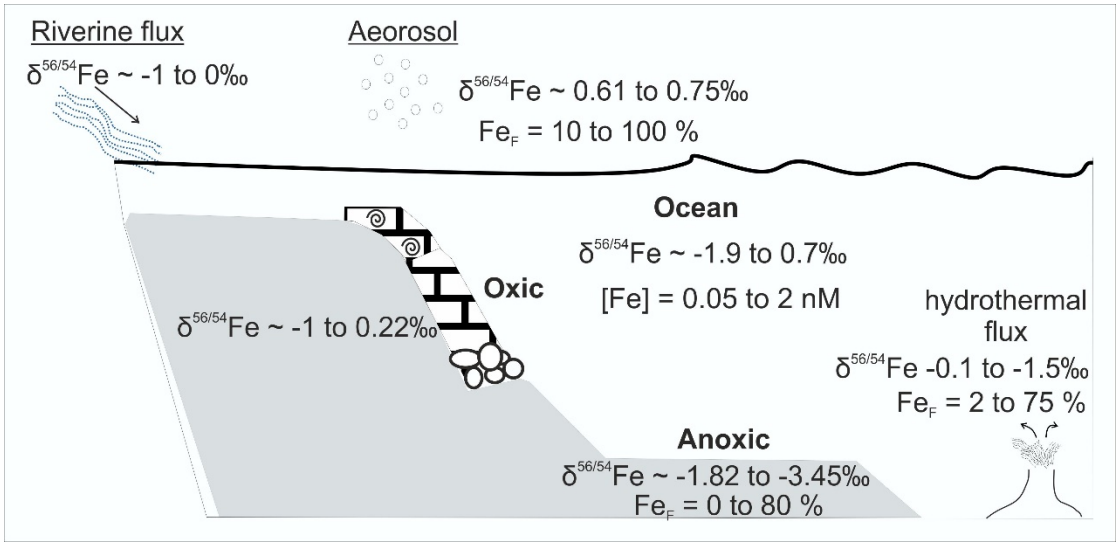

Figure 1-6. The mass balance of Fe fluxes and sinks in modern seawater (e.g. Anbar et al., 2005; Conway and John, 2014; Johnson et al., 2002; Beard et al., 2003; Bergquist and Boyle 2006; Radic et al., 2011, Rouxel et al., 2004; 2008; 2016; Severmann et al, 2004; Sharma et al., 2001; Welch et al., 2003). Fe_F indicates the fraction of Fe.

Stable iron isotopic fractionations under low temperature conditions can be governed by both equilibrium and/or kinetic processes. The equilibrium fractionation during aerobic oxidation of Fe^{2+}_{aq} to Fe^{3+}_{aq} generates an $\varepsilon_{Fe(III)aq\text{-}Fe(II)aq}$ value of ~3 ‰, enriching the more oxidized species in heavy isotopes (Beard and Johnson, 2004; Croal et al., 2004; Welch et al., 2003). The consequent kinetic fractionation during Fe^{3+}_{ppt} precipitation leaves the precipitate 1-2 ‰ lighter in heavy isotopes (Skulan et al., 2002). Therefore, the reaction from the oxidation of Fe^{2+}_{aq} to precipitation of Fe^{3+}_{ppt} results in a fractionation value of + 1 to + 2 ‰ (Beard et al., 2003; Bullen et al., 2001). Anaerobic microbial oxidation processes also generate similar Fe isotopic signatures (Croal et al., 2004; Swanner et al., 2015). Bacterial

reduction of Fe^{3+} causes significant Fe isotope fractionations, depleting the product (Fe^{2+}_{aq}) in heavy isotopes (Johnson et al., 2005). Iron sinks and fluxes in modern oceans are summarized in Figure 1-6.

1.4.5. Stable U isotope systematics

Uranium occurs in two main oxidation states as U^{4+} and U^{6+} in natural environments (Langmuir, 1978). An estimate for the U abundance in the primitive mantle is 22 ng/g, while the chondritic abundance is approximately 8 ng/g (Palme and O´Neill, 2003). Uranium as a refractory and lithophile element has a concentration of 1.3 µg/g in continental crust (Taylor and McLennan, 1985; Rudnick and Gao, 2003). Under reducing or low atmospheric oxygen conditions the mineral uraninite ($U^{4+}O_2$) is stable and can thus be found in Archean continental sediments. However, under oxidizing atmospheric conditions uraninite is oxidized and U occurs as U^{6+}, which is much more soluble and mobile than U^{4+}. Hence, the disappearance of detrital uraninite from terrestrial sediments in early Proterozoic (at ~2.3 Ga) was one of the most striking lines of evidence for a significant rise of atmospheric oxygen (Holland, 1984). In modern oceans, U mainly occurs as uranyl carbonate complexes and has a relatively long residence time of 400,000 years (Ku et al., 1977; Langmuir, 1978; Henderson and Anderson, 2003). Uranium is removed from the seawater mainly by reducing sediments and carbonate deposits (Dunk et al., 2002; Henderson and Anderson, 2003) (Figure 1-7).

^{238}U and ^{235}U are two parent isotopes of decay series, which lead to the formation of the stable ^{206}Pb and ^{207}Pb with half-lives of 4.5 and 0.7 billion years, respectively. The upper mantle is heterogeneous in terms of U isotopic composition (Andersen et al., 2015). An average $\delta^{238/235}U$ value for the continental crust was determined as - 0.29 ‰ and a mean $\delta^{238/235}U$ value for modern seawater was determined as - 0.39 ‰ (Tissot and Dauphas, 2015). Anoxic sediments have $\delta^{238/235}U$ values (- 0.20 to + 0.40 ‰) that are significantly higher than the seawater and the continental crust average, due to the isotopic fractionation during reduction and back diffusion of isotopically light U to the water column (Weyer et al., 2008; Montoya-Pino et al., 2010; Andersen et al., 2014; Holmden et al., 2015; Noordmann et al., 2015; Hinojosa et al., 2016). A light U isotopic composition for the residual seawater in Archean is inferred as a result of reduction, as recorded in some late Archean BIFs that reflect the coeval seawater isotopic composition ($\delta^{238/235}U$ = - 0.90 to - 0.70 ‰) (Weyer et al., 2008).

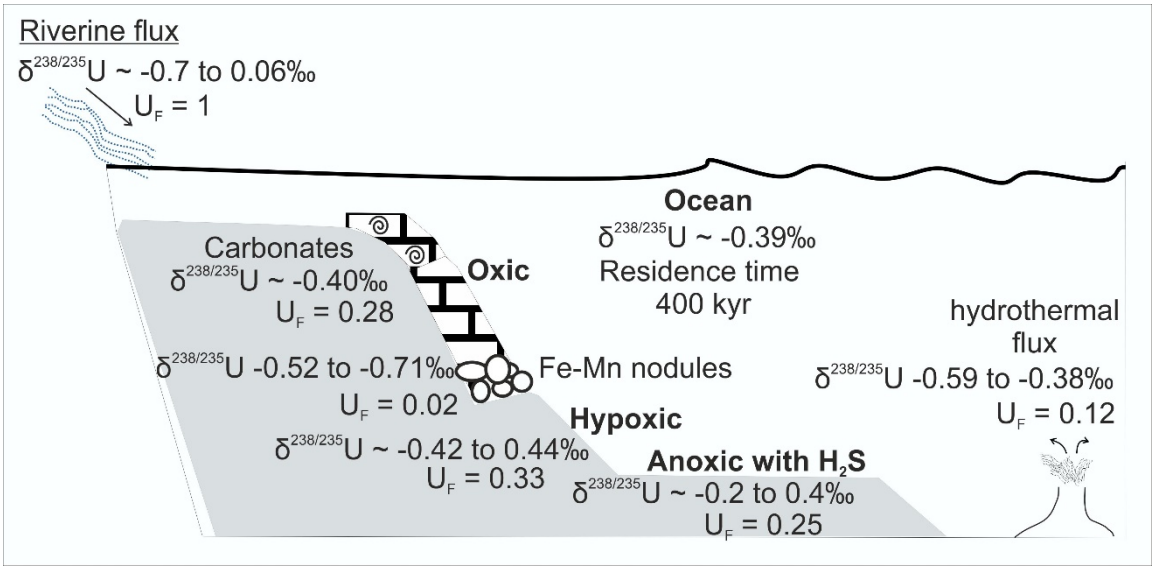

Figure 1-7. The mass balance of U fluxes and sinks in modern seawater (e.g. Andersen et al., 2014; 2016; Brennecka et al., 2011; Dahl et al., 2014; Dunk et al., 2002; Goto et al., 2014; Holmden et al., 2015; Hinojosa et al., 2016; Ku et al., 1977; Lau et al., 2016; Noordmann et al.; 2015; 2016; Romaniello et al., 2013; Stirling et al., 2007; Tissot and Dauphas, 2015; Wang et al., 2016; Weyer et al., 2008). U_F indicates the fraction of U.

2. Geological/Hydrological Setting and Sampling

2.1. Geology of the Pongola Supergroup and sampling of the Ijzermijn Iron Formation

The Pongola Supergroup is a volcano-sedimentary succession, 3.0–2.85 Ga in age at the southeastern margin of Kaapvaal Craton, which is exposed in an area that extends ~ 250 km from north to south between Amsterdam and Nkandla, in South Africa as well as in southern Swaziland (Gold and von Veh, 1995; Nhleko, 2003; Figure 2-1). The upper Mozaan Group of the Pongola Supegroup correlates to the lower West Rand Group of the Witwatersrand Supergroup of South Africa (Beukes and Cairncross, 1991). The Pongola Supergroup is divided into two subgroups (Figure 2-1), the lower Nsuze Group which is composed of volcano-sedimentary rocks, and the upper Mozaan Group, that mainly consists of siliciclastic sequences with minor interspersed volcanic rocks (Cole, 1994; Gold, 2006; Nhleko, 2003; SACS, 1980; Weilers, 1990; Wilson et al., 2013). The contact between the Mozaan and Nsuze Groups is characterized by an angular unconformity, with the uppermost part of the Nsuze Group revealing subsurface weathering features of the Nsuze paleosol (Crowe et al., 2013; Nhleko, 2003). Uranium-Pb zircon dating for an andesitic flow near the base of the Nsuze Subgroup gave an age of 2980 ± 10 Ma, while a rhyolite flow further up in the stratigraphy yielded an age of 2968 ± 6 Ma (Mukasa et al., 2013). A U-Pb SHRIMP zircon date of 2977 ± 5 Ma was determined earlier on another rhyolite flow from the Nsuze Subgroup (Nhleko, 2003). A minimum age for the Mozaan Group of 2837 ± 5 Ma was obtained by U-Pb zircon dating of a quartz porphyry sill (Gutzmer et al., 1999). "Post-Pongola granites" revealed an age range between 2.8 and 2.7 Ga (Mukasa et al., 2013) while a U-Pb age of 2902 ± 9 Ma was determined from detrital zircons of the sedimentary succession at the top of

the Mozaan Group (Nhleko, 2003). All volcanic and sedimentary rocks of the Pongola Supergroup have only undergone greenschist facies metamorphism (Beukes and Cairncross, 1991; Nelson et al., 1995; Nhleko, 2003). The 1800 m thick Nsuze Group consists of mafic to felsic volcanic rocks, alternating with shallow marine and siliciclastic deposits (Cole, 1994; Matthews, 1967). The sediments of the Nsuze Group were suggested to be deposited in a near-shore, shallow water environment due to the presence of stromatolite bearing carbonates (Beukes and Lowe, 1989; Mason and von Brunn, 1977; Matthews, 1967; Tankard et al., 1982).

The 4800 m thick Mozaan Group consists of quartz-rich sandstones, and shales, along with minor conglomerates, jaspilitic banded iron formation (BIF), and diamictites of possible glacial origin (Nhleko, 2003). The depositional environment of Mozaan Group sediments is generally recognized as fluvial braid-plain and shallow marine shelf with its iron formations being deposited on a shallow, sediment-starved outer shelf during the peak of a marine transgression (Beukes and Cairncross, 1991). The Sinqeni Formation, which is the focus of this study, consists of the basal Dipka and the upper Kwaaiman quartz arenite members, the latter stratigraphically overlain by the Ntombe Formation, consisting of dominantly shales, siltstones and sandstones (Beukes and Cairncross, 1991; Hicks and Hoffmann, 2012).

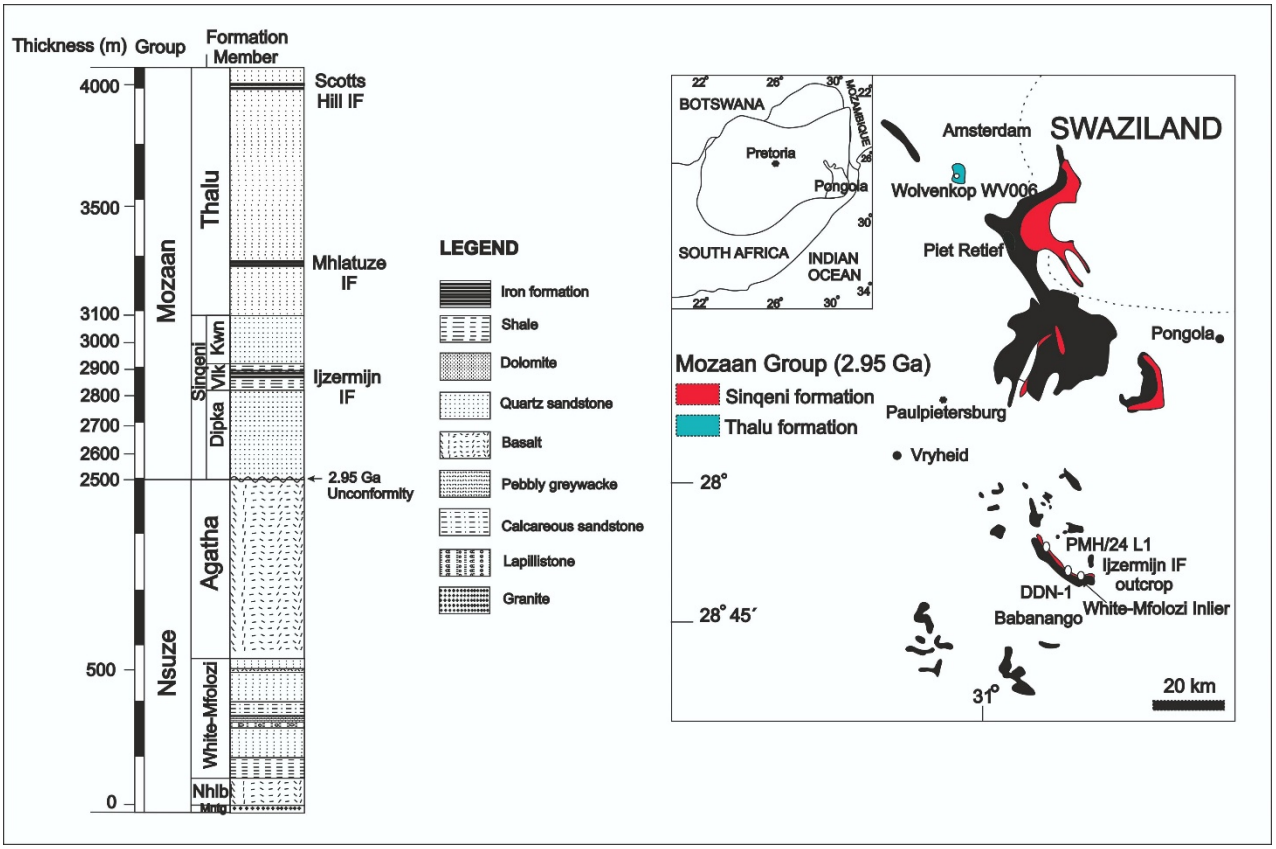

Figure 2-1: Simplified geological map of the studied iron formations from Ijzermijn, Sinqeni formation and Scotts Hill IF of Mozaan Group of the Pongola Supergroup, South Africa. The locations of the studied drillcores DDN-1 and PMH2-24 L1 and outcrop of Ijzermijn IF, Sinqeni formation as well as the drillcore WV006 from Scotts Hill IF are shown in the map (after Gold and van Veh, 1995) and lithostratigraphic column (after Beukes and Cairncross, 1991; Matthews, 1967).

The two quartzite units are separated by the Vlakhoek Member (Figure 2-1) that consists of shale and magnetite-bearing mudstone with an interbed of iron formation known as the Ijzermijn iron formation (Beukes and Cairncross 1991; Dix, 1984; Hicks and Hofmann, 2012; Von Brunn and Hobday, 1976; Von Brunn and Mason, 1977; Noffke et al., 2008).

2.1.1. Sampling of Ijzermijn IF, Mozaan Group, Pongola Supegroup

In order to establish the effect of weathering on the geochemistry of the Ijzermijn IF, two drill cores (DDN-1 and PMH24/L1) and one outcrop profile along the gorge of the White Mfolozi River were sampled (Figures 2-1 and 2-2). Drill hole DDN-1 is located just a couple of kilometers north of the river outcrop (Figures 2-1 and 2-2) and probably provides the best fresh analog for the outcrop samples (Figure 2-3). Core PMH24/L1 is situated several km north of DDN-1 (Figure 2-2) and preserves a marked facies change in the composition of the iron formation (Figure 2-3).

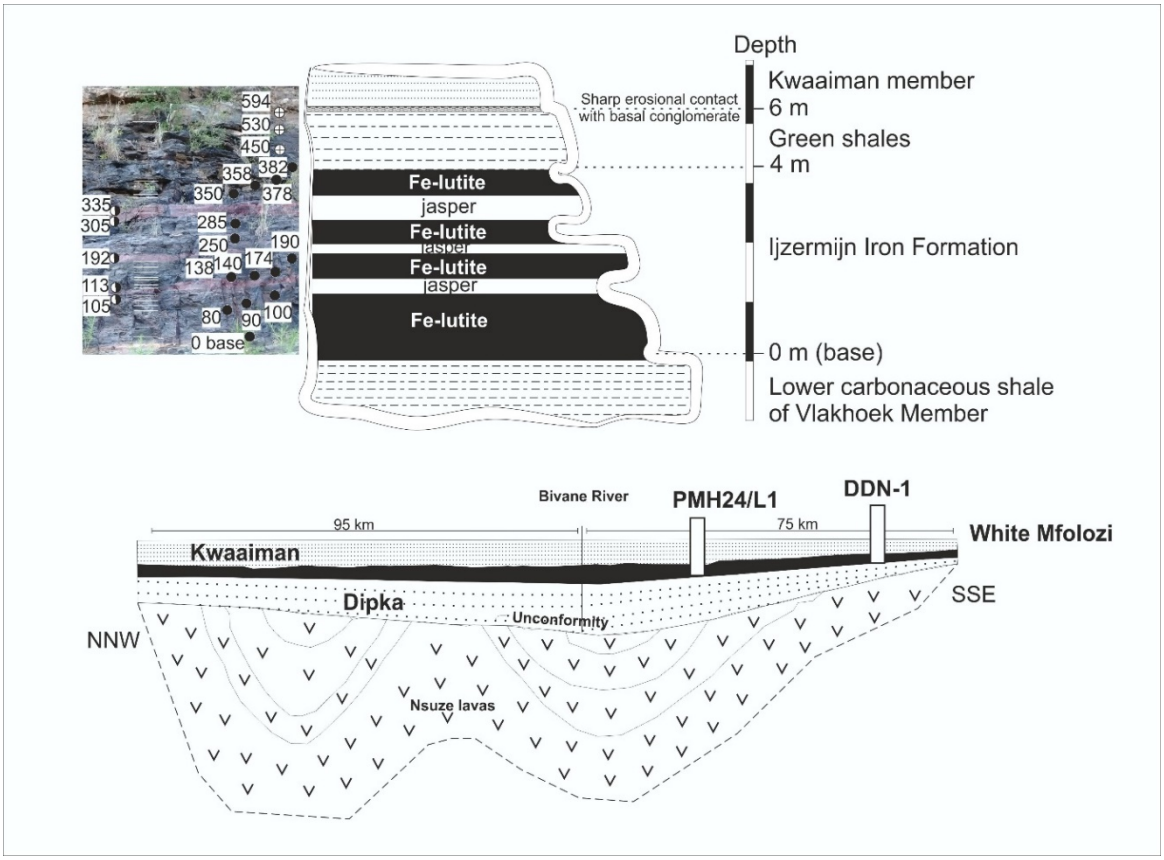

Figure 2-2: Ijzermijn IF outcrop picture and simplified profile sketch of the outcrop, and the respective positions of the drill holes as well as river bed outcrop are shown in a cross section below (Beukes and Cairncross, 1991; Smith et al., 2007).

The correlation of distinct rock units between the two aforementioned drill holes and the outcrop is clear, but there are large differences in the mineralogical composition of these units in both drill cores and the outcrop (Figure 2-3). At all three localities the Ijzermijn IF overlies the lower carbonaceous

shale unit of the Vlakhoek Member with a sharp transgressive contact. The proper IF unit has a consistent thickness of about 4 m. Drill core DDN-1 is composed of a lower lutitic (terminology after Beukes and Gutzmer, 2008) rhodochrosite-rich iron formation with no clear well defined chert band. This unit is overlain by a magnetite-rhodochrosite±Fe-carbonate and iron silicate (stilpnomelane) banded iron formation with well-defined chert mesobands. This manganese-rich iron formation is laterally represented by magnetite-siderite-silicate iron formation that is finely laminated in its lower part and chert-mesobanded in its upper part in core PMH24/L1 (Figure 2-3). In both drill cores there is only minor hematite present in the iron formation and chert bands are light grey in color containing iron and manganese carbonates but no jasper bands. This is in stark contrast to the outcrop where all clearly defined chert bands are represented by red jasper (Figure 2-3).

In both drill cores, the iron formation bed is gradationally overlain by magnetic chamositic mudstone that contains abundant rhodochrosite in core DDN-1 and siderite and ankerite in core PMH24/L1. This magnetic mudstone is in turn overlain by slightly magnetic chamositic shale in both of the cores. In the White Mfolozi River outcrop the iron formation is overlain by green chloritic shale (Figure 2-3) that appears to be less magnetic than in the two drill cores perhaps due to martitization of some original magnetite. In drill core DDN-1 a thin decimeter-thick jasper band is developed along the contact between the magnetic chamositic mudstone and overlying slightly magnetic chamositic shale (Figure 2-3). The upper chamositic shale unit of the Vlakhoek Member is overlain with sharp erosional surface by a thin conglomerate at base of the overlying Kwaaiman Quartzite Member of the Sinqeni Formation in outcrop and in core PMH24/L1. However, in core DDN-1 late Carboniferous-Early Permian glacial diamictite of the Dwyka Formation of the Karoo Supergroup directly overlies the upper chamositic shale of the Vlakhoek Member. A thin red hematitic supergene alteration zone is developed in the chamositic shale immediately in contact with the overlying diamictite.

For this study, five samples from different depths of the Mn-bearing magnetite-rhodochrosite chert banded unit (including three chert samples) and one sample from magnetic chamositic mudstone ± rhodochrosite unit of DDN-1 drill core; as well as four samples from different depths of magnetite-siderite- silicate chert banded unit of the PMH24/L1 drill core were collected from the Ijzermijn IF of the Sinqeni Formation (Figure 2-3). In outcrop along the White Mfolozi River Gorge section, 20 samples of the Ijzermijn IF and three upper chloritic shale of the Vlakhoek Member were collected along a depth profile (Figure 2-3).

2.1.2. Sampling of Scotts Hill IF, Mozaan Group, Pongola Supegroup

Apart from the samples of the Ijzermijn IF, nine samples from the Scotts Hill IF of the Thalu Formation (Beukes and Cairncross, 1991) were collected from the WV006 drill core (Wolvenkopp farm, Figure 2-1). The Scotts Hill IF in drill core WV006 has been altered to a hematite-bearing banded iron formation i.e. jaspilite) in the upper 16 m of the drill core as part of the post-depositional alteration profile in the area. Below the weathering profile the iron formation is composed of a magnetite ± iron carbonate and silicate banded iron formation with green chert bands and only a few rare red jasper mesobands. Nine samples were selected through the altered jaspilitic upper part of the iron formation into the fresh lower green chert and magnetite-rich part.

2.2. Hydrology of the Arvadi Spring and sampling

The mineralized Arvadi Spring is located near Bad Alvaneu in the Albula Valley, ca. 6 km east of Tiefencastel, in the canton of Grisons (Graubünden), Switzerland (46°40’17.4”N 9°39’18.8”E). The spring is located at an altitude of 928 m above sea level. A schematic sketch of the spring and its feeding tunnel shaft is given in Figure 2-4. Two different sources of water mix in a mixing tunnel Figure 2-4 and the mixed water flows ca. 35 m downhill through a pipe system and crops out into a manmade pond, the Arvadi Spring, which has a 3.3 m diameter and ~20 cm water depth (Koeksoy et al., 2018). From the pond, the spring outflow feeds into a little creek of approximately 14.70 m length, and mixes with a second creek, the forest brook, which dilutes the iron and sulphur concentration of the spring water (Figure 2-4). The geological framework of the area is the alpine orogeny and the spring is situated in the Engadine tectonic window, where the Austroalpine overthrusts have been eroded and the underlying rocks of the Penninic nappe, comprising of Jurassic oceanic crustal and overlying sedimentary rocks, have become exposed (Strauss et al., 2016). The discharge of the Arvadi Spring is from the crystalline rocks of the Silvretta nappe, underlain by carbonates and evaporitic gypsum (Strauss et al., 2016).

Figure 2-3: Correlation of the lithostratigraphic logs of the outcrop, and the two drill cores of Ijzermijn IF from left to right (sh: shale, J: jasper, mag: magnetite, c: carbonaceous shale), the "x" numbers on the right indicate sample depths

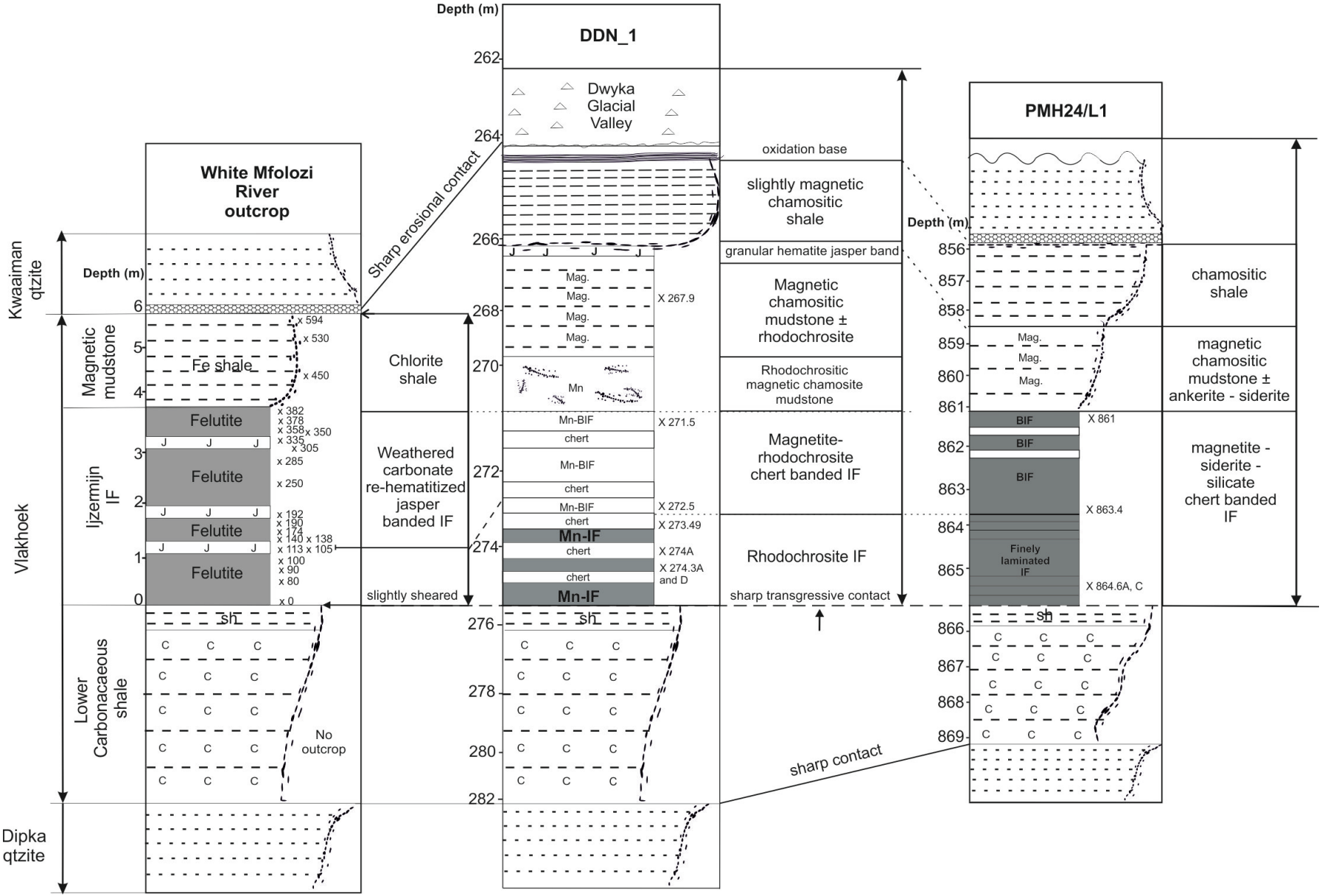

Arvadi is an iron- and sulphur-rich spring originating from a subsurface water source. The sediments in the spring are covered by soft, red particles and, which are in turn overlain by soft, white flocs (Figure 2-4). The rocks in the spring are covered by white biofilms and an orange-brown biofilm-like crust/coating which will be referred as red flocs throughout this study. The soft white flocs and red soft particulate matter are not present in the creek, but restricted to the pond. The sampling points from all sampling campaigns are provided in Figure 2-4. Overall, 4 sampling campaigns were carried out in the Arvadi Spring in October 2014, April 2015, April 2017 and June 2018. In this thesis, results from the sampling campaigns of October 2014 and June 2018 are presented. The filters were flushed with N_2 to avoid oxidation, which led to the consequent reduction of $Fe(III)_{aq}$ during the water sampling in April 2015. Hence, the data from the sampling campaign of April 2015 are incorrect, and will not be published. Furthermore, no data could be collected from the sampling campaign of April 2017, due to the loss of limited amount of sample material during instrument malfunction.

Seven water, and 6 red floc samples were collected during the field campaign of October 2014 from the Arvadi Spring. One water and 3 red floc samples were collected from the mixing shaft in the tunnel, during the October 2014 field campaign. Seven water, and 6 iron floc samples were collected during the June 2018 campaign, from the same sampling points as of October 2014 campaign. No samples were acquired from the mixing shaft in the tunnel during June 2018 campaign, due to the lack of accessibility.

The water samples were filtered using 30 mL Luer-Lock syringes with polyamide (Nylon) Chromafil® filters of 0.45 µM pore size which were pre-rinsed with Arvadi water. The water samples were collected in 250 mL, acid cleaned Polypropylene bottles and immediately acidified with the required volume of 1M HCl to reach to the pH = 2 in order to stabilize the $Fe(II)_{aq}$ during storage. The red flocs were scraped off from the flowbed and the rocks along the flow path, and were collected in plastic bags.

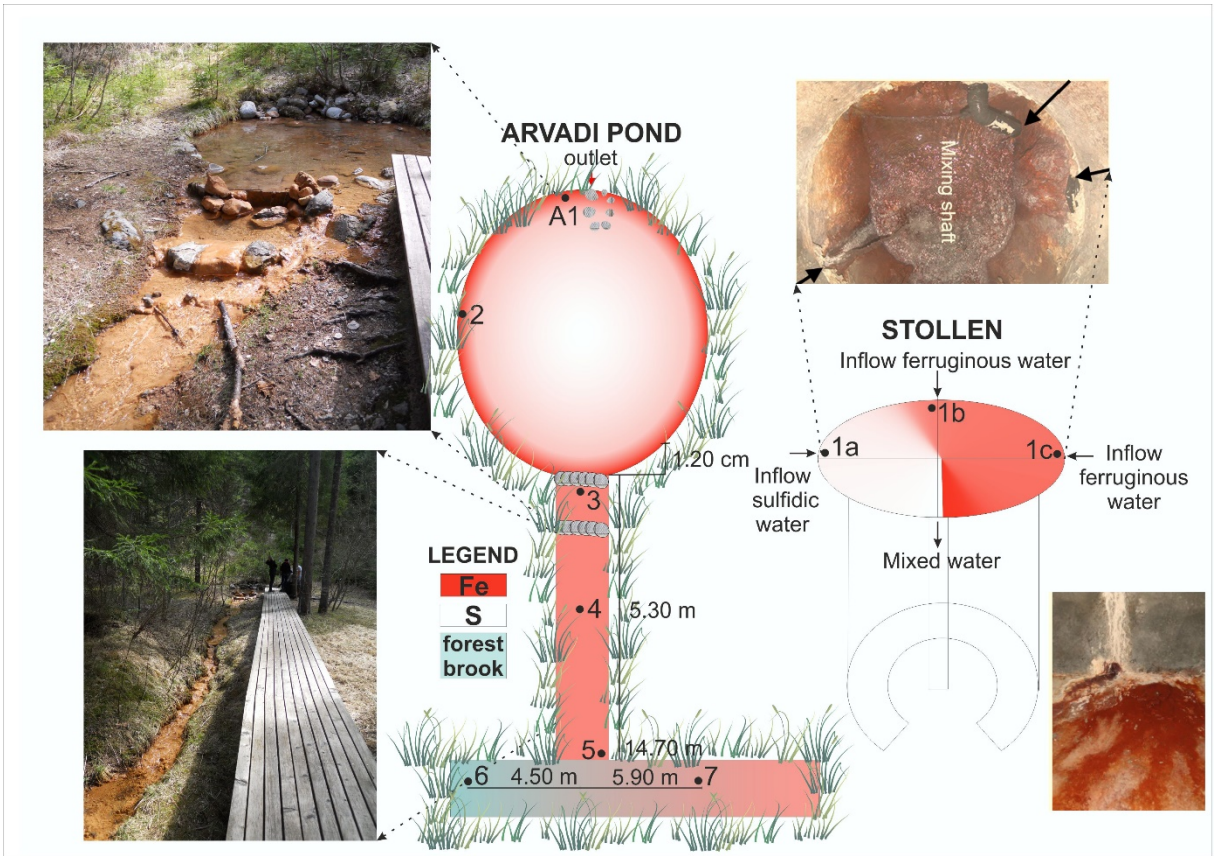

Figure 2-4: Schematic sketch of Arvadi Spring and the feeding mixing shaft and tunnel (Stollen).

3. Analytical methods

3.1. Mozaan Group samples and bulk sample powder preparation

The Scotts Hill IF samples were obtained as agate mortar milled bulk powders. The drill core DDN-1 and PMH24/L1 samples and White Mfolozi River outcrop samples from the Ijzermijn IF were all sawed with a diamond blade, crushed between steel plates in a hydraulic press and ground in an agate mill. Sawing was used on the Ijzermijn IF samples to remove any obvious surface staining, particularly on the outcrop samples, as done in previous studies on these IF (Alexander et al., 2008; Planavsky et al,. 2014a).

3.1.1. Major element analyses of the Mozaan Group samples

3.1.1.1. Ijzermijn IF outcrop samples

An aliquot of 1 g from all samples was taken and ashed overnight in a furnace at 1200 °C for determination of the loss on ignition (LOI) that is predominantly in the form of carbonate CO_2. The samples were weighed immediately after the ashing procedure upon cooling, and the weight difference between the original and ashed samples was calculated as the weight per cent (%) LOI,

although it is recognized that some mass gain may have accompanied Fe oxidation. X-Ray fluorescence analyses (XRF) were performed for the determination of the major elements using a wavelength dispersive Bruker AXS Pioneer S4 (Rh-tube at 4 kW) with 32 standardized samples at the University of Tuebingen. For these measurements, a separate 1.5 g aliquot of unashed sample powder was mixed with 7.5 g of Merck Spectromelt®A12 (mixture of 66 % Li-tetraborate and 34 % Li-metaborate), and melted at 1200 °C to prepare glass beads with an Oxiflux system from CBR analytical service.

3.1.1.2. Scotts Hill IF and Ijzermijn IF drill core samples

The same ashing procedure (section 3.2.1) was applied to the drill core samples of both Ijzermijn IF and the Scotts Hill IF, to determine their LOI. Due to the limited amount of sample powder for these samples, an alternate method was used for the determination of major elements. A powder aliquot of 50 mg (Ijzermijn IF) or 100 mg Scotts Hill IF samples were mixed with 500 mg of Merck Spectromelt®A12 and heated as described above to prepare glass beads. The beads were then dissolved in 100 g of 0.3 M HNO_3 and gravimetrically diluted with additional 0.3 M HNO_3 in polypropylene bottles to a final measurement dilution factor of 1:30,000. Major element determinations were performed on a ThermoFisher Scientific iCap-Qc quadrupole inductively coupled plasma mass spectrometer (Q-ICP-MS) using a similar experimental design as described in detail below for the trace element determinations (Section 3.1.3.). Calibration for sample unknowns used the powder reference materials W-2a (United States Geological Survey; USGS) and GS-N (French National Center for Scientific Research; CRNS) prepared as above and using the major element values reported in Govindaraju et al., (1989). Secondary quality control standards were also prepared from the reference materials SCo-1 (USGS), IF-G (CRNS), and OU-6 (Kane, 2004), and the precision range of major elements relative to the recommended values from GeoReM (compiled) or as reported in Jochum et al. (2016) are presented in Appendix Table A2.

3.1.2. Ferrous iron [Fe(II)] content determination of Ijzermijn IF samples

A colorimetric titration method was used for determining the ferrous iron content in the drill core and outcrop samples of both IFs. Samples were digested in a mixture of HF and H_2SO_4 heated at 170 °C for 12 minutes. The dissolved sample was then diluted with water, H_3BO_3, and H_3PO_4 and immediately titrated with 0.1 M $KMnO_4^-$ using a burette. Blanks and standards (powder reference materials) were measured before each session and every 8-12 samples for quality control. Procedural blanks were equivalent to ≤ 0.02 wt % FeO and 12 measurements of OU-6 reference material gave a mean FeO wt % of 1.71 ± 0.24 (1 s.d), in excellent agreement with the cited FeO value of 1.70 wt % (Kane et al., 2004; Potts et al., 2005).

3.1.3. Trace elements analysis of the Mozaan Group samples

An aliquot of 100 mg of sample powder was weighed and digested in sealed, screw-top Savillex© PFA beakers in a 4 mL (4:1) HF-HNO3 volumetric mixture on a hot plate at 160 C° for three days with periodic agitation. Following digestion, the dissolved sample mixture was evaporated, and the residue was reacted with 0.5 mL 6 M HCl for 12 h at 80 C°, which was evaporated to incipient dryness and reacted twice with 1 mL aliquots of concentrated HNO_3 with evaporation in between to remove excess F and Cl. The sample residues were dissolved in 3 M HNO_3 for 24 hrs and gravimetrically diluted to a 0.3 M HNO_3 stock solutions with a nominal dilution factor of ~250 for jaspers, and cherts and ~1000 for Fe-lutites, shales and the Scotts Hill IF samples. Samples were macroscopically inspected after digestion for undissolved materials, which were not observed. All powder reference materials used for calibration and quality control were also digested with this procedure.

For analyses, stock solutions were further diluted with 0.3 M HNO_3 to a nominal, gravimetric dilution factor of 2,500-20,000, depending on the sample lithology. The 0.3 M HNO_3 used for dilution contained a spike mixture of ^{6}Li (~3 ppb), In (~1 ppb), Re (~1 ppb), and Bi (~1 ppb) to be used as an internal standard during ICP-MS analysis. All samples were measured in batches of 20-25 on the iCap - Qc ICP-MS coupled to an ESI SC-2 DX autosampler with an ESI Fast uptake system equipped with a 4 mL sample loop. All sample liquid was introduced from the loop using the iCap-Qc's peristaltic pump (at 30-35 rpm) and aspirated with a PFA nebulizer into a Peltier-cooled cyclonic spray chamber. The nebulizer and cool gas flow rates were typically ~1 and 14 L min^{-1}, respectively, the plasma forward power was at 1550 W, and the interface was configured with Ni sampler cone, with a Cu core and Ni skimmer cone with a high-matrix insert.

The analytical procedure was similar to that described in previous studies (Babechuk et al., 2010; 2015, Kamber et al., 2005) as modified originally from Eggins et al. (1997). Oxide/hydroxide interference rates of Ba on Eu, Nd on the MREE to HREE (Gd, Tb, Dy, Er), Zr on Ag, and the isobaric overlap of ^{160}Dy on ^{160}Gd were quantified prior to each experiment. Remaining interference 'rates' were determined based on a previous quantification (measured at least once approximately every ~ 6 months) scaled to the daily Nd oxide on Gd production rate (Aries et al., 2000; Ulrich et al. 2010). A daily measurement of the $^{6}Li/^{7}Li$ ratio in USGS standard AGV-2 (unspiked) was also used to determine a correction factor for the natural ^{6}Li contribution in sample unknowns. Experiment sequences consisted of measurements of the internal standard-bearing carrier acid, procedural blanks, rock calibration (W-2a) and accuracy control standards (BIR-1, BHVO-2, OU-6, and IF-G), sample unknowns, and a final set of standards. Repeated measurement of a monitor solution (mixture of dissolved rock standards) was made every 5-7 samples for external drift correction remaining after internal standard

spike correction. After each sample was introduced into the ICP - MS, the sample uptake probe and tubing was rinsed with 0.7 M HNO_3. Additional wash with acid blank (treated as a sample) bracketed monitor samples or were placed between samples known or expected to have contrasting matrices or analyte abundance.

During the experiments, analyte isotopes were measured in the iCap-Q STD mode, typically with 5 repeats of 25-30 sweeps at 3 channels (0.1 amu spacing) and analyte dwell times ranging from 10 - 30 ms. Mean analyte intensities were corrected offline for blank, isobaric interferences, and internal and external drift. Corrected intensities were calibrated using the average response of repeated measurements (5-8) of the USGS reference material W-2a at varying dilution factors and derived from at least 4 separate powder digestions. The calibration lines were constructed using the lab's preferred analyte concentrations for the W-2a standard (see Appendix Table A1). For elements exhibiting some heterogeneity in the W-2a powder (e.g., Mo, As, Ag, Cd, Pb; e.g., Lin et al., 2000) 1 of the 4 digests was rejected from the calibration line if it selectively deviated (i.e., outlier) from a tighter range in the remaining 3; otherwise, all 4 digests were included to average out heterogeneity.

The overall intermediate method precision bias are monitored using the repeated measurements of BIR-1, BHVO-2, OU-6, and IF-G, reference materials, representing a range in analyte concentrations and sample matrices. The mean concentrations and 1 s.d are reported in Appendix Table A1 for these elements determined over two years (2015-2017). The method precision, estimated from the 1 r.s.d of the mean, is often better than 3 % for most elements (Li, Sc, Ti, V, Cr, Co, Ni, Cu, Zn, Ga, Rb, Sr, Y, Zr, Nb, Cs, Ba, REE, Hf, Ta, Th, Pb, U). However, precision levels decrease to between 5-15% for elements that are either at very low abundance or documented to be heterogeneous in either calibration or the quality control standard powders (e.g., Ag, Cd, Mo, Sb, W, Pb), as noted in the Appendix. Note that IF-G is known to be heavily contaminated in W and this standard was run at the end of all experiments to prevent carryover into sample unknowns. Excellent agreement (low bias) is obtained for most elements and selected element ratios relative to other studies employing the same technique and calibration values (Babechuk et al., 2010; 2015; Kamber, 2009) and good to excellent agreement is also obtained for the majority of elements relative to GeoReM information or reference values (Jochum et al., 2016) or certificate values (Appendix Table A1). The high-precision trace element data for the Ijzermijn IF drill core and outcrop samples, and Scotts Hill IF drill core samples are reported in Tables 1, and 2 respectively.

3.1.4. U isotopic analyses of the Mozaan Group samples

3.1.4.1. Determination of ($^{234}U/^{238}U$) activity and stable $^{238}U/^{235}U$ isotopic ratios of the Sinqeni Formation samples at the University of Hannover (LUH)

The detailed method for high-precision U-isotope ratio determination by MC-ICP-MS can be found in Noordmann et al. (2015) and Weyer et al. (2008) and only a brief summary is given here. To destroy organic and volatile compounds, samples were oxidized in a furnace at 500 °C for 10 hours and loss on ignition (LOI) was calculated. Powdered ignited samples, containing between 208 ng and 629 ng U, were then doped with the $^{233}U/^{236}U$ double-spike IRMM3636a (Richter et al., 2008) and digested using 2:1 HF and HNO_3 at 120 °C for three days. After evaporating this solution, samples were treated with 3:1 HCl and HNO_3 at 120 °C for another three days. Finally, fluorides were re-dissolved with 5 ml 6 M HNO_3 and evaporated again to take samples up in 3 M HNO_3 for further ion chromatography using Eichrom UTEVA resin (Weyer et al., 2008). The purified U fractions were treated with a 1:1 solution of hydrogen peroxide and HNO_3 and were then diluted to ~50 ppb U with 3 vol % HNO_3. All measurements were performed with the Thermo Fisher Scientific Neptune MC-ICP-MS in Hannover at dry plasma conditions using a Cetac Aridus 2. Nickel H sampler and X skimmer cones were used and in addition, a 0.8 mm copper spacer was inserted between both cones. All ion beams were measured on faraday detectors attached to a 10^{13} Ω resistors for ^{234}U, to a 10^{11} Ω resistors for ^{233}U, ^{235}U and ^{236}U and to a 10^{10} Ω resistors for ^{238}U. Internal standard errors for the ratio of $^{234}U/^{238}U$ were about 100 ppm on average (1SE). Abundance sensitivity of ^{238}U on ^{236}U was monitored throughout the session, but was < 1 ppm and thus negligible. Isotope data was integrated each 4 s in 80 cycles. Instrumental mass bias was corrected using mass discrimination factors calculated from $^{233}U/^{236}U$ with the exponential law. All measurements were performed using a standard-sample-bracketing method relative to a CRM-112A standard solution that matched the U concentration of samples within 10 %. Results for $\delta^{238}U$ are given in the delta notation relative to CRM-112A for which a $^{238}U/^{235}U$ ratio of 137.837 ± 0.015 was assumed (Richter et al., 2010) and are expressed in ‰ (per mil) units by multiplication with a factor of 1000.

$$\delta^{238/235}U = [(^{238}U/^{235}U)_{sample}/ (^{238}U/^{235}U)_{CRM112A}] - 1 \quad (7)$$

Activity ratios of ($^{234}U/^{238}U$) were calculated using the secular equilibrium (Cheng et al., 2000). To check instrument performance, the reference materials SDO-1, Reimep-18a and IRMM-184 were measured repeatedly. SDO-1 gave $\delta^{238}U$ = - 0.08 ± 0.07 ‰, ($^{234}U/^{238}U$) = 0.9971 (n = 6), Reimep-18a gave $\delta^{238}U$ = - 0.25 ± 0.04 ‰, ($^{234}U/^{238}U$) = 1.0276 (n = 9) and IRMM-184 gave $\delta^{238}U$ = - 1.17 ± 0.04 ‰, ($^{234}U/^{238}U$) = 0.9663 (n = 9) which are in agreement with previously reported values (Richter et al., 2005; Richter et al., 2010; Goldmann et al., 2015; Kendall et al., 2015; Andersen et al., 2017; Lu et al., 2017). All samples were measured as triplicates and given uncertainties are two standard deviations

of replicate measurements (2SD), which lay generally between ± 0.01 ‰ and ± 0.07 ‰. Isotope measurements were also used to calculate U concentrations by isotope dilution and concentrations were corrected for LOI. The results agree with those measured by ICP-MS in Tuebingen within 2 % to 10 % (Section 3.1.3.). The total procedural blanks for U was 1.8 ng that included digestion, matrix separation and measurement which was negligible compared to the processed sample U.

3.1.4.2. Determination of ($^{234}U/^{238}U$) activity ratios of the Sinqeni Formation samples at Trinity College Dublin (TCD)

Medium-precision ($^{234}U/^{238}U$) activity data were also obtained for a larger suite of samples by solution Q-ICP-MS following the method detailed in Suhr et al. (2018). In brief, for all but the two most U-depleted samples, 100 mg of rock powder was digested with 2.5mL HF and 0.5mL HNO_3 in closed teflon beakers at 160°C for 72 hours. For the most U-depleted samples, two separate 100 mg digests were prepared. After dry-down at 110°C, the fluoride residue was converted with 1 mL of concentrated HCl and twice with 1 mL 50% HNO_3. Uranium from the resulting solution was then purified on Eichrom UTEVA resin. The purified U from the duplicate digests of the most U-depleted samples was combined to achieve a larger signal. All U-isotope analyses were performed in 2% ultrapure HNO_3 on a Thermo iCapQs Q-ICP-MS using a Peltier-cooled spray-chamber and low-flow nebulizer delivering ca. 70 µL of solution per minute. Two analyses were performed per sample. The first was the $^{235}U/^{238}U$ ratio from a solution diluted to yield ca. 1e6 cps 238 signal (to keep both analytes in pulse count mode) and the second was the $^{234}U/^{235}U$ ratio from a more concentrated solution yielding a 235 signal below 1e6 cps. Mass bias for both analyses was corrected with the standard-sample-standard bracketing approach using the $^{235}U/^{238}U$ ratio of a 1.3 ppb solution of IRMM 3184. Accuracy was tested with two separate digests of BCR-2, which yielded ($^{234}U/^{238}U$) of 1.0020±19 and 1.0039±17, within the range determined by MC-ICP-MS (1.001-1.006; e.g. Prytulak et al., 2008; Eppich et al., 2012).

3.1.5. Stable Cr isotope analysis of the Mozaan Group samples

Based on the Cr concentration determinations from the trace element measurements adequate amounts of sample powder and ^{50}Cr–^{54}Cr double spike solution allowing accurate double spike deconvolution (Schoenberg et al., 2008) were added to Savillex© PFA beakers and digested using a similar strategy as described for trace element analyses. After digestion in HF-HNO_3, samples were evaporated, refluxed twice with 1 mL of 6 M HCl with intervening evaporation, and dissolved for 12 hrs in 6 M HCl at 120 °C. Chromium purification from sample matrix was achieved with a three-step column procedure as described in detail in Schoenberg et al., (2016) aimed to remove sample Fe by a first anion exchange column, followed by two cation exchange columns to remove additional matrix

elements and Ti and V to eliminate the isobaric interferences of ^{54}Fe on ^{54}Cr, as well as ^{50}Ti and ^{50}V on ^{50}Cr, respectively.

The chromium isotope analyses were performed at the University of Tuebingen, Germany using a ThermoFisher Scientific NeptunePlus MC-ICP-MS operated in medium resolution (Weyer & Schwieters, 2003). All samples were introduced using an Aridus II desolvating nebulizer due to the low Cr abundance of the samples. Stable chromium isotope data are presented using the $^{53}Cr/^{52}Cr$ ratio in the δ notation normalized to NIST SRM979 according to the formula:

$$\delta^{53/52}Cr = [(^{53}Cr/^{52}Cr)_{sample} / (^{53}Cr/^{52}Cr)_{SRM979}] - 1 \quad (8)$$

The δ values are expressed in ‰ (per mil) by multiplication with a factor of 1,000. Over three combined analytical sessions for this study repeated measurements of NIST SRM979 and our in-house Merck Cr(III) standard yielded $\delta^{53/52}Cr_{SRM979}$ values of 0.000 ± 0.019 ‰ (2 s.d; n = 27) and - 0.425 ± 0.024 ‰ (2 s.d; n = 19), respectively. These $\delta^{53/52}Cr_{SRM979}$ values for NIST SRM979 and Merck Cr(III) standards are in excellent agreement with previous studies (Babechuk et al., 2018; Schoenberg et al., 2008, 2016; Zink et al., 2010) and the long-term reproducibilities of 0.000 ± 0.021 ‰ (2 s.d; n = 263) and - 0.429 ± 0.024 ‰ (2 s.d; n = 165) obtained at the Universiy of Tübingen Isotope Geochemistry laboratory since January 2014. Duplicate determinations of three hot plate digestions in Teflon beakers and single analyses of three bomb digestions of the ironstone rock reference material IF-G, which has a similar matrix compared to our samples, yielded an average $\delta^{53/52}Cr_{SRM979}$ value of - 0.032 ± 0.020 ‰ (2 s.d; n = 9, Appendix Table A3). IF-G's average Cr concentration was determined to be 3.74 ± 0.36 µg/g (1 s.d; n = 6, Appendix Table A3). The observed variation in Cr concentrations is independent of the digestion method, and most likely due to sample heterogeneity of the IF-G rock reference material. The chromium blank contribution during chemical purification of maximally 1.26 ng contributed 0.5 % or less to the total analyte Cr and was thus deemed negligible.

3.1.6. Stable Mo isotopic analysis of the Mozaan Group samples

The methods for chemical Mo purification from natural samples and Mo isotope analysis used in this study are described in detail in Wille et al. (2013) and Kurzweil et al. (2015). Organic compounds in powdered samples were broken down for ease of dissolution by ashing in a furnace at 600 °C for 12 h. The loss on ignition (LOI) for ashing was determined for later concentration corrections. 30-200 mg of ashed sample containing ~ 50 ng Mo were weighed into Teflon vials and spiked with an adequate amount of a ^{100}Mo-^{97}Mo enriched isotope tracer solution. The Mo concentrations of samples necessary for this step were previously determined by ICP-MS (ThermoFisher Scientific iCAP Qc) trace element measurements. Samples were digested in a 3:1 mixture of concentrated HF and HNO_3,

evaporated and refluxed twice with 1 mL of 6 M HCl, and dissolved for 12 hrs in 6 M HCl at 120 °C. Mo was then purified with a combination of anion and cation exchange chromatographies using Dowex 1X8, 200-400 mesh and Dowex 50WX8 200-400 mesh resins, respectively (Wille et al., 2013). Mo isotopic measurements were performed on a ThermoFisher Scientific Neptune Plus MC-ICP-MS at the University of Tuebingen, using a CETAC Aridus II^{TM} desolvating nebulizer sample introduction system in dry plasma mode. The ^{100}Mo-^{97}Mo double spike allows for in-run correction of the instrumental mass bias and also corrects for possible Mo isotope fractionation during chemical separation (Rudge et al., 2009). Mo isotopic data are reported in δ-notation relative to the isotopically certified international reference material NIST 3134 (Greber, et al., 2012; Goldberg et al., 2013)

$$\delta^{98/95}Mo = ([^{98}Mo/^{95}Mo]_{sample} / [^{98}Mo/^{95}Mo]_{NIST3134+0.25} -1) \quad (9)$$

and expressed in ‰ by multiplication with 1000. NIST 3134 was set to + 0.25 ‰ to allow comparison with earlier published data – which were reported against the Johnson and Matthey ICP standard 602332B (Siebert et al., 2001) – following the suggestion of Nägler et al. (2014). It is noted that, however, that other publications report their data directly against NIST 3134 as the δ-zero reference point without an offset value of + 0.25 ‰, especially in high-temperature applications for stable Mo isotopes (Willbold et al., 2017; Wang et al., 2018; King et al., 2018; Malinovsky et al., 2018). This situation leads to an unnecessary complication especially in studies where high-temperature stable Mo isotope applications overlap with low-temperature ones, such as recycling of marine sediments in subduction zones (Koenig et al., 2016; Wille et al., 2018). Both scales to report stable Mo isotope data arguably have their pros and cons, but this situation needs to be resolved within the stable Mo isotope community in the near future to prevent unnecessary confusion. The repeated cross-calibration with the Johnson Matthey ICP standard 602332B (Siebert et al., 2001) during two measurement sequences of this study showed isotopic differences $\Delta^{98/95}Mo_{NIST3134\text{-}JM}$ = 0.258 ± 0.047 ‰ (2SD, n = 5) and $\Delta^{98/95}Mo_{NIST3134\text{-}JM}$ = 0.266 ± 0.025 ‰ (2SD, n = 6), respectively. These are within uncertainties identical to the added offset value above and in agreement with previously reported short and long term average $\Delta^{98/95}Mo_{NIST3134\text{-}JM}$ values reported from the Isotope Geochemistry Laboratory in Tübingen (Kurzweil et al., 2016, Wille et al., 2018) and other literature values (Burkhardt et al., 2011; 2014; Greber et al., 2012). Measurements of in-house standard ZH-2 which was purified along with samples yielded a $\delta^{98/95}Mo_{NIST\ SRM\ 3134+0.25}$ value of 0.989 ± 0.050 ‰ (2SE) and 0.984 ± 0.040 ‰ (2SE), respectively, consistent with the long term reproducibility of 0.994 ± 0.082 ‰ (2SD; n=18). USGS rock reference material BHVO-2, similarly purified along with samples yields an average value of 0.171 ± 0.037 ‰ (2SD; n=4) on $\delta^{98/95}Mo_{NIST\ 3134+0.25}$ consistent with the values determined by Burkhardt et al. (2014) as 0.19 ± 0.03 ‰ (2SD; n= 23) on $\delta^{98/95}Mo_{NIST\ 3134+0.25}$. The total procedural blank contribution was below

0.3 ng Mo and as such is negligible compared to the amount of processed sample Mo. The Mo isotopic compositions of the samples are given in Table 5.

3.1.7. Stable Fe isotopic analysis of the Mozaan Group samples

For Fe isotope analyses ~50 mg of sample powders were independently digested using the same procedure as for Mo isotopic analyses. From the resulting solutions in 6 M HCl aliquots containing 10 µg Fe, calculated from the X-Ray Fluorescence Spectrometry (XRF) major element analyses of the respective samples, were transferred to new Teflon vials and spiked with an adequate amount of a ^{57}Fe-^{58}Fe double spike solution targeting 1:1 sample to spike concentration ratios. Sample and spike Fe were homogenized by heating the mixture in the closed vial at 120 °C overnight. Upon drying down and refluxing the sample in 1 mL 6 M HCl the samples were ready for chemical Fe purification by anion exchange (AG1-X8, 100-200 mesh) using the method described by Schoenberg and Von Blanckenburg (2005). Purified samples were dissolved in 0.3 M HNO_3 and Fe isotopic analyses were performed on the ThermoFisher Scientific Neptune Plus MC-ICP-MS hosted at the University of Tuebingen, using the instrument's standard dual spray chamber system. Isotopic ratios were determined at high resolution, to separate polyatomic interferences such as $^{40}Ar^{16}O^+$ and $^{40}Ar^{14}N^+$ on ^{56}Fe and $^{54}Fe^+$ (Weyer and Schwieters, 2003), respectively. Simultaneous monitoring of $^{52}Cr^+$ and $^{60}Ni^+$ signals allowed for small corrections of isobaric interferences from $^{54}Cr^+$ on $^{54}Fe^+$ and $^{58}Ni^+$ on $^{58}Fe^+$, respectively. For these corrections the samples' $^{54}Cr/^{52}Cr$ and $^{60}Ni/^{58}Ni$ ratios were calculated iteratively using individual run cycle's instrumental mass bias obtained from the Fe isotope deconvolution by the double spike and isotope abundance data for Cr and Ni published by the International Union of Pure and Applied Chemistry (IUPAC; Wieser et al., 2013). Uncertainties in this correction resulting from the assumption that Cr and Ni undergo the same instrumental fractionation and that the samples' Cr and Ni isotopic compositions correspond to the IUPAC values are <1 ppm on the ^{54}Fe and <5 ppm on the ^{58}Fe signals and are thus deemed negligible. Fe isotopic ratios of samples, rock reference materials and control standard solutions are presented using the $^{56}Fe/^{54}Fe$ ratio in the δ-notation relative to the isotopically certified reference material IRMM-014 according to

$$\delta^{56/54}Fe = [(^{56}Fe/^{54}Fe)_{sample}/ (^{56}Fe/^{54}Fe)_{IRMM\text{-}014}] - 1 \quad (10)$$

and are expressed in ‰ (per mil) units by multiplication with a factor of 1000. The long-term reproducibility for IRMM-014 on $\delta^{56/54}Fe$ is 0.000 ± 0.040 (2SD; n=108). Measurements of the in-house HanFe standard solution during the course of this study yielded an average $\delta^{56/54}Fe_{IRMM\text{-}014}$ of + 0.298 ± 0.035 ‰ (2SD; n=10), which agrees well with our long-term reproducibility of +0.289 ± 0.043 ‰ (2SD; n=61), and previously published values (Moeller et al., 2014). The in-house standard solution TuebFe

yielded an average $\delta^{56/54}Fe_{IRMM\text{-}014}$ value of - 0.370 ± 0.016 ‰ (2SD; n=4) during the course of this study, in excellent agreement with the published values (Wu et al., 2017) and with the long-term reproducibility of - 0.376 ± 0.049 ‰ (2SD; n=31). Rock reference materials that were purified along with the samples yielded single measurement $\delta^{56/54}Fe_{IRMM\text{-}014}$ values of + 0.646 ± 0.021 ‰ (2SE) for the Isua Greenstone Belt banded iron formation (BIF) IF- G, - 0.042 ± 0.028 ‰ (2SE) for the Green River Shale SGR-1b, and 0.311 ± 0.023 ‰ for an in-house ferryhydride (FeOH) that was biogenically precipitated from a ferrous solution by photoferrotroph (*Rhodovulum iodosum*) consistent with previously published values (Craddock & Dauphas, 2010; Dauphas and Rouxel, 2006; Swanner et al., 2015; 2017; Wu et al., 2017). The corrections for isobaric Cr and Ni interferences were always lower than 0.017 ‰ in $\delta^{56}Fe$ values. Total chemical procedural blanks were ~3.7 ng Fe, contributing less than 0.04 % to the amount of processed sample iron such that blank corrections are negligible.

3.2. Stable Fe isotope analyses of the Arvadi Samples

For stable Fe isotopic analyses of red floc samples from the Arvadi Spring and the tunnel in which different sources of water gets mixed (referred as mixing tunnel or Stollen), ~15 mg of sample powders were independently digested in a 3:1 mixture of concentrated HF and HNO_3, evaporated and refluxed twice with 1 mL of 6 M HCl, and dissolved for 12 hrs in 6 M HCl at 120 °C. From the resulting solutions in 6 M HCl aliquots containing 5 µg Fe, calculated from ICP-MS (ThermoFisher Scientific iCAP Qc) analyses of the respective samples, were transferred to new Teflon vials and spiked with an adequate amount of a ^{57}Fe-^{58}Fe double spike solution targeting 1:1 sample to spike concentration ratios. 15 to 30 g of water sample containing 1 µg of Fe from the Arvadi Spring was treated with the same procedure, also calculated from Fe concentrations determined previously by ICP-MS (ThermoFisher Scientific iCAP Qc) measurements. Similar to sediment samples, the dried- down water samples were spiked with an adequate amount of a ^{57}Fe-^{58}Fe double spike solution targeting 1:1 sample to spike concentration ratios. Sample and spike Fe were homogenized by heating the mixtures in the closed vial at 120 °C overnight. Upon drying down and refluxing the sample in 1 mL 6 M HCl the samples were treated with the same chemical Fe purification procedures as in Mesoarchean Mozaan Group samples, described above in section 3.6.1. Purified samples were dissolved in 0.3 M HNO_3 and Fe isotopic analyses were performed on the ThermoFisher Scientific Neptune Plus MC-ICP-MS hosted at the University of Tuebingen. Measurements were performed in the high-resolution mode (Weyer and Schwieters, 2003), using an Aridus II desolvating nebulizer in dry plasma conditions due to the lower Fe abundance of these samples, compared to the Mozaan Group samples. The measurements of IRMM- 014 yielded an average $\delta^{56/54}Fe_{IRMM\text{-}014}$ of 0.000 ± 0.044 ‰ (2SD, n=7) for the April 2015 session and 0.000 ± 0.070 ‰ (2SD, n=8) for the June 2018 session, respectively. Measurements of the in-house

HanFe standard solution yielded an average $\delta^{56/54}Fe_{IRMM\text{-}014}$ of + 0.282 ± 0.040 ‰ (2SD, n= 6) during the course of April 2015 session and an average $\delta^{56/54}Fe_{IRMM\text{-}014}$ of + 0.322 ± 0.061 ‰ (2SD; n=5) during the course of June 2018 session, which agree with long term reproducibility as given in section 3.1.7., and previously published values (Moeller et al., 2014). The in-house standard solution TuebFe yielded an average $\delta^{56/54}Fe_{IRMM\text{-}014}$ value of - 0.389 ± 0.192 ‰ (2SD; n=2) during the course of June 2018 session, in agreement with the long term reproducibility as given in section 3.6.1., and published values (Wu et al., 2017). Rock reference materials that were purified along with the samples (June 2018) yielded single measurement $\delta^{56/54}Fe_{IRMM\text{-}014}$ values of + 0.589 ± 0.023 ‰ (2SE) for the Isua Greenstone Belt banded iron formation (BIF) IF- G, + 0.017 ± 0.029 ‰ (2SE) for the OU-6 Penrhyn Slate consistent with previously published values (Craddock and Dauphas, 2010; Dauphas et al., 2004). Total chemical procedural blanks were ~3.0 ng Fe for red floc samples, and ~4.8 ng for water samples, contributing less than 0.1 % to the amount of processed red floc sample iron and less than 0.05 % to the amount of water sample iron, respectively, such that blank corrections were negligible.

4. Results

4.1. The Mozaan Group samples

4.1.1. Major element systematics and LOI

The two main lithology units of the Ijzermijn IF (jaspers and Fe-lutites) as well as the difference between drill core and outcrop samples of the same lithology are readily distinguished based on their dominant major element and LOI geochemical characteristics (Table 1). Within the Ijzermijn IF, in both outcrop and drill core, jasper and chert layers have SiO_2 ranging from of 70.84 – 89.50 wt % (mean of 84.30 ± 6.150 wt % ,1 s.d) and Fe_2O_{3TOT} between 3.060 – 21.25 wt %, whereas Fe-lutites have SiO_2 ranging between 11.20 – 67.00 wt % and Fe_2O_{3TOT} between 13.60 – 73.37 wt %. Apart from the higher Fe/Si ratio in the Fe-lutites, they also bear higher Al_2O_3 and TiO_2 contents, ranging from 0.320 – 3.984 wt % and 0.005 – 0.127 wt %, compared to jaspers with maximum values of 0.320 wt % and a range of 0.001–0.013 wt %, respectively. The Fe-lutite sample 16-S-90 has exceptionally low contents of Al_2O_3 and TiO_2, (0.076 and 0.011 wt %), that is close to the levels observed in the jasper samples.

Within the full suite of Ijzermijn IF, the outcrop vs. drill core samples of the same lithology are readily distinguished based on their ferrous iron (FeO*) contents (and accompanying $Fe(II)/Fe_{tot}$ ratios) and LOI. The FeO* of the drill core Fe-lutites range from 9.120 – 37.79 wt % compared to the significantly lower FeO* range of 0.148 – 1.735 wt % for the outcrop samples. Similarly, the drill core chert samples have FeO* of 2.989 – 2.983 wt % (mean of 2.941 ± 0.042 wt %, 1 s.d) compared to the

lower values in the outcrop jasper samples with FeO* between 0.159 – 1.639 wt %. Expressed with a ratio of Fe(II)/Fe_{tot}, higher mean values of 0.738 ± 0.192 (1 s.d) and 0.949 ± 0.148 (1 s.d) are observed for drill core Fe-lutites and jaspers, respectively, compared to mean values of 0.012 ± 0.014 (1 s.d) and 0.079 ± 0.063 (1 s.d) for the respective lithology in outcrop. The aforementioned differences in FeO* - Al-Si between the lithology units and between outcrop vs. drill core are summarized in a ternary plot (Figure 4-1) and are consistent with the values determined in previous studies of the same IF (Alexander et al., 2008; Bolhar et al., 2015; Delvigne et al., 2012).

Table 1 XRF and ICP - MS data

Sample ID	DDN_1 267.9	DDN_1 271.5	DDN_1 273.49A	DDN_1 274A	DDN_1 274.3A	DDN_1 274.3D	PMH24L1 861A	PMH24L1 863.4	PMH24L1 864.6A	PMH24L1 864.6C
Lithotype	Magnetic chamosite	Fe-lutite	chert	chert	Fe-lutite	chert	Fe-lutite	Fe-lutite	Fe-lutite	Fe-lutite
Sample type	drill	drill	drill	drill	drill	drill	drill	drill	drill	drill
Major[wt%]										
SiO_2	36.40	67.00	89.00	89.50	31.50	89.20	27.20	19.60	11.20	15.80
TiO_2	0.295	0.041	0.001	0.007	0.021	0.003	0.023	0.022	0.127	0.005
Al_2O_3	6.930	1.340	0.060	0.320	1.670	0.160	0.970	1.370	4.030	0.320
Fe_2O_3tot	28.60	13.60	5.560	3.930	24.30	3.060	46.50	56.70	44.40	40.60
MnO	7.930	8.710	0.330	2.480	19.40	1.970	2.930	4.740	7.710	8.640
MgO	2.070	0.920	0.030	0.290	1.360	0.120	3.400	3.160	6.950	6.550
CaO	<0.02	<0.02	0.320	<0.02	<0.02	<0.02	7.290	2.050	0.330	1.320
Na_2O	0.004	0.002	0.007	0.002	0.005	0.001	0.143	0.002	0.001	0.004
K_2O	0.011	0.006	0.002	0.012	0.017	0.010	0.325	0.002	0.012	<0.001
P_2O_5	0.056	0.101	0.137	0.139	0.047	0.137	0.042	0.055	0.035	0.029
Sum**	96.30	102.6	96.45	100.0	100.7	97.56	100.7	104.0	102.3	103.1
LOI	14.00	10.90	1.000	3.300	22.40	2.900	11.90	16.30	27.50	29.80
FeO*	N.D	9.120	N.D	2.983	18.39	2.899	18.43	29.93	37.79	31.92
$Fe(II)/Fe_{tot}$	N.D	0.745	N.D	0.844	0.841	1.053	0.440	0.587	0.946	0.874
*ICP - MS (ppb)****										
Li	15640	4362	2650	3057	6500	3154	2830	3593	5826	3269
Be	518	218	127	70	207	54	6128	410	695	423
Sc	10410	3389	2193	2311	4057	2509	3852	4061	6436	3311
V	42590	6967	680.6	2303	9761	1257	11180	19430	33320	2662
Co	23950	6279	1105	2187	10760	3197	9324	9818	14130	9510
Ni	82190	20020	1980	4727	32250	3430	14990	30770	43820	16670
Cr	213300	32600	2637	5608	27530	5548	6335	17080	87730	4458
Cu	2050	2073	1331	690.6	11490	68810	4642	904.8	3073	764.9
Zn	98480	30320	5841	8601	50480	6813	17720	25110	62590	24150
Ga	11270	4240	234	1272	8995	1080	2991	3718	8579	3191
As	657	237	1317	174	345	735	794	225	4027	422
Rb	714.1	112.1	199.7	102.2	225.5	152.8	32940	206.9	138.0	84.46
Sr	2915	1385	8987	2123	2498	1362	188300	101500	11400	22650
Y	10970	1801	1555	658.8	5293	599.8	2546	3347	10580	3530
Zr	41110	7692	181.0	1328	5657	756.6	1558	4573	21440	1304
Nb	2175	577.6	45.82	117.4	185.6	42.43	706.5	318.3	2103	96.65
Mo	451.2	162.2	4133	375.5	1426	4269	470.2	426.4	315.8	68.13
Ag	27.5	9.9	46.8	7.4	27.3	83.3	13.4	14.0	18.7	12.5
Cd	85.1	66.0	3.6	7.6	95.5	11.4	25.9	22.8	25.3	16.4
Sn	90.6	42.0	327.8	50.5	139.3	23.6	276.1	227.9	121.6	34.1
Sb	92.9	100.7	612.1	57.2	131.1	146.0	776.4	44.9	92.6	25.1
Cs	175.2	20.23	122.4	18.03	49.10	29.55	13530	46.45	82.91	12.12
Ba	2764	906.3	1242	858.0	1584	714.0	216200	1443	3013	1992
La	3914	1166	127.6	170.0	1802	106.1	3165	2245	6862	440.5
Ce	7821	2265	232.1	346.8	3329	213.8	5872	4546	13690	971.4
Pr	913.0	261.2	31.43	44.80	386.7	26.85	685.1	563.0	1630	146.9
Nd	3436	989.8	134.8	185.7	1534	109.1	2604	2233	6373	757.5
Sm	804.1	203.4	53.79	48.73	336.1	35.08	597.3	519.5	1455	338.3
Eu	297.9	60.75	29.49	17.24	104.2	12.66	409.6	193.4	419.4	127.9

Table 1 continued XRF and ICP - MS data

Sample ID	DDN_1 267.9	DDN_1 271.5	DDN_1 273.49A	DDN_1 274A	DDN_1 274.3A	DDN_1 274.3D	PMH24L1 861A	PMH24L1 863.4	PMH24L1 864.6A	PMH24L1 864.6C
Lithotype	Magnetic chamosite	Fe-lutite	chert	chert	Fe-lutite	chert	Fe-lutite	Fe-lutite	Fe-lutite	Fe-lutite
Sample type	drill	drill	drill	drill	drill	drill	drill	drill	drill	drill
Gd	1242	195.1	136.8	77.16	539.1	67.24	582.8	566.2	1853	483.5
Tb	266.5	34.76	25.02	12.58	98.76	12.96	91.56	87.26	317	82.24
Dy	1892	237.7	156.2	81.38	668.1	79.01	519.9	539.7	1910	505.3
Ho	420.9	56.95	34.93	18.13	149.7	17.19	102.5	114.4	380.8	111.5
Er	1215	189.8	90.73	51.94	416.9	47.14	282.5	331.4	977.7	343.8
Tm	188.3	33.01	11.24	8.418	59.32	7.029	43.98	51.33	136.3	59.9
Yb	1203	234.4	57.65	55.77	364.3	43.49	297.9	345	811.5	422.8
Lu	175.2	36.64	7.518	8.672	55.37	6.426	44.96	53.22	119.5	64.41
Hf	1225	206.3	4.587	31.39	153	18.96	45.16	107	546	33.32
W	200	1376	527.9	173.2	286.9	207.2	400.2	389.8	571.4	369.6
Tl	5.453	1.26	9.762	1.453	5.817	8.539	36.93	1.976	1.683	2.748
Pb	761.5	385.4	1755	463.4	574.9	752.8	1414	591.8	1704	998.8
Th	2237	400.5	15.5	78.86	327.4	47.01	333.3	270.5	1266	82.17
U	602.4	73.27	16.27	34.1	140.4	28.48	201.1	132.5	808.5	80.18
ΣREY (ppm)	34.76	7.770	8.390	17.85	47.51	1.380	1.790	15.14	2.690	15.74
$(La/La^*)_{SN}$	1.06	1.123	1.31	1.144	1.29	1.144	1.17	1.10	1.13	1.40
$(Gd/Gd^*)_{SN}$	1.01	0.97	1.32	1.22	1.13	1.162	1.06	1.12	1.10	1.15
$(Eu/Eu^*)_{SN}$	1.06	1.07	1.40	1.1	0.92	1.00	2.54	1.34	0.95	1.20
$(Ce/Ce^*)_{SN}$	1.014	1.03	1.00	1.01	1.075	1.02	1.03	1.01	1.03	1.07
$(Pr/Yb)_{SN}$	0.21	0.31	0.15	0.22	0.30	0.17	0.64	0.45	0.56	0.10
Pr/Pr*	0.99	0.98	0.99	0.99	0.96	0.99	0.99	0.99	0.98	0.92
Y/Ho	26.07	31.63	44.53	36.34	35.35	34.9	24.84	29.25	27.77	31.66
$(Dy/Yb)_{SN}$	1.01	0.65	1.74	0.94	1.18	1.17	1.12	1.01	1.51	0.77
U/Th	0.27	0.18	1.05	0.43	0.43	0.61	0.60	0.49	0.64	0.98
Zr/Hf	33.56	37.29	39.47	42.31	36.98	39.91	34.51	42.73	39.27	39.12

** Including LOI

*** data given in ppb rather than ppm to allow accurate calculation of concentration ratios from our data or normalization to other standards

FeO* ferrous iron

Out vs. drill: outcrop vs. Drillcore

BD: below detection limit, ND: not determined, IF: iron formation SN: TSB07 shale average Bolhar et al. (2015)

Equations for anomaly calculations according to Lawrence & Kamber (2006) Pr/Pr* calculation according to Bau & Dulski (1996)

Table 1 continued

Sample ID	16 - S- 0 - base	16 - S- 80	16 - S- 90	16 -S -100	16 - S- 105	16 - S -113	16 - S - 138middle	16 - S - 138 top	16 - S- 140	16 - S-174
Lithotype	Fe-lutite	Fe-lutite	Fe-lutite	Fe-lutite	jasper	jasper	Fe-lutite	Fe-lutite	Fe-lutite	Fe-lutite
Sample type	out	out	out	out	out	out	out	out	out	out
Major [wt %]										
SiO_2	54.51	36.92	57.94	20.60	81.98	86.02	50.45	55.31	30.59	35.68
TiO_2	0.078	0.036	0.011	0.084	0.013	0.012	0.029	0.067	0.049	0.084
Al_2O_3	3.984	0.931	0.076	0.853	0	0	0.556	0.973	1.225	1.243
Fe_2O_3tot	35.19	58.23	37.01	73.37	16.22	11.17	45.73	40.35	56.99	40.66
MnO	0.009	2.310	3.810	2.860	1.100	0.950	1.750	1.360	5.900	10.14
MgO	0.541	0.230	0.072	0.181	0.074	0.264	0.200	0.312	0.251	1.379
CaO	0.014	0.017	0.017	0.035	0.005	0.015	0.031	0.036	0.066	0.875
Na_2O	0.075	0.057	0.061	0.051	0.056	0.051	0.049	0.051	0.058	0.051
K_2O	0.240	0	0.004	0	0.007	0	0	0.033	0.145	0
P_2O_5	0.175	0.021	0.034	0.050	0.023	0.015	0.045	0.032	0.179	0.149
Total Sum**	99.89	99.94	100.0	99.79	100.1	100.2	100.0	100.1	99.74	99.74
LOI	4.970	1.160	0.970	1.660	0.590	1.650	1.190	1.510	4.230	9.460
FeO*	1.186	0.383	0.289	0.252	0.477	1.639	1.317	0.372	0.253	0.240
$Fe(II)/Fe_{tot}$	0.037	0.007	0.009	0.004	0.033	0.163	0.032	0.010	0.005	0.007
*ICP-MS (ppb)****										
Li	31860	5546	686.9	3192	808.8	276.0	3705	5879	8985	5075
Be	1215	2322	1606	6179	617	201	801	1258	1025	583
Sc	4937	854.4	226.1	2120	131.8	54.25	967.7	1384	1827	2063
V	32140	15530	6252	27540	2866	810.5	18760	16900	24810	8661
Co	15720	7566	5280	7535	2750	1756	7163	9034	13490	13930
Ni	76070	39240	17070	55800	7887	5541	25500	25660	57220	32750
Cr	56730	19350	3849	68350	4340	1576	10210	24890	26920	54120
Cu	361900	7764	15590	8709	6547	582.6	967.6	1849	3612	1060
Zn	33930	13790	22360	17880	3774	3178	24190	29780	59490	75260
Ga	5288	2478	887	2013	338	379	1646	1655	2511	1487
As	30030	16660	9013	26980	8739	1043	8149	11770	2964	1178
Rb	3923	2052	373.6	4922	364.7	156.4	2455	4161	23200	1283
Sr	17140	16610	18150	26790	7240	4552	24330	26360	52240	49100
Y	6680	4748	3334	9750	1934	783.2	8227	17350	5221	5006
Zr	18200	5874	571.2	14910	488.1	299.0	4452	7659	8234	12350
Nb	1046.0	427.8	67.09	1101	47.36	25.83	322.3	1018.0	585.1	974.4
Mo	1865	3344	2820	6003	1197	301.9	1250	1852	494.1	424.0
Ag	59	15	149	23	15	3	9	18	39	12
Cd	9	24	78	50	21	3	28	36	79	94
Sn	186	240	162	145	105	16	210	208	2147	280
Sb	979	2278	1075	4178	750	268	494	717	249	108
Cs	337.5	641.1	205.8	1244	109.70	19.73	107.1	196.4	426.5	22.23
Ba	23350	117700	250100	243900	81500	12840	34080	21980	358600	8523
La	3837	1924	2727	3282	651.4	246.1	2303	2304	5345	4707
Ce	7437	3534	5026	6292	1225	499.1	3850	4025	8462	8198
Pr	1083.0	462.7	575.2	863.3	162.7	60.80	430.8	468.6	994.3	909.3
Nd	4892	1855	2202	3640	707.9	249.9	1598	1858	3692	3372
Sm	979.9	523.9	514.8	1113.0	208.6	56.04	358.2	560.6	703.9	630.2
Eu	249.5	208.0	190.0	450.4	82.46	20.02	145.3	270.3	193.3	187.7

Table 1 continued

Sample ID	16 - S- 0 - base	16 - S- 80	16 - S- 90	16 -S -100	16 - S- 105	16-S-113	16 - S - 138mid	16 - S - 138 top	16 - S- 140	16 - S-174
Lithotype	Fe-lutite	Fe-lutite	Fe-lutite	Fe-lutite	jasper	jasper	Fe-lutite	Fe-lutite	Fe-lutite	Fe-lutite
Sample type	out	out	out	out	out	out	out	out	out	out
Gd	965.6	759.7	636.2	1657	315.2	77.60	577.1	1101	730.1	614.3
Tb	161.6	141.2	102.5	290.1	51.82	11.46	113.1	232.0	107.5	91.72
Dy	989.4	848.7	577.4	1703	298.7	70.09	791.3	1683	636.5	565.1
Ho	210.2	166.8	110.7	332.3	57.87	16.00	185.7	396.7	141.2	131.1
Er	570.0	426.2	269.2	850.3	141.0	44.02	515.1	1089	399.0	401.0
Tm	79.26	56.92	34.80	113.9	17.69	6.04	68.07	141.1	57.92	64.22
Yb	468.7	307.7	187.6	649.4	93.18	34.62	373.2	780.5	364.8	434.0
Lu	69.38	42.04	24.34	90.43	12.53	5.237	52.78	107.7	55.88	69.09
Hf	492.3	143.7	12.19	384.1	12.34	7.292	82.76	185.3	189.5	328.0
Ta	94.99	30.27	3.926	91.61	3.36	1.82	16.02	47.60	39.67	86.04
W	9141	4204	1638	8265	7579	141.0	1979	1653.0	365.9	314.2
Tl	4.17	34.48	62.82	52.09	11.53	2.182	4.932	4.297	50.20	3.513
Pb	4075	3571	3097	8040	3391	381.7	1505	2824	1628	930.2
Th	823.9	264.5	55.61	765.3	36.26	24.27	272.8	570.1	512.2	837.5
U	2084	1586	700.3	2553	378.2	33.44	1485	2622	662.4	219.1
ΣREY (ppm)	28.67	16.00	16.51	31.08	5.960	2.180	19.59	32.37	27.10	25.38
$(La/La^*)_{SN}$	1.27	1.17	1.22	1.19	1.33	1.20	1.29	1.36	1.30	1.25
$(Gd/Gd^*)_{SN}$	1.02	1.09	1.13	1.14	1.19	1.25	1.09	1.10	1.13	1.10
$(Eu/Eu^*)_{SN}$	0.92	1.22	1.25	1.25	1.24	1.20	1.18	1.28	1.02	1.12
$(Ce/Ce^*)_{SN}$	0.98	0.96	1.05	0.97	1.03	1.06	1.04	1.07	0.99	1.05
$(Pr/Yb)_{SN}$	0.64	0.42	0.85	0.37	0.48	0.49	0.32	0.17	0.76	0.58
Pr/Pr*	0.99	1.01	0.97	1.00	0.97	0.97	0.98	0.96	1.00	0.98
Y/Ho	31.78	28.47	30.11	29.34	33.41	48.96	44.31	43.74	36.98	38.18
$(Dy/Yb)_{SN}$	1.36	1.77	1.98	1.69	2.06	1.30	1.36	1.39	1.12	0.84
U/Th	2.53	5.99	12.59	3.34	10.43	1.38	5.44	4.60	1.29	0.26
Nb/Ta	11.01	14.13	17.09	12.02	14.09	14.20	20.11	21.38	14.75	11.32
Zr/Hf	36.87	40.68	47.10	39.12	39.95	41.23	53.54	41.27	43.34	37.48

** Including LOI

*** data given in ppb rather than ppm to allow accurate calculation of concentration ratios from our data or normalization to other standards

FeO* ferrous iron

Out vs. drill: outcrop vs. Drillcore

BD: below detection limit, ND: not determined, IF: iron formation

SN: TSB07 shale average Bolhar et al. (2015)

Equations for anomaly calculations according to Lawrence & Kamber (2006)

Pr/Pr* calculation according to Bau & Dulski (1996)

Major element concentrations of outcrop samples were determined by ICP-MS

Table 1 continued

Sample ID	16-S-190	16-S-192	16-S-250	16-S-285	16-S-305	16-S-335	16-S-350	16-S-358	16-S-378	16-S-382	16-S-450	16-S-530	16-S-594
Lithotype	Fe-lutite	jasper	Fe-lutite	Fe-lutite	Jasper	jasper	Fe-lutite	Fe-lutite	Fe-lutite	Fe-lutite	shale	shale	shale
Sample type	out	out	out	out	out	out	out	out	out	out	out	out	out
Major [wt %]													
SiO_2	39.29	85.00	38.27	35.87	82.97	70.84	31.53	32.82	31.60	32.17	52.39	50.31	52.86
TiO_2	0.045	0.013	0.101	0.042	0.012	0.013	0.069	0.028	0.086	0.048	0.556	0.541	0.532
Al_2O_3	0.438	0	2.792	1.232	0	0.199	1.883	0.452	2.207	1.118	12.07	12.50	11.80
Fe_2O_3tot	50.02	11.33	47.57	52.20	13.23	21.25	49.74	53.93	52.90	53.90	27.08	27.54	26.74
MnO	6.520	1.780	4.080	5.040	1.520	2.480	7.170	5.920	6.180	6.960	0.230	0.330	0.220
MgO	0.257	0.207	0.807	0.591	0.261	0.749	0.959	0.395	0.589	0.603	3.437	4.063	3.393
CaO	0.155	0.059	0.149	0.207	0.070	0.753	0.257	0.101	0.075	0.155	0.093	0.170	0.071
Na_2O	0.054	0	0.053	0.066	0	0.057	0.057	0.049	0.053	0.068	B.D	B.D	B.D
K_2O	0	0	0.253	0.120	0	0	0.098	0.003	0.174	0.052	B.D	B.D	B.D
P_2O_5	0.078	0.014	0.093	0.093	0.040	0.046	0.071	0.071	0.174	0.068	0.125	0.199	0.105
Total Sum**	100.0	100.1	99.86	99.77	100.1	100.2	99.74	99.91	99.72	99.88	100.6	100.5	100.4
LOI	3.150	1.680	5.660	4.270	2.010	3.760	7.880	6.120	5.660	4.720	4.560	4.770	4.590
FeO*	N.D	1.207	1.735	0.159	0.850	0.159	0.148	0.251	0.204	0.186	21.16	20.40	20.58
$Fe(II)/Fe_{tot}$	N.D	0.118	0.041	0.003	0.071	0.008	0.003	0.005	0.004	0.004	0.868	0.823	0.855
*ICP-MS (ppb)****													
Li	1985	341.0	20740	8247	353.9	285.8	1780	562.3	2979	2728	6402	6506	6230
Be	639	210	1803	1070	205	286	547	524	1029	1012	1965	1349	1895
Sc	762.6	67.9	5431	2278	64.74	729.4	2531	1457	3922	2284	14260	16190	14640
V	8275	597.8	42100	37710	291.8	3155	21220	20430	43200	15670	101900	107800	103000
Co	10560	2855	13910	11510	1895	3648	13190	12890	11700	10160	18330	26180	18630
Ni	17010	5364	50430	42000	5583	10320	38890	27240	40170	31620	112800	130700	113800
Cr	22390	4403	73900	19770	1877	3244	43830	13590	49450	31130	344300	331000	341700
Cu	2812	1222	1976	6392	564.1	2057	802.8	22370	3466	2736	1316	1591	1180
Zn	35290	5929	46010	34700	7421	13710	45610	27890	42220	33820	109800	116400	108900
Ga	1022	348	4681	3223	211	681	2730	1901	3481	2535	15270	16030	15090
As	2069	1131	1132	843	810	1531	210	342	1606	609	337	278	276
Rb	863.0	389.2	12080	4356	495.9	442.3	6015	2291	11230	3807	236.1	911.0	211.7
Sr	45490	5887	58690	157300	9787	38980	127200	99380	38280	85600	5602	5323	4868
Y	3923	870.3	6108	4332	1274	2040	4957	4376	6689	7370	15150	15000	14050
Zr	5573	369.8	20070	7968	154.8	829.6	11910	4938	16000	7596	86690	88320	86560
Nb	442.6	29.67	2130	802.6	9.711	59.50	1032.0	280.9	1270.0	583.4	8067	7743	7752
Mo	294.2	624.8	460.6	393.8	498.0	397.0	629.9	305.1	582.3	360.5	571.9	533.4	794.8
Ag	5.2	2.1	12.5	7.0	1.7	5.7	5.2	5.4	5.4	7.8	26.4	31.0	23.7
Cd	54.1	8.1	54.7	33.9	4.2	18.5	46.1	33.8	53.4	44.9	31.5	30.4	28.2
Sn	330.2	22.8	283.4	297.3	268.0	323.2	188.6	220.0	366.5	364.2	376.1	316.3	335.8
Sb	202.4	259.1	129.7	109.1	120.5	215.9	61.3	94.7	259.0	149.8	76.7	67.9	66.5
Cs	48.61	22.11	300.2	81.30	45.83	108.4	49.80	19.58	133.8	55.99	18.94	31.74	18.50
Ba	20660	2461	81280	95070	1007	12510	21770	9650	45660	28150	4240	4303	2610
La	3406	244.2	6662	4764	1164	982.5	3072	2409	5359	2605	26080	29610	23730
Ce	6170	461.7	13090	8964	1568	1882	5590	4920	11070	5171	50570	58810	45790
Pr	714.7	56.10	1487	1066	160.9	230.5	635.4	614.9	1464	667.9	5650	6728	5105
Nd	2751	227.0	5590	4079	604.2	934.4	2430	2565	6194	2836	20120	24990	18050
Sm	553.9	52.70	1139	820.2	104.6	217.5	530.1	614.3	1452	782.9	3560	4827	3209
Eu	174.3	21.04	299.4	222.9	38.69	97.87	230.6	249.5	485.2	401.9	895.5	1058	812.5

Table 1 continued

Sample ID	16-S-190	16-S-192	16-S-250	16-S-285	16-S-305	16-S-335	16-S-350	16-S-358	16-S-378	16-S-382	16-S-450	16-S-530	16-S-594
Lithotype	Fe-lutite	jasper	Fe-lutite	Fe-lutite	jasper	jasper	Fe-lutite	Fe-lutite	Fe-lutite	Fe-lutite	shale	shale	shale
Sample type	out	out	out	out	out	out	out	out	out	out	out	out	out
Gd	577.6	73.48	1123	769.6	137.4	249.5	582.0	677.1	1464	1050	3120	3874	2830
Tb	86.58	11.52	168.3	115.3	17.66	37.14	96.71	104.8	208.4	174.9	469.3	526.0	423.5
Dy	522.2	74.28	983.2	678.8	107.0	222.8	626.8	618.7	1151	1077	2736	2945	2518
Ho	111.4	17.43	211.0	146.8	25.46	49.68	149.8	134.1	232.8	237.1	577.0	599.0	538.8
Er	313.4	50.10	607.9	425.4	73.27	144.3	486.4	405.1	627.5	679.0	1636	1677	1521
Tm	45.20	6.815	93.81	65.86	10.09	20.82	83.29	65.60	93.2	103.6	243.6	253.0	231.3
Yb	275.5	38.43	622.4	427.9	57.96	129.3	598.2	455.1	614.1	685.1	1545	1634	1460
Lu	41.41	5.847	95.09	61.97	9.544	20.37	96.81	73.46	95.4	103.3	224.1	238.9	214.3
Hf	145.4	8.912	480.1	152.2	3.812	18.47	289.6	91.91	357.8	184.1	2295	2305	2256
Ta	34.70	2.003	120.0	38.92	0.64	4.19	75.29	16.88	89.67	42.11	628.0	612.8	601.4
W	820.3	165.8	270.4	398.9	100.6	223.0	301.6	276.4	6404	853.0	254.1	1694	241.2
Tl	2.030	0.651	16.91	16.75	0.840	3.161	7.902	2.942	12.38	22.41	1.020	1.793	0.526
Pb	968.7	357.3	1720	890.8	399.7	2497	1037	955.3	1406	969	1599	723.4	1456
Th	385.9	26.10	1068	363.8	11.53	49.33	580.3	241.5	695.5	407.5	5049	4757	4754
U	148.2	24.25	410.7	333.6	33.53	71.23	205.5	194.4	556.7	361.4	869.1	845.1	825.8
ΣREY (ppm)	19.70	2.200	38.30	26.90	5.400	7.300	20.20	18.30	37.20	23.90	132.6	152.8	120.5
$(La/La^*)_{SN}$	1.24	1.25	1.11	1.15	1.79	1.23	1.24	1.20	1.15	1.23	1.03	1.07	1.02
$(Gd/Gd^*)_{SN}$	1.12	1.20	1.10	1.08	1.34	1.16	1.07	1.12	1.15	1.14	1.06	1.10	1.06
$(Eu/Eu^*)_{SN}$	1.16	1.31	0.98	1.03	1.32	1.61	1.52	1.45	1.26	1.67	0.98	0.91	0.98
$(Ce/Ce^*)_{SN}$	1.05	1.05	1.04	1.01	1.15	1.04	1.06	1.05	1.01	1.03	1.00	1.02	1.00
$(Pr/Yb)_{SN}$	0.72	0.41	0.66	0.69	0.77	0.50	0.30	0.38	0.66	0.27	1.02	1.14	0.97
Pr/Pr*	0.98	0.97	0.98	0.99	0.93	0.98	0.97	0.97	0.98	0.97	1.00	0.99	1.00
Y/Ho	35.2	49.9	28.9	29.5	50.0	41.1	33.1	32.6	28.7	31.1	26.3	25.0	26.1
$(Dy/Yb)_{SN}$	1.22	1.24	1.02	1.02	1.19	1.11	0.67	0.87	1.21	1.01	1.14	1.16	1.11
U/Th	0.38	0.93	0.39	0.92	2.91	1.44	0.35	0.81	0.80	0.89	0.17	0.18	0.17
Nb/Ta	12.8	14.8	17.7	20.6	15.2	14.2	13.7	16.6	14.2	13.9	12.9	12.6	12.9
Zr/Hf	38.3	41.4	41.9	52.2	41.0	45.0	41.1	54.0	44.7	41.2	37.9	38.4	38.4

** Including LOI

*** data given in ppb rather than ppm to allow accurate calculation of concentration ratios from our data or normalization to other standards

FeO* ferrous iron

Out vs. drill: outcrop vs. Drillcore

BD: below detection limit, ND: not determined, IF: iron formation

SN: TSB07 shale average Bolhar et al. (2015)

Equations for anomaly calculations according to Lawrence & Kamber (2006) Pr/Pr* calculation according to Bau & Dulski (1996)

Major element concentrations of outcrop samples were determined by ICP-MS

Exceptionally high MnO contents were previously reported for the IF (Alexander et al., 2008; Ossa et al., 2016) and also found here, with a range of 2.480 – 19.40 wt % for the drill core samples and a range of 0.009 – 10.14 wt % for outcrop samples. The LOI contents of the Fe-lutites of the drill cores (10.90 – 29.80 wt %, mean of 19.80 ± 7.998 wt %, 1 s.d) are much higher compared to the Fe-lutites from the outcrop (0.970 – 9.460 wt %, mean of 4.174 ± 2.585 wt %, 1 s.d) and a strong correlation (R^2 = 0.90) between the LOI and MnO is only found within the group of for the drill core samples. The remaining major elements are present at low concentrations (<1 wt %). However, variations in K are broadly correlated with Al, and variations in Mg and Ca are broadly correlated with Mn, suggesting that the latter elements are associated with clay minerals and carbonate, respectively. Similar to the Mn and LOI, most of the drill core Ijzermijn IF samples have higher total Mg+Ca relative to the outcrop samples (Figure 4-1).

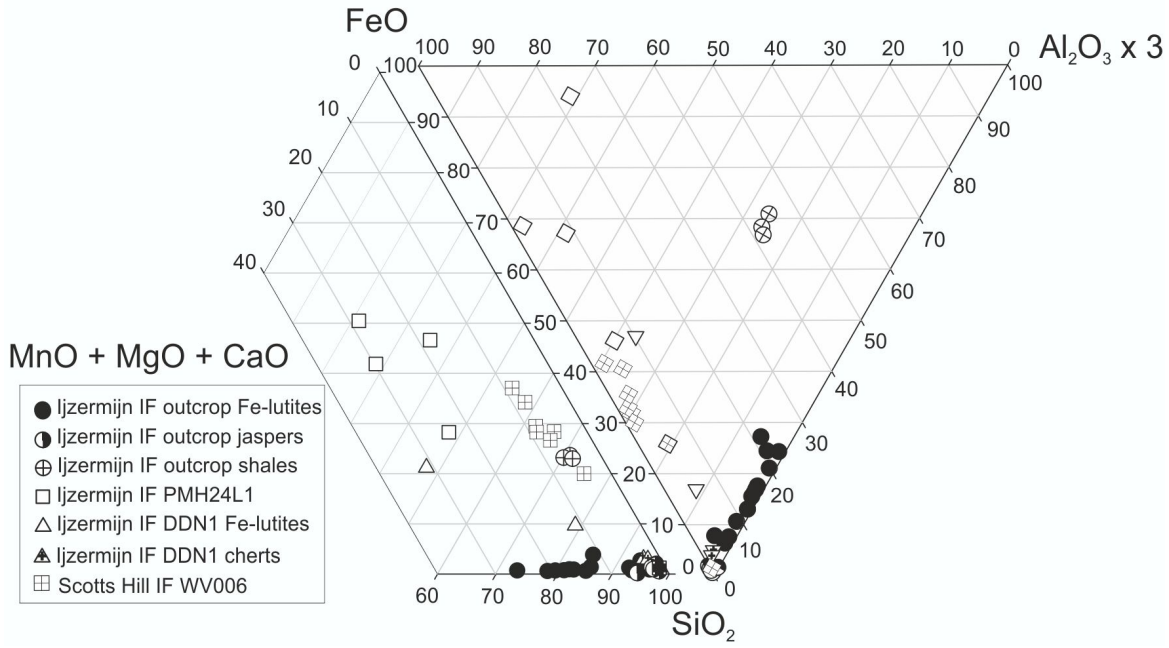

Figure 4-1. FeO-(MnO+MgO+CaO)-SiO_2-Al_2O_3 ternary plots of all samples from this study. Note that Al_2O_3 is exaggerated (x3) to display the distribution of samples in higher resolution and that FeO represents the sample ferrous iron content. Drillcore samples DDN_1 267.9 and 273.49A and WV006_70.53 are not included as their FeO contents could not be determined due to low sample amount. Jaspers from outcrop and both drillcores cluster closest to SiO_2 with near - zero Al_2O_3 consistent with minimal detrital mineral contribution. The Fe-lutite samples from drillcores and the outcrop, as well as Scotts Hill IF, range from low to Al_2O_3 of shales from Ijzermijn IF outcrop, indicating variable detrital mineral content. The significantly higher MnO+MgO+CaO and FeO for drillcore Fe-lutite samples of the Ijzermijn IF relative to the outcrop samples reflects the greater abundance of carbonate and lack of extensive Fe oxidation in the former, a feature that was altered during outcrop exposure weathering. Scotts Hill IF have generally lower carbonate contents relative to both drillcore and outcrop Fe-lutites of the Ijzermijn IF.

Three samples of green shale directly overlying the Ijzermijn IF exhibit higher Al_2O_3 (11.80 – 12.07 wt %) and TiO_2 (0.532 – 0.556 wt %) relative to the IF jasper and Fe-lutite, as well as the highest FeO* (21.16 wt %) and MgO (4.063 wt %) concentrations in outcrop due to the greater abundance of clay minerals, which are dominated by chlorite (chamosite). The SiO_2 – Fe_2O_{3TOT} contents of the green shale are 50.31 – 52.86 wt % with a mean of 51.85 ± 1.357 wt % (1 s.d) and 26.74 – 27.54

wt % with a mean of 27.12 ± 0.401 wt % (1 s.d), respectively, matching closely to other shale samples from the Mozaan Group (Bolhar et al., 2015).

The drill core samples from the Scotts Hill IF are similar in composition to the Ijzermijn IF. The SiO_2 contents are between 29.53 – 59.03 wt % and Fe_2O_{3TOT} contents are 28.95 – 61.63 wt % comparable to the Ijzermijn Fe-lutites. One exception is the chert-rich sample (WV006-92) with an exceptionally high Si/Fe ratio and SiO_2 and Fe_2O_{3TOT} content of 92.78 wt %, and 1.426 wt %, respectively (Table 2), comparable to the Ijzermijn jaspers. Consistent with the drill core Ijzermijn IF samples, ferrous iron levels are high, with FeO* and $Fe(II)/Fe_{tot}$ ranging from 14.45 – 22.12 [wt] % (mean of 17.49 ± 2.829 wt %, 1 s.d), and 0.270 – 0.600 (mean of 0.410 ± 0.128, 1 s.d), respectively excluding the WV006-92 sample (FeO* and $Fe(II)/Fe_{tot}$ are 1.476 wt % and 1.150, respectively). The Scotts Hill IF LOI and MnO contents are lower than the Ijzermijn IF drill core samples. The LOI ranges from 0.884 - 4.698 wt % (mean of 3.287 ± 1.726 wt %, 1 s.d) and the MnO ranges from 0.033-0.690 wt %, with the chert sample WV006-92 bearing the lowest values.

4.1.2. Detrital component of the Mozaan Group IFs

The geochemical composition of the green shale samples can be used to compare data to previous siliciclastic rocks in the Mozaan Group and assess the composition of the detrital element budget in the Ijzermijn IF basin. The mean (n=3, ± 1s.d) Nb/Ta and Zr/Hf ratios of the shales are 12.8 ± 0.14 and 38.4 ± 0.29, respectively, near to the average of 5 Pongola shale values reported by Bolhar et al., (2015) used for REE+Y normalization (the TSB07 composite), with Nb/Ta and Zr/Hf ratios of 12.1 and 35.8, confirming that similar mixed basin signatures were recorded at the Ijzermijn outcrop locality. The Nb/Ta of jaspers in the Ijzermijn IF outcrop is very uniform and only changes from 14.1 to 15.2 (with a mean value of 14.5 ± 0.48), whereas Fe-lutites show more variability with values ranging from 11.0 to 20.1. Zr/Hf values of jaspers are between 39.6 and 44.9 and Fe-lutites are 36.9-53.8. The Fe-lutites with Zr/Hf and Nb/Ta ratios scattering close to shale average is consistent with most of these elements being detritally derived (Bau, 1996; Bau & Alexander, 2009), although, the ones above 50 are outside of the CHARAC field (Bau, 1996) and could imply a more seawater-like signature.

Within the iron formation samples, impurities in the form of detrital siliciclastic minerals, can be tracked with the elements that are typically immobile and poorly soluble during chemical weathering and alteration (Al, Ti, Zr, Hf, Nb, Ta, Ga, Th). The lowest concentrations are found in the jasper samples (e.g., Al_2O_3 less than 0.32 wt. %), whereas concentrations intermediate between the jaspers and shales are found in the Fe-lutites.

For this study, Th concentrations, tested and in good accord with Al_2O_3 (R^2 = 0.90), TiO_2 (R^2 = 0.90), Zr (R^2 = 0.90 for Ijzermijn and 0.80 for Scotts Hill IF) and Nb (R^2 = 0.90) contents, are used as a parameter to determine the degree of detrital contamination in the IF samples; samples with > 100 ppb Th are accepted as having some degree of detrital contamination, (Figure 4-2) allowing a direct comparison with the previously published Th concentrations on Ijzermijn IF (Alexander et al., 2008; Delvigne et al. 2012; Bolhar et al., 2015), whereby jasper samples almost exclusively fall below this level and Fe-lutites are above 100 ppb. The three shale samples have a mean Th concentration of 4850 ± 170 ppb (1 s.d) and the continentally-derived detrital component to the Archean Mozaan Basin is estimated in this study using these values. Recasting the 100 ppb division using a two-component mixture that assumes a Th-free pure chemical sedimentary composition corresponds to a value of 2 % of 'contamination'. Detrital contamination (%) is estimated from $[Th_{sample}/Th_{local\ shale\ average}]$ x 100 calculation. The Th concentration in the Ijzermijn IF outcrop jaspers is low at 11-50 ppb (0.50-1.02 % contamination) and ranges from 56-1068 ppb in Fe-lutites (1.15-22.0 % contamination). Similar values are found in the drill core Ijzermijn IF samples with a Th range of 15.5-47 ppb (0.32-1.62 % contamination) for cherts, and 82.2-2237 ppb (1.70-46.1 % contamination) for the Fe-lutites. The Th concentrations of the Scotts Hill IF exceed 100 ppb with an average of 222.7 ppb (4.60 % contamination), reaching a maximum of 482.5 ppb (9.90 % contamination) (WV006- 67) (Table 2). Most pertinent to the present study is an evaluation of the detrital source of Cr and the REE+Y. The ΣREE+Y is lowest in the jasper samples and intermediate between the shale and jasper in the Fe-lutites. The changes in the ΣREE+Y is broadly correlated with the variation in Th concentration (Figure 4-2), indicating the REE+Y are associated through some mechanism with the detrital component of the IF despite the preservation of seawater-associated anomalies in all samples.

The three shale samples have the highest Cr concentration, averaging 339,000 ± 7050 ppb (1 s.d) and contain a very consistent Cr/Th ratio of 69.9 ± 1.90 (1 s.d). Within both the Ijzermijn IF drill and outcrop samples, the Cr and Th concentrations are highly correlated and samples scatter closely to the shale average ratio of ~70 in the mudstone samples (Cr ranging from 3,849-213,300 ppb) and only deviating substantially in the most Cr-depleted jasper and chert samples (Cr ranging from 1,576- 5,608 ppb). This close relationship is taken to indicate that most Cr is directly associated with the same detrital component that bears the Th and variations in the Cr/Th ratio can be used as an estimate of Cr gains or losses relative to the detrital component as demonstrated in Gailladeu et al., (2015).

Table 2

Sample ID	WV006-43.98 m	WV006-45.45 m	WV006-58.75 m	WV006-58.77 m	WV006-59.59 m	WV006-67 m	WV006-70.53 m	WV006-80.30 m	WV006-92 m
Lithotype	jaspilite	jaspilite	jaspilite	jaspilite	jaspilite	mgn+carb+sil	mgnt+carb+sil	mgnt+carb+sil	Chert
Sample type	drill	drill	drill	drill	drill	drill	drill	drill	drill
Major [wt %]									
SiO_2	42.85	36.74	31.83	36.21	29.53	38.61	53.06	59.03	92.78
TiO_2	0.020	0.034	0.013	0.015	0.017	0.049	0.010	0.033	0.002
Al_2O_3	0.413	0.620	0.286	0.272	0.344	1.004	0.285	1.167	0.050
Fe_2O_{3tot}	47.50	53.06	58.41	56.88	61.63	43.52	35.79	28.95	1.426
MnO	0.683	0.690	0.504	0.577	0.668	0.561	0.099	0.277	0.033
MgO	1.923	2.391	2.142	1.927	1.554	2.132	1.420	2.386	0.078
CaO	1.341	1.939	1.979	1.689	2.489	2.794	2.160	1.436	1.186
Na_2O	0.039	0.051	0.020	0.031	0.032	0.086	0.032	0.043	0.008
K_2O	0.138	0.206	0.101	0.156	0.105	0.336	0.113	0.197	0.020
P_2O_5	0.168	0.143	0.103	0.232	0.186	0.180	0.151	0.112	0.160
Total Sum**	99.77	98.67	96.46	99.91	98.25	95.44	97.24	97.47	96.62
LOI	4.698	2.799	1.060	1.917	1.702	6.166	4.113	3.839	0.884
FeO*	18.39	17.79	14.45	14.60	19.54	22.12	N.D	15.52	1.476
$Fe(II)/Fe_{tot}$	0.430	0.370	0.270	0.290	0.350	0.560	N.D	0.600	1.150
ICP - MS (ppb)									
Li	1425	N.D	4625	4111	2878	386.3	N.D	745.3	63.77
Be	726	N.D	826	630	834	949	N.D	1251	85
Sc	563.0	N.D	518.8	799.8	894.9	1986	N.D	1907	141.1
V	5691	N.D	5567	5787	6959	11730	N.D	14690	742.5
Co	2402	N.D	1923	2232	2567	2928	N.D	4331	387.7
Ni	6749	N.D	5151	7258	7327	16280	N.D	22000	1123
Cr	14320	N.D	9133	15200	14780	35250	N.D	30160	2689
Cu	1661	N.D	2091	1676	920.3	3241	N.D	3424	944.6
Zn	8528	N.D	7709	7875	7489	15720	N.D	16650	1455
Ga	796	N.D	524	542	795	1281	N.D	2251	137
As	3695	N.D	2913	1857	818	2761	N.D	5094	161
Rb	15900	N.D	6170	7337	10820	35830	N.D	21430	2219
Sr	34350	N.D	47150	46570	120200	70550	N.D	36480	15180
Y	4556	N.D	3645	7249	5927	6025	N.D	5695	378.9
Zr	3835	N.D	1940	3330	3793	9455	N.D	11950	524.1
Nb	308.2	N.D	179.4	183.1	214.6	732.5	N.D	691.8	35.37
Mo	157.6	N.D	119.3	173.1	210.1	308.0	N.D	216.5	53.49

Table 2 continued

Sample ID	WV006-43.98 m	WV006-45.45 m	WV006-58.75 m	WV006-58.77 m	WV006-59.59 m	WV006-67 m	WV006-70.53 m	WV006-80.30 m	WV006-92 m
Lithotype	jaspilite	jaspilite	jaspilite	jaspilite	jaspilite	mgnt+carb+sil	mgnt+carb+sil	mgnt+carb+sil	chert
Sample type	drill	drill	drill	drill	drill	drill	drill	drill	drill
Ag	6.3	N.D	2.2	3.7	6.9	1292.0	N.D	12.0	2.6
Cd	3.0	N.D	8.0	6.8	10.9	13.3	N.D	11.9	2.0
Sn	107.9	N.D	107.8	58.8	91.9	107.7	N.D	386.6	92.5
Sb	104.5	N.D	302.1	170.1	217.4	256.5	N.D	413.7	75.0
Cs	4657	N.D	795.4	466.3	3064	12810	N.D	6896	612.4
Ba	223000	N.D	56400	282000	198600	287500	N.D	104300	8277
La	2792	N.D	1719	3723	3865	3614	N.D	3622	285.9
Ce	4710	N.D	3733	6847	7717	6623	N.D	8245	527.8
Pr	576.5	N.D	470.5	812.9	964.9	810.5	N.D	1065	60.17
Nd	2394	N.D	2124	3530	4249	3362	N.D	4240	234.2
Sm	532.4	N.D	498.3	817.1	998.7	752.1	N.D	943.8	51.13
Eu	234.1	N.D	164.7	297.4	349.5	303.9	N.D	325.6	17.31
Gd	635.9	N.D	625.5	1073	1259	915.7	N.D	957.7	55.27
Tb	93.2	N.D	95.5	163.3	188.3	140.3	N.D	158.6	8.759
Dy	568.4	N.D	578.6	1002	1096	863.5	N.D	992.2	53.58
Ho	128.1	N.D	128.5	221.8	228.0	194.2	N.D	220.1	11.90
Er	366.6	N.D	372.2	624.0	621.0	551.5	N.D	642.1	33.49
Tm	53.59	N.D	55.98	87.81	87.40	81.09	N.D	99.7	4.961
Yb	354.2	N.D	373.6	546.0	554.5	520.4	N.D	657.6	29.69
Lu	56.89	N.D	60.67	84.25	84.10	79.61	N.D	99.9	4.420
Hf	96.17	N.D	46.67	77.8	88.51	238.4	N.D	277.7	13.52
Ta	20.87	N.D	10.25	14.89	16.68	50.61	N.D	39.78	2.412
W	268.2	N.D	711.6	201.4	207.5	381.6	N.D	257.8	95.39
Tl	10.81	N.D	45.91	20.10	30.99	53.79	N.D	122.8	7.289
Pb	438.2	N.D	871.7	426.2	791.5	832.1	N.D	1179	121.8
Th	189.0	N.D	96.2	155.1	179.6	482.5	N.D	372.7	23.14
U	54.82	N.D	33.65	40.31	42.25	124.1	N.D	166.8	6.875
ΣREY (ppm)	18.05	N.D	14.64	27.08	28.19	24.84	N.D	27.97	1.760
$(La/La^*)_{SN}$	1.46	N.D	1.31	1.52	1.36	1.35	N.D	0.95	1.26
$(Gd/Gd^*)_{SN}$	1.19	N.D	1.18	1.20	1.20	1.16	N.D	1.04	1.09
$(Eu/Eu^*)_{SN}$	1.56	N.D	1.13	1.23	1.21	1.40	N.D	1.24	1.21
$(Ce/Ce^*)_{SN}$	1.07	N.D	1.13	1.15	1.11	1.07	N.D	0.97	1.07
$(Pr/Yb)_{SN}$	0.45	N.D	0.35	0.41	0.48	0.43	N.D	0.45	0.56
Pr/Pr*	0.96	N.D	0.93	0.93	0.94	0.96	N.D	1.01	0.96
Y/Ho	35.6	N.D	28.4	32.7	26.0	31.0	N.D	25.9	31.8

Table 2 continued

Sample ID	WV006-43.98 m	WV006-45.45 m	WV006-58.75 m	WV006-58.77 m	WV006-59.59 m	WV006-67 m	WV006-70.53 m	WV006-80.30 m	WV006-92 m
Lithotype	jaspilite	jaspilite	jaspilite	jaspilite	jaspilite	mgnt+carb+sil	mgnt+carb+sil	mgnt+carb+sil	chert
Sample type	drill	drill	drill	drill	drill	drill	drill	drill	drill
$(Dy/Yb)_{SN}$	1.03	N.D	1.00	1.18	1.27	1.07	N.D	0.97	1.16
U/Th	0.29	N.D	0.35	0.26	0.24	0.26	N.D	0.45	0.30
Nb/Ta	14.8	N.D	17.5	12.3	12.9	14.5	N.D	17.4	14.7
Zr/Hf	39.9	N.D	41.6	42.8	42.9	39.7	N.D	43.1	38.8

** Including LOI

data given in ppb rather than ppm to allow accurate calculation of concentration ratios from our data or normalization to other standards

FeO* ferrous iron

Out vs. drill: outcrop vs. Drillcore

BD: below detection limit, ND: not determined, IF: iron formation

SN: TSB07 shale average Bolhar et al. (2015)

Equations for anomaly calculations according to Lawrence & Kamber (2006)

Pr/Pr* calculation according to Bau & Dulski (1996)

Major element concentrations of the Redcliff IF samples were determined by ICP-MS

Scotts Hill IF samples also fall close to the Cr-Th trend line defined by the Ijzermijn IF, with Cr concentrations between 9,140 to 35,250 ppb, in magnetite bearing carbonate – silicate iron formation samples and jaspilites and the lowest Cr concentration (2,690 ppb) in chert sample WV006-92 the only sample matching the Th division of less than 100 ppb that appears to overlap with the jasper-Fe-lutite boundary defined from the Ijzermijn IF samples.

4.1.3. Additional trace element parameters in the Mozaan Group IFs

Independent of the inferred variations in detrital component in the IF based on Th (and other immobile element) concentration changes, several Th-normalized element enrichments, calculated as $EF = [(X/Th)_{sample}]/[(X/Th)_{local\ shale\ average}]$, where X is the concentration of the tested element, are evident in the Ijzermijn outcrop IF. A division of 2 is assigned to the EF values, in which those that are equal or greater than 2 are classified as enriched. Notably, enrichment of As, Tl, Ba, W, and U over Th are present in the stratigraphically deepest areas of the IF. For Cr, major deviations occur in jaspers, whereas Fe-lutite samples scatter around a Cr_{EF} of 1, except for sample 16-S-100 which show slightly higher enrichment. The upper chloritic shale samples from the Vlakhoek member show the lowest U_{EF} and Mo_{EF}, due to their predominant continentally derived clastic components (Figure 4-3). The Fe-lutites from both the drill cores and the outcrop of the Ijzermijn IF, with the exception of basal <140 cm of the outcrop samples, have Mo_{EF} and U_{EF} that vary between 1.9 to 17.7 and 1.1 to 7.4 respectively, showing none to moderate enrichments (Figure 4-3). Mo_{EF} of the Ijzermijn IF outcrop Fe-lutites fall in a range between 3.3 and 9.7, and U_{EF} between 2.0 to 7.4. Fe- lutites from two drill cores of the Ijzermijn IF have Mo_{EF} from 3.0 to 12.1, and U_{EF} from 1 to 14.3. The Fe-lutite samples of the basal <140 cm of the White Mfolozi River outcrop of the Ijzermijn IF, show strikingly high U_{EF} with values ranging from 8.0 to 72.0 as well as extreme enrichments of Mo with Mo_{EF} ranging from 17 to 388 (Figure 4-3). The jasper samples of the outcrop of Ijzermijn IF have also moderate to high U_{EF} (5.0 to 60.0), but extreme enrichments of Mo (Mo_{EF} = 61 to 253). Similarly, chert samples from drill core DDN-1 as well as one Fe-lutite sample (274.3A) show extreme enrichments of Mo (Mo_{EF} = 36.0 to 2043), but only relatively small enrichments of U (U_{EF} = 2.5 to 6.0). Both U and Mo enrichments are in general higher in jasper and chert samples compared to the Fe- lutites.

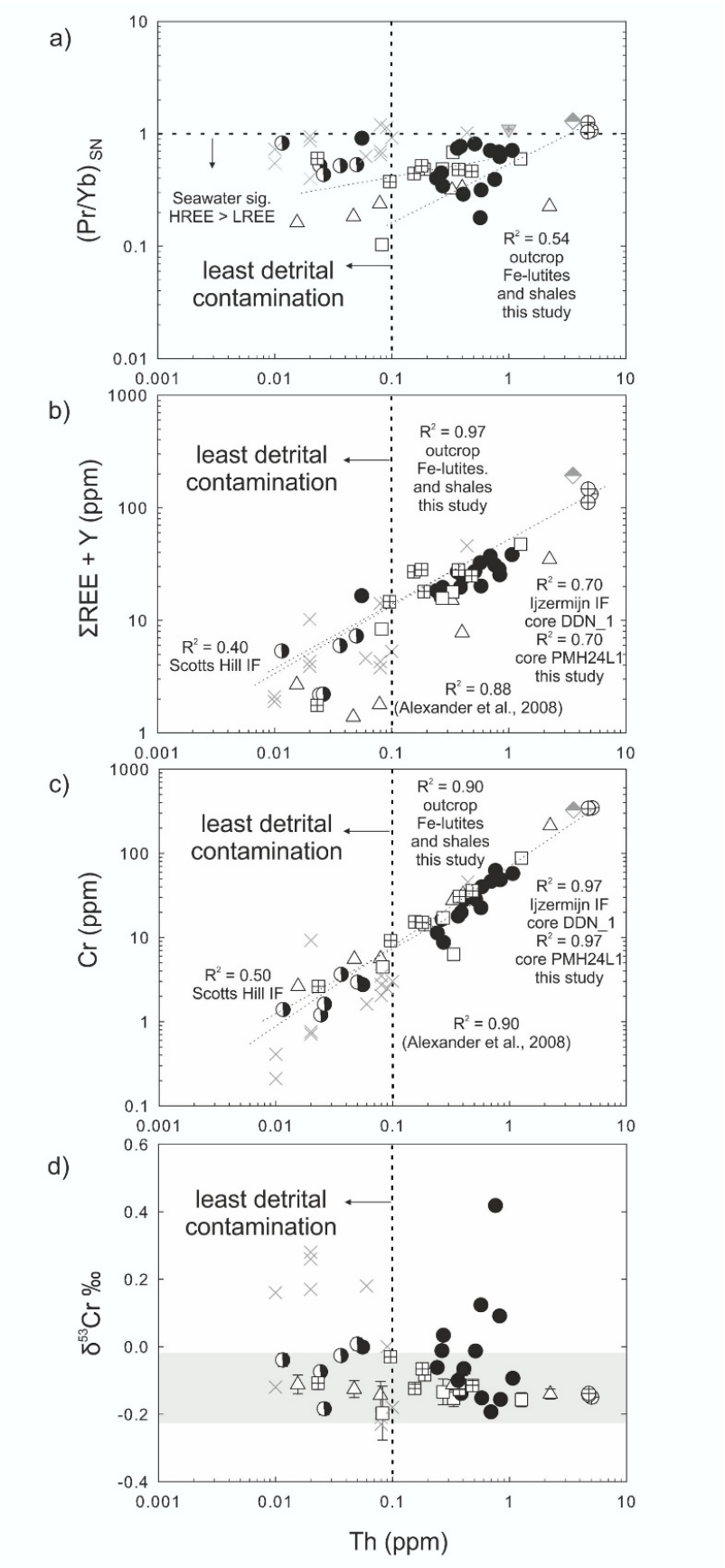

Figure 4-2. Cross plots of the Th concentration against the Pr_{SN}/Yb_{SN} ratio (a), total REE+Y (ΣREE+Y) concentration (b), Cr concentration (c), and $\delta^{53/52}Cr$ ratio (d) showing all IF and shale of this study (symbols as per Figure 2 and 5) and the data of Alexander et al. (2008) and Crowe et al. (2013) (gray crosses). Note that concentrations are in ppm to allow direct comparison to previous studies, and all axes are on a logarithmic scale. The concentration of Th is used as monitor of the detrital element contribution to the IF with a value of 0.1 ppm (vertical dashed line) established as a division below which IF samples are 'least-contaminated' with detrital material based on the results of this study and that of Alexander et al. (2008) to correspond to the approximate difference between jasper (<0.1 ppm) and Fe-lutite samples (>0.1 ppm) of the Ijzermijn IF. Horizontal dashed line in (a) indicates the shale average value for Pr_{SN}/Yb_{SN}. $Pr_{SN}/Yb_{SN}<1$ are present in all IF samples, consistent with a seawater-derived origin, but a broad correlation between Pr_{SN}/Yb_{SN} and Th in Fe-lutite and shale samples from the outcrop of Sinqeni formation suggests a modification of the pattern (increased Pr/Yb) with greater detrital mineral influence. The strong positive correlation of the ΣREE+Y concentrations with Th (b) for all data suggests that the REE are directly or indirectly associated with detrital phyllosilicates in both IF. Similarly, the Cr concentrations show a very strong correlation with Th (c) in all samples, indicating the most of the Cr is associated with detrital material. Most samples of both jasper and Fe-lutite from the Ijzermijn and Scotts Hill IF measured in this study, with varying levels of detrital contamination, show $\delta^{53/52}Cr$ values (d) within the igneous inventory (Schoenberg et al. 2008; denoted by horizontal gray bar). Only four Fe-lutite samples from the outcrop of Ijzermijn IF, although having most of the detrital contamination, display heavy Cr isotope values up to 0.42 ‰. The latter observation stands in contrast to the findings of Crowe et al. (2013) that found isotopically heavy values up to 0.28 ‰ in least detritally contaminated (possibly jasper) samples.

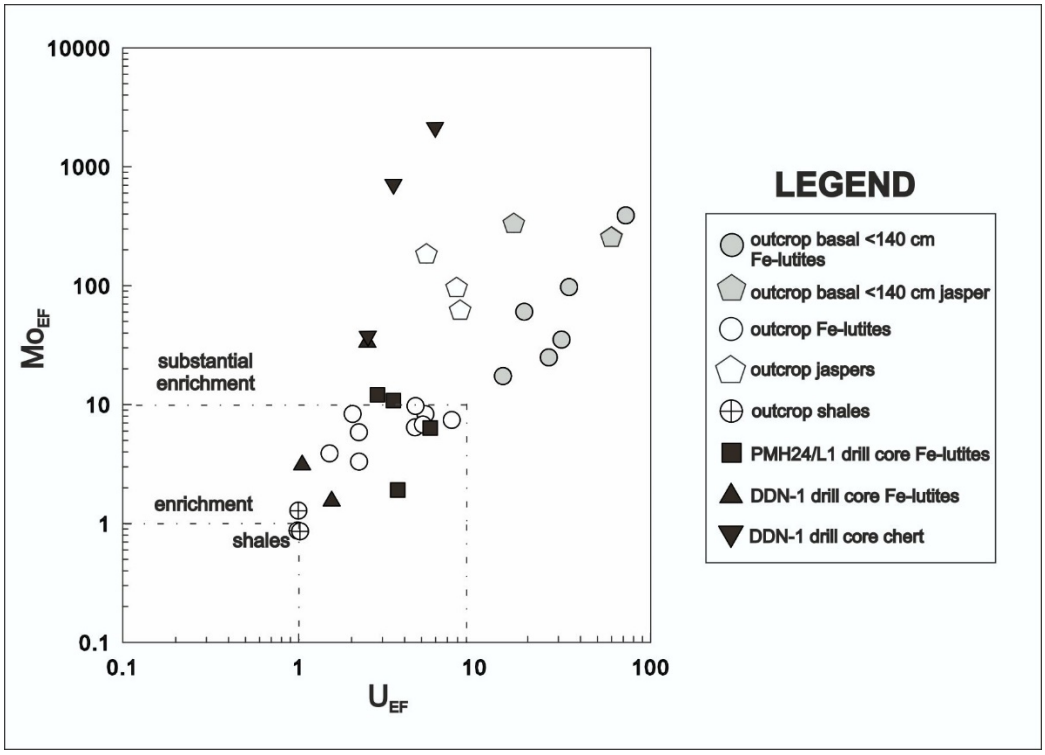

Figure 4-3. Enrichment factors (EF) of Mo and U showing a range of detrital and authigenic sources for all samples from the shales to the Fe-lutites and cherts. Cherts from the DNN-1 drill core show the highest Mo_{EF} values. Note the extraordinarily high U_{EF} from the basal <140 cm section of the White Mfolozi River outcrop.

Authigenic Fe enrichments (Fe_{EF}) range between 2.41 and 87.6 in Fe-lutite samples of both drill cores but Fe-lutite samples from drill core PMH24/L1 have generally higher Fe_{EF} (6.26 to 87.6) compared to the ones from the DDN-1 drill core (2.41 to 13.7). However, the chert samples from DDN-1 drill core also have quite high enrichments of authigenic Fe, despite lower total Fe concentrations (Fe_{EF} = 10.6 to 73.3). Therefore, most samples (both Fe-lutite and chert) reflect an authigenic iron isotope signature. The Fe-lutite samples from the outcrop have a Fe_{EF} range of 8.4 to 132, both the smallest and largest Fe_{EF} values observed in the basal <140 cm section. The jasper samples from the outcrop generally have the highest authigenic Fe enrichments with Fe_{EF} values of 81.9 to 198. The chloritic shale samples of the Vlakhoek member from the outcrop have Fe_{EF} values of 0.95 to 1.07, smaller than the accepted authigenic enrichment cut-off value of "2", thus bearing a detrital Fe signature and lacking authigenic Fe enrichment.

Uranium is another element of interest due to its redox-dependent mobility and proposed use in tracking oxidative U delivery in marine basins through iron formation geochemistry (e.g., Bau & Alexander, 2009; Partin et al., 2013). The U/Th ratios of the outcrop are significantly higher at the bottom of the outcrop of Ijzermijn IF, reaching up to 12.6, but decrease to ≤1 values above 140 cm, except for upper jasper samples with slightly higher U/Th values of 2.9 and 1.4. These outcrop U/Th ratios are also much higher relative to the drill cores which have a mean U/Th value of 0.6 ± 0.3 (1 s.d) and a maximum value of 1.1 (Table 1).

4.1.4. Rare earth elements and yttrium in the Mozaan Group IFs

The ΣREE + Y varies from 1.380 to 47.51 ppm in all Ijzermijn IF drill core samples, with Fe-lutites generally having higher ΣREE + Y contents relative to the cherts (maximum value of 47.51 and 17.85 ppm, respectively, Table 1). The ΣREE + Y varies from 2.18 ppm to 38.28 ppm in all Ijzermijn IF outcrop samples. Similar to drill core samples, jaspers have smaller ΣREE + Y compared to the Fe- lutites, which have maximum values of 7.300 and 38.30 ppm, respectively (Table 1). The ΣREE + Y of Scotts Hill IF varies between 14.64 – 28.19 ppm (mean of 24.74 ± 5.792 ppm, 1 s.d), with the exception of WV006-92 sample with a very low ΣREE + Y of 1.76 ppm (Table 1).

The most pertinent features of the iron formation REE+Y data outside of the concentration ranges are the slopes of the normalized patterns and expression of La-Ce-Gd-Y anomalies that reveal insight into solute source and processes during soluble transport in the hydrosphere, especially when observed in the samples with the purest chemogenic signatures (e.g., Bau and Dulski, 1996). The REE+Y patterns of IF are commonly normalized to an upper continental crust composite such as the Post-Archean Australian Shale (PAAS) average or the alluvial sediment average known as 'Mud from Queensland' MuQ (Kamber et al., 2005), or, alternatively, local basin siliciclastic compositions. Here, both strategies were adopted using MuQ and an average shale composition calculated from 5 samples (TSB07/26-175, -174, -173, -170.6, -169.4) reported by Bolhar et al. (2015) that is henceforth abbreviated as TSB07. The TSB07 shale composite bears higher REE+Y concentrations (ΣREE+Y=229 ppm) and a lower mean of Y/Ho (22.9 ± 0.33, 1 s.d) than the mean composition of the three outcrop shale samples of the Vlakhoek Member of the Sinqeni Formation from this study (mean Y/Ho of 25.8 ± 0.70, 1 s.d; ΣREE+Y = 135.3 ± 16.32 ppm, 1 s.d), although when the mean of the outcrop shale samples is normalized to the TSB07 composite a relatively flat REE pattern is produced with a $(Pr/Yb)_{TSB07}$ of 1.04. Moreover, the REE+Y pattern of the mean outcrop shale is consistent with other previously published studies for Mozaan clastic sedimentary rocks (Alexander et al., 2008; McLennan and Taylor, 1983; Wronkiewicz, 1989). Nevertheless, the TSB07 composite is preferred due to any potential surface weathering effects on the outcrop shale and thus for the remainder of the text, shale-normalized (SN) data refer to those reported relative to TSB07 unless otherwise stated. Further, all data from previous studies presented here for comparison, are recalculated to this same normalized composition. The TSB07 data are also viewed as a better approximation of the Mozaan basin geochemistry and a better way to account for local influences on the soluble REE+Y weathering flux when compared to a bulk upper continental crust composite, as adopted in previous Ijzermijn IF studies (Alexander et al., 2008). This is evident from the relationship of $(Pr/Yb)_{TSB07}<(Pr/Yb)_{MuQ}$ (Appendix Supplemetary Figure 1) The normalized REE+Y patterns for the Ijzermijn IF drill core and outcrop samples and for the Scotts Hill IF drill core samples are found in Figure 4-4 and in Appendix

Supplemetary Figure 2, respectively. The shale-normalized REE + Y patterns of all samples from both IFs show a depletion of LREE relative to HREE with $(Pr/Yb)_{SN}$ ranging from 0.10 – 0.85 (Table 1 and 2, Appendix Supplementary Figure 2). However, drill core samples have lower $(Pr/Yb)_{SN}$ ratios (mean of 0.31 ± 0.18) relative to the outcrop samples (mean of 0.52 ± 0.19). The jasper $(Pr/Yb)_{SN}$ values are in good accord with the previously published Alexander et al., (2008) and Delvigne et al., (2012) studies, which range from 0.30 - 0.94. A small suite of Ijzermijn IF Fe-lutites reported in the Alexander et al., (2008) study are also similar to those of this study with $(Pr/Yb)_{SN}$ ranging from 0.70-1.10.

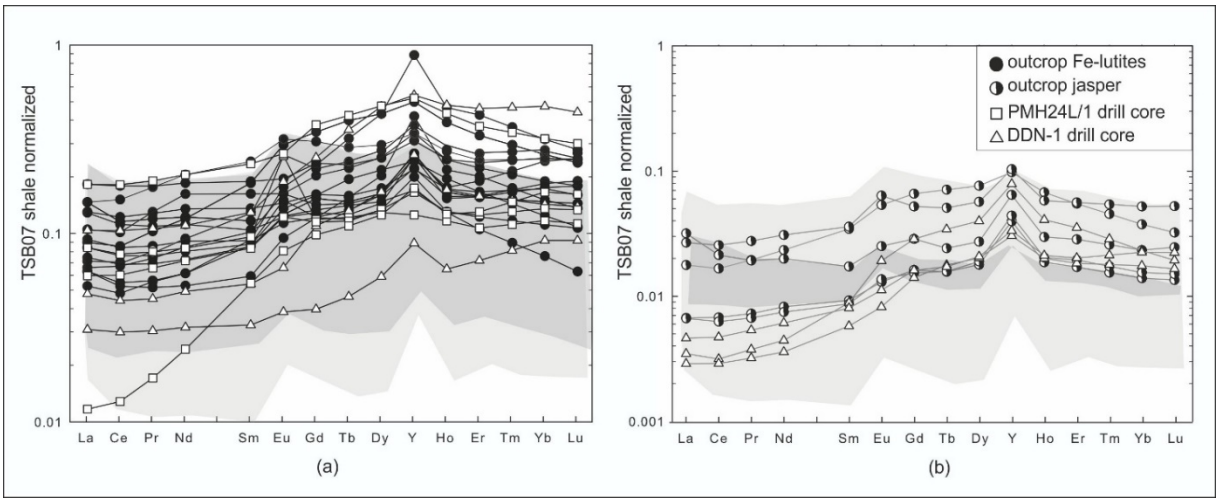

Figure 4-4. Rare earth element plus yttrium (REE+Y) patterns of the Fe-lutite samples from the drill cores and the outcrop of Ijzermijn IF (a) and chert samples from the the drill core DDN-1 and jasper samples from the outcrop of Ijzermijn IF (b). All data are normalized to the TSB07 shale average from the Bolhar et al., (2015) study, as described in the text. The dark and light gray areas denote REE+Y data from Alexander et al. (2008) and Delvigne et al. (2012) studies, respectively, which largely overlapping with both jasper and Fe-lutite data of the drill cores and outcrop from this study. Jaspers have lower REE+Y concentrations than Fe-lutites on average and both sets of samples show anomalies (positive Y, La, and Gd) and LREE/HREE depletion that are typical of Archean chemical sedimentary rocks. Some variability in the relative LREE/HREE depletion, REE+Y concentration, and variability in anomalies are interpreted to variable levels of detrital mixing and the potential influence of surficial weathering, as discussed in the text.

A common feature of marine chemical precipitates is an overabundance of Y over Ho, commonly expressed as a Y/Ho mass ratio beyond chondritic (~27; Pack et al., 2007) and upper continental crust values (~26; e.g., Kamber et al., 2005), due to differences in aqueous complexation behavior. Bau (1996) also defined a field of Y/Ho ratios of 24 to 34 that could be attributed to charge-and-radius-controlled (CHARAC) behaviour of the element pair, but beyond which aqueous fluids are generally implied to have an influence on fractionation. The highest Y/Ho values are among jasper samples (Y/Ho from 33.41 to 50.00), although the Fe-lutite samples 16-S-138_{mid} and 138_{top} display highly superchondritic Y/Ho ratios as well (44.31 and 43.74, respectively). The Y/Ho of the remaining Fe-lutite samples ranges from 24.84 to 38.18. Scotts Hill IF display Y/Ho ratios from 25.88 to 38.02 (Table 2). These observations match previous studies on the Ijzermijn IF by Alexander et al., (2008) and Delvigne et al., (2012) where Y/Ho ranges from 35.7 - 38 and 26.4 - 33.7, respectively, with the highest of these ratios expressed in samples with the lowest Fe/Si ratio (a proxy for relative amount of jasper or chert

in the samples; see Figure 4-1). The jasper samples characterized as silica-rich by Delvigne et al., (2012) range from 31.4 - 65.5 and between 32.1- 52.9 in Alexander et al. (2008) study.

Similar to Y/Ho fractionation, marine precipitates, including Precambrian IFs, often have a selective over-abundance of La and Gd relative to neighbouring lanthanides in shale-normalized patterns due to slight complexation differences related to filling patterns of the f-orbital electrons (e.g., Lawrence & Kamber, 2006). These overabundances are quantified here using the geometric anomaly calculations of Lawrence & Kamber (2006) from the shale-normalized data. All samples show (Table 1, Appendix Supplementary Figure 3), calculations according to Lawrence & Kamber, 2006) positive Gd [$(Gd/Gd)^*_{SN}$ = 1.00 – 1.33] and La [$(La/La)^*_{SN}$ = 1.05 – 1.38] anomalies, except for one sample from the Scotts Hill IF [WV006 – 80.30 with $(La/La)^*_{SN}$ = 0.94, Table 2].

Positive anomalies of Eu (Eu/Eu*) in iron formation are often used as a proxy for hydrothermal solute input due to the highly contrasting abundance of Eu in hydrothermal fluids compared to open seawater (e.g., Alexander et al., 2008). Distinct, positive Eu anomalies (calculated as above for La and Gd) are observed in all jasper samples [$(Eu/Eu^*)_{SN}$ = 1.00 – 1.60], as well as most of the Fe-lutite samples [$(Eu/Eu^*)_{SN}$ = 1.00 – 2.50] and Scotts Hill IF [$(Eu/Eu^*)_{SN}$ = 1.13 – 1.56] (Table 2). The Fe-lutite samples 16- S-0, DDN-1 274.3A, PMH24/L1 864.6A display slightly negative Eu anomalies [$(Eu/Eu^*)_{SN}$ = 0.90]. Although the significance of the magnitude of the Eu anomaly is dependent on the normalization data (e.g., often chondrite are used), the remainder of the consideration of Eu data focuses on relative differences between samples.

The presence or absence of Ce anomalies in IF is an established proxy for Ce fractionation related to a redox-state change and as typical for most Archean IF, samples from the present study have insignificant to minor Ce anomalies (Figure 4-5). Calculated using the geometric projection from Nd and Pr after Lawrence & Kamber (2006), the $(Ce/Ce^*)_{SN}$ values of the outcrop and drill core Ijzermijn IF range from 0.96 - 1.15. The pervasive lack of significant Ce anomaly is supported using the $(Ce/Ce^*)_{SN}$ vs. $(Pr/Pr^*)_{SN}$ plot of Bau & Dulski (1996) (Figure 4-5) where the Ijzermijn IF outcrop and drill core samples fall within a $(Pr/Pr^*)_{SN}$ range of 0.96 and 1.01, with the exclusion of outcrop sample 16-S-305 (0.93) and drill core sample PMH24L1 864.6C (0.92). The two latter samples, 16-S-305 and PMH24L1 864.6C, reaching the highest $(Ce/Ce^*)_{SN}$ and lowest $(Pr/Pr^*)_{SN}$, possess the most extreme range of LREE enrichment and depletion, respectively (Figure 4-5), that influences the magnitude of the calculated anomaly values, as discussed in Kamber et al., (2014). The previous studies of the Ijzermijn IF contain a full range in $(Ce/Ce^*)_{SN}$ (recalculated to the TSB07 mean used in this study) of 0.80-1.00 (e.g Delvigne et al., 2012). Within the Scotts Hill IF, 6 samples plot with a $(Ce/Ce^*)_{SN}$ and $(Pr/Pr^*)_{SN}$ values ranging from 0.97-1.07 and 0.96- 1.01, respectively, whereas samples (WV006 58.75, 58.77, 59.59) plot to

distinctly higher $(Ce/Ce^*)_{SN}$ (1.11-1.15) and lower $(Pr/Pr^*)_{SN}$ (0.93-0.94). These samples, the only ones to plot in the field of a true positive Ce anomaly, do not bear unusual LREE enrichment or depletion. However, they are notably found stratigraphically within the post-depositionally oxidized and hematite-bearing section of the Scotts Hill IF drill core.

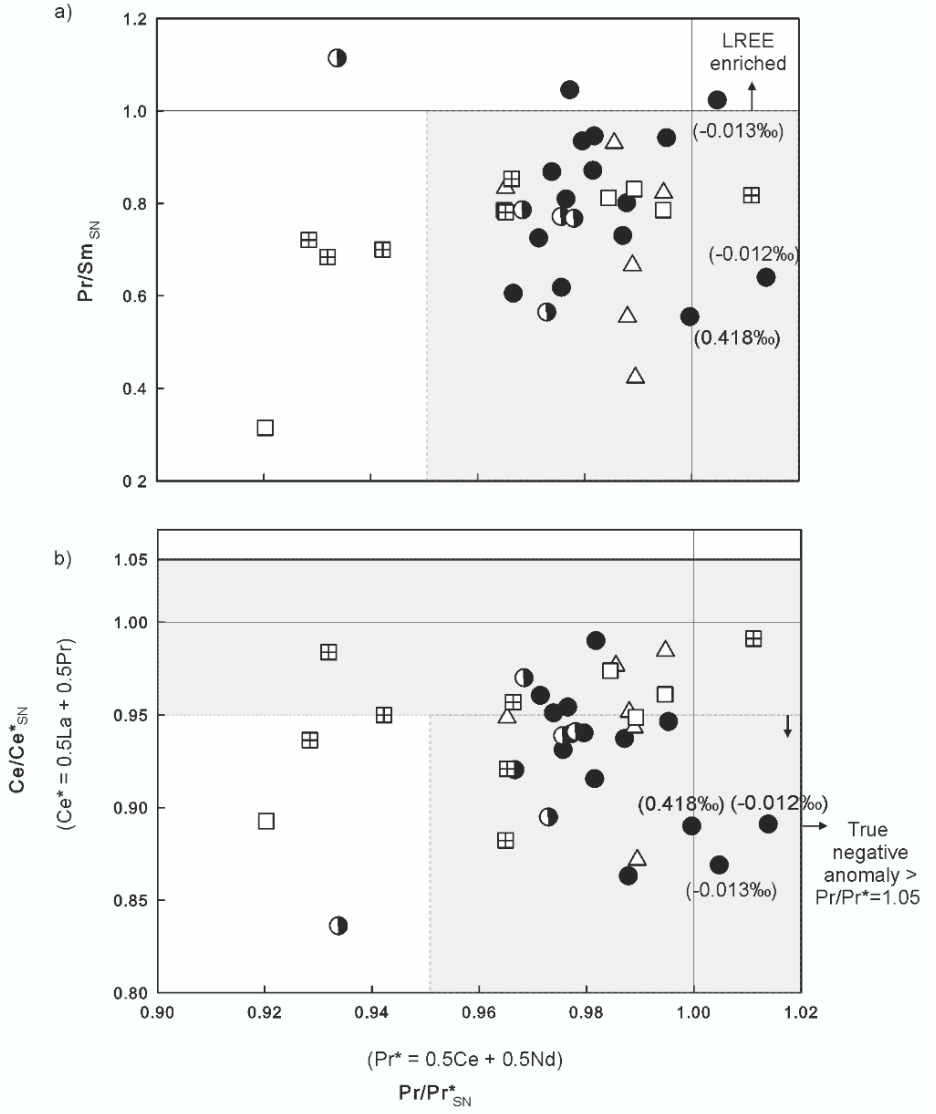

Figure 4-5. A combination of a) Pr_{SN}/Sm_{SN} versus Pr_{SN}/Pr_{SN}*and b) Ce_{SN}/Ce_{SN}* versus Pr_{SN}/Pr_{SN}*. Plot b) is according to Bau & Dulski (1996) to isolate true Ce anomalies that occur at the correspondence of a negative Ce anomaly and a positive Pr anomaly. Five samples plot to low Pr_{SN}/Pr_{SN}*: 3 samples from Scotts Hill IF, 1 sample of Izjermijn outcrop jaspilitic IF, and 1 sample of Izjermijn drillcore IF. The latter two samples possess more extreme LREE enrichment or depletion, as evident using Pr_{SN}/Sm_{SN} in plot a) and influences the anomaly calculations of Ce. The 3 Scotts Hill IF samples appear to have true positive Ce anomalies, as demonstrated from the alternative calculation of the Ce_{SN}/Ce_{SN}* using a projection from Pr and Nd, as discussed in the text. Plot b) also reveals that samples 16-S-100 with the heaviest $\delta^{53/52}Cr$ value of 0.42 ‰ as well as samples 16-S-80 and 16-S-140 within the border of igneous inventory $\delta^{53/52}Cr$ values show Ce_{SN}/Ce_{SN}* near the threshold of true negative Ce anomaly. Vertical gray areas indicate the threshold values for Ce anomalies that are typically adopted (0.95-1.05). All values are normalized to the TSB07 shale average of Bolhar et al. (2015), which are denoted as SN.

A conspicuous MREE enrichment in shale-normalized REE patterns was recognized in previous investigations of the Ijzermijn IF (Alexander et al., 2008) and of shallow water carbonates from Pongola Supergroup (Bolhar et al., 2015). Within the Ijzermijn outcrop, MREE enrichment was identified selectively towards the base and top of the IF sequence by Alexander et al., (2008). In our study, the three shale samples overlying the IF do not have significant MREE enrichment, measured here using $(Dy/Yb)_{SN}$ ratios which fall within a narrow range of 1.11-1.16 (Table 1). By contrast, the outcrop IF

$(Dy/Yb)_{SN}$ ranges between 0.67-1.77 with an overall mean of 1.27 ± 0.37 including both jasper and Fe-lutite samples. Comparable to Alexander et al., (2008), the highest Dy/Yb is measured at the bottom of the Ijzermijn IF outcrop sequence (ranging from 1.35 to 2), followed by a return to lower values in the stratigraphically higher samples. However, values as high as those reported by Alexander et al., (2008) were not found in the upper section of the IF in this study. By contrast to the outcrop Ijzermijn IF samples, the Ijzermijn drill core IF reach lower $(Dy/Yb)_{SN}$ values and do not extend as high as the outcrop (ranging from 0.64 to 1.72) and have a lower overall mean of 1.1. For comparison, the IF samples of Alexander et al., (2008) have $(Dy/Yb)_{SN}$ ranging from 0.94-2.53, those of Delvigne et al., (2012) range from 1.04-2.08, respectively.

Collectively, apart from some differences noted between drill core and outcrop samples, the REE+Y systematics of the IF reported in this study overlap with concentrations and ratio ranges reported in previous studies, indicating that comparably representative expressions of the IF have been covered by the sampling of this study (Alexander et al., 2008; Delvigne et al., 2012; see shaded area in (Figure 4-4). Moreover, most of the drill core and outcrop IF samples of both lithology show REE+Y patterns and anomalies (LREE depletion relative HREE, Y/Ho mass ratios >27, and positive SN-normalized Gd and La anomalies) that are viewed as typical of Archean seawater (Bau & Dulski, 1996).

4.1.5. ($^{234}U/^{238}U$) activity ratios and stable $^{238}U/^{235}U$ isotopic compositions of the Sinqeni Formation

Samples from both drill cores (DDN-1 and PMH24/L1) have ($^{234}U/^{238}U$) activity ratios in the range of 0.967 to 1.014, all very close to secular equilibrium (($^{234}U/^{238}U$) activity ratio=1, Table 3, Figure 4-6). By contrast, the ($^{234}U/^{238}U$) activity ratios for White Mfolozi River outcrop Ijzermijn IF samples show a very large range from 1.047 to 1.768, consistently well above secular equilibrium (Table 3). The Vlakhoek member shale samples from the same outcrop display a ($^{234}U/^{238}U$) activity ratio range of 0.890 to 0.956, below secular equilibrium (Table 3). The ($^{234}U/^{238}U$) activity ratio data from the two laboratories, for sample 16-S-90 (LUH value of 1.260; TCD value of 1.249) and sample 16-S-100 (LUH value of 1.123; TCD value of 1.140) obtained from separate digests, show very close agreement (Table 3). The $\delta^{238/235}U_{CRM112\text{-}A}$ values of the outcrop shale and IF samples range from - 0.227 to - 0.456 ‰, within error all in the range of the continental crust values of - 0.20 to - 0.40 ‰ (Weyer et al., 2008) (Table 3).

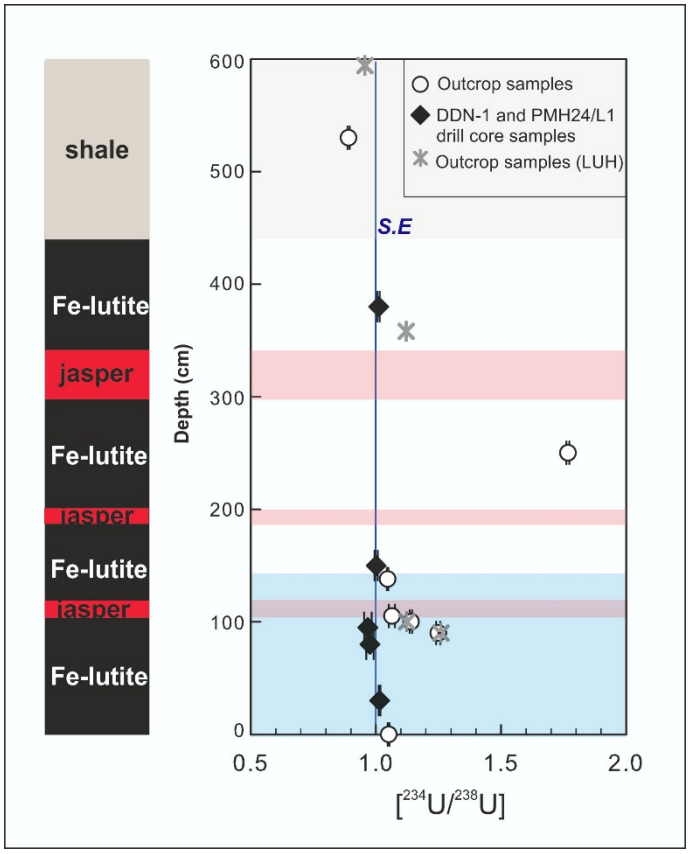

Figure 4-6. Stratigraphic plots of U activity ratios for the Ijzermijn IF outcrop and drill core samples. The deviation of U activity ratios of outcrop samples from secular equilibrium, compared to the drill cores, shows the strongest evidence on the modern weathering induced alteration of the outcrop. The horizontal red bars indicate jasper samples, and horizontal gray bar indicates the shale samples. The depth positions for the drill core samples were estimated from the lithostratigraphic correlation between the drill cores and the outcrop.

4.1.6. Stable Cr isotopes of the Mozaan Group samples

The stable Cr isotopic data for all samples are presented in Table 4. All chert layers and Fe-lutite samples from the Ijzermijn IF drill core samples display $\delta^{53/52}Cr_{SRM979}$ values in the range of -0.197 to - 0.068‰, with an average of -0.130 ± 0.069 ‰ (2 s.d, n= 10) and thus lie within the unaltered igneous rock inventory of -0.124 ± 0.101 ‰ (Schoenberg et al., 2008). Scotts Hill IF drill core samples reveal similarly unfractionated values with a range of -0.124 to -0.021 ‰ and an average of - 0.08 ± 0.077 ‰ (2 s.d, n = 9). The outcrop samples from the Ijzermijn IF, however, display a wider range of Cr isotopic signature, including both heavy and unfractionated $\delta^{53/52}Cr_{SRM979}$ values. The Fe-lutite samples "16 - S - 0", "16 -S -100" and "16 -S -138$_{mid}$ and 138$_{top}$" display heavy $\delta^{53/52}Cr_{SRM979}$ values of + 0.091, + 0.418, + 0.034 and + 0.124 ‰, respectively. The rest of the Fe-lutite and shale samples from the outcrop show $\delta^{53/52}Cr_{SRM979}$ values within the range of the igneous inventory, like the drill core samples, ranging from - 0.193 to - 0.013 ‰, with an average of - 0.100 ± 0.11 ‰ (2 s.d, n = 13). Jasper samples from the outcrop reveal bulk silicate earth values from - 0.184 to 0.008 ‰ with an average of - 0.060 ± 0.14 ‰ (2 s.d, n = 5).

Table 3

Sample ID	Lithotype		Sampling Laboratory	* U (ng/g)	$^{\$}$ (^{234}U/^{238}U)	2SE	$\delta^{238/235}U_{CRM112\text{-}A}$ (‰)	2SE	U_{EF}
DDN_1 274A	Fe-lutite	drill	TCD	*34.10*	0.967	0.015			2.46
DDN_1 274.3D	Chert	drill	TCD	*28.48*	0.976	0.015			3.47
PMH24L1 861A	Fe-lutite	drill	TCD	*201.1*	1.011	0.005			3.46
PMH24L1 863.4	Fe-lutite	drill	TCD	*132.5*	1.001	0.007			2.81
PMH24L1 864.6A	Fe-lutite	drill	TCD	*808.5*	1.014	0.003			3.66
16-S-594	shale	out	LUH	**817.1**	0.956	0.002	-0.227	0.008	1.00
16-S-530	shale	out	TCD	*845.1*	0.890	0.004			1.02
16-S-358	Fe-lutite	out	LUH	**168.7**	1.121	0.002	-0.346	0.037	4.61
16-S-250	Fe-lutite	out	TCD	*410.7*	1.768	0.006			2.20
16 - S -138top	Fe-lutite	out	TCD	*2622*	1.047	0.003			26.4
16 -S- 105	jasper	out	TCD	*378.2*	1.064	0.012			59.8
16 -S -100	Fe-lutite	out	TCD	*2553*	1.140	0.004			19.1
			LUH	**2489**	1.123	0.003	-0.387	0.030	
16 - S- 90	Fe-lutite	out	TCD	*700.3*	1.249	0.008			72.2
			LUH	**689**	1.260	0.007	-0.456	0.026	
16 - S- 0 - base	Fe-lutite	out	TCD	*2084*	1.051	0.003			14.5

* Concentrations given in bold font are isotope dilution data from double spike MC-ICP-MS analyses (LUH);
italic font are solution ICP-MS data from University of Tuebingen

$^{\$}$ activity ratios of the samples, i.e. measured ^{234}U/^{238}U isotopic ratios multiplied with the inverse ratio of the decay constants

§ data measured at TCD = Trinity College Dublin or LUH = Leibniz University of Hannover

4.1.7. Stable Mo isotopic compositions and Mo concentrations of the Sinqeni Formation samples

The concentration of Mo in Fe-lutites in Ijzermijn IF drill cores vary between 162 and 1425 ng g^{-1} while the cherts have concentrations between 375 and 4270 ng g^{-1}. Thereby, the Fe-lutites of the drill core PMH24/L1 show a lower range of 315 to 470 ng g^{-1} than those of the DDN-1 drill core. Both jaspers and Fe-lutites from the White Mfolozi River outcrop of the Ijzermijn IF show a range in Mo concentrations between 294 to 630 ng g^{-1}, with the exception of the basal samples (i.e. below < 140 cm depth), which have very high Mo concentrations of 1250 to 6003 ng g^{-1} (Table 5, Figure 4-7). These basal samples also display the lowest $\delta^{98/95}Mo_{NIST\ 3134+0.25}$ signatures among all outcrop samples with values ranging from + 0.407 to - 0.476 ‰ while samples above 140 cm from the base range from + 0.112 to + 1.160 ‰ in $\delta^{98/95}Mo_{NIST3134+0.25}$ (Table 5, Figure 4-7). The upper chlorite- and chamosite-bearing shale samples of the Vlakhoek member from the White Mfolozi outcrop have $\delta^{98/95}Mo_{NIST3134+0.25}$ values from + 0.267 to + 0.630 ‰ and Mo concentrations ranging from 533.4 to 794.8 ng g^{-1}. The chert samples from the drill core DDN-1 (273.49A, 274A and 274.3D) have similarly negative $\delta^{98/95}Mo_{NIST\ 3134+0.25}$ values as the basal outcrop samples with values between - 0.313 and - 0.546 ‰. Some Fe-lutite samples from both of the Ijzermijn IF drill cores have slightly positive values (+ 0.315 to + 0.382 ‰), which are in the crustal igneous range (average ~0.3 to + 0.4 ‰) (Voegelin et al., 2014).

Table 4

	Formation	Sample ID	Lithotype	Sample Type	Cr (µg g-1) MC- ICP - MS	$\delta^{53/52}$Cr (‰)	2SE
Magnetic chamosite	Sinqeni	DDN_1 267.9	mudstone	drill	213.0	-0.141	0.02
Rhodochrositic IF	Sinqeni	DDN_1 271.5	Fe-lutite	drill	32.13	-0.068	0.02
Chert	Sinqeni	DDN_1 273.49A	Chert	drill	2.43	-0.112	0.03
Chert	Sinqeni	DDN_1 274A	Chert	drill	5.21	-0.144	0.04
Rhodochrositic IF	Sinqeni	DDN_1 274.3A	Fe-lutite	drill	25.79	-0.113	0.02
Chert	Sinqeni	DDN_1 274.3D	Chert	drill	4.26	-0.126	0.03
Banded magnetic siderite-silicate IF	Sinqeni	PMH24L1 861A	Fe-lutite	drill	6.12	-0.153	0.03
Banded magnetic siderite-silicate IF	Sinqeni	PMH24L1 863.4	Fe-lutite	drill	15.33	-0.134	0.04
Banded magnetic siderite-silicate IF	Sinqeni	PMH24L1 864.6A	Fe-lutite	drill	83.87	-0.158	0.02
Banded magnetic siderite-silicate IF	Sinqeni	PMH24L1 864.6C	Fe-lutite	drill	4.03	-0.197	0.08
chlorite shale	Sinqeni	16-S-594	shale	out	313.5	-0.139	0.01
chlorite shale	Sinqeni	16-S-530	shale	out	301.3	-0.143	0.01
chlorite shale	Sinqeni	16-S-450	shale	out	322.9	-0.150	0.02
Fe-lutite IF	Sinqeni	16-S-382	Fe-lutite	out	27.96	-0.065	0.01
Fe-lutite IF	Sinqeni	16-S-378	Fe-lutite	out	46.35	-0.193	0.01
Fe-lutite IF	Sinqeni	16-S-358	Fe-lutite	out	11.29	-0.062	0.01
Fe-lutite IF	Sinqeni	16-S-350	Fe-lutite	out	39.97	-0.152	0.01
Hematitized IF jasper	Sinqeni	16-S-335	jasper	out	2.94	0.008	0.02
Hematitized IF jasper	Sinqeni	16-S-305	jasper	out	1.39	-0.039	0.02
Fe-lutite IF	Sinqeni	16-S-285	Fe-lutite	out	17.93	-0.100	0.01
Fe-lutite IF	Sinqeni	16-S-250	Fe-lutite	out	57.54	-0.094	0.02
Hematitized IF jasper	Sinqeni	16- S -192	jasper	out	1.62	-0.184	0.02
Fe-lutite IF	Sinqeni	16-S- 190	Fe-lutite	out	19.84	-0.139	0.01
IFe-lutite IF	Sinqeni	16 - S-174	Fe-lutite	out	48.74	-0.156	0.01
Fe-lutite IF	Sinqeni	16 - S- 140	Fe-lutite	out	28.51	-0.013	0.01
Fe-lutite IF	Sinqeni	16 - S -138 top	Fe-lutite	out	22.55	0.124	0.01
Fe-lutite IF	Sinqeni	16 - S - 138middle	Fe-lutite	out	8.76	0.034	0.01
Hematitized IF jasper	Sinqeni	16 - S -113	jasper	out	1.20	-0.074	0.01
Hematitized IF jasper	Sinqeni	16 - S- 105	jasper	out	3.65	-0.026	0.02
Hematitized Fe-lutite IF	Sinqeni	16 -S -100	Fe-lutite	out	62.74	0.418	0.01
Hematitized Fe-lutite IF	Sinqeni	16 - S- 90	Fe-lutite	out	2.75	-0.001	0.02
Hematitized Fe-lutite IF	Sinqeni	16 - S- 80	Fe-lutite	out	16.46	-0.012	0.02
Hematitized Fe-lutite IF	Sinqeni	16 - S- 0 - base	Fe-lutite	out	48.55	0.091	0.01
Supergene altered IF	Thalu	WV006-43.98 m	jaspilite	drill	7.99	-0.083	0.01
Supergene altered IF	Thalu	WV006-45.45 m	jaspilite	drill	2.38	-0.021	0.03
Supergene altered IF	Thalu	WV006-58.75 m	jaspilite	drill	10.50	-0.030	0.01
Supergene altered IF	Thalu	WV006-58.77 m	jaspilite	drill	36.69	-0.124	0.01
Supergene altered IF	Thalu	WV006-59.59 m	jaspilite	drill	14.24	-0.066	0.02
IF	Thalu	WV006-67 m	magnetite Fe-carb/sil	drill	29.53	-0.115	0.01
IF	Thalu	WV006-70.53 m	magnetite Fe-carb/sil	drill	14.58	-0.077	0.01
IF	Thalu	WV006-80.30 m	magnetite Fe-carb/sil	drill	22.04	-0.127	0.02
Chert	Thalu	WV006-92 m	chert	drill	13.97	-0.108	0.02

Table 5. Mo and Fe concentrations and stable isotopic data with Fe/Mn ratios and enrichment factors for Ijzermijn IF

Sample ID	Lithotype	Sampling	*Mo (ng/g)	$\delta^{98/95}Mo_{NIST3134+0.25}$ ‰	2SE	Fe wt %	$\delta^{56/54}Fe_{IRMM-014}$ ‰	2SE	Mo_{EF}	Fe_{EF}	Fe/Mn
DDN_1 267.9	Fe-lutite	drill	451.2	0.352	0.006	17.77	-0.852	0.023	1.55	2.41	3.00
DDN_1 271.5	Fe-lutite	drill	162.2	0.360	0.010	8.289	-2.114	0.024	3.10	6.29	1.27
DDN_1 273.49A	Chert	drill	4133	-0.354	0.004	3.743	-1.341	0.021	2043	73.3	15.2
DDN_1 274A	Chert	drill	375.5	-0.313	0.008	2.741	-2.416	0.021	36.5	10.6	1.49
DDN_1 274.3A	Fe-lutite	drill	1426	-0.519	0.006	14.77	-2.522	0.022	33.4	13.7	1.02
DDN_1 274.3D	Chert	drill	4269	-0.546	0.004	1.815	-2.378	0.022	696	11.7	1.23
PMH24L1 861A	Fe-lutite	drill	470.2	0.341	0.007	27.99	-0.753	0.024	10.8	25.5	12.8
PMH24L1 863.4	Fe-lutite	drill	426.4	0.382	0.007	33.25	-1.233	0.022	12.1	37.3	9.37
PMH24L1 864.6A	Fe-lutite	drill	315.8	0.315	0.006	26.08	-1.019	0.022	1.91	6.26	4.52
PMH24L1 864.6C	Fe-lutite	drill	N.D	N.D	N.D	23.70	-1.265	0.026	N.D	87.6	3.67
16-S-594	shale	out	794.8	0.267	0.011	14.91	-0.462	0.021	1.28	0.95	74.7
16-S-530	shale	out	533.4	0.630	0.012	16.73	-0.441	0.024	0.86	1.07	57.4
16-S-450	shale	out	571.9	0.466	0.019	16.30	-0.464	0.019	0.87	0.98	77.9
16-S-382	Fe-lutite	out	360.5	0.340	0.009	37.32	-0.526	0.020	6.78	29.0	8.12
16-S-378	Fe-lutite	out	582.3	0.282	0.011	31.89	-0.624	0.021	6.42	14.5	7.71
16-S-358	Fe-lutite	out	305.1	0.892	0.023	38.19	-0.654	0.024	9.68	46.9	9.91
16-S-350	Fe-lutite	out	629.9	0.319	0.009	31.56	-0.905	0.019	8.32	16.7	6.63
16-S-335	jasper	out	397.0	0.676	0.010	13.31	-1.169	0.023	61.7	81.9	7.11
16-S-305	jasper	out	498.0	0.637	0.012	7.498	-1.472	0.021	331	197	6.43
16-S-285	Fe-lutite	out	393.8	0.434	0.010	34.21	-1.174	0.026	8.29	28.6	10.2
16-S-250	Fe-lutite	out	460.6	0.538	0.010	31.76	-1.208	0.023	3.30	9.03	11.3
16- S -192	jasper	out	624.8	0.112	0.017	7.137	-1.172	0.023	183	83.0	5.33
16-S- 190	Fe-lutite	out	294.2	0.418	0.014	33.22	-1.159	0.019	5.84	26.1	7.62
16 - S-174	Fe-lutite	out	424.0	0.142	0.008	26.89	-1.729	0.022	3.88	9.75	3.81
16 - S- 140	Fe-lutite	out	494.1	1.160	0.009	33.80	-1.332	0.021	7.39	20.0	8.68
16 - S -138 top	Fe-lutite	out	1852	0.407	0.008	28.75	-0.864	0.024	24.9	15.3	25.8
16 - S - 138middle	Fe-lutite	out	1250	0.318	0.010	30.13	-0.961	0.029	35.1	33.5	23.6
16 - S -113	jasper	out	301.9	0.210	0.009	7.417	-0.527	0.020	95.3	92.8	10.1
16 - S- 105	jasper	out	1197	-0.306	0.011	9.81	-0.682	0.019	253	82.2	11.5
16 -S -100	Fe-lutite	out	6003	0.289	0.011	47.23	-0.819	0.020	60.1	18.7	26.5
16 - S- 90	Fe-lutite	out	2820	-0.450	0.009	24.11	-0.546	0.019	389	132	9.02
16 - S- 80	Fe-lutite	out	3344	0.228	0.008	37.11	-0.438	0.019	96.9	42.6	24.3
16 - S- 0 - base	Fe-lutite	out	1865	-0.476	0.009	22.84	-1.147	0.027	17.3	8.42	229

* Concentration determined by isotope dilution during double spike MC-ICP-MS analyses for isotopic composition

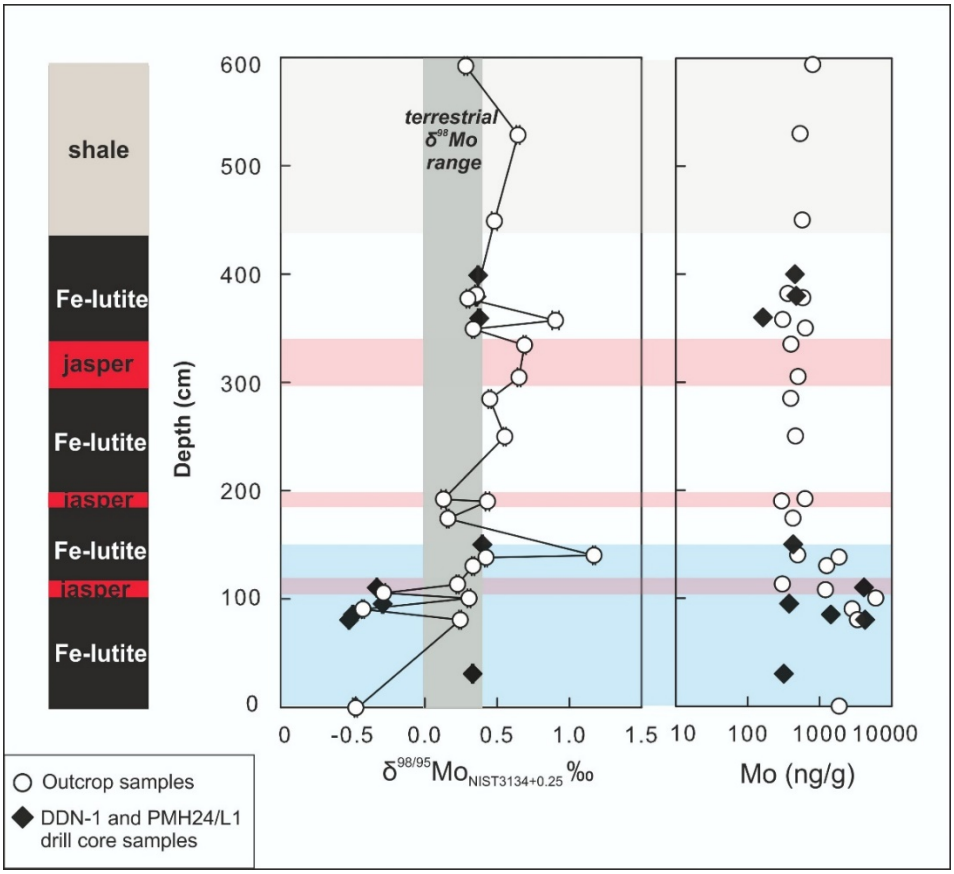

Figure 4-7. Stratigraphic plots of $\delta^{98/95}Mo_{NIST3134+0.25}$, Mo (ppb) for the Ijzermijn IF outcrop and drill core samples. The horizontal red bars indicate jasper samples, and horizontal gray bar indicates the shale samples. The depth positions for the drill core samples were estimated from the lithostratigraphic correlation between the drill cores and the outcrop.

4.1.8. Stable Fe isotopic composition and Fe concentrations of the Sinqeni Formation samples

Fe-lutite samples in Ijzermijn IF drill cores DDN-1 and PMH24/L1 are characterized by iron concentrations ranging from 8.289 to 33.25 wt % (Table 5). Chert samples from the DDN-1 drill core have lower Fe concentrations ranging from 1.815 to 3.743 wt %. White Mfolozi outcrop Fe-lutites have Fe concentrations of 22.84 - 47.23 wt %, with no clear difference between the basal <140 cm and the upper profile sections. Jasper samples from the Ijzermijn IF outcrop have lower Fe contents than Fe-lutites with 7.14-13.31 wt %. The chlorite- and chamosite-bearing shale samples of the Vlakhoek member overlying the Ijzermijn IF have an iron concentration range of 14.91-16.73 wt % (Table 5). Despite slightly different ranges, there is not a significant difference in total Fe contents between the drill core and outcrop samples. All samples from the Ijzermijn IF in this study have negative $\delta^{56/54}Fe_{IRMM-014}$ values, with chlorite-chamosite-bearing shales from the White Mfolozi River outcrop having the heaviest $\delta^{56/54}Fe_{IRMM-014}$ values of - 0.441 to - 0.464 ‰ (Table 5, Figure 4-8). Fe lutites from DDN-1 drill core have the lightest $\delta^{56/54}Fe_{IRMM-014}$ values with a range from - 2.522 to - 1.341 ‰, whereas PMH24/L1 drill core samples have slightly heavier $\delta^{56/54}Fe_{IRMM-014}$ values from - 1.265 to - 0.753 ‰

(Figure 4-8). There is not a significant difference in Fe isotopic composition between drill core chert and Fe-lutite samples, except for sample DDN-1-267.9 which carries a very high detrital component, and thus a heavier $\delta^{56/54}Fe_{IRMM-014}$ (- 0.852 ‰) value. A trend in $\delta^{56/54}Fe_{IRMM-014}$ values in the White Mfolozi River outcrop of the Ijzermijn IF, is recorded by relatively heavier (- 0.961 to - 0.438 ‰) in the basal <140 cm, followed by lighter (- 1.729 to - 1.159 ‰) in the middle - up to 335 cm - in the profile, returning back to heavier values (- 0.905 to - 0.464 ‰) in the top section underlying the chloritic shales of the Vlakhoek member (Figure 4-8). A difference in $\delta^{56/54}Fe_{IRMM-014}$ values between different lithologies of the Fe-lutites and the jaspers is not observed, similar to the drill core cherts vs. Fe-lutites. The outcrop samples have heavier $\delta^{56/54}Fe_{IRMM-014}$ values compared to the DDN-1 drill core, however the mid-section shows a similar range to the PMH24/L1 drill core in isotopic composition (Figure 4-8). The overlying chloritic shales have an average $\delta^{56}Fe$ value of - 0.455 ± 0.013 ‰ (1SD).

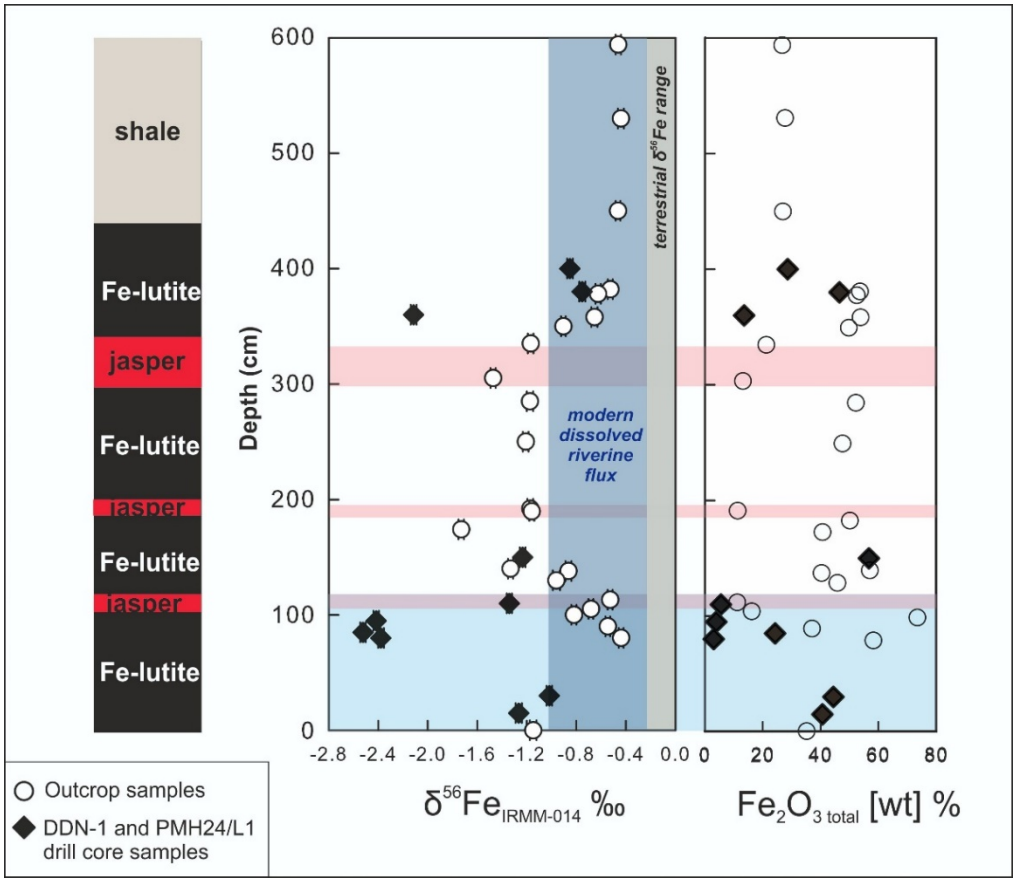

Figure 4-8. Stratigraphic plots of $\delta^{56/54}Fe_{IRMM-014}$ values, and Fe_2O_{3total} wt % for the Ijzermijn IF outcrop and drill core samples. The horizontal red bars indicate jasper samples, and horizontal gray bar indicates the shale samples. The depth positions for the drill core samples were estimated from the lithostratigraphic correlation between the drill cores and the outcrop.

4.2. Arvadi Spring samples

4.2.1. Stable Fe isotopic composition and Fe concentration of Arvadi Spring samples

The water from the mixing shaft (Stollen) as the source of the Arvadi pond has a $\delta^{56/54}Fe_{IRMM-014}$ value of - 0.359 ‰, which is slightly heavier than the water composition of the pond. The heaviest $\delta^{56/54}Fe_{IRMM-014}$ values of the Arvadi pond of - 0.487 ‰ (by October 2014), and - 0.528 ‰ (by June 2018) are detected at its outlet (sampling point A1, Figure 4-9 and 4-10, Table 6), with values becoming isotopically much lighter towards the middle of the pond (- 1.482 ‰ by October 2014, - 1.065 ‰ by June 2018) (sampling point 2, Figure 4-9 and 4-10). Fe isotope values remain light at the creek (from - 1.371 to - 1.479 ‰ by October 2014, and - 0.979 to - 1.155 ‰ by June 2018) even after mixing with the forest brook. The iron concentration of the water in the mixing shaft is slightly higher (0.436 ppm), and becomes lower at the outlet of the pond (0.136 ppm by October 2014, 0.093 ppm by June 2018) (sampling point A1, Figure 4-9 and 4-10) and decreases towards the middle of the pond (0.083 ppm by October 2014, 0.082 ppm by June 2018) (sampling point 2, Figure 4-9 and 4-10), and becomes lowest after mixing with the forest brook (0.011 ppm by October 2014, 0.016 ppm by June 2018) (sampling point 7, Figure 4-9 and 4-10). The iron concentration of the forest brook (in sampling point 6) was determined to be very low, 0.0003 ppm, with a light Fe isotopic composition of - 1.032 ‰ (October 2014). An extra water sample acquired from the outlet of the creek to the mixing point during sampling excursion of June 2018 (sampling point 8) revealed a lower Fe concentration (0.027 ppm) and the lightest $\delta^{56/54}Fe_{IRMM-014}$ value of - 1.392 ‰ (Figure 4-9).

The stable Fe isotopic composition of the Fe-rich red flocs varies in three different sampling points in the mixing shaft. The sampling point 1a where the sulfidic water flows in, and which has the lowest Fe concentration in the shaft (0.300 wt %), has a slightly lighter $\delta^{56/54}Fe_{IRMM-014}$ value of - 0.069 ‰ compared to the points 1b and 1c where the ferruginous water flows in, which have Fe concentrations of 12.19 wt % and 32.69 wt %, and $\delta^{56/54}Fe_{IRMM-014}$ values of 0.323 ‰ and 0.100 ‰, respectively (Figure 4-9). The high iron concentration of the red flocs in the mixing shaft (32.69 wt %) sharply decreases towards the red flocs on the rock surface at the outlet of the pond (2.18 wt % by October 2014, 4.11 wt % by June 2018) (sampling point A1, Figure 4-9 and 4-10). The total Fe concentration remains at around 2.59 wt % by October 2014, and 3.01 wt % by June 2018 in the red flocs in the pond (sampling point 2, Figure 4-9 and 4-10) and increases to 3.09 to 3.59 wt % by October 2014, and 4.47 to 4.94 wt % by June 2018 in the red flocs by the creek (sampling points 3 and 4 respectively, Figure 4-9 and 4-10). It decreases down to 1.80 wt % by October 2014, and 1.87 wt % by June 2018 at the mixing point with the forest brook (sampling point 5), and remains at 2.00 wt % by October 2014, and 3.41 wt % by June 2018 after the mixing point (at sampling point 7).

The stable Fe isotopic composition in red flocs shows some variation in the pond from sampling point A1 (with $\delta^{56/54}Fe_{IRMM-014}$ of - 0.015 ‰ by October 2014 and 0.327 ‰ by June 2018) to sampling point 2 (with $\delta^{56/54}Fe_{IRMM-014}$ of 0.222 ‰ by October 2014 and 0.354 ‰ by June 2018). $\delta^{56/54}Fe_{IRMM-014}$ values of the red flocs at the creek remain stable (- 0.357 to - 0.328 ‰ by October 2014, - 0.467 to - 0.228 ‰ by June 2018) between the sampling points of 4 and 3 (Figure 4-9 and 4-10). $\delta^{56/54}Fe_{IRMM-014}$ becomes slightly heavier, at the sampling point 7, after mixing with the forest brook (- 0.192 ‰ by October 2014, 0.308 ‰ by June 2018). However, this value is still slightly lighter compared to the $\delta^{56/54}Fe_{IRMM-014}$ values from the outlet and the middle of the pond. Therefore, a trend in $\delta^{56/54}Fe_{IRMM-014}$ values is observed for the red floc samples becoming lighter from the mixing shaft to the pond, and even lighter from the pond to the creek (Figure 4-9 and 4-10).

	October 2014	***October 2014***	***October 2014***	***June 2018***	***June 2018***	***June 2018***
Red Flocs	**$\delta^{56/54}$Fe (‰)**	**2SE**	**Fe wt %**	**$\delta^{56/54}$Fe (‰)**	**2SE**	**Fe wt %**
A1	-0.015	0.01	2.18	0.327	0.02	4.11
2	0.222	0.02	2.59	0.354	0.05	3.01
3	-0.328	0.01	3.09	-0.467	0.02	4.94
4	-0.357	0.01	3.59	-0.228	0.02	4.47
5	-0.250	0.02	1.80	-0.355	0.03	1.87
7	-0.192	0.02	2.00	0.308	0.03	3.41
1a	-0.069	0.02	0.30	N.D	N.D	N.D
1b	0.323	0.02	12.89	N.D	N.D	N.D
1c	0.100	0.01	32.69	N.D	N.D	N.D
Water samples	**$\delta^{56/54}$Fe (‰)**	**2SE**	**Fe (ppm)**	**$\delta^{56/54}$Fe (‰)**	**2SE**	**Fe (ppm)**
A1	-0.487	0.02	0.136	-0.528	0.02	0.093
2	-1.482	0.02	0.083	-1.065	0.02	0.082
3	-1.371	0.02	0.083	-0.979	0.02	0.079
4	-1.338	0.02	0.082	-0.882	0.04	0.080
5	-1.598	0.02	0.057	-0.952	0.03	0.073
6	-1.032	0.1756	0.0003	N.D	N.D	N.D
7	-1.479	0.02	0.011	-1.155	0.04	0.016
8	N.D	N.D	N.D	-1.392	0.03	0.027
Stollen	-0.359	0.01	0.436	N.D	N.D	N.D

Table 6. Iron concentration and $\delta^{56/54}Fe_{IRMM-014}$ of Arvadi Spring, N.D signifies not determined.

$\delta^{56/54}Fe_{IRMM-014}$ values of water samples show a strong trend of becoming lighter from the mixing shaft (- 0.359 ‰) to the outlet in the pond (- 0.487 ‰ by October 2014, and - 0.528 ‰ by June 2018) (sampling point A1, Figure 4-9 and 4-10), and finally towards the creek (- 1.598 ‰ by October 2014,

- 0.952 ‰ by June 2018). Similarly, Fe concentration of both the water and red floc samples show a decreasing trend from the mixing shaft to the pond, and the Fe concentration of water samples continue decreasing in the pond and towards the creek. However, in contrast, Fe concentration of precipitating red flocs slightly increases from the outlet of the pond to the middle of the pond, and towards the creek (Figures 4-9 and 4-10).

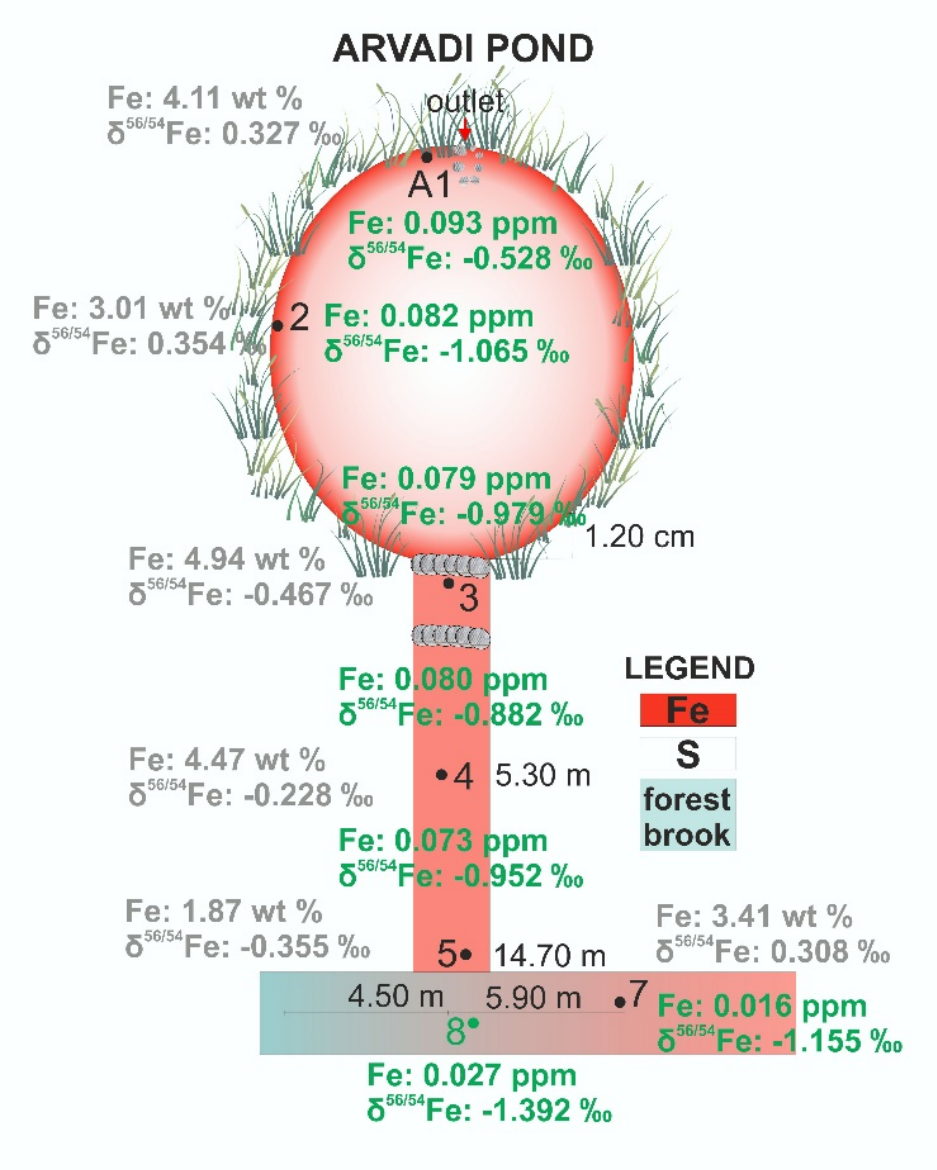

Figure 4-9. Stable Fe isotopic composition and Fe concentration data from sampling excursion in June 2018 (gray=red flocs, green=water).

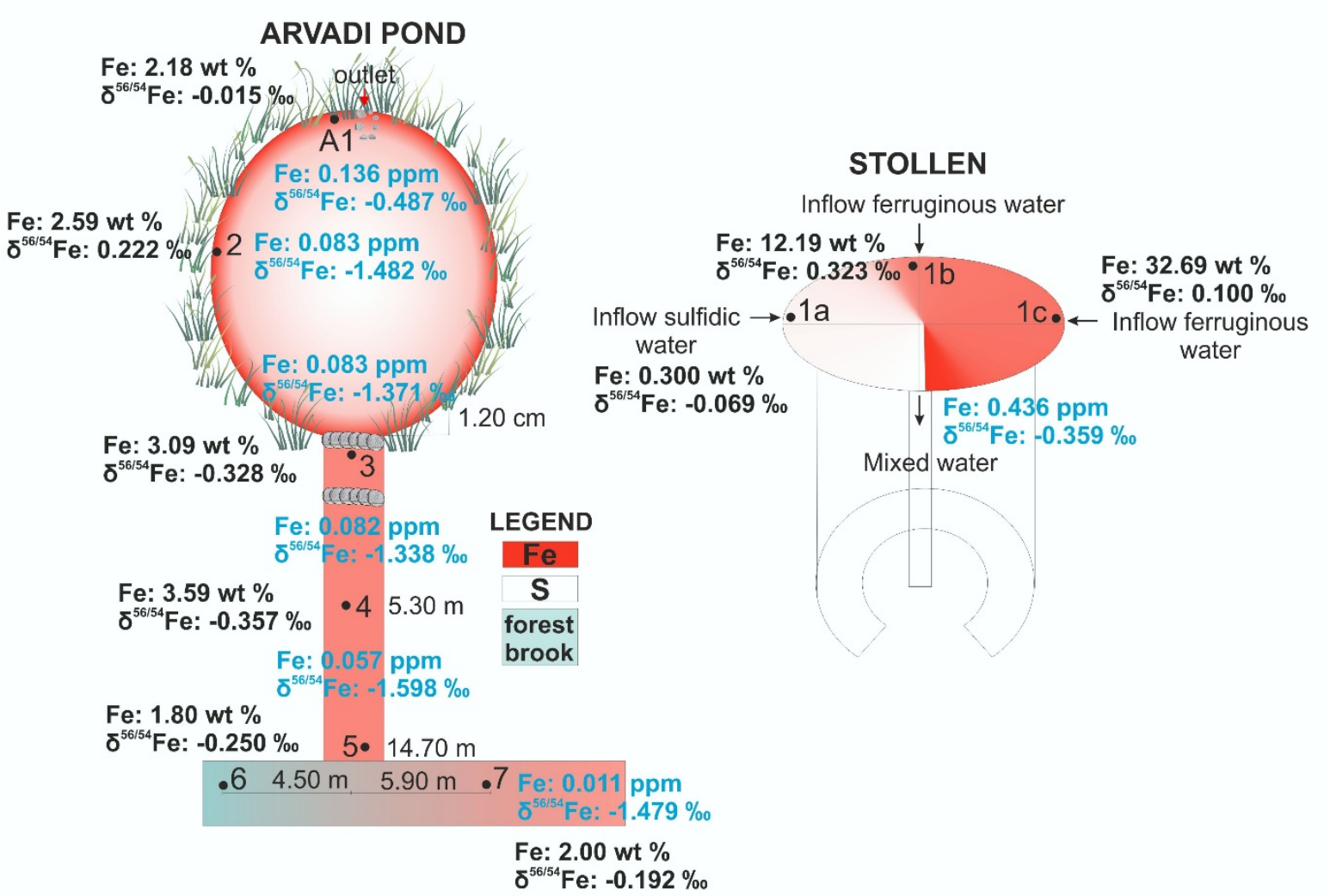

Figure 4-10. Stable Fe isotopic composition and Fe concentration data from sampling excursion in October 2014 (**black**=red flocs, **blue**=water).

5. Modern weathering versus Mesoarchean oxidative weathering signatures

5.1.1. Trace element indicators for modern aqueous overprinting

Uranium is immobile in its reduced tetravalent state and is closely associated with Th(IV) or Al(III) in clastic sediments deposited under reducing conditions, such that U remains detritally associated and U/Th and U/Al_2O_3 ratios would closely match their source rocks. However, U oxidizes to the more soluble and mobile U(VI) in the presence of free oxygen, allowing it to decouple from the insoluble Th and Al during oxidative weathering. Consequently, an increase in the U/Th or U/Al_2O_3 ratios can be exploited as a monitor of authigenic U enrichment in chemical sediments from scavenged U(VI) and provide insight into the redox conditions of their depositional environment (Partin et al., 2013).

Ijzermijn IF drill core samples show a moderately strong positive correlation between U and Th (R^2=0.74; see Table 1) indicating a significant influence of detrital input to the Pongola Basin at the time of deposition (Alexander et al., 2008; Bolhar et al., 2015). The correlation between Mo and U enrichment factors (EF), however, points to a dominantly authigenic addition of these elements to the Ijzermijn IF, most likely by redox cycling in the water column (Figure 4-3). Previous geochemical and mineralogical studies have inferred the existence of free oxygen in the surface water of the Pongola Basin (Eickmann et al., 2018; Ossa et al., 2016; Planavsky et al., 2014a). Such an oxygen oasis would enable the oxidation of Mo and U to soluble molybdate (MoO_4^{2-}) and uranyl (UO_2^{2+}) from the near-shore water-lain sediments and/or partly from the coastal continental area. Consequently, these elements would become authigenically enriched in the deeper water Ijzermijn IF.

In their previous Cr isotope study of Ijzemijn IF samples from the White Mfolozi River Gorge outcrop Crowe et al. (2013) discovered that heavy $\delta^{53/52}$Cr values were accompanied by an enrichment of U relative to Al_2O_3 in their samples. These authors noted that the Ijzermijn IF U/Al_2O_3 enrichment factors exceed those of average Meso- and Neoarchean crust and Paleoarchean BIFs from the Isua Greenstone Belt in Greenland. However, the reported U/Al_2O_3 enrichments of the Ijzermijn IF also exceed those of Neoarchean BIFs and notably also those of the Neoproterozoic Rapitan (Baldwin et al., 2012) and Urucum IFs (730-580 Ma old). The latter IFs might be expected to bear a higher U enrichment signature, compared to the older Mesoarchean Ijzermijn IF, due to increased oxidative U(VI) mobility after the GOE (Figure S15 in Crowe et al., 2013; Frei et al., 2016; Partin et al., 2013), and thus the magnitude of U enrichment recorded by the U/Al_2O_3 ratios is unusual. Our study here also supports this correlation of U enrichment with heavy Cr isotope signatures (Figure 5-1) through the U/Th ratios measured in the outcrop samples. The extremely high U/Th ratios in the outcrop samples of up to 12.6 are well beyond the average ratio of 0.175 ± 0.003 (1 s.d) measured in the three chlorite - bearing shale samples overlying the Ijzermijn IF from the same member (Vlakhoek). The most extreme U enrichment

inferred from the U/Th ratios is stratigraphically restricted to the lowermost IF (<140 cm). It is important to note that several drill core U/Th ratios (gray bar in Figure 5-1) also exceed the aforementioned U/Th ratios of the shale samples, but only reach a maximum value of 1.05 (chert DDN-1 273.49A). Thus, it is evident that the most extreme U enrichment of all measured samples is restricted to the lower section of the outcrop where the only fractionated $\delta^{53/52}$Cr values are recorded (Figure 5-1). In contrast, the upper outcrop section and DDN-1 and PMH- 24/L1 drill core samples revealed unfractionated stable Cr isotopes corresponding to the igneous inventory composition (Schoenberg et al., 2008) (Figure 5-1). Because the U enrichment and heavy Cr isotope excursions reported for the Ijzermijn IF by both Crowe et al., (2013) and this study are restricted to the White Mfolozi River outcrop where oxidative weathering signatures are apparent, a secondary process capable of scavenging excess U needs to be considered.

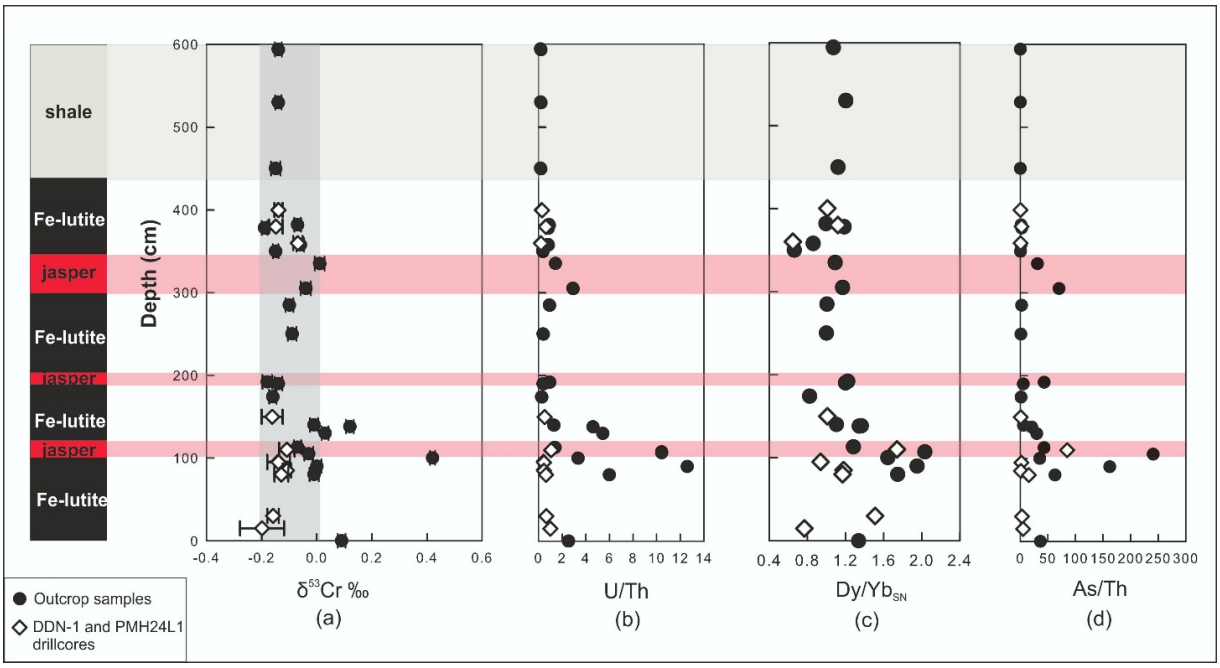

Figure 5.1. Stratigraphic plots of (a) $\delta^{53/52}$Cr values for the Ijzermijn IF outcrop samples, (b) U/Th (c) Dy_{SN}/Yb_{SN} , and (d) Sb/Th. In (a) the vertical gray bars indicates the igneous inventory range for $\delta^{53/52}$Cr values (Schoenberg et al., 2008). These plots emphasize that the heavy Cr isotope enrichment in the outcrop is restricted to the lowermost Fe-lutite layer and correlates with extreme enrichment in U, as noted by Crowe et al. (2013), and a selective enrichment in the MREE. However, the U/Th and Dy_{SN}/Yb_{SN} and As/Th exceed the values observed in the drillcore samples and suggest that the features may reflect a secondary process influencing only the outcrop samples or enhanced by surficial weathering. The horizontal red bars indicate jasper samples, and horizontal gray bar indicates the shales. The depth positions for the drillcore samples were estimated from the lithostratigraphic correlation between the drillcores and the outcrop.

Following the interpretation of authigenic U enrichments in different IFs from previous studies (e.g., Bau & Alexander, 2009; Partin et al., 2013), slightly higher U/Th observed in drill core IF samples compared to the three outcrop shale samples of the Vlahkhoek member from this study and the shale average of Pongola sediments reported by Bolhar et al., (2015), might indeed point to a process capable of selective U over Th capture at some stage from chemical weathering, aqueous transport, shallow marine water cycling, and sediment diagenesis. However, the small authigenic U enrichments

observed in drill cores are not accompanied by Cr isotopic anomalies. Thus, the extent of primary oxidative U(VI) mobilization in the Pongola Basin during the Mesoarchean requires further work.

Finally, attention is drawn to the enhanced enrichments of several other elements in the lower section (<140 cm) of the White Mfolozi River Gorge outcrop where the extreme U enrichment and only heavy Cr isotope signatures are documented. These elements such as As, Cs, Li, Pb, Sb, Tl, and W show the highest enrichment factors, as well as a MREE in normalized REE+Y patterns, measured here with $(Dy/Yb)_{SN}$ ratios (Fig. Cr isotopes and U/Th ratios). Thus, while the general MREE enrichment in the Pongola appears to be an inarguable feature of the original basinal REE+Y systematics (Alexander et al., 2008; Delvigne et al., 2012; Bolhar et al., 2015), the overlap of the extreme U/Th and $(Dy/Yb)_{SN}$ excursions in the <140 cm section of the outcrop, suggests that these features are coupled and linked to modern oxidative weathering. The enrichments of other elements are less easily explained under a direct oxidative weathering model since they are not redox-sensitive themselves and thus will require further work to disentangle in greater detail.

5.1.2. ($^{234}U/^{238}U$) activity ratios as an indicator for modern weathering-induced alteration on White Mfolozi River outcrop

To further investigate whether the U enrichment in White Mfolozi outcrop samples is indeed due to modern weathering processes, their ($^{234}U/^{238}U$) activity ratios were determined and compared to DDN-1 and PMH-24/L1 drill core samples. U-Th series nuclides are powerful tools to investigate weathering processes in surface environments (Fleischer and Raabe, 1978; Hansen and Stout, 1968; Rosholt et al., 1966). In the case of the ^{234}U-^{238}U disequilibrium system, ^{238}U is bound in a mineral's crystal lattice and decays to ^{206}Pb through a chain of intermediate radioactive nuclides by a series of α- and β^--decays. The strong energy release mainly by emission of α particles, termed the "recoil effect", causes damage to the crystal lattice and thus displacement of the nuclides in the decay chain (e.g. ^{234}Th, ^{234}Pa, ^{234}U, etc.) from the original crystal lattice position of the mother nuclide ^{238}U (Chabaux et al., 2003). Therefore, the recoil nuclide ^{234}U can be more easily removed/leached from the damage site in the mineral compared to its crystal-bound parent nuclide ^{238}U during rock-water interaction (Chabaux et al., 2003; Fleischer and Raabe, 1978; Kigoshi et al., 1971; Osmond and Cowart, 1976).
Any reservoir that shows a disequilibrium activity ratio, i.e. $(^{234}U/^{238}U) \neq 1$, must have been disturbed within the last 1.25 million years (~ 5 times the half-life of ^{234}U; Kraemer and Genereux, 1998). Preferential release of ^{234}U over ^{238}U from minerals, rocks and soils by aqueous solutions leads to ($^{234}U/^{238}U$) activity ratios in ground- and surface waters that are above unity (>1), and in residual solids that are generally less than unity (<1) (Osmond and Cowart, 1976; Moreira-Nordemann, 1980; Carl, 1987; Plater et al., 1988). These trends are shown in a compilation of literature data from modern

rivers (Chabaux et al., 2001; Dosseto et al., 2008; Vigier et al., 2005; data compiled in Suhr et al., 2018), groundwaters (Cizdziel et al., 2005; Paces et al., 2002; Riotte and Chabaux, 1999; Suksi et al., 2006) and weathering profiles (Bonotto and Jiménez-Rueda, 2007; Claude et al., 2016; Chabaux et al., 2013; Dequincey et al., 2002; Dosseto et al., 2008; Dosseto et al., 2012; Engel et al., 2016; Hansen and Stout, 1968; Huckle et al., 2016; Keech et al., 2013; Ma et al., 2010; Ma et al., 2012; Ma et al., 2013; Mathieu et al., 1995; Menozzi et al., 2016; Moragues-Quiroga et al., 2017; Moreira-Nordemann, 1980; Pelt et al., 2008; Rezzoug et al., 2009; Rosholt et al., 1966; Suresh et al., 2013; data compiled in Suhr et al., 2018) in Figure 5-2. Modern river ($^{234}U/^{238}U$) activity ratios compiled by Suhr et al. (2018) range from 1 to 1.9 with a median value of 1.26 (n=61; Figure 5-2b). Modern groundwaters have a range in ($^{234}U/^{238}U$) activity ratios of 1 to 16, with a median of 3.23 (n=452; Figure 5-2a). Modern weathering profiles range in ($^{234}U/^{238}U$) activity ratios from 0.58 to 1.8 with most profiles having values between 0.7 to 1.1 with an overall median of 0.995 (Suhr et al., 2018; n=335; Figure 5-2c). Weathering residues with ($^{234}U/^{238}U$) activity ratios above unity are generally interpreted to have experienced U-exchange with ^{234}U-enriched groundwater.

The five DDN-1 and PMH24/L1 drill core samples from the Ijzermijn IF have ($^{234}U/^{238}U$) activity ratios in secular equilibrium within uncertainties (Table 3; Figure 5-2), and thus were not affected by modern weathering or deeper alteration from rock-groundwater interaction. All White Mfolozi River outcrop samples of the Ijzermijn IF, on the other hand, have ($^{234}U/^{238}U$) activity ratios above unity, ranging from 1.05 to 1.77. This range in ($^{234}U/^{238}U$) activity ratios is very similar to that of modern river water (Figure 5-2b). The two Vlakhoek member shale samples that overly the Ijzermijn IF in the White Mfolozi River outcrop show ($^{234}U/^{238}U$) activity ratios below unity, with values ranging from 0.89 to 0.96, which are similar to values of a weathered saprolite developed on Deccan trap basalt reported by Suhr et al. (2018).

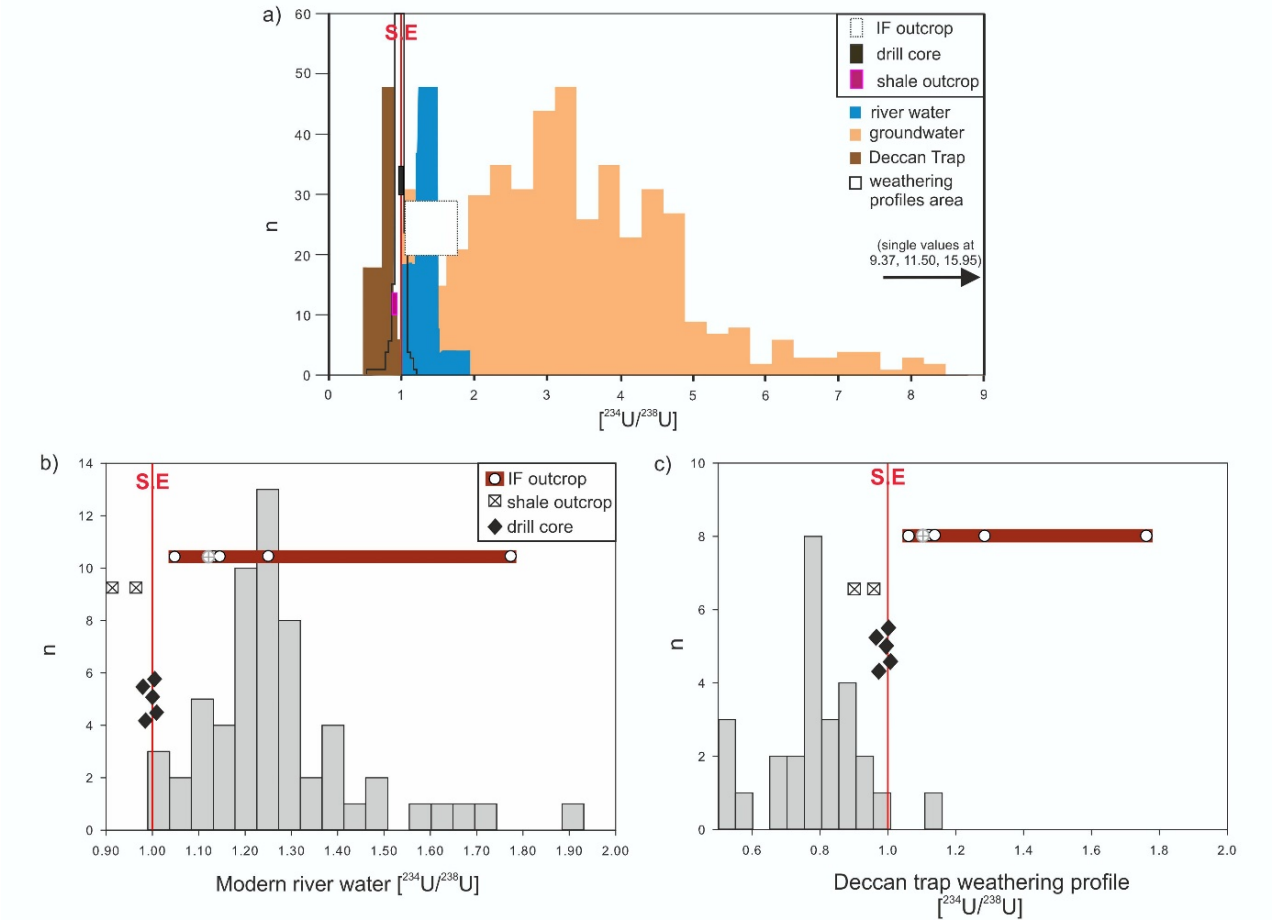

Figure 5-2. a) Compilation of ($^{234/238}$U) activity ratios of the weathering profiles, modern river waters and Deccan trap (Suhr et al., 2018), as well as the modern ground waters (Cizdiel et al., 2005; Paces et al., 2002; Riotte and Chabaux, 1999; Suksi et al., 2006), compared to the data from this study. The drill core samples (DDN-1 and PMH24/L1) from the Ijzermijn IF (black rectangle) are in secular equilibrium (red vertical line, shown as S.E.), whereas the outcrop IF samples (white rectangle with dotted line) and the outcrop shale samples (pink rectangle) show disequilibrium, former showing excess ^{234}U, latter showing depleted ^{234}U, respectively, b) sample points compared to the histograms of modern river waters, and c) Deccan trap weathering profile (Suhr et al., 2018). As seen above, outcrop shale samples plot in disequilibrium values similar to Deccan trap weathering profile, whereas the outcrop IF samples plot in a range similar to modern river water activity ratios (red bar). The median of the outcrop IF samples (1.12) is shown as the gray circle with a cross. The drill core samples from the Ijzermijn IF, all plot in secular equilibrium (S.E) activity ratios.

There, intermediate to advanced weathering of basalt to phylosilicates resulted in a median (^{234}U/^{238}U) of 0.78 (n=27; Figure 5-2c). These deviations from the secular equilibrium of (^{234}U/^{238}U) activity ratios for the White Mfolozi River outcrop Ijzermijn IF samples and Vlakhoek Member shale samples are clear evidences that modern weathering processes affected the U budget of these samples. The measured (^{234}U/^{238}U) activity ratios of White Mfolozi River outcrop samples indicate that percolating meteoric water preferentially leached out ^{234}U over ^{238}U from the Vlakhoek Member shale unit. The excess ^{234}U was either lost to runoff or re-deposited in other lithologies, where its incorporation could cause (^{234}U/^{238}U) greater than unity. The chemically very different IF samples, with inherently low original U concentrations were apparently very prone to up-take of foreign U with a high (^{234}U/^{238}U). The source of this U could have been river water, weathering solutions further up-slope or fluctuating ground water-fed springs.

Importantly, there are no clear correlations between ($^{234}U/^{238}U$) and other geochemical parameters that would permit correction for the U-uptake or identify the mineral phase in the IF samples, which hosts the delivered U, such as LOI wt % for goethite, Fe^{2+}/Fe_{tot} for magnetite or Th (ppm) for detrital components. However, many studies of Fe-oxide bearing laterites show that U mobilization is related to Fe-enrichment (e.g. Dequnicey et al., 2002) and that high ($^{234}U/^{238}U$) are often found in the ferruginous parts of weathering residues (e.g. Chabaux et al., 2003). Despite these complexities and the lack of a clear correlation ($^{234}U/^{238}U$) with geochemical or other isotopic parameters, it is clear that the strong deviations from secular equilibrium ratios of outcrop but not the drill core samples, certainly provide very strong evidence for modern weathering induced alteration of original geochemical fingerprints of Ijzermijn IF samples from the White Mfolozi River outcrop.

Interestingly, $\delta^{238/235}U_{CRM112\text{-}A}$ values of all U-enriched White Mfolozi River outcrop Ijzermijn IF and Vlakhoek Member shale samples are unfractionated relative to the igneous continental crust (Weyer et al., 2008). These strong U enrichments are potentially the result of exposure to ground-and/or river water, which might have led to the scavenging of dissolved U(VI) onto reactive Fe(II)-bearing mineral surfaces such as magnetite. Adsorption of U(VI) onto common aquifer minerals is known to produce U isotope fractionation (Jemison et al., 2016), which is not observed in the current dataset. This could possibly imply abiotic U reduction onto zero-valent iron, which yielded no significant stable U isotopic fractionation in experiments (Stirling et al., 2007; Stylo et al., 2015). It should be noted that dissolved U in modern oxic river water has a U isotopic span from $\delta^{238/235}U_{CRM112\text{-}}$ - 0.31 ± 0.08 ‰ (2SD) to - 0.13 ± 0.07 ‰ (2SD), which is in the range of $\delta^{238/235}U_{CRM112\text{-}A}$ values for igneous continental crust (Noordmann et al., 2016; Weyer et al., 2008) and the values observed in this study.

5.1.3. Surface weathering of carbonates

Higher contents of MnO and increased LOI (Figure 5-3) as well as the existence of significant amounts of ferrous iron (FeO*, Figure 5-4) in Fe-lutites relative to jaspers and cherts indicate the existence of a substantial proportion of kutnahorite, siderite and ankerite carbonate mineral phases in the Ijzermijn IF as were identified in previous studies (Ossa et al., 2016, Planavsky et al., 2014a). Within the drill core Fe-lutites, LOI wt % correlates very well with MnO wt % (with an R^2 of 0.90 for DNN-1 (n=3) and 0.99 for PMH24/L1 (n=4) samples), as does FeO* (divalent iron) with LOI (R^2 = 0.68) and MnO (R^2 = 0.71) for PMH24/L1 samples. Collectively, these observations agree with previously published mineralogical observations that Fe(II) and Mn(II)-bearing carbonates are abundant in the Fe-lutites of the Ijzermijn IF (Bolhar et al., 2015; Ossa et al., 2016, Planavsky et al., 2014a), which release CO_2 during determination of the LOI. However, a significant observation is that both the LOI and ferrous iron contents are significantly lower in outcrop compared to drill core samples (Table 1; Figure 5-3).

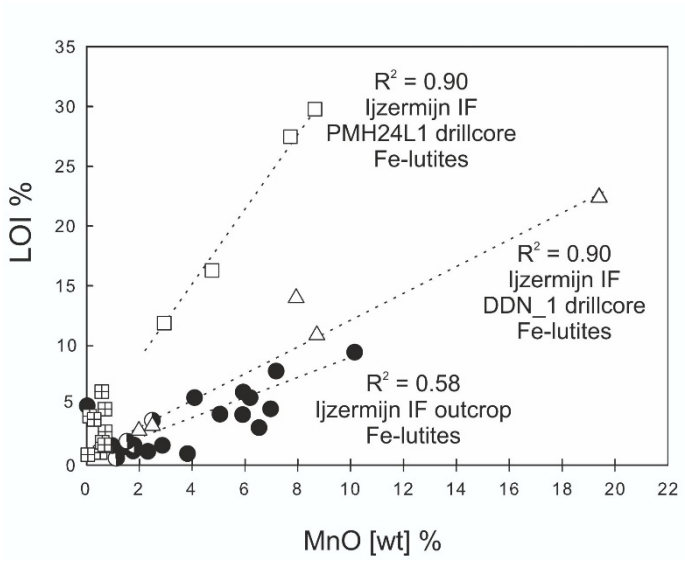

Figure 5-3. MnO [wt] % versus LOI [wt] % (for all data from this study. LOI [wt] % is significantly higher in Ijzermijn IF drillcore relative to outcrop samples of the Ijzermijn IF and a strong correlation between MnO and LOI is observed only in the drillcore Fe-lutite samples of the Ijzermijn IF. The latter observations indicate that the LOI traces the presence of Mn-bearing carbonate in the drillcore samples (R^2 = 0.90 in both drillcores), but is disrupted by a process affecting the outcrop samples only that is thought to represent the loss of carbonate during surface weathering. A lower carbonate content in the Scotts Hill IF is implied by the lower LOI and MnO [wt] % relative to both outcrop and drillcore samples of the Ijzermijn IF. The symbols are per se figure 4-1.

The previous study of the Ijzermijn IF from the White Mfolozi River Gorge outcrop by Alexander et al. (2008) – the same samples for which Crowe et al. (2013) reported heavy Cr isotopic compositions – reports non-detectable LOI. The drastic change in divalent iron is best shown as Fe(II)/Fe_{total} ratios (Figure 5-4) with values between 0.003 to 0.037 for outcrop and 0.396 to 0.851 for drill core Fe-lutite samples of this study. However, the Fe_2O_{3tot} wt % and MnO wt % contents of the Fe-lutites, are in the same range for both drill core and outcrop samples (Figure 5-4). Collectively, these observations point to an almost complete carbonate dissolution in outcrop samples by modern oxidative weathering. The reduced Mn(II) and Fe(II) were released from siderite, kutnahorite and ankerite and consecutively oxidized and incorporated into oxide phases or adsorbed onto mineral surfaces, resulting in no or little net loss of MnO and Fe_2O_{3tot} contents in bulk Fe-lutites (Figure 5-4), but loss of C-O (likely as bicarbonate). Modern weathering of carbonate phases from outcrop samples of the Ijzermijn IF is also supported by a mineralogical investigation by Planavsky et al., (2014a) which revealed much lower abundances of carbonate phases in outcrop compared to drill core samples (see Table SI 2 in Planavsky et al., 2014a).

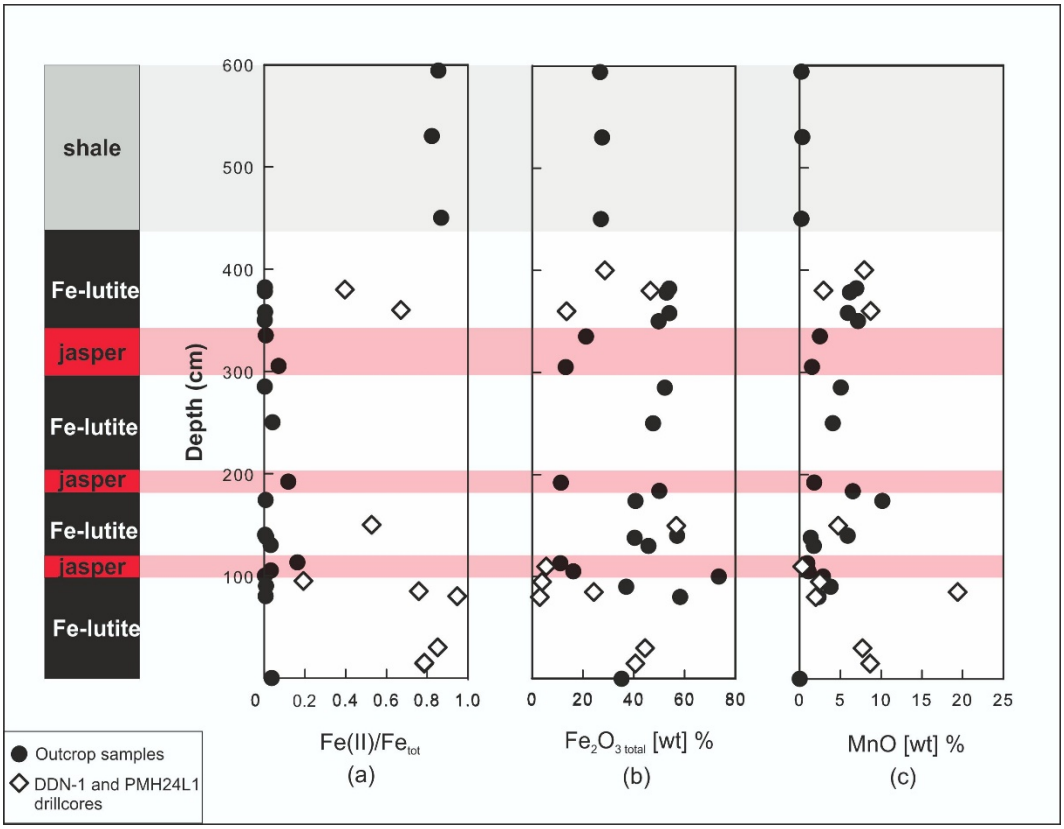

Figure 5-4. a) $Fe^{2+}/\Sigma Fe$ for drill core and the outcrop samples of the Ijzermijn IF, with much higher Fe^{2+} contents for the drill core samples, b) Total Fe_2O_3 [wt] % range is similar between drill cores and outcrop Ijzermijn IF, despite the large difference in Fe^{2+} contents, c) MnO [w] % range is also similar between drill core and outcrop samples. Red horizontal bars represent the jasper samples, and the gray horizontal bar represents the shale samples. The depth positions for the drill core samples were estimated from the lithostratigraphic correlation between the drill cores and the outcrop.

To further assess the mineralogy of the White Mfolozi River Gorge outcrop samples of the Ijzermijn IF, bulk powder X-ray diffraction (XRD) analysis was undertaken (see Appendix and Table A4 for details). These data reveal that samples from the basal <140 cm of the White Mfolozi River Gorge outcrop of the Ijzermijn IF contain more hematite (Fe_2O_3) than magnetite (Fe_3O_4) as opposed to samples from the upper >140 cm section where magnetite is more abundant relative to hematite (Appendix Table A4). The upper section of the outcrop (>140 cm) also contains significant amounts of chlorite and trace amounts (<5 wt %) of goethite in contrast to the lower section. Thus, most of the Fe(II) released from carbonate dissolution during exposure of the outcrop seems to have been oxidized and retained in secondary hematite and, in the case of the upper >140 cm outcrop section, also of goethite. The presence of both chlorite and goethite of samples in the upper section is also likely the primary cause of the high LOI, up to 9.46 wt %, observed in these samples. This is in contrast to the drill core samples, where the primary contributor to the higher LOI, up to 29.80 wt %, is likely decarbonization of the Fe/Mn-carbonate minerals (Figure 5-3). The observed positive correlation between MnO and LOI (R^2 of 0.58) for outcrop samples may thus be explained by preferential adsorption of Mn(II) released during carbonate dissolution onto goethite (Bleam & McBride, 1984;

Coughlin & Stone, 1995) in mainly the upper section of the outcrop. The fate of Mn(II) released from carbonates from samples of the lower <140 cm section of the outcrop is more enigmatic.

5.1.4. Potential origins of the heavy Cr isotopic compositions of Ijzermijn IF outcrop samples

This study shows that fractionated Cr isotopes (up to + 0.418 ‰ in $\delta^{53/52}$Cr values) are only observed in samples from the same Ijzermijn IF outcrop in the White Mfolozi river bed. This outcrop was the same locality from which Crowe et al., (2013) reported heavy $\delta^{53/52}$Cr values. In this study isotopically heavy $\delta^{53/52}$Cr was found only in the Fe-lutite samples, whereas the Crowe et al., (2013) study had a greater suite of jasper samples showing isotopically heavy values. Nevertheless, Ijzermijn IF samples from two different drill core localities in Plananvsky et al., (2014) and two more drill cores of this study are all characterized by a lack of Cr isotopic fractionation relative to igneous inventory (Schoenberg et al., 2008) and thus there is a distinct difference observed between outcrop and drill core samples measured to date. The geochemical and mineralogical evidence shows that unlike the drill core samples, the White Mfolozi river outcrop was strongly affected by modern oxidation and other alteration processes which led to the observed heavy $\delta^{53/52}$Cr values and enhanced enrichment in U, as well as other elements such as As, Cs, Li, Pb, Sb, Tl, W, MREE (Figure 5-1). Accordingly, we disagree with the interpretation of Crowe et al., (2013) that the heavy $\delta^{53/52}$Cr values and U enrichment recorded in Ijzermijn IF outcrop of the White Mfolozi river reflect Mesoarchean seawater and atmosphere redox conditions that drove coupled soluble Cr(VI) and U(VI) delivery to the Mozaan basin.

It is noted that Planavsky et al., (2014a) report unfractionated $\delta^{53/52}$Cr values from surface samples of the Ijzermijn IF taken from the White Mfolozi inlier. These outcrop samples also show a significant loss of carbonate phases compared to drill core samples (see SI Table 2 in Planavsky et al., 2014a) due to surface weathering processes. This observation suggests that the loss of carbonates (mainly siderite, ankerite and kutnahorite) from the Ijzermijn IF outcrop samples by modern weathering is unlikely to be responsible for the heavy Cr isotopic composition and extreme U enrichment, found in White Mfolozi River Gorge outcrop samples reported by Crowe et al., (2013) and this study. An obvious difference between the two outcrop localities is their geographical location relative to the White Mfolozi River Gorge. While the samples used in Crowe et al., (2013) and this study originate from an outcrop in the river bed (S28°13’53.52”; E31°11’49.00”), the coordinates given by Planavsky et al., (2014a) point to a location 3.5 km to the SE further uphill (S28°15’21.09”; E31°13’13.08” PG and PO outcrop samples). We speculate that the lower 140 cm of the outcrop in the White Mfolozi River bed was subject to capillary groundwater rise and maybe also to seasonal submergence during river water high-stands. Exposure to ground- and/or river water might have led to reductive scavenging of dissolved U(VI) and Cr(VI) onto reactive Fe(II)-bearing mineral surfaces such as magnetite (e.g. Ellis et

al., 2002; Latta et al., 2014; Wang et al., 2015) or adsorption onto ferric oxides such as goethite or hematite (e.g. Bargar et al., 2000; Hsi & Langmuir, 1985; Ellis et al., 2004; Marshall et al., 2014; Nico et al. 2009). Reductive Cr(VI) adsorption onto magnetite is known to cause large kinetic Cr isotopic fractionation with $\varepsilon^{53/52}Cr_{(Cr(III)-Cr(VI))}$ of - 3.4 ‰ (Ellis et al. 2002) while Cr(VI) adsorption onto goethite leads to negligible isotopic fractionation of $\varepsilon^{53/52}Cr_{(adsorbed-aquous)}$ of less 0.04 ‰ (Ellis et al., 2004). Modern groundwater Cr is isotopically heavy (+ 0.7 to + 5.1 ‰ in $\delta^{53/52}$Cr; Izbicki et al., 2008) as is most of modern river Cr with such $\delta^{53/52}$Cr values of + 3.95 ‰ (Farkaš et al., 2013), + 0.35 ‰ (Frei et al., 2014), + 1.6 ‰ (Novak et al., 2014), + 1.32 ‰ (Paulukat et al., 2015), + 0.55 ‰ (D´Arcy et al., 2016) and moderate reductive scavenging or adsorption of Cr(VI) might be plausible explanations for the observed heavy Cr isotopic compositions for the White Mfolozi River outcrop samples. The outcrop samples from the up-hill location of the Planavsky et al., (2014a) study might have been less exposed to groundwater infiltration and surface water run-off and thus do not show heavy Cr isotopic compositions. Unfractionated $\delta^{53/52}$Cr values are also reported in this study for samples from the upper 16 m section of the Scotts Hill IF drill core that underwent strong supergene alteration. Note that this alteration of the IF appears to have caused a slight positive Ce anomaly (Section 4.2), likely derived from preferential retention of oxidized Ce, which is not recorded by the Cr isotopes. Notably, this drill core (WV006) was taken ca. 200 km to the North of the White Mfolozi inlier from which all other drill core and outcrop samples of the Ijzermijn IF reported in Crowe et al. (2013), Planavsky et al., (2014a) and this study originate. Here we can only speculate that somewhat different mineralogy of the Scotts Hill compared to the Ijzermijn IF and less exposure to groundwater and no exposure to river water did not cause a shift in the original Cr isotopic composition of these samples, although the higher magnitude of detritally sourced Cr in the Scotts Hill samples (Section 4.4) is also likely a factor.

Our findings suggest that the origin of the heavy $\delta^{53/52}$Cr values on the White Mfolozi River Gorge outcrop of the Ijzermijn IF from the Pongola Supergroup is modern weathering. Nevertheless, Crowe et al., (2013) also reported $\delta^{53/52}$Cr values (- 0.98 ‰) below the igneous inventory, from a paleosol belonging to the 3.0 Ga old Nsuze Group. These light $\delta^{53/52}$Cr values recorded in the paleosol were interpreted to be from a light Cr(III) reservoir that remained in soils, after mobile Cr(VI) removal due to oxidative weathering process that occurred on land during Mesoarchean. Our study includes samples exclusively from iron formations of the Mozaan Group, hence the interpretations of Crowe et al., (2013) on the origin of the light Cr isotopic values observed in Nsuze paleosol cannot be entirely ruled out by our findings. However, it was recently shown that Cr isotopic fractionation can occur via non-redox processes e.g between co-existing Cr(III)-chloride complexes (Babechuk et al., 2018; Larsen et al., 2016). Furthermore, very heavy $\delta^{53/52}$Cr values were reported from Cr depleted upper part of the 1.85 Ga old Flin Flon paleosol in Canada deviating from the oxidative Cr weathering model

(Babechuk et al., 2017). Most recently, Wille et al., (2018) reported Cr enrichment accompanied by a wide range in Cr isotopic composition, including both light and heavy $\delta^{53/52}$Cr values in an altered laterite from Paleogene Bidar profile. Therefore, the light $\delta^{53/52}$Cr values, outside the igneous inventory, recorded in Nsuze paleosol by Crowe et al., (2013) might have been caused by a different process than the proposed model.

5.1.5. Implications for the Cr weathering cycle in the Mesoarchean and the first expression of oxidative weathering

Another significant point on the interpretation of the Cr isotopic data of the Ijzermijn IF is the effect of detrital contamination during deposition. If Cr in the Ijzermijn IF is dominated by terrestrial Cr input, the authigenic $\delta^{53/52}$Cr signature may be overprinted by the continentally derived, unfractionated bulk silicate Earth isotopic values. In this study we identified samples containing < 0.5 [wt] % Al_2O_3 as well as < 0.1 ppm Th as the least affected from clastic contamination (Figure 4- 2), according to cut-off values of previously published studies on the Ijzermijn IF (Alexander et al., 2008; Delvigne et al., 2012; Bolhar et al., 2015). These are mainly outcrop jasper and drill core chert samples with the exception of one outcrop (16-S-90) and one drill core (PMH24/L1 864.6C) Fe-lutite, respectively. However, there is still a slight positive correlation between Cr and Th (R^2 = 0.58) observeable in the outcrop jasper samples suggesting some influence by detrital input. As such the potential authigenic Cr isotopic signatures of these samples might still be strongly influenced by a detrital igneous Cr isotopic composition. Indeed, all outcrop and drill core samples falling into the category of 'least-detritally contaminated' in this study did not reveal any stable Cr isotope fractionation beyond the defined $\delta^{53/52}$Cr range of 0.124±0.101 ‰ for the igneous inventory. All of the Ijzermijn Fe-lutite samples of this study exhibited highly correlated Cr and Th concentrations (R^2 = 0.90) that correspond to a mean average of 11.95 % contamination from a detrital component with the same Cr - Th concentrations as the three shale samples from the Vlakhoek Member. These shales have high Cr contents between 331,000 to 344,300 ppb and are themselves unfractionated such that the Cr isotope compositions of Fe-lutites would be expected to be overwhelmed by the detrital signature of the igneous inventory. These observations appears to further support a secondary origin of the fractionated isotopic signatures in the outcrop Fe-lutites.

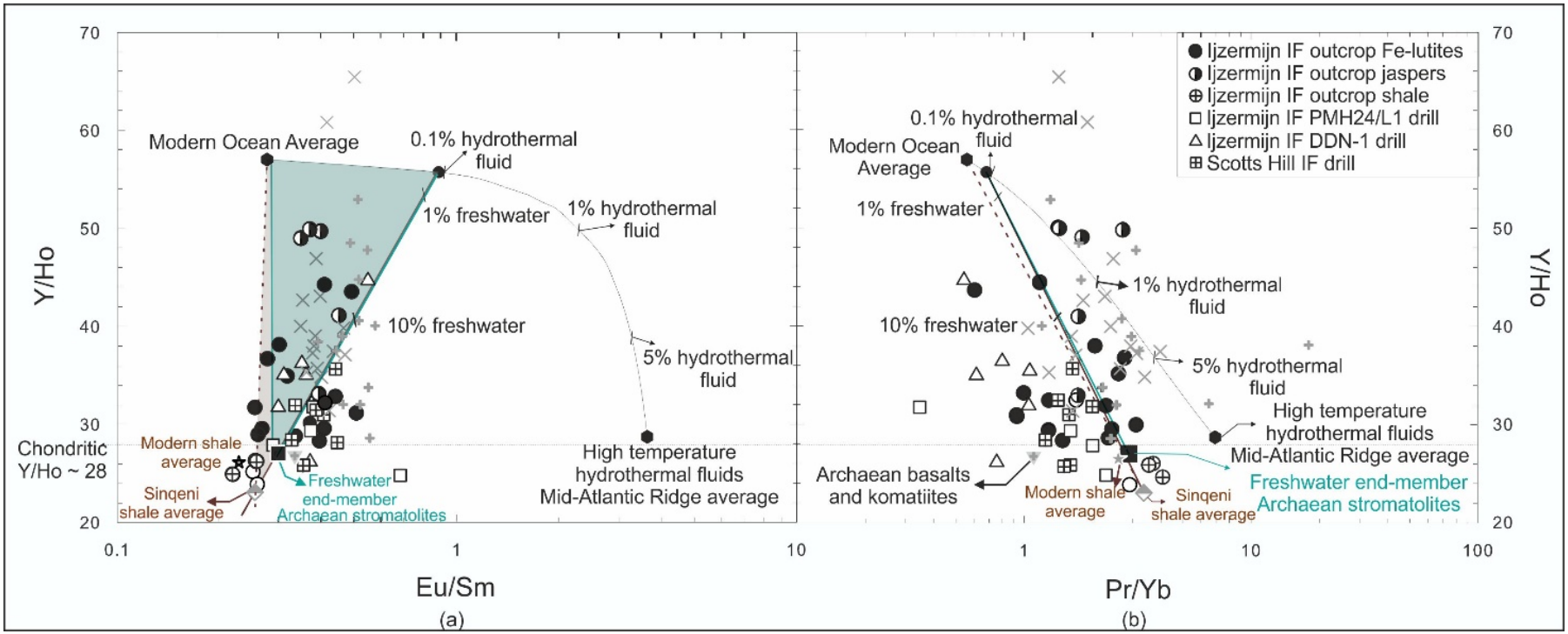

Figure 5-5. REE + Y ratio plots Y/Ho vs. Eu/Sm (a) and Y/Ho vs. Pr/Yb (b) with data from this study (Table 1 and 2) and from previously published studies on 2.95 Ga Ijzermijn IF (Alexander et al., 2008; Delvigne et al., 2010; Bolhar et al., 2015). As per the previously published studies, the plot of Y/Ho vs. Eu/Sm shows that a mixture of an open seawater composition (represented by a Pacific seawater average; Alibo and Nozaki, 1999) with approximately 0.1% contribution of a high-T hydrothermal fluid (represented by a Mid–Atlantic Ridge average; Bau and Dulski, 1999) can account for changes in Eu/Sm, but not Y/Ho. Instead, a third component with lower Y/Ho is required and inferred in previous studies to be a freshwater contribution (represented by lacustrine stromatolites from Bolhar and Van Kranendonk, 2007). However, the trend toward lower Y/Ho and higher Pr/Yb (b) can also be partially accommodated with a contribution of detrital material, represented in both plots with a modern upper continental crust composite (Kamber et al., 2005), three shale samples from the outcrop of this study, and drillcore shales of 2.95 Ga Sinqeni IF from Bolhar et al., (2015), and Archean basalt and komatiite average compositions (Condie, 1993). Three component mixing regions between the modern seawater, 0.1% hydrothermal fluid, and either freshwater or the Sinqeni shale average are shown in both plots. Remaining scatter in Pr/Yb suggests an additional factor modifying the REE+Y patterns; generally lower Pr/Yb of drillcore relative to outcrop samples from this study and others, suggests that modification during surface exposure cannot be excluded as a factor, as discussed in the text.

5.1.6. Geochemical tracing of the element sources of the Mozaan IFs in outcrop and drill core samples

Whether from hydrothermal fluid or continental run-off, the sources and fate of REE + Y can give insight about the conditions and processes of IF deposition (Bau, 1993; Bau and Dulski, 1996; Bekker et al., 2010). The processes that can affect the REE + Y distribution of the Mozaan IFs have been discussed in detail previously (Alexander et al., 2008; Bolhar et al., 2015; Delvigne et al., 2012). In our study, the data from both iron formation facies, divided into outcrop vs. drill core, are evaluated in comparable plots along with previously published data from the same sequence (Figure 5-5).

Using the same end-member compositions of previous publications (Alexander et al., 2008; Delvigne et al., 2012), i.e., seawater (estimated from near modern Pacific seawater average Y/Ho values < 500 m depth; Alibo and Nozaki, 1999), freshwater (represented by the Achaean stromatolites precipitated in a freshwater dominated setting; Bolhar and Van Kranendonk, 2007), and high-T (>350 °C) hydrothermal fluids (Mid-Atlantic ridge averages of Bau & Dulski, 1999), similar conclusions can be derived in this study for the Ijzermijn IF. A plot of Eu/Sm vs. Y/Ho confirms that a maximum hydrothermal fluid contribution of ~0.1% can account for the variation in Eu/Sm in the IF, with remaining variability in Y/Ho accounted for potentially by a freshwater fluid component with near - chondritic Y/Ho ratio (Delvigne et al., 2012). As discussed by Alexander et al., (2008), remaining variation in the slope of the REE pattern, represented here using Pr/Yb, cannot be accounted for by hydrothermal fluid composition since it is decoupled from changes in Eu by contrast to many Archean Algoma-type IF (Bau and Dulski, 1996). Expressed in a plot of Pr/Yb vs. Y/Ho, there is significant scatter in the samples beyond the mixing line relationship between the three aforementioned end-members (Figure 5-5) that also points to an additional influence on the REE+Y ratios. Alexander et al., (2008) attribute this variability to changes in the REE pattern associated with a greater abundance of riverine-derived colloidal REE+Y at specific intervals of shallowest water IF deposition. Notably, however, detrital material derived from continental sources, represented in Figure 7a-b by the TSB07 shale average of Sinqeni formation (Bolhar et al., 2015), a modern upper continental crust average (Kamber et al., 2005), and Archean basalt and komatiite averages (Condie, 1993) could also account for some of the variation in Y/Ho and perhaps other REE+Y characteristics and are largely indistinguishable from the inferred freshwater component composition in terms of Y/Ho ratio.

In general, the REE+Y results of this study support the previous REE+Y models and geologically constrained context of a near–shore depositional environment for the Ijzermijn IF, where only a minor amount of hydrothermally derived fluids would have survived in anoxic, deeper waters that upwelled into shallower depositional setting. However, an interesting observation, also made evident on the

REE+Y mixing plots, is that Y/Ho and $(Pr/Yb)_{SN}$ ratios appear to differ between drill core and outcrop samples (Figure 5-5). A shift towards higher $(Pr/Yb)_{SN}$ ratios is observed in the outcrop samples of Ijzermijn IF relative to correlative drill core samples to outcrop samples of Ijzermijn IF in this study and samples from previously published studies (Alexander et al., 2008; Bolhar et al., 2015; Delvigne et al., 2012). Scotts Hill IF samples also cluster towards lower $(Pr/Yb)_{SN}$ ratios relative to the outcrop samples from the Ijzermijn IF (Figure 5-5). This study provides analyses for several more Fe-lutite samples than in the previous studies and all IF samples show typical Archean seawater signatures such as LREE depletions ($(Pr/Yb)_{SN} < 1$, Bau and Dulski et al., 1996), as well as Gd and La anomalies. However, the ΣREE + Y of Fe-lutites and shales from this study correlate well with Th concentrations (R^2 =0.97). Thus, ΣREE + Y in Fe-lutite samples from Ijzermijn IF should be considered at least partly affected by detrital mixing. Some scatter can be attributed to a more complicated mixture of detritally bound REE+Y, and REE+Y scavenged by particles during IF deposition. Even within Fe-lutite samples, however, the shift in signatures between outcrop and drill core samples is noteworthy and could suggest that REE signatures can be affected by post–depositional processes, despite the general notion that REE remain immobile during lithification, diagenesis or metamorphism (Bau, 1991; 1993, Bau and Dulski, 1996; Bolhar et al., 2004; Planavsky et al., 2010; Viehmann et al., 2014).

5.1.7. Effects of modern weathering on Mo and Fe concentration and stable isotopic compositions

Planavsky et al. (2014a) reported a positive correlation of $\delta^{98/95}$Mo versus log [Fe/Mn] for Ijzermijn IF samples with a clear distinction between outcrop and drill core samples (i.e. generally outcrop $\delta^{98/95}$Mo and Fe/Mn > drill core $\delta^{98/95}$Mo and Fe/Mn; Figure 1-3). The data from this sudy (Table 5) follow the general trend of those reported by Planavsky et al. (2014a). However, White Mfolozi River outcrop samples do not show the clear distinction in $\delta^{98/95}Mo_{NIST3134+0.25}$ values and Fe/Mn ratios or MnO wt % contents from drill core samples (Figure 1-3, and Figure 5-6a). Despite loss of carbonate phases, MnO and Fe_2O_{3tot} contents did not show much difference between drill core and outcrop samples used in this study. As discussed above reduced Mn(II) and Fe(II) were released from siderite, kutnahorite and ankerite during modern weathering and consecutively in situ oxidized and incorporated into hydroxide phases (mainly goethite) or adsorbed onto other mineral surfaces, resulting in no or little net loss of MnO and Fe_2O_{3tot} contents in bulk Fe-lutites. If indeed no Fe was lost from the outcrop samples during modern weathering then there should be no fractionation of their stable Fe isotopic compositions and the original $\delta^{56/54}Fe_{IRMM-014}$ values of the samples should be retained. However, there is a myriad of geochemical evidence showing that the White Mfolozi River outcrop samples were altered by modern weathering processes, and that we refrain from using Mo

and Fe concentration and stable isotope data of these samples for any further interpretation of the depositional environment of the Ijzermijn IF.

As already discussed above, the outcrop samples used in the study of Planavsky et al. (2014a) originate from a different geographical location (S28°15´21.09´´; E31°13´13.08´´ PG and PO outcrop samples) compared to the White Mfolozi River outcrops sampled here. Outcrop samples reported in Planavsky et al. (2014a) show considerably lower siderite and carbonate contents than drill core samples but overall higher hematite contents (see SI Table 2 of Planavsky et al. 2014a), indicating alteration by modern weathering as well.

Weathering after prolonged exposure introduces substantial complexities to trace element, radiogenic and stable isotope systematics (e.g. Babechuk et al., 2014; Wille et al., 2018) particularly for redox-sensitive elements (e.g. Babechuk et al., 2015; Dequincey et al., 2002). At the outcrop level studied here, shale samples show a consistent modest ^{234}U-deficit whereas IF samples have ($^{234}U/^{238}U$) greater than 1. At higher elevations, the influence of meteoric fluids on U, Mo, Fe and Mn-systematics of exposed rocks were almost certainly different. This may also explain why the outcrop samples studied by Planavsky et al. (2014a) do not show heavy stable Cr isotopic compositions as those from the White Mfolozi River outcrop used in this study. Alternatively, the separate Cr, Mo and log [Fe/Mn] systematics may record original stratigraphic/ lateral depositional facies variations between the two outcrop and the drill core locations.

5.2.1. Concluding remarks and outlook

As a summary, the findings discussed in Chapter 5 show that the previously reported Cr isotopic signatures (Crowe et al., 2013) outside of the igneous inventory range (Schoenberg et al., 2008) from the Ijzermijn IF, are unlikely to reflect Mesoarchean atmospheric oxidative weathering, but are rather a modern weathering overprint. The data from Nsuze paleosol (Crowe et al., 2013) remain to argue for the presence of atmospheric oxygen (>10^{-5} PAL) before the GOE, however, the stable Cr isotopic composition of the ~2.9 Ga paleosol might indicate other processes than simply surface redox processes, as stable Cr isotopic fractionations are not only driven by redox reactions. Therefore, the findings of this study as presented in Chapter 5 cast some doubt on the presence of an oxidizing atmosphere at around 2.95 Ga, enough to mobilize redox sensitive elements. However, the plausibility of an oxic shallow seawater (oxygen oasis) and a redox stratified ocean, under a reducing atmosphere will be discussed in the following chapter.

6. Implications of the stable Mo and Fe isotopic data for a Mesoarchean oxygen oasis

While the results of this study cast doubt on the efficacy of the Cr geochemistry of the Ijzermijn IF as fingerprints of the earliest evidence for oxidative chemical weathering and thus free atmospheric oxygen in the Mesoarchean, they do still support a subtle preferential U over Th enrichment and, importantly, do not stand in contradiction to the evidence remaining from fractionated Mo isotopes that support Mo redox cycling and the presence of oxidized Mn(IV) in form of Mn-oxides in the Pongola basin (Barling and Anbar, 2004; Wasylenki et al., 2008; Planavsky et al., 2014a). The lack of Cr isotopic fractionation in chemical sediments and thus the lack of oxidative Cr weathering in the Mesoarchean does not exclude that diagenetic Mn(II)-carbonates originated from Mn(IV)-oxides which infer the presence of free O_2 in Mesoarchean seawater (Planavsky et al., 2014a; Ossa et al., 2016). Growing evidence for the presence of free O_2 in the Mesoarchean seawater of the Pongola basin yet lack of free atmospheric O_2 at that time – a typical oxygen oasis – stems from a combined S-Fe isotope study (Eickmann et al., 2018). As a consequence, stable Mo isotopes in chemical sediments might be a more sensitive tracer for oceanic and/or atmospheric redox changes than stable Cr isotopes, but further work is necessary to unravel the conditions necessary to initiate Cr oxidative weathering on land and potentially result in the deposition of heavy isotopic signatures in marine environments.

6.1.1. $\delta^{98/95}Mo_{NIST3134+0.25}$ and $\delta^{56/54}Fe_{IRMM-014}$ values of drill core samples and MnO_2 shuttle in 2.95 Ga Ijzermijn IF

Previous studies found positive correlations between $\delta^{98/95}$Mo values and the logarithm of Fe/Mn ratios as well as $\delta^{98/95}$Mo and $\delta^{56/54}$Fe values for 2.95 to 1.85 Ga old IFs (Planavsky et al., 2014a; Kurzweil et al., 2016). These correlations were interpreted to reflect stable Mo isotopic fractionation resulting from the preferential adsorption of isotopically light dissolved molybdate (MoO_4^{2-}) onto Mn-and Fe-oxide particle surfaces that formed in oxic seawater, a process which can readily be observed in modern marine settings (Barling et al., 2001; Barling and Anbar, 2004; Goldberg et al., 2009, 2012; Kashiwabara et al., 2011; McManus et al., 2006; Siebert et al., 2003). Thereby, adsorption of Mo onto MnO_2 particles causes a larger stable Mo isotopic fractionation than adsorption onto Fe-oxyhydroxides (Barling & Anbar, 2004; Malinovsky et al., 2007; Wasylenki et al., 2008; Goldberg et al., 2009). During subsequent diagenesis, dissolution of Mn- and Fe-oxides in the anoxic sediments may liberate isotopically light Mo to the pore water from which Fe(II) and Mn(II)–carbonates precipitate by microbially induced oxidation of organic matter (Johnson et al., 2013). This process has been referred to as the "Mn-oxide shuttle" (Algeo and Tribovillard, 2009; Scholz, 2013). Effective scavenging of the

liberated isotopically light Mo by the Fe-Mn-carbonates can preserve the light isotopic signatures originating from the Mn- and Fe-oxides. According to this model, the light Mo isotopic signatures in Ijzermijn IF samples could be the result of Mo adsorption mainly onto Mn-oxides in the oxic water column and organic matter oxidation coupled to Mn(VI)- and/or Fe(III)-reduction below the sediment-water interface during early diagenesis. Mn-oxide shuttling has been reported for the 2.46 Ga Koegas IF, where it facilitated the delivery of lower Mo and Fe isotopic signatures to the sediments deposited within, compared to those deposited below the Mn-chemocline (Kurzweil et al., 2016). A modern example of this process has been described for the redox stratified Lac Pavin, France, with oxygenated surface waters, and anoxic, ferruginous deep waters (Busigny et al., 2014).

If this mechanism operated in the Pongola Basin, it would indicate the presence of sufficient free O_2 in the surface water of the near-shore continental margin area to form Mn(IV)-oxides, and thus was interpreted to be as evidence for an oxygen oasis 2.95 Ga ago (Planavsky et al., 2014a). In this study, a strong negative correlation between $\delta^{98/95}Mo_{NIST3124+0.25}$ values and MnO contents for Fe-lutite samples from both drill cores DDN-1 and PMH24/L1 (Figure 6-1a, $R^2 = 0.86$) is observed. Generally, the MnO contents of near-shore drill core DDN-1 samples are higher than those of the less proximal drill core PMH24/L1 samples, and in consequence the lower are their $\delta^{98/95}Mo_{NIST3134+0.25}$ values, respectively (Figure 2-2 and Figure 6-1a). This observation fits well with a more effective MnO shuttling in near-shore waters of the Pongola Basin (Planavsky et al., 2014a, Kurzweil 2016). Interestingly, the chert samples from drill core DDN-1 show generally much lower MnO contents than the Fe-lutites (Figure 6-1a), but are highly enriched in Mo and have light $\delta^{98/95}Mo_{NIST3134+0.25}$ values similar to the one Fe-lutite sample (DNN-1 274.3A) with lower $\delta^{98/95}Mo_{NIST3134+0.25}$ values than the terrestrial average (Figure 6-1b). Preservation of original MnO_2-shuttling of light Mo isotopic signatures seems thus limited to samples with very high authigenic Mo enrichment (Figure 6-1b) and least detrital contamination.

Similar to the Mo isotopic composition, there is a negative correlation between the $\delta^{56/54}Fe_{IRMM-014}$ values and MnO contents (Figure 6-1a, $R^2 = 0.67$) for Fe-lutite samples from both drill cores DNN-1 and PMH24/L1. A weak positive correlation between the $\delta^{56/54}Fe_{IRMM-014}$ and $\delta^{98/95}Mo_{NIST3134+0.25}$ values (Figure 6-1e, $R^2 = 0.52$) of all drill core samples (including chert samples) from the Ijzermijn IF points to a coupling of isotopic fractionation for these two elements. The positive correlation in $\delta^{56/54}Fe_{IRMM-014}$ vs. log [Fe/Mn] (Figure 6-1d), and the lack of a negative correlation between $\delta^{56/54}Fe_{IRMM-014}$ and $\delta^{98/95}Mo_{NIST3134+0.25}$ values for drill core DDN-1 and PMH24/L1 samples (Figure 6-1e) also point to MnO_2-shuttling and rule out a strong influence of preferential adsorption of Mo onto Fe-hydroxide particles in the Pongola basin as has been pointed out before on other drill core samples from this basin (Eroglu et al., 2018; Kurzweil et al., 2016; Planavsky 2014a). Dissolved ferrous iron concentration in the Meso- to Neoarchean oceans, and thus its $\delta^{56/54}Fe_{IRMM-014}$ signature decrease due to continuous iron oxidation

from deep to shallow water masses (Czaja et al., 2012; Eroglu et al. 2018, Kurzweil et al., 2016). Substantial Mo adsorption onto Fe-hydroxides, however, would have caused heavier $\delta^{98/95}Mo_{NIST3134+0.25}$ values than those observed for the Ijzermijn IF samples (Goldberg et al., 2009; Kashiwabara et al., 2011) and, thus MnO_2 formation must have dominated over Fe-hydroxide precipitation, as Fe(II) was already depleted in the near-shore depositional setting of the IF (e.g DDN- 1 drill hole).

Interpretation of the stable Mo and Fe isotopic variations in Ijzermijn IF is currently best explained with the MnO_2-shuttling model summarized in Figure 6-2. According to the model, Ijzermijn IF was deposited within and above the Mn-chemocline in an 'oxygen oasis' environment, due to the combination of very light $\delta^{98/95}Mo_{NIST3134+0.25}$ and $\delta^{56/54}Fe_{IRMM-014}$ values (Figure 6-2). The model suggests that the origin of iron oxides of the Ijzermijn IF is a combination of partly partial oxidation of Fe(II) with dissolved O_2 in seawater, and mainly abiotic oxidation of Fe(II) by Mn(IV)-oxide particles in the Mn-chemocline in seawater, as recorded in this study. Upwelling and partial oxidation of deep water Fe(II) (directly with seawater O_2 and MnO_2 particles), led to the depletion of heavy Fe isotopes in the remaining $Fe(II)_{aq}$ pool, thus leading to a decrease in $\delta^{56/54}Fe_{IRMM-014}$ towards the redoxcline, similar to 2.46 Ga Koegas IF (Kurzweil et al., 2016). Hence, Fe-oxides with lighter $\delta^{56/54}Fe_{IRMM-014}$ values formed in heavy Fe depleted, Mn-rich upper water column in the shallower setting (such as in DDN-1 drill core, Figure 6-2). The sediments with heavier $\delta^{56/54}Fe_{IRMM-014}$ values were deposited in deeper water facies, below the Mn-chemocline (Figure 6-2). Similarly, octahedrally coordinated, isotopically light Mo preferentially adsorbed onto the MnO_2 particles, leading to a lighter Mo isotopic composition in the proximally deposited IF, where the Mn-flux was the highest (Figure 6-2). In contrast, the sediments deposited in distal settings have a heavier stable Mo isotopic signature, and contain less MnO. As seen in the model, drill holes are located at different depths of the basin, exposing them to the different intensities of Mn-oxide-shuttling, thus leading to different $\delta^{98/95}Mo_{NIST3134+0.25}$ and $\delta^{56/54}Fe_{IRMM-014}$ values (Figure 6-2).

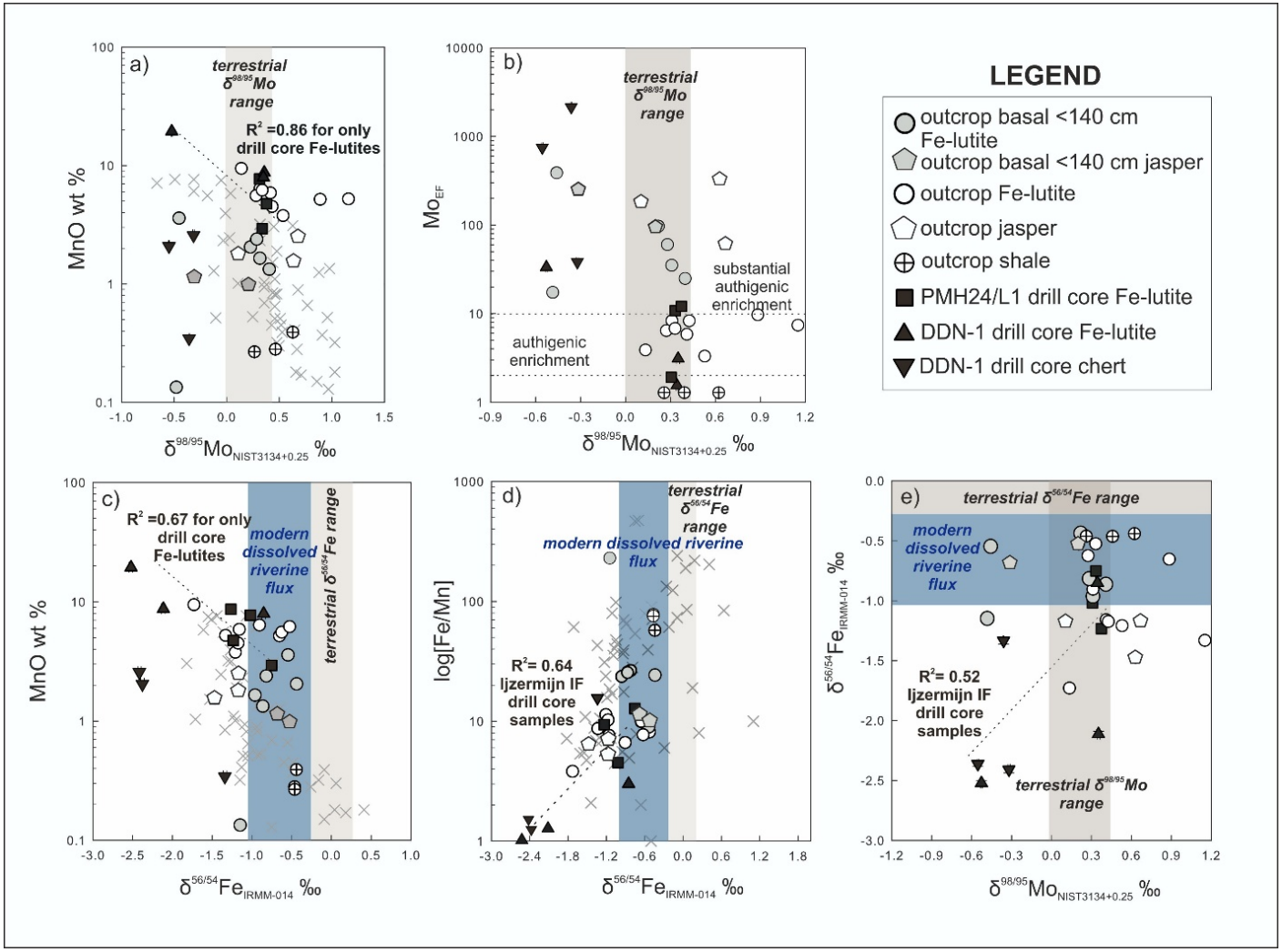

Figure 6-1. a) Note the negative correlation between the $\delta^{98/95}Mo_{NIST3134+0.25}$ and MnO for the Fe-lutites among drill core samples. The correlation is not preserved in the outcrop samples, due to modern weathering, and is only preserved in Fe-lutites of the drill cores because of the high MnO contents in the Fe-Mn carbonates of the Fe-lutite lithology compared to cherts. The gray filled symbols are the samples from the basal <140 cm section of the White Mfolozi River outcrop. The gray "X" symbols represent data from other IFs and previous data from Ijzermijn IF (Planavsky et al., 2014a), including the 2.46 Ga Koegas IF (Kurzweil et al., 2016). b) Mo_{EF} compared to the stable Mo isotopic composition shows that one Fe-lutite (274.3A) and all chert samples from the drill core DDN-1 have $\delta^{98/95}Mo_{NIST3134+0.25}$ very light values and substantial authigenic enrichments, and are associated with Mn-oxide shuttling. The other Fe-lutite samples from both drill cores also show some authigenic enrichment, however lie in the terrestrial $\delta^{98/95}Mo_{NIST3134+0.25}$ range (Voegelin et al., 2014). The DDN-1 drill core samples with the highest authigenic enrichment shows the lightest $\delta^{98/95}Mo_{NIST3134+0.25}$ values, due to DDN-1 drill hole being located in a shallower depositional setting compared to the drill hole PMH24/L1, thus preserving the record of Mn-oxide shuttling. c) The negative correlation is shown between MnO and the $\delta^{56/54}Fe_{IRMM-014}$. Similar to Mo isotopic composition, Fe isotopic composition is controlled by the MnO shuttle, thus Fe-oxides form during oxidation of Fe(II) by the Mn-oxides. The heavier $\delta^{56/54}Fe_{IRMM-014}$ values, resulting from oxidation and deposition below the Mn-chemocline are recorded in the off-shore, deep-facies of the Mozaan Group.

Figure 6-2. The inferred Mn- oxide-shuttling model for the stable Mo and Fe isotopic composition, and the deposition of the Ijzermijn IF (see the explanation in the text). The IF records formation of Fe-oxides with lighter $\delta^{56/54}Fe_{IRMM-014}$ values, having deposited in heavy Fe depleted, Mn-rich upper water column in the shallower setting. Upwelling and partial oxidation of deep water Fe(II) (directly with seawater O_2 and MnO_2 particles), led to the depletion of heavy Fe isotopes in the remaining $Fe(II)_{aq}$ pool, thus leading to a decrease in $\delta^{56/54}Fe_{IRMM-014}$ towards the redoxcline, similar to 2.46 Ga Koegas IF (Kurzweil et al., 2016). Octahedrally coordinated, isotopically light Mo preferentially adsorbs onto the MnO_2 particles, leading to a lighter Mo isotopic composition in the proximally deposited IF, where the Mn-flux is the highest. In contrast, the Mo isotopic signature of the sediments deposited in distal settings is heavier, with less MnO. As seen in the model, drill holes are located at different depths of the basin, exposing them to the different intensities of Mn-oxide-shuttling, thus leading to different $\delta^{98/95}Mo_{NIST3134+0.25}$ and $\delta^{56/54}Fe_{IRMM-014}$ values. Drill core PMH24/L1, being located in a deeper facies, displays slightly heavier $\delta^{98/95}Mo_{NIST3134+0.25}$ and $\delta^{56/54}Fe_{IRMM-014}$ values, and less MnO. Fe-lutites contain more MnO, relative to the chert, due to the preservation of primary Mn(II) in the early diagenetic carbonates (th: tetrahedrally coordinated, oh: octahedrally coordinated, DIR: dissimilatory iron reduction).

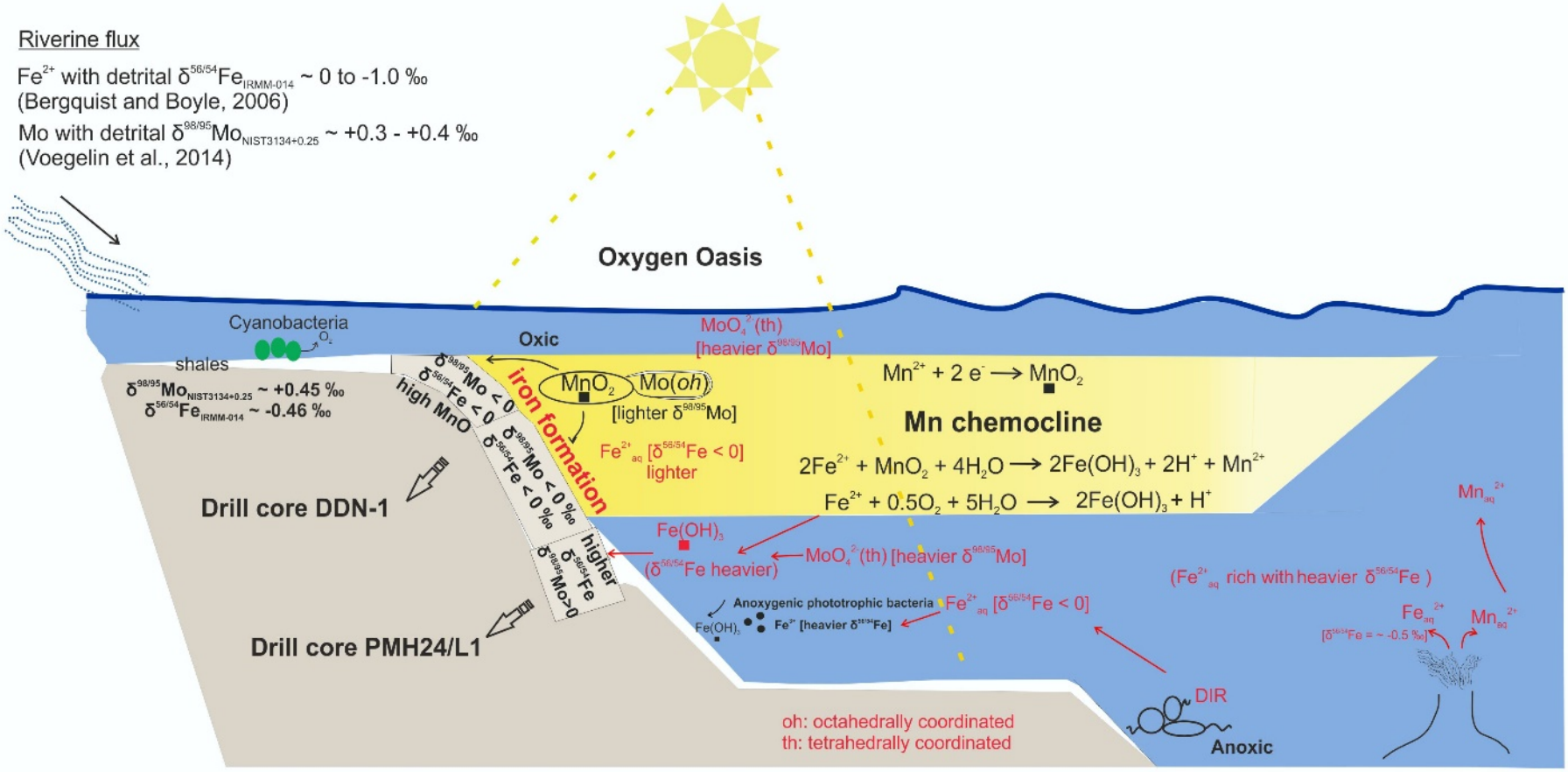

6.1.2. Lack of a Ce anomaly

The lack of a 'true' Ce anomaly in all samples (i.e., within 1.05 and 0.95) is consistent with observations from previous studies (e.g Bolhar et al., 2015; Delvigne et al., 2012). However, two of the three Fe-lutite samples that fall closest to the threshold of a true negative Ce anomaly also display isotopically heavy or nearest to isotopically heavy $\delta^{53/52}$Cr values. Thus, it is plausible that modern oxidative weathering also contributed to this shift closer to negative Ce anomaly, for example through retaining small amounts of Ce(IV) elsewhere on oxide minerals prior to subtle mobility of the trivalent LREE.

The lack of Ce anomalies in Mozaan Group sediments (Alexander et al., 2008; Bolhar et al., 2015; Delvigne et al., 2012) and the general complete absence of evidence for Ce anomalies in shallow-water microbial carbonates of Archean age (Kamber et al., 2014) suggests that Ce oxidation on particulate matter (Bau and Dulski, 1996; Fryer, 1977; Derry and Jacobsen 1990; Elderfield, 1988; Kato et al., 1998, Sholkovitz et al., 1994; Planavsky et al., 2010) was not yet operational, even in environments of high microbial productivity. This observation from REE systematics conflicts with the suggestion that MnO_2 was present during the formation of the Ijzermijn IF because Mn-oxides are capable of catalyzing the oxidation of Ce^{3+} to Ce^{4+} enabling preferential scavenging of the less soluble Ce^{4+} compared to the seawater REE^{3+} at their surface (Feng, 2010; Koppi et al., 1996; Ohnuki et al., 2008; Takahashi et al., 2000; 2007). This process eventually leads to positive Ce-anomalies in hydrogenous ferromanganese nodules (Elderfield et al., 1981; De Carlo and McMurtry, 1992; Piper, 1974) and negative Ce-anomalies in seawater.

One explanation for the lack of negative Ce anomalies in Archean shallow seawater precipitates (e.g. Kamber et al., 2014) is that the development of a Ce anomaly facilitated by Mn-oxides can be inhibited by organic matter due to shielding by humate molecules (Davranche et al., 2005; 2008). Therefore, Meso- to Neoarchean sediments, which contain sufficient organic matter, may not develop or preserve a Ce anomaly despite the presence of a redox gradient that allows Mn oxide formation and, thus still show typical Archean seawater REE+Y signatures free of a Ce-anomaly (Alexander et al., 2008; Delvigne et al., 2012). Indeed, the Ijzermijn IF is over- and underlain by shales that were originally rich in organic matter, but which was then oxidized during early diagenesis and incorporated into carbonate minerals. As such, the organic matter which was deposited together with the Mn-oxides on the Pongola basin might have prevented the formation of a Ce-anomaly.

In a study of trace metal incorporation of shallow-water microbial carbonate, Gallagher et al. (2015) noted the stark contrast between Archean 'stromatolites' with generally much higher content of kerogen and other forms of reduced C compared with post-Archean samples. Furthermore,

Gallagher et al. (2015) also showed that preservation of pyrite within reduced C-rich portions of microbial carbonate is much richer in Archean samples than post-GOE stromatolites. Collectively, the current evidence suggests that the presence of organic molecules in Archean seawater and their influence on redox-sensitive metals is an area requiring further study. It should be noted that the presently available experiments were conducted at very different conditions (e.g. pH; Bau, 1999; Davranche et al., 2005; Ohta and Kawabe, 2001) than those prevailing during the deposition of the Ijzermijn IF some 2.95 Ga ago and that the organic matter was almost certainly of different character.

7. Arvadi Spring as a modern analog for Archean oxygen oases

As discussed in the above section, 6.1.1., evidence shows that iron oxide precursors of the early diagenetic iron- manganese carbonates of the Ijzermijn IF (Ossa et al., 2018) partly formed by partial oxidation of Fe(II) with dissolved O_2 generated by cyanobacteria in seawater (Haqq-Misra et al., 2011; Hoashi et al., 2009; Kappler et al., 2005; Kasting et al., 1979; Konhauser et al., 2002; Konhauser et al., 2007; Lalonde & Konhauser, 2015; Rasmussen et al., 2008), and mainly by abiotic oxidation of $Fe(II)_{aq}$ by Mn(IV)-oxide particle shuttling at the Mn-chemocline of the water column, under redox-stratified conditions in an *oxygen oasis*. A mechanism postulated earlier for the formation of Fe(III) minerals of the Precambrian IFs at the absence of oxygen was $Fe(II)_{aq}$ oxidation by the anoxygenic photoautotrphic bacteria (Balci et al., 2006; Croal et al., 2004; Crowe et al., 2008; Kappler et al., 2005; Widdel et al., 1993; Swanner et al., 2015). This mechanism might have co-occurred in Mesoarchean seawater during the deposition of Ijzermijn IF, simultaneously with abiotic oxidation of $Fe(II)_{aq}$ via Mn(IV) oxide shuttling, but below the redoxcline, in deeper water facies than the depositional setting of the Ijzermijn IF (Figure 6-2). Formation of $Fe(OH)_3$ during anoxygenic photosynthetic Fe(II) oxidation with the formula:

$$4Fe^{2+}_{aq} + HCO_3^- + 10H_2O + h\nu \longrightarrow 4Fe(OH)_3 + CH_2O + 7H^+ \qquad (11)$$

requires energy from sunlight (*hv*), thus occurs at a relatively shallow water depth, to which sunlight can penetrate to, as much as 100 m water depth as reported by Kappler et al. (2005), under anoxic conditions (Figure 5-7).

From the stable Fe isotopic perspective, depositional model for the Ijzermijn IF shows that upwelling and partial oxidation of deep water $Fe(II)_{aq}$ (with $\delta^{56/54}Fe_{IRMM\text{-}014}$ values from - 0.1 to - 1.35 ‰, Beard et al., 2003; Conway and John, 2014; Rouxel et al., 2004; 2008; 2016; Severmann et al., 2004; Sharma et al., 2001) directly by seawater O_2 and MnO_2 particles, resulted in the depletion of heavy Fe isotopes in the remaining $Fe(II)_{aq}$ pool at the shallower water depths, leading to increasingly lighter $\delta^{56/54}Fe_{IRMM\text{-}014}$ values along the way from the redoxcline to paleoshoreline (Busigny et al., 2014;

Kurzweil et al., 2016; Ossa et al., 2018; Planavsky et al., 2012; Rouxel et al., 2005; Steinhoefel et al., 2009; Tsikos et al., 2010). Hence, iron oxides with lighter $\delta^{56/54}Fe_{IRMM\text{-}014}$ values had precipitated in the heavy Fe depleted, MnO_2 rich upper water column in a shallower setting, whereas the ones with heavier $\delta^{56/54}Fe_{IRMM\text{-}014}$ values had precipitated in a more distal setting, below the Mn-chemocline (Figure 6-2).

Our current understanding of the abiotic and biotic processes during the evolution of such redox-stratified depositional conditions, mostly stems from the geochemical and isotopic analyses of the sedimentary rocks. Some additional information is provided from laboratory experiments under controlled conditions. However, data are lacking from modern sites that could mimic the depositional conditions of the Archean or Proterozoic during high oxygen intervals, such as Lac Pavin in France as an Archean ocean analog (Busigny et al., 2014). Arvadi Spring comprises of an approximately 20 cm deep, fully oxic water, thus can potentially represent the near-shore, surface water conditions above the redoxcline of an Archean oxygen oasis.

Arvadi Spring, with its chemical characteristics (high $Fe(II)_{aq}$ and SO_4^{2-}), and co-existence of dissolved Fe(II), Fe(III) minerals, dissolved sulfur (HS^-) and H_2S resembles the conditions that were inferred to have prevailed in Proterozoic shallow ocean, and may also resemble the conditions during high oxygen intervals in Meso to Neoarchean. However, it should be noted that there are differences in the depositional environment of the Ijzermijn IF and Arvadi Spring, e.g. lack of Mn-oxides and a Mn-chemocline, or a redox-stratified water column in the Arvadi Spring, unlike in Lac Pavin in France (Busigny et al., 2014), marine vs. freshwater conditions, as well as differences in Fe(II) and Fe(III) concentrations of Arvadi water as well as precipitates, and in estimates of Fe(II) and Fe(III) concentrations for Precambrian seawater (see the discussion in section 7.1.1 below). Particularly, sulfate concentration in the Arvadi Spring is with 8.3 mM (Koeksoy et al. 2018) much higher, than the earlier estimates for Archean seawater of <200 µM (Habicht et al., 2002) or even <2.5 µM (Crowe et al., 2014). However, a recent study in 2.97 Gyr-old stromatolitic dolomites from the Nsuze Group, Pongola Supergroup, South Africa, showed the presence of a dissolved sulfate pool (> 5 µM) and identified the activity of sulfate reducers (microbial sulfate reduction- MSR) in a shallow-marine environment (Eickmann et al., 2018). Similarly, MSR activity was identified in Arvadi Spring which has positive $\delta^{34/32}S$ values (15.3 ‰) of dissolved sulfate, light $\delta^{34/32}S$ values (- 25.6 ‰) of elemental sulfur and dissolved sulphide (- 25.1 to -21.5 ‰) in the nearby Zuelper Spring (Strauss et al., 2016). These $\delta^{34/32}S$ values indicate dissolved sulphide generation via microbial sulfate reduction under anoxic conditions in the subsurface, and subsequent oxidation by sulphide oxidizing bacteria, for example, Thiothrix, at the anoxic–oxic transition within the discharge area of the springs. It should be noted that, however, Ijzermijn IF itself must have deposited in a period of low MSR activity, due to the obvious

predominance of precursor Fe and Mn oxy-hydroxides over dissolved sulfate as the thermodynamically favored electron acceptors (Froelich et al., 1979; Canfield et al., 2005). Nevertheless, the Arvadi Spring might not be too far from being analogous to the depositional environment shortly before the deposition of Mozaan Group sedimentary rocks.

Interestingly, anaerobic phototrophic Fe(II) oxidizers were still recorded in red flocs of the Arvadi Spring, although low in abundance, despite fully oxic conditions of the spring water (Koeksoy et al., 2018). The most abundant species were aerobes (microaerophilic and nitrate reducing Fe(II) oxidizing microorganisms along with microareophilic sulphide- oxidizers), followed by Fe(III) reducing anaerobes in the red flocs (Koeksoy et al., 2018). Koeksoy et al. (2018) concluded that different metabolic types of microorganisms co-occur in different ecological niches (anoxic and microoxic microniches) throughout the seasons, and a significant fraction of dissolved Fe(II) in spring water is consumed by their metabolic pathways. Furthermore, some fraction of dissolved Fe(II) in the spring water might stem from dissimilatory Fe(III) reduction, possibly along with abiotic Fe(III) reduction processes such as photoreduction of ligand-bound Fe(III) (Barbeau et al., 2001), the abiotic reaction of O_2 with ligand-bound or dissociated Fe(III) (Rush & Bielski, 1985), or Fe(III) reduction coupled to abiotic sulphide oxidation (Lohmayer et al., 2014, Yao & Millero, 1996). All of these processes might have also occurred during high oxygen intervals throughout the Mesoarchean to the Proterozoic. Low but stable dissolved Fe(II) concentration in spring water is notable, and indicates that $Fe(II)_{aq}$ avoids being completely consumed by abiotic and biotic oxidation processes. High background Fe(II) concentration together with contribution from reductive processes or presence of humic substances that stabilize Fe(II) (Hopwood et al., 2012) or large amounts of dissolved sulphate retarding Fe(II) oxidation (Millero, 1985) are among the suggested plausible mechanisms to explain the persistence $Fe(II)_{aq}$ in Arvadi spring water (Koeksoy et al., 2018).

The Arvadi Spring sheds light to the role and interplay of Fe(II) oxidizing, as well as Fe(III) reducing microorganisms, combined with abiotic, direct oxidation of Fe(II) with dissolved O_2. Anaerobic photosynthetic Fe(II) oxidation or aerobic microbial Fe(II) oxidation in low O_2 microniches (microaerophilic), along with abiotic oxidation of O_2 might all have competed and played a role in the deposition of the Ijzermijn IF. However, from the resulting in a stable Fe isotopic signature of the Fe-deposits it is impossible to distinguish one process from the other or even estimate their relative contributions to the Fe oxidation. The oxidation of $Fe(II)_{aq}$ to $Fe(III)_{aq}$ followed by precipitation of $Fe(III)_{aq}$ to ferric oxide or hydroxide generates similar Fe isotopic fractionation (ranging from ~+ 1 to + 3 ‰, smaller fractionations being dominated by kinetic effects) in all of these processes at neutral pH (Bullen et al., 2001; Beard et al., 2003; Croal et al., 2004; Balci et al., 2006; Kappler et al., 2010; Staton et al., 2006; Swanner et al., 2015). Therefore, the contribution of these microbial Fe(II) oxidation

and Fe(III) reduction processes during the deposition of the Ijzermijn IF, and their influence on the net resulting stable Fe isotopic composition before early diagenesis cannot be ruled out.

7.1.1. $Fe(II)_{aq}$ oxidation, Fe(III) reduction and the role of iron metabolizing microorganisms in the Arvadi Spring and implications for the Mesoarchean Ijzermijn IF of the Pongola Basin

Earlier estimates for $Fe(II)_{aq}$ concentration in the Archean anoxic ocean which were constrained between 3 - 360 µM (Holland, 1973; Morris, 1993; Canfield, 2005), were updated with recent work to 0.9 - 12 µM in the deep ocean, also considering greenalite formation (Tosca et al., 2016). Archean shallow water $Fe(II)_{aq}$ concentration, on the other hand, was estimated to be less than 10 µM in order to allow calcite precipitation (Herzog et al., 1989; Riding et al., 2014). Most recently, in their study Eroglu et al. (2018) estimated the $Fe(II)_{aq}$ concentration in Neoarchean shallow seawater to be in a range from 30 to 928 µM, decreasing two to three-fold from slope (61 - 928 µM) to the shelf area (30 - 310 µM) in Neoarchean Campellrand-Malmani carbonate platform in South Africa. Total Fe concentration of the Arvadi Spring water was determined from water samples collected during two sampling excursions (October 2014 and June 2018) and were recorded in a range from 1.48 to 2.42 µM (October 2014), and from 0.29 to 1.66 µM (June 2018), decreasing from the pond to the creek. Notably, dissolved $Fe(III)_{aq}$ was not detected in the spring water, hence the total $Fe_{(aq)}$ concentration of the water samples represents mainly the $Fe(II)_{aq}$ fraction (Koeksoy et al., 2018). The concentration of $Fe(II)_{aq}$ in Arvadi Spring water is lower than the estimates of Eroglu et al. (2018) for the proximal shelf area in redox stratified Neoarchean seawater. The concentration of the total iron in precipitates (red flocs) of the Arvadi pond and the creek (October 2014: 2.18 to 3.59 wt %, June 2018: 4.11 to 3.25 wt %) are higher compared to the $Fe(II)_{aq}$ concentration of the spring water, but are lower compared to the Precambrian IFs such as Ijzermijn IF (7 to 48 wt %) (Figure 7-2).

The $\delta^{56/54}Fe_{IRMM-014}$ values of the spring water (from - 1.598 to - 0.487 ‰) are slightly heavier, but are in a similarly light range with the 2.95 Ga Ijzermijn IF samples (- 2.522 to - 0.852 ‰) (Figure 7-2). However, red flocs from Arvadi have a heavier $\delta^{56/54}Fe_{IRMM-014}$ range (- 0.357 to 0.327 ‰) compared to the Ijzermijn IF samples.

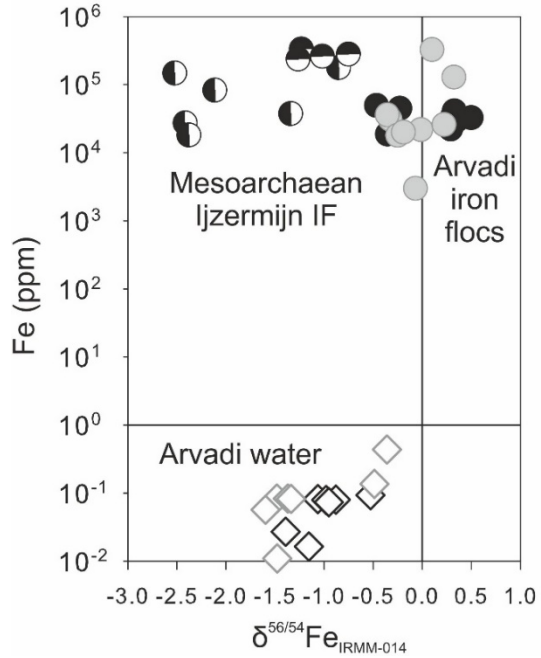

Figure 7-2. Comparison of stable Fe isotopic composition and Fe concentration of 2.95 Ga Ijzermijn IF drill core samples (vertical half-filled rings DDN-1, horizontal half-filled rings PMH24/L1) with modern Arvadi Spring water (gray diamonds from October 2014, black diamonds from June 2018) and precipitate (red floc) samples (gray filled rings from October 2014, black filled rings from June 2018).

The significantly higher Fe concentration, and heavier $\delta^{56/54}Fe_{IRMM-014}$ values of the red flocs compared to the water in the mixing shaft, outlet, pond and the creek, indicate $Fe(II)_{aq}$ oxidation, either biotically or abiotically, and eventual precipitation of iron oxide species, such as $Fe(OH)_3$.

The decreasing trend in $\delta^{56/54}Fe_{IRMM-014}$ values as well as Fe concentrations of both red flocs and water from mixing shaft to the pond are noteworthy, as are a slight decrease in $\delta^{56/54}Fe_{IRMM-014}$ values and Fe concentration of the water samples from the outlet to the middle of the pond (Figures 4-9 and 4-10). Furthermore, $\delta^{56/54}Fe_{IRMM-014}$ values of Arvadi water becomes lighter at the mixing point with the forest brook and after becoming diluted with the forest brook (sampling point 7). Similarly, $\delta^{56/54}Fe_{IRMM-014}$ values of the red flocs become lighter from pond to the creek, and remain relatively unchanged throughout the creek until the mixing point (Figures 4-9 and 4-10).

The initial $\delta^{56/54}Fe_{IRMM-014}$ value of the $Fe(II)_{aq}$ in source water (with a fraction of $Fe(II)_{aq} = 1$), starting from the isotopic composition of the Stollen in October 2014 samples (Figure 7-3), and A1 sampling point in June 2018 samples (Figure 7-4), was chosen as the initial Fe isotopic composition of the Rayleigh distillation curves with different $\Delta_{Fe(II)initial-Fe(II)aq}$ fractionation factors (1.05 ‰ for October 2014 samples and 1.05 ‰ and 3.20 ‰ for June 2018 samples), that were inferred from earlier literature from experiments on Fe oxidation (Beard et al., 2003; Bullen et al., 2001; Johnson et al., 2002; Skulan et al., 2002; Welch et al., 2003; Wu et al., 2011). The horizontal axes indicate the fractions of $Fe(II)_{aq}$ remaining in the dissolved Fe pool during the complete oxidation of all $Fe(II)_{aq}$ along the flow path.

Different fractions of $Fe(II)_{aq}$ of the water samples were calculated assuming the concentration of the source of the Arvadi spring as the initial $Fe(II)_{aq}$ concentration (in October 2014 sampling location Stollen, in June 2018 sampling location A1) and the fractions of the other water samples from different sampling points were determined relative to this initial concentration (see Table 6 and Figures 7-3, 7- 4, and 7-5).

The data from water samples (white circles) were fit to Rayleigh curves (Figures 7-3 and 7-4), showing progressively decreasing $\delta^{56/54}Fe(II)_{aq}$ values with decreasing $Fe(II)_{aq}$ concentration in the remaining water pool from the source to the pond and to the creek along the flow path. Similarly the red floc data (black circles) were fit to Rayleigh curves with a fractionation factor of 1.05 ‰, and despite an overall decrease in both $\delta^{56/54}Fe_{ppt}$ values and Fe concentrations, the red floc samples show somewhat decoupling from the relationship between the $\delta^{56/54}Fe_{ppt}$ values and the Fe concentrations with increasing distance from the pond, unlike the water samples (Figures 7-3 and 7-4) (from the Stollen to A1 to the mixing point). Closed system equilibrium fractionation lines are represented by the black solid lines, and were calculated using a linear fit with the initial $\delta^{56/54}Fe(II)_{aq}$ values of - 0.528 ‰ and - 1.392 ‰, and extrapolated $\delta^{56/54}Fe_{ppt}$ values of 0.500 ‰ and - 0.400 ‰ using an equilibrium fractionation factor of $\Delta_{Fe(II)aq\text{-}Fe(III)ppt}$ of 1.05 ‰, chosen from aforementioned literature. The equilibrium fractionation lines do not represent the Fe(II) oxidation along the flow path of the Arvadi, but rather expected oxidation trends in a closed system, per each sampling point. Furthermore, the fraction F for the dissolved $Fe(II)_{aq}$ on the x axis represent different variables for Rayleigh curves (the fraction of $Fe(II)_{aq}$ along the Arvadi flow path) and for equilibrium fractionation lines (the fraction of $Fe(II)_{aq}$ becoming oxidized in each sampling point). These lines assume an equilibrium fractionation model in a closed system from $Fe(II)_{aq}$ to $Fe(III)_{ppt}$, for the initial sampling point (Stollen, October 2014 in Figure 7-3, and location A1 in June 2018 in Figure 7-4), to the resulting extrapolated $\delta^{56/54}Fe_{ppt}$ value for the precipitated red floc in location Stollen (October 2014) and A1 (June 2018). The measured data (black circle Stollen for October 2014 and A1 red floc for June 2018) show a good fit to the extrapolated value (Figures 7-3 and 7-4). A lighter initial $\delta^{56/54}Fe(II)_{aq}$ value was also used (equilibrium fractionation 2) to calculate a second line to represent the water samples with lighter isotopic composition which can be found in sampling locations further away from the source of the Arvadi, and as seen in the Figure 7-3, the oxidation deviates from a closed system equilibrium fractionation for those samples, as the measured data from the corresponding red flocs (black circles) fall on much higher $\delta^{56/54}Fe_{ppt}$ values than estimated in the equilibrium fractionation line 2.

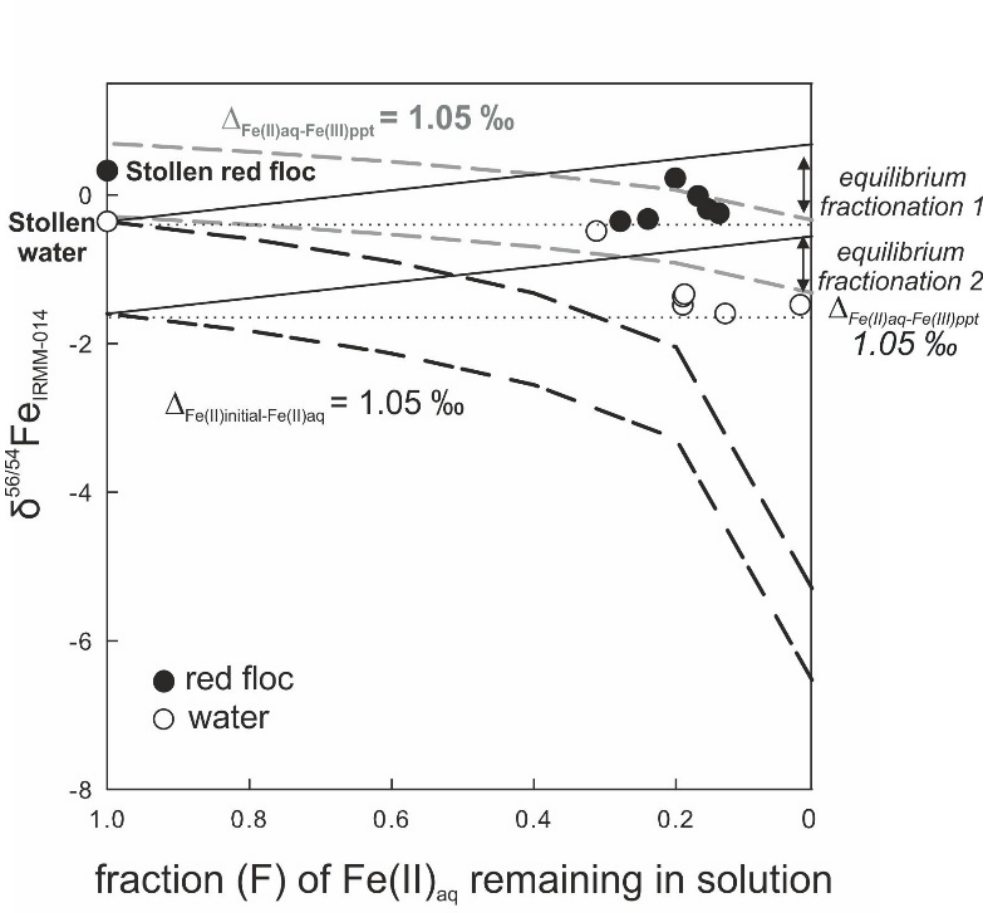

Figure 7-3. White circles are $\delta^{56/54}Fe(II)_{aq}$ (water) data and black circles are $\delta^{56/54}Fe_{ppt}$ (red floc) data, both from October 2014 sampling. The dashed black lines are Rayleigh fits for the $\delta^{56/54}Fe(II)_{aq}$ data and the gray dashed lines are Rayleigh fits for the $\delta^{56/54}Fe_{ppt}$ data, both with $\Delta_{Fe(II)initial-\ Fe(III)aq}$ and $\Delta_{Fe(II)aq-Fe(III)ppt}$ values of 1.05 ‰, respectively (arbitrarily assigned approximate value according to the literature on experiments (e.g. Beard et al., 2003; Bullen et al., 2001, Croal et al., 2004). There are two Rayleigh curves for each water and red floc samples which are set to different initial $\delta^{56/54}Fe(II)_{aq}$ values of - 0.359 ‰ and - 1.598 ‰ for water and - 0.359 ‰ and - 1.338 ‰ for the red floc samples. Closed system equilibrium fractionation lines are represented by the black solid lines, and were calculated using the linear fit with the initial $\delta^{56/54}Fe(II)_{aq}$ values of - 0.359 ‰ and - 1.598 ‰ and an equilibrium fractionation value $\Delta_{Fe(II)aq-Fe(III)ppt}$ of 1.05 ‰, obtained from earlier experiments of equilibrium fractionation during Fe oxidation. See text for further discussion.

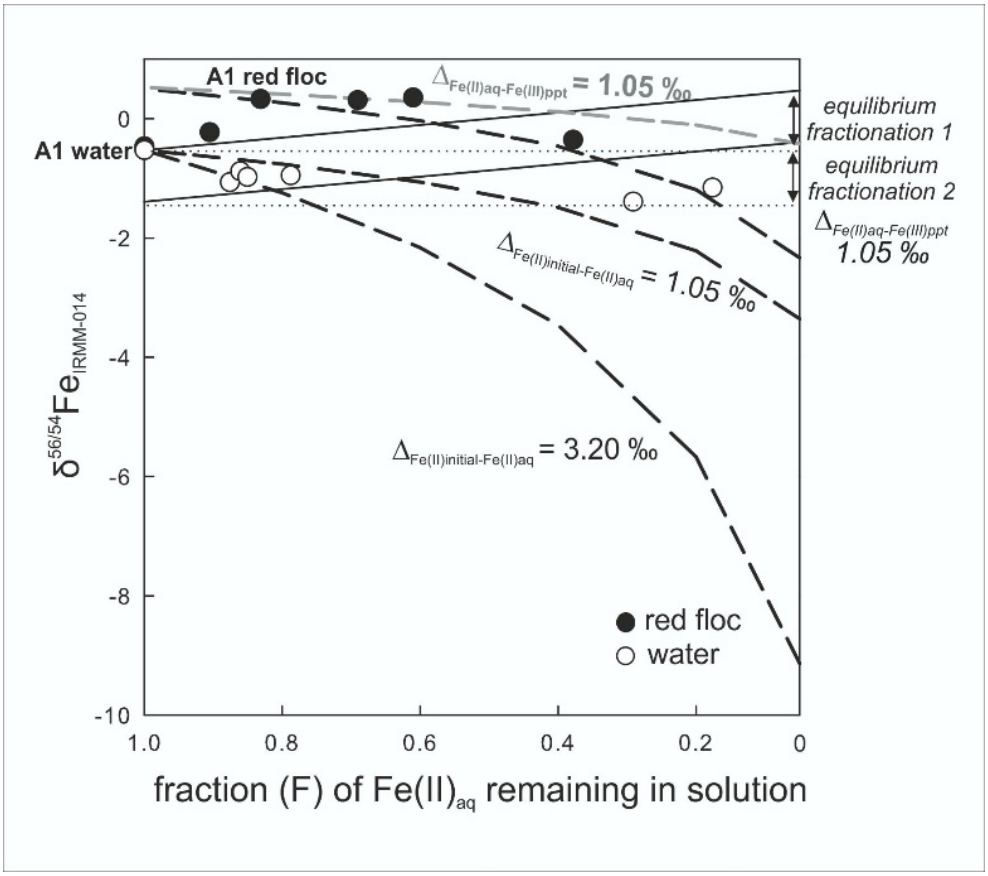

Figure 7-4. White circles are $\delta^{56/54}Fe(II)_{aq}$ (water) data and black circles are $\delta^{56/54}Fe_{ppt}$ (red floc) data, both from June 2018 sampling. The dashed black lines are Rayleigh fits for the $\delta^{56/54}Fe(II)_{aq}$ data with $\Delta_{Fe(II)initial\text{-}Fe(III)aq}$ fractionation factors of 1.05 ‰ (Beard et al., 2003; Bullen et al., 2001) and 3.2 ‰ (Johnson et al., 2002; Skulan et al., 2002; Welch et al., 2003; Wu et al., 2011) and the gray dashed line is Rayleigh fit for the $\delta^{56/54}Fe_{ppt}$ data, with a $\Delta_{Fe(II)aq\text{-}Fe(III)ppt}$ value of 1.05 ‰ (arbitrarily assigned approximate values according to the literature on experiments on Fe oxidation). There are three Rayleigh curves for water and one Rayleigh curve for red floc samples which are set to different initial $\delta^{56/54}Fe(II)_{aq}$ values of - 0.528 ‰ and 0.50 ‰ for water samples and - 0.528 ‰ for the red floc samples as representing Fe isotopic composition of the source of the Arvadi Pond. Closed system equilibrium fractionation lines are represented by the black solid lines, and were calculated using a linear fit with the initial $\delta^{56/54}Fe(II)_{aq}$ values of - 0.528 ‰ and - 1.392 ‰ and $\delta^{56/54}Fe_{ppt}$ values of 0.50 ‰ and - 0.40 ‰ were extrapolated using the equilibrium fractionation factor of $\Delta_{Fe(II)aq\text{-}Fe(III)ppt}$ of 1.05 ‰, chosen value from aforementioned literature. See text for further discussion.

The $\delta^{56/54}Fe_{IRMM\text{-}014}$ values of both water and red floc samples were also fit to logarithmic curves in cross plots against total Fe contents (Figure 7-5). The iron contents of red floc samples are readily given in wt %, and the Fe contents of water samples were also set to wt % scale, calculated in terms of fractions, as described above (relative to the initial water sample Fe concentration), for the convenience of the plot. The data show very good correlation between the Fe contents and the $\delta^{56/54}Fe_{IRMM\text{-}014}$ values (R^2= 0.71 for June 2018 samples, and R^2= 0.82 for October 2014 samples). The higher Fe content and heavier $\delta^{56/54}Fe_{IRMM\text{-}014}$ values of red floc samples decrease from the source (Stollen for October 2014, and A1 for June 2018) to the creek, followed by the water samples from Stollen (October 2014) and outlet of the pond (sampling point A1), and continue to decrease towards the creek until the mixing point with the forest brook (Figure 7-5). The correlation between Fe contents and the $\delta^{56/54}Fe_{IRMM\text{-}014}$ values for water samples, dependent on the sampling points (both decreasing with increasing distance from the source), is much better as clearly shown in the cross-plots (linear

regression fits for water samples with R^2= 0.66 from October 2014, and R^2= 0.61 from June 2018, Figure 7-5). The iron isotopic compositions and Fe concentrations of red flocs lack a strong correlation, unlike the water samples.

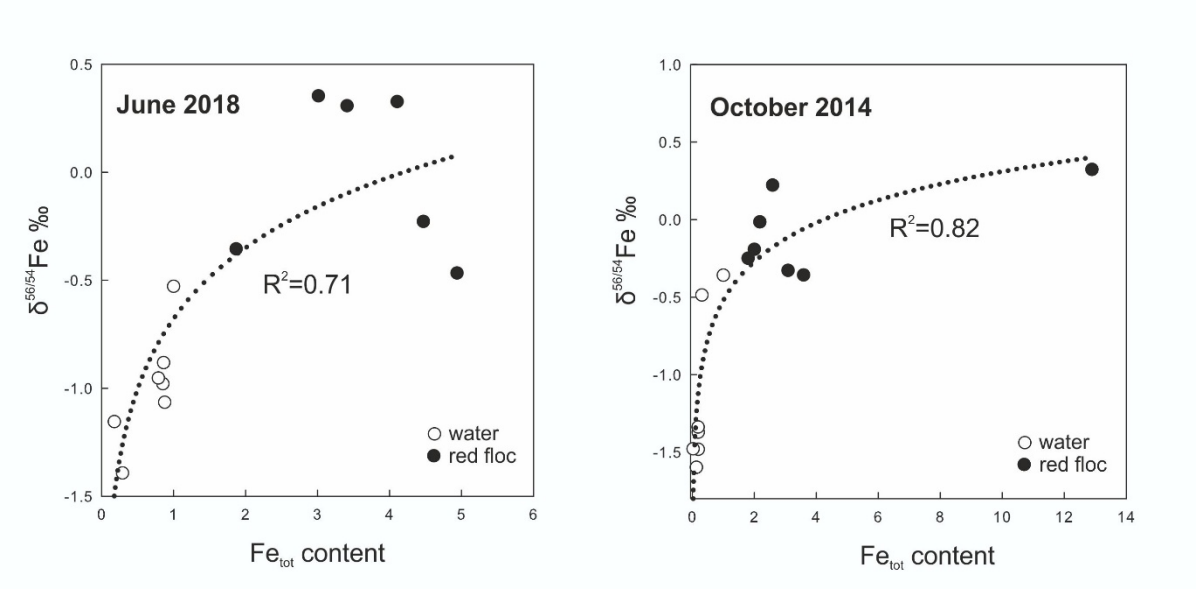

Figure 7-5. White circles are $\delta^{56/54}Fe(II)_{aq}$ (water) data and black circles are $\delta^{56/54}Fe_{ppt}$ (red floc) data. The dashed black lines are logarithmic fits for the whole dataset. Fe contents are readily given in (wt %) for the red floc data, and for the water samples Fe contents were normalized to (wt %) according to their relative fractions from the source (similar to the fraction calculations in Figures 7-3 and 7-4). The higher Fe contents and heavier $\delta^{56/54}Fe_{IRMM-014}$ values of red floc samples decrease from the source (Stollen for October 2014, and A1 for June 2018) to the creek, followed by the water samples from Stollen (October 2014) and outlet of the pond (sampling point A1), and continue to decrease towards the creek until the mixing point with the forest brook. Linear regression fits for water samples which are R^2= 0.66 from October 2014, and R^2= 0.61 from June 2018, are not shown in the figure.

This decreasing trend in stable Fe isotopic composition from the source to the pond and from pond to the creek, stems from oxidation of $Fe(II)_{aq}$ in a gradually heavy Fe depleted $Fe(II)_{aq}$ pool, following an open system, Rayleigh distillation model (Figures 7-3 and 7-4), similar to the trend observed in the depositional environment of the 2.95 Gyr old Ijzermijn IF, as discussed above. Therefore, we can find similarities in the oxidation path of the $Fe(II)_{aq}$ from the source of the Arvadi Spring to the mixing point, with the oxidation path of the $Fe(II)_{aq}$ in an Archean oxygen oasis, from the deep anoxic hydrothermal ocean source with heavier $\delta^{56/54}Fe_{IRMM-014}$ values, to the shallowest, relatively oxic surface water with lighter $\delta^{56/54}Fe_{IRMM-014}$ values (down to - 2.5 ‰, data from the Ijzermijn IF drill core DNN-1). Therefore, modern Arvadi flow path Fe isotope pattern gives an insight on the existing Fe(II) oxidation model for the Precambrian oxygen oases.

Despite the $\delta^{56/54}Fe_{IRMM-014}$ values of the red flocs remaining heavier than the $\delta^{56/54}Fe_{IRMM-014}$ values of the water samples throughout the flow system (Figure 7-6), the difference between these values do not remain stable across the sampling points from the source to the mixing point, as also shown in Figure 7-7. Thus, the decreasing trend in overall stable Fe isotopic composition from the outlet of the pond to the creek, and along the creek not being stable is another indicator for the deviation from

$Fe(II)_{aq}$ oxidation in a closed system with a single point source. The unchanging Fe concentration of the Arvadi red flocs from the pond to the creek, despite a relatively decreasing trend in the stable Fe isotopic composition (i.e. a slight decoupling between the Fe concentration and $\delta^{56/54}Fe_{IRMM\text{-}014}$ values), is a significant indicator that the Arvadi flow system is unlike a pond or a lake in which Fe concentration and stable Fe isotopic composition become relatively homogenized. The complexity of the modern Arvadi flow system shows that assuming a simple model for ancient sediment samples just based on their stable Fe isotopic composition and Fe concentrations, is an oversimplification, as there might have been inflows and outflows that modified the initial isotopic composition of the system before deposition and preservation in the marine sedimentary rocks.

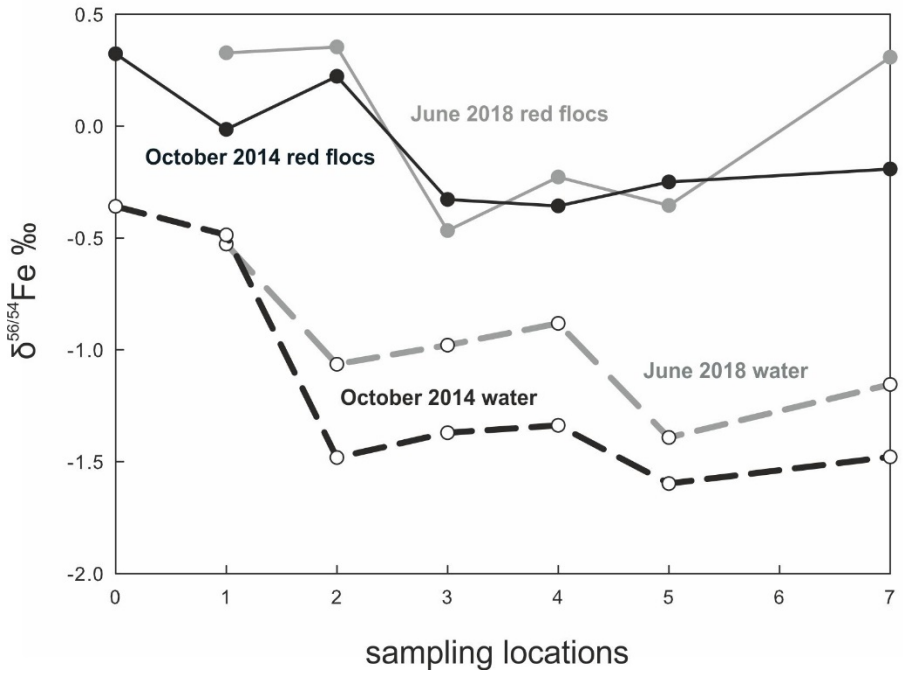

Figure 7-6. Sampling locations in x axis from 0 to 7 indicate sampling points Stollen to the 7, thus June 2018 samples start from 1, which corresponds to the sampling point A1. The solid lines indicate changing $\delta^{56/54}Fe_{IRMM\text{-}014}$ values of the red floc samples, whereas dashed lines indicate the changing $\delta^{56/54}Fe_{IRMM\text{-}014}$ values of the water samples. A general decrease in $\delta^{56/54}Fe_{IRMM\text{-}014}$ values of the water samples (both in October 2014 and June 2018) from the source to the creek is apparent. The $\delta^{56/54}Fe_{IRMM\text{-}014}$ values of the red floc samples are consistenly higher than the respective water samples, as a result of Fe(II) oxidation, however the difference between them does not remain stable and varies throughout the flow path, as a result of the open system behavior. Furthermore, there are slight differences in isotopic compositions between sampling years.

The deviations of the data from the closed system fractionation lines and the Rayleigh trendlines in the Arvadi Spring are most possibly caused by incomplete reduction of Fe(III). Fe(III) reduction is typically driven by microbes, dissimilatory iron reduction (DIR), or abiotically, by the sulfides which are produced by MSR mediated reductive dissolution at the precipitates of the Arvadi Spring (Koeksoy et al., 2018). Reduced $Fe(II)_{aq}$ becomes mobilized via DIR and then immobilized via sulfide-reduction by fixation onto Fe-sulfides (Raiswell and Canfield 1998; Butler et al., 2005). FeS minerals were recorded

in Arvadi Spring according to the Mössbauer analysis from a previous study, making the latter process plausible (Koeksoy et al., 2018).

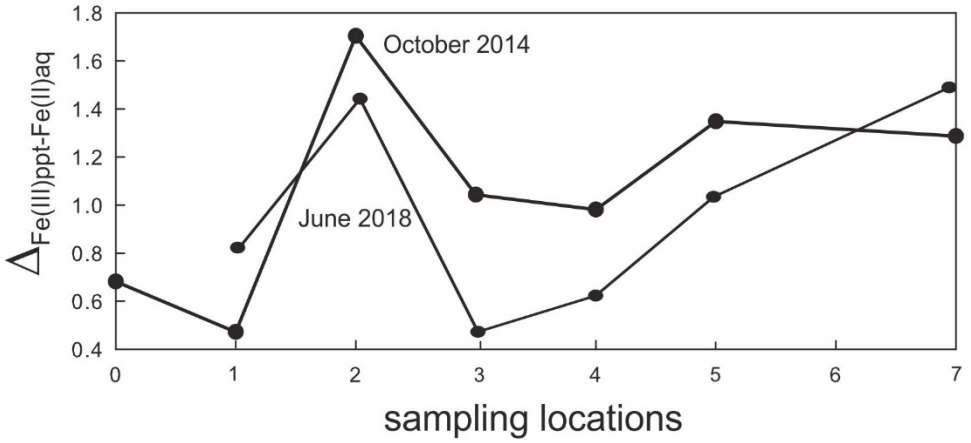

Figure 7-7. The changing $\Delta_{Fe(III)ppt\text{-}Fe(II)aq}$ values from the source (Stollen=0) to the mixing point (sampling location 7), calculated from the measured differences in $\delta^{56/54}Fe_{red\ floc}$- $\delta^{56/54}Fe_{water}$. As shown in the figure, fractionation factor varies throughout the flow path, instead a straight, stable line, due to the open system behviour.

Low $\delta^{56/54}$Fe values in bulk analyses of soils have been interpreted to reflect a combination of organically bound iron and iron that has been cycled through multiple oxidation and reduction steps (Fantle and DePaolo, 2004; Emmanuel et al., 2005). The low $\delta^{56/54}$Fe values for ferric oxides and hydroxides in modern marine sediments have been interpreted to reflect oxidation of low $\delta^{56/54}$Fe $Fe(II)_{aq}$ that was produced by microbial DIR (Severmann et al., 2006; Staubwasser et al., 2006), as experimental studies revealed that bacterial DIR generates low $\delta^{56/54}$Fe values of - 1 to - 3 ‰ for $Fe(II)_{aq}$ (Johnson et al., 2005; Yamaguchi et al., 2005). This process occurs via partial reduction of Fe oxides and oxidation of organic carbon, reacting to Fe-carbonate, typically siderite, and generating very negative $\delta^{56/54}$Fe values (Johnson et al., 2008; Heimann et al., 2010). Siderite was also recorded among minerals in precipitates of the Arvadi Spring (Koeksoy et al., 2018), which makes this process also highly plausible for the generation of the isotopically light $Fe(II)_{aq}$ and $Fe(III)_{ppt}$ in water and red floc samples. Furthermore, Fe(III) reducing anaerobes in the red flocs were reported to be among the most abundant species in the Arvadi Spring (Koeksoy et al., 2018), as pointed out earlier in section 7.1., which is an evidence for ongoing microbial DIR activity. The question whether siderites of the Precambrian sedimentary rocks record primary seawater Fe isotope signatures have been debated due to secondary diagenetic Fe redox cycling in organic-rich sediments, e.g DIR and the precipitation and dissolution of Fe(II) sulfide (Johnson et al., 2013; Matthews et al., 2004; Rouxel et al., 2006; Yamaguchi et al., 2005).

The modification of stable Fe isotopic composition in modern Arvadi Spring is recorded already during the deposition of the red flocs via biotic and abiotic Fe(III) reduction and consequent generation of isotopically lighter dissolved $Fe(II)_{aq}$ and slightly heavier $Fe(III)_{ppt}$, followed by the oxidation of this

lighter $Fe(II)_{aq}$ (biotic and abiotic) and further progressive depletion of isotopically heavy Fe in the dissolved Fe(II) pool with increasing distance from the source point, similar to the path of $Fe(II)_{aq}$ in the ancient marine systems. This combination of abiotic and biotic Fe(II) oxidation in the water and microbial Fe(III) reduction in the sediment causes the observed decoupling of Fe concentrations and $\delta^{56/54}Fe_{IRMM\text{-}014}$ values in the red flocs. The complexity of this modern spring is an indicator for the complexity of deciphering ancient marine systems in terms of Fe cycling, revealing the enigmatic nature of the past stable Fe isotopic records.

8. Summary and Conclusions

The main objectives are revisited to summarize the findings of this thesis and to present a general overview.

1) Testing whether the widely cited Cr-stable isotope and redox-sensitive elemental evidence (Crowe et al. 2013) for the late Mesoarchean oxidative weathering is a true original signal or generated by secondary overprint

A previous Cr isotope study on the 2.95 Ga old Ijzermijn IF by Crowe et al., (2013) concluded that free oxygen was already present in the atmosphere ca. 600 Ma prior to the GOE in concentrations (~ 3×10^{-4} present atmospheric levels) that enabled terrestrial oxidation of Cr(III) to Cr(VI), delivering the isotopically heavy Cr, identified in these sediments, via riverine or groundwater transport. In this study, similarly heavy Cr isotopic compositions were identified for the Ijzermijn IF, but exclusively in the lower <140 cm section of the same 4 m high White Mfolozi River outcrop, that Crowe et al., (2013) retrieved their samples from. No Cr isotopic fractionation was detected in Ijzermijn IF samples from two drill cores recovered from the White Mfolozi Inlier. Samples from the White Mfolozi River outcrop of the Ijzermijn IF, as well as from other outcrop localities (Planavsky et al., 2014a), show strong surficial weathering effects such as full dissolution of the originally abundant Fe- and Mn-carbonates and almost complete oxidation of Fe(II) and Mn(II) to Fe(III) and Mn(IV), respectively. Enrichment of other elements (e.g. U) that are soluble under oxidative conditions is restricted to the same lower section of the White Mfolozi River outcrop where heavy Cr isotope signatures are detected, but not found in any of the drill core samples. It is thus much more likely that the Cr isotopic fractionation recorded in some of Ijzermijn IF outcrop samples reflects a modern weathering effect rather than a Mesoarchean oxidative weathering process.

Furthermore, Drill core DNN-1 and PMH24/L1 samples from the Ijzermijn IF have ($^{234}U/^{238}U$) activity ratios within uncertainties of secular equilibrium and thus were not affected by modern weathering or other recent rock-water interaction processes. All White Mfolozi River outcrop samples

of the Ijzermijn IF, on the other hand, have ($^{234}U/^{238}U$) activity ratios above unity, similar to that of modern river water, while the overlying Vlakhoek member shales have ($^{234}U/^{238}U$) activity ratios below unity, which are typical of moderately weathered soils. These deviations from secular equilibrium for the White Mfolozi River outcrop Ijzermijn IF samples and Vlakhoek Member shales are clear evidences of modern disturbance of the U inventory of these rocks, calling into question their suitability for reconstructing the ancient marine redox evolution.

In the present sample set, it is inferred that percolating meteoric water preferentially leached out ^{234}U over ^{238}U from the overlying Vlakhoek Member shale unit whereas the Ijzermijn IF samples gained ^{234}U-enriched U from meteoric and river waters. However, it should be noted that the substantial U enrichment and the heavy stable Cr isotope ratios, which are only observed in the basal <140 cm section of the White Mfolozi River outcrop do not directly correlate with the magnitude of the deviation in the ($^{234}U/^{238}U$) activity ratio from secular equilibrium, and thus U enrichment cannot be reduced to a single source. Nevertheless, ($^{234}U/^{238}U$) activity ratios are a very strong tool to test whether redox signals in ancient rocks are primary or have been imprinted by exposure to the modern oxidized atmosphere.

2) The reconstruction of paleoredox conditions in the depositional environment of the Ijzermijn IF as a potential Mesoarchean *oxygen oasis*

The $\delta^{98/95}Mo$ values and Fe/Mn ratios are higher in outcrop compared to drill core samples from Planavsky et al. (2014a), however, this signature cannot be attributed to modern weathering by analogy without further data, especially considering that these outcrop samples are from higher elevation and do not show heavy stable Cr isotopic compositions (Planavsky et al., 2014a). As such the heavy $\delta^{98/95}Mo$ values and elevated Fe/Mn ratios reported for outcrop samples by Planavsky et al. (2014a) might still be original fingerprints due to different depositional environments for outcrop and drill core samples. It would, however, be desirable to measure ($^{234}U/^{238}U$) on these outcrop samples to assess potential alteration by modern weathering. Similarly**,** the slightly higher $\delta^{56/54}Fe_{IRMM\text{-}014}$ values as well as the stable Mo isotopic composition of the White Mfolozi River bed outcrop in this study do not necessarily reflect modern weathering alone, as there is no significant correlation with ($^{234}U/^{238}U$).

Oxygen oasis before the Great Oxidation Event (GOE) have been reported from Meso- and Neoarchean (3.2 to 2.8 Ga) shallow marine depositional environments (Eickmann et al., 2018; Planavsky et al., 2014a; Satkoski et al., 2015). Particularly, the 2.95-2.8 Ga Pongola Basin has been subject to various studies that investigated its redox conditions and potential as a pre-GOE oxygen oasis (Alexander et al., 2008; Crowe et al., 2013; Eickmann et al., 2018; Ossa et al., 2016; Planavsky et al., 2014a). Octahedrally coordinated, isotopically light Mo preferentially adsorbed onto the MnO_2

particles, leading to a lighter Mo isotopic composition in the proximally deposited IF, where the Mn-flux was the highest. In contrast, the sediments deposited in distal settings have a heavier stable Mo isotopic signature, and contain less MnO. Thus, the evidence from this study shows that iron oxide precursors of the early diagenetic iron- manganese carbonates of the Ijzermijn IF partly formed by partial oxidation of Fe(II) with dissolved O_2 generated by cyanobacteria in seawater, and mainly by abiotic oxidation of $Fe(II)_{aq}$ by Mn(IV)-oxide particle shuttling at the Mn-chemocline of the water column, under redox-stratified conditions in an *oxygen oasis*. In this study of the 2.95 Ga Ijzermijn IF, the MnO_2 shuttling model previously reported for the 2.46 Ga old Koegas IFs (Kurzweil et al., 2016) is extended to very shallow-marine, near-shore IF depositional settings.

3) Comparison of the stable Fe isotopic evidence from a potential Mesoarchean oxygen oasis with a modern analog depositional environment

From the stable Fe isotopic perspective, depositional model for the Ijzermijn IF shows that upwelling and partial oxidation of deep water $Fe(II)_{aq}$ directly by seawater O_2 and MnO_2 particles, led to the depletion of heavy Fe isotopes in the remaining $Fe(II)_{aq}$ pool at the shallower water depths (Rouxel et al., 2005), leading to increasingly lighter $\delta^{56/54}Fe_{IRMM\text{-}014}$ values along the way from the redoxcline to paleoshoreline. Hence, iron oxides with lighter $\delta^{56/54}Fe_{IRMM\text{-}014}$ values had precipitated in the heavy Fe depleted, MnO_2 rich upper water column in a shallower setting, whereas the ones with heavier $\delta^{56/54}Fe_{IRMM\text{-}014}$ values had precipitated in a more distal setting. The iron from Ijzermijn IF follows a Rayleigh distillation trend from the hydrothermal source to the shallow water, until its precipitation in this Mesoarchean oxygen oasis.

The significantly higher Fe concentration, and heavier $\delta^{56/54}Fe_{IRMM\text{-}014}$ values of the red flocs compared to the water in the mixing shaft, outlet, pond and the creek, indicate $Fe(II)_{aq}$ oxidation, either biotically or abiotically, and eventual precipitation of iron oxide species in the Arvadi system. However, the iron in modern Arvadi Spring follows a similar Rayleigh distillation trend from its source, to the outlet, along its flow path, mimicking the depositional environment of the 2.95 Gyr Ijzermijn IF. Furthermore, the data from Arvadi show decoupling of Fe concentrations and $\delta^{56/54}Fe_{IRMM\text{-}014}$ values in the red flocs, and deviations from the closed system fractionation lines and the Rayleigh trendlines, which are most possibly caused by incomplete reduction of Fe(III) by DIR. Fe(III) reducing anaerobes in the red flocs were reported to be among the most abundant species in the Arvadi Spring (Koeksoy et al., 2018). Arvadi system can be modeled as a combination of biotic and abiotic Fe(III) reduction and consequent generation of isotopically lighter dissolved $Fe(II)_{aq}$, followed by the oxidation of this lighter $Fe(II)_{aq}$ (biotic and abiotic) and further progressive depletion of heavy Fe in the remaining dissolved Fe(II) pool along the flow path with increasing distance from the source point, similar to the path of

$Fe(II)_{aq}$ from the hydrothermal source to the shallow ocean in the ancient marine systems. The lighter Fe isotopic composition in red flocs of Arvadi, despite production of isotopically heavier $Fe(III)_{ppt}$ during to microbial Fe(III) reduction, implies that the light Fe isotopic composition of 2.95 Gyr old Ijzermijn IF might partly reflect the lighter $\delta^{56/54}Fe_{IRMM\text{-}014}$ values of the seawater $Fe(II)_{aq}$ that was recycled by a similar DIR activity in the ancient environment and became further depleted in isotopically heavy Fe.

The complexity of the modern Arvadi flow system shows the complexity of the ancient marine depositional systems, as it is difficult to constrain inflows and outflows that modified the initial isotopic composition of the system before deposition and preservation in the marine sedimentary rocks.

Appendices

Trace element method precision and reference material data

Repeated measurements (m) over several experiments on multiple digestions (d) of four geochemical reference materials, the United States Geological Survey (USGS) basalts BIR-1 (d=7; m=46) and BHVO- 2 (d=6; m=38), the shale OU-6 (d=4; m=12), and the iron formation IF-G (d=3; m=7), were undertaken to monitor intermediate method precision over 2 years and assess accuracy. The mean concentration data and selected mass ratios (Y/Ho, Nb/Ta, Zr/Hf, Th/U, Sm/Nd) with % r.s.d (1s) determined with the rock calibrated Q-ICP-MS technique are provided in Table A1 for each standard, along with the preferred USGS W-2a concentrations used for calibration. Data are compared to previously published values using the same technique and GeoReM preferred/compiled or certified values, where appropriate. Excellent method reproducibility is found for most elements apart from those known to be variably heterogeneous in the USGS standards (Sb, Mo, Pb) and excellent agreement with external data sets is demonstrated. For elements like Pb, it is clear that any bias check and the method precision is not well represented by the mean and uncertainty reported for Pb in BHVO-2, where individual digests show better consistency (e.g., multiple measurements of three separate digests show separate but repeatable abundances in ppb 1832 ± 41, 2602 ± 29, and 1527 ± 86) and reveal the powder heterogeneity. Additional information and references are provided in the table footnote. A notable exception in bias is the concentration of Cr in IF-G. This study finds a reasonably consistent value of 4383 ± 258 ppb that has a statistically significant bias relative to the concentration of 3348 ppb reported by Frei et al., (2016) by 31%. However, both of these values are substantially lower than the concentration of 17650 ppb reported by Bolhar et al., (2004; 2015) that was determined using a similar method to that of this study. The discrepancy in concentrations could point to powder heterogeneity that needs to be further addressed at the level of separate splits in future studies.

		Standard	BIR-1						
		Source	UT		LU[a]			GeoReM[b]	
		# Digestions	7						
	*W-2 calibration values**	# Analyses	46	%RSD		%RSD	UT/LU		UT/GeoReM
Li	*9158*		3114	1.4	3136	1.2	0.99	3203	0.97
Be	*617.5*		91.5	3.6	93.4	3.5	0.98	102	0.90
Sc	*36074*		44520	1.5	44500	1.4	1.00	43210	1.03
Ti	*6354611*		5830000	3.4	5790000	1.2	1.01	5746000	1.01
V	*261597*		326800	2.3	322500	1.1	1.01	320600	1.02
Cr	*92791*		411600	1.2	410600	1.8	1.00	392900	1.05
Mn	*1293000*		1277000	2.0				1341000	0.95
Co	*44526*		53150	1.1	53330	1.1	1.00	52220	1.02
Ni	*69993*		169700	1.1	171200	1.9	0.99	168900	1.00
Cu	*103000*		117100	1.2	119500	1.7	0.98	120700	0.97
Zn	*77000*		70960	1.4	70730	2.3	1.00	70400	1.01
Ga	*17424*		15350	1.3	15430	1.0	0.99	15460	0.99
As*	*1260*		71.7	11.2	146.7	12.0	0.49	170	0.42
Rb	*19803*		192.7	3.1	193.8	3.0	0.99	210	0.92
Sr	*194828*		108600	1.2	109500	1.0	0.99	108600	1.00
Y	*20113*		14720	1.7	14660	1.1	1.00	15600	0.94
Zr	*87866*		14200	1.9	14600	2.3	0.97	14800	0.96
Nb	*7275*		534.5	1.2	534.8	1.2	1.00	553	0.97
Mo^	*423.3*		43.27	15.3	43.75	45	0.99	68	0.64
Ag	*77*		40.3	15				41	0.98
Cd	*77*		58.8	7.3	65.17	7.5	0.90	77	0.76
Sn	*1950*		730	7.4	815.3	9.0	0.90	701	1.04
Sb*,^	*800*		467	6.4	536.5	14	0.87	462	1.01
Cs	*888.2*		4.83	4.4	5.05	4.9	0.96	6.46	0.75
Ba	*169680*		6482	1.4	6599	3.5	0.98	6750	0.96
La	*10521*		599.6	1.5	604.3	1.2	0.99	627	0.96

Ce	*23216*	1891	1.4	1900	1.4	1.00	1920	0.98
Pr	*3025*	375.9	1.5	378.2	1.1	0.99	372.3	1.01
Nd	*12911*	2366	1.4	2382	1.1	0.99	2397	0.99
Sm	*3266*	1100	1.6	1099	1.1	1.00	1113	0.99
Eu	*1094*	520.5	1.4	524.6	0.8	0.99	520.1	1.00
Gd	*3708.2*	1877.0	1.3	1874	1.1	1.00	1809	1.04
Tb	*615*	364.7	1.3	365.4	0.9	1.00	362.3	1.01
Dy	*3808*	2544	1.4	2543	1.1	1.00	2544	1.00
Ho	*803.3*	585.6	1.4	583.2	1.0	1.00	571.8	1.02
Er	*2222*	1708	1.3	1701	0.9	1.00	1680	1.02
Tm	*327.2*	258.6	1.6	258.5	0.9	1.00	255.8	1.01
Yb	*2058*	1661	1.5	1663	0.9	1.00	1631	1.02
Lu	*301.3*	248.9	1.8	248.2	1.0	1.00	248.4	1.00
Hf	*2356*	560	2.0	570.7	1.4	0.98	582.2	0.96
Ta	*454.2*	37.28	3.4	37.01	1.4	1.01	41.4	0.90
W	*240*	5.61	24	5.96	9.5	0.94	27	0.21
Tl	*94*	1.27	8.9	1.25	7.5	1.02	2.1	0.60
Pb^	*7528*	2828	4.0	3268	15	0.87	3037	0.93
Th	*2104*	29.66	2.3	29.37	4.0	1.01	32.8	0.90
U	*505*	10.32	3.2	10.09	2.1	1.02	10.51	0.98
Y/Ho		25.13	1.4	25.17	0.8	1.00		
Nb/Ta		14.38	2.9	14.49	1.1	0.99		
Zr/Hf		25.34	1.7	25.55	1.3	0.99		
Th/U		2.876	3.7	2.871	4.1	1.00		
Sm/Nd		0.4648	0.9					

		Standard	BHVO-2						
		Source	UT		LU[a]			GeoReM[b]	
	*W-2 calibration values**	# Digestions # Analyses	6 38	%RSD		%RSD	UT/LU		UT/GeoReM
Li	*9158*		4462	2.5	4496	0.7	0.99	4500	0.99
Be	*617.5*		1003.0	4.7	1004	3.5	1.00	1076	0.93
Sc	*36074*		32350	1.2	32120	1.1	1.01	31830	1.02
Ti	*6354611*		16460000	3.1	16480000	1.1	1.00	16370000	1.01
V	*261597*		319600	2.5	314800	1.2	1.02	318200	1.00
Cr	*92791*		304100	1.5	299100	1.4	1.02	287200	1.06
Mn	*1293000*		1295000	3.4			0.00	1309000	0.99
Co	*44526*		45510	1.1	45300	1.3	1.00	44890	1.01
Ni	*69993*		118800	1.3	117900	1.0	1.01	119800	0.99
Cu	*103000*		127000	1.3	125500	2.1	1.01	129300	0.98
Zn	*77000*		103800	3.2	102400	3.0	1.01	103900	1.00
Ga	*17424*		21010	1.2	21090	0.8	1.00	21370	0.98
As*	*1260*		929	12.7	1032	3.4	0.90	700	1.33
Rb	*19803*		9120	1.0	9161	1.0	1.00	9261	0.98
Sr	*194828*		394900	1.1	394900	1.1	1.00	394100	1.00
Y	*20113*		24300	1.7	24300	0.7	1.00	25910	0.94
Zr	*87866*		165400	1.4	169600	1.6	0.98	171200	0.97
Nb	*7275*		18290	1.6	18300	0.9	1.00	18100	1.01
Mo^	*423.3*		3326	17.0	4541	19	0.73	4070	0.82
Ag	*77*		110.2	12.3				89	1.24
Cd	*77*		113.3	4.5	115.2	5.7	0.98	152	0.75
Sn	*1950*		1824	6.1	1928	5.6	0.95	1776	1.03
Sb*,^	*800*		105.60	18	101.5	16	1.04	103.4	1.02

Cs	*888.2*	95.95	2.7	96.67	1.7	0.99	99.6	0.96
Ba	*169680*	131000	1.4	131300	0.7	1.00	130900	1.00
La	*10521*	15140	1.7	15190	0.7	1.00	15200	1.00
Ce	*23216*	37600	1.6	37760	1.0	1.00	37530	1.00
Pr	*3025*	5376	1.5	5383	0.7	1.00	5339	1.01
Nd	*12911*	24340	1.6	24360	0.6	1.00	24270	1.00
Sm	*3266*	6067	1.7	6059	0.6	1.00	6023	1.01
Eu	*1094*	2048	1.6	2050	0.6	1.00	2043	1.00
Gd	*3708.2*	6230.0	1.8	6210.0	0.7	1.00	6207.0	1.00
Tb	*615*	938	1.9	934.0	0.7	1.00	939.2	1.00
Dy	*3808*	5235	1.6	5228	0.7	1.00	5280	0.99
Ho	*803.3*	1000	1.4	997.8	0.6	1.00	988.7	1.01
Er	*2222*	2517	1.3	2502	0.6	1.01	2511	1.00
Tm	*327.2*	339.6	1.4	338.7	0.7	1.00	334.9	1.01
Yb	*2058*	1987	1.4	1984	0.6	1.00	1994	1.00
Lu	*301.3*	274	1.4	273.9	0.7	1.00	275.4	0.99
Hf	*2356*	4261	1.3	4335	1.2	0.98	4470	0.95
Ta	*454.2*	1134	2.3	1144	0.8	0.99	1154	0.98
W	*240*	193	5.8	192	2.3	1.01	251	0.77
Tl	*94*	20.17	2.4	19.33	1.1	1.04	22.4	0.90
Pb^	*7528*	1836	25	1530	11	1.20	1653	1.11
Th	*2104*	1196	3.2	1179	1.1	1.01	1224	0.98
U	*505*	427	2.2	420.5	1.0	1.02	412	1.04
Y/Ho		24.27	1.0	24.37	0.7	1.00		
Nb/Ta		16.30	2.5	15.98	0.7	1.02		
Zr/Hf		38.86	1.1	39.08	0.9	0.99		
Th/U		2.801	1.4	2.802	1.1	1.00		
Sm/Nd		0.2495	0.6	0.2487	0.5	1.00		

		Standard	OU-6			
		Source	UT		Certified[c] or GeoReM[d]	
		# Digestions	4			
	*W-2 calibration values**	# Analyses	12	%RSD		UT/Certified
Li	*9158*		101700	5.8	95300[d]	1.07
Be	*617.5*		2458	3.6	2530[d]	0.97
Sc	*36074*		23400	3.2	23100	1.01
Ti	*6354611*		5765000	2.2	5934000	0.97
V	*261597*		123200	1.8	129800	0.95
Cr	*92791*		71630	4.0	70700	1.01
Mn	*1293000*					
Co	*44526*		28370	3.2	29200	0.97
Ni	*69993*		38720	2.0	40200	0.96
Cu	*103000*		40220	8.8	40400	1.00
Zn	*77000*		109900	1.6	111400	0.99
Ga	*17424*		23770	1.7	24170	0.98
As*	*1260*		14890	6.6	13230	1.13
Rb	*19803*		123800	3.1	121300	1.02
Sr	*194828*		131300	1.4	131700	1.00
Y	*20113*		25910	1.7	27750	0.93
Zr	*87866*		155400	6.6	174200	0.89
Nb	*7275*		14460	2.3	14490	1.00
Mo^	*423.3*		468	9.0		
Ag	*77*					
Cd	*77*					
Sn	*1950*		2605	2.4	2670	0.98
Sb*,^	*800*		521.0	2.3	560[d]	0.93
Cs	*888.2*		8141	0.7	8100	1.01
Ba	*169680*		479400	1.3	480000	1.00
La	*10521*		33490	1.9	33200	1.01
Ce	*23216*		80810	2.5	77100	1.05
Pr	*3025*		8204	1.9	7910	1.04
Nd	*12911*		30590	1.8	30200	1.01

Sm	*3266*	6060	1.8	6010	1.01
Eu	*1094*	1347	1.8	1360	0.99
Gd	*3708.2*	5304.0	1.9	5300	1.00
Tb	*615*	840.9	1.7	860	0.98
Dy	*3808*	5011	1.9	5060	0.99
Ho	*803.3*	1047	2.1	1040	1.01
Er	*2222*	2978	2.0	2930	1.02
Tm	*327.2*	462.1	1.9	450	1.03
Yb	*2058*	3031	1.5	2980	1.02
Lu	*301.3*	456.0	1.6	450	1.01
Hf	*2356*	4274	5.7	4700	0.91
Ta	*454.2*	951.8	1.9	1020	0.93
W	*240*	1205	3.5		
Tl	*94*	535.5	2.4	540	0.99
Pb^	*7528*	27130	3.0	28800	0.94
Th	*2104*	10940	3.6	11300	0.97
U	*505*	1913	2.9	1920	1.00
Y/Ho		24.77	1.2		
Nb/Ta		15.45	1.8		
Zr/Hf		36.34	2.1		
Th/U		5.718	1.5		
Sm/Nd		0.1981	0.5		

		Standard	IF-G							
		Source	UT		Literature 1[e,f]			Literature 2[g]		
		# Digestions	3		2					
	*W-2 calibration values**	# Analyses	7	%RSD	3	%RSD	UT/Literature 1		%RSD	UT/Literature 2
Li	*9158*		198.9	9.3	225[f]		0.88			
Be	*617.5*		4345	1.9			0.00			
Sc	*36074*		269.9	6.9	284.6	3.2	0.95	751.4	37	0.36
Ti	*6354611*		21876	6.0	11200[f]		1.95	16228.3	7.3	1.35
V	*261597*		1768	3.2	1662[f]		1.06	21369	10	0.08
Cr	*92791*		4384	5.9	17645	1.2	0.25	3348	3.9	1.31
Mn	*1293000*		331393	0.2				217337	4.0	1.52
Co	*44526*		29417	2.1				19327	4.1	1.52
Ni	*69993*		24504	2.3	23856	0.2	1.03	17871	3.3	1.37
Cu	*103000*		9008	4.3	8596[f]		1.05	6531	14	1.38
Zn	*77000*		20879	6.8	21560[f]		0.97	14810	6.8	1.41
Ga	*17424*		639.1	2.3	1409[f]		0.45	582.2	4.1	1.10
As*	*1260*		1513	9.8						
Rb	*19803*		287.7	2.2	290.9	0.3	0.99	322.1	6.1	0.89
Sr	*194828*		3572	8.5	3610	0.6	0.99	3619	6.5	0.99
Y	*20113*		8940	2.6	9135	0.5	0.98	9809	7.6	0.91
Zr	*87866*		701.3	11.8	563.7	1.4	1.24	472.8	13	1.48
Nb	*7275*		96.60	5.5	98.9	0.4	0.98	170.6	9.6	0.57
Mo^	*423.3*		487.6	2.9				515.6	8.0	0.95
Ag	*77*									
Cd	*77*									
Sn	*1950*									
Sb*,^	*800*		551.0	7.6						
Cs	*888.2*		58.59	2.1	62.3	1.3	0.94	53.82	5.9	1.09

Ba	*169680*	1995	5.8	2024	0.3	0.99	2752	9.0	0.72
La	*10521*	2520	3.4	2706	0.5	0.93	2578	10	0.98
Ce	*23216*	3704	3.0	3902	0.3	0.95	3787	8.5	0.98
Pr	*3025*	412.4	2.5	430.2	0.4	0.96	424.3	8.1	0.97
Nd	*12911*	1698	2.2	1731	0.9	0.98	1819	8.0	0.93
Sm	*3266*	383.7	2.5	399	0.6	0.96	405.1	9.0	0.95
Eu	*1094*	359.8	1.7	362.1	0.4	0.99	360.8	8.4	1.00
Gd	*3708.2*	666.3	1.3	666.9	1.2	1.00	669.3	8.4	1.00
Tb	*615*	109.6	1.3	112.3	0.8	0.98	110.3	7.9	0.99
Dy	*3808*	787.5	2.1	791.4	1.7	1.00	840.0	7.2	0.94
Ho	*803.3*	203.6	0.8	206.6	0.5	0.99	198.3	7.4	1.03
Er	*2222*	624.6	1.4	618.8	0.6	1.01	628.6	6.6	0.99
Tm	*327.2*	91.68	1.1	92.3	0.4	0.99	92.24	6.5	0.99
Yb	*2058*	572.8	1.0	580.2	1.4	0.99	559.6	6.7	1.02
Lu	*301.3*	90.66	1.1	90.4	2.3	1.00	90.86	4.4	1.00
Hf	*2356*	17.21	10.6	18.2	0.6	0.95	19.36	13	0.89
Ta	*454.2*	169.1	1.1	171.5	0.2	0.99	187.2	6.9	0.90
W	*240*	0	0.0						
Tl	*94*	10.12	9.8						
Pb^	*7528*	2418	2.3	2518	1.5	0.96	2904	9.2	0.83
Th	*2104*	42.40	1.5	43.4	3.2	0.98	44.61	5.9	0.95
U	*505*	20.80	2.1	21.3	2.5	0.98	23.59	8.5	0.88
Y/Ho		44.46	1.6	44.23	0.5	1.01	49.46	1.0	0.90
Nb/Ta		0.557	2.0	0.577	0.6	0.97	0.911	4.9	0.61
Zr/Hf		40.51	3.0	30.97	1.6	1.31	24.81	19	1.63
Th/U		2.035	2.6	2.037	3.4	1.00	1.895	4.8	1.07
Sm/Nd		0.2259	1.0						

Footnotes:

a Values from Laurentian University (LU) determined on a Thermo X Series II compiled from: Kamber (2009); Babechuk et al. (2010; 2015); Babechuk and Kamber (2011)

b Reference or information values from GeoReM as reported in Jochum et al. (2016)

c Certified reference values reported in Kane (2004; 2005)

d GeoReM (http://georem.mpch-mainz.gwdg.de) preferred values as of July 2016 for elements not reported in certified list

e Average concentration and calculated ratio from 3 measurements of 2 digests reported in Bolhar et al. (2004)

f Concentrations from Kamber et al. (2004) for elements not reported in Bolhar et al. (2004)

g Average concentration and %RSD calculated from five measurements of IF-G reported in Frei et al. (2016)

***** Preferred calibration values for As and Sb updated based on experiments of Baldwin et al. (2012) with all LU data previously reported adjusted for these elements accordingly

^ Values in BHVO-2 express heterogeneity between individual digests compiled from Tübingen laboratory (see accompanying discussion).

		Standard	GS-N				Sco-1			
		Source	UT		Certified[a]		UT		Certified[b]	
		# Digestions	3				3			
	*W-2 calibration values**	# Analyses	7				14			
				%RSD		UT/Certified		%RSD		UT/Certified
SiO_2	*52.70*		66.40	2.1	65.80	1.01	63.39	3.1	62.80	1.01
Al_2O_3	*15.50*		14.63	1.0	14.67	1.00	13.88	2.5	13.7	1.01
Fe_2O_{3tot}	*10.80*		3.87	3.3	3.75	1.03	5.12	3.4	5.13	1.00
TiO_2	*1.06*		0.643	1.9	0.680	0.95	0.585	3.0	0.630	0.93
MnO	*0.167*		0.053	3.2	0.056	0.95	0.051	3.3	0.053	0.96
MgO	*6.37*		2.20	1.0	2.30	0.96	2.68	2.1	2.72	0.99
CaO	*10.90*		2.83	11.7	2.50	1.13	2.74	3.8	2.62	1.05
Na_2O	*2.20*		3.67	1.7	3.77	0.97	0.902	2.2	0.900	1.00
K_2O	*0.626*		4.68	7.4	4.63	1.01	2.86	6.6	2.77	1.03
P_2O_5	*0.140*		0.245	15.5	0.280	0.88	0.195	11.6	0.210	0.93

Table A2. S-Q-ICP-MS concentration data (ng g-1) and uncertainty (1σ SD) for four rock standards (GS-N, Sco-1, OU-6, IF-G) determined at University of Tuebingen (UT) and compared with certified and compiled values (continued below).

		Standard	OU-6				IF-G*			
		Source	UT		Certified[c]		UT		Certified[a]	
		# Digestions	1				2			
	*W-2 calibration values**	# Analyses	6				6			
				%RSD		UT/Certified		%RSD		UT/Certified
SiO_2	*52.70*		57.05	6.7	57.35	0.99	40.32	5.1	41.20	0.98
Al_2O_3	*15.50*		20.36	1.8	20.45	1.00	0.13	0.9	0.15	0.89
Fe_2O_{3tot}	*10.80*		8.84	1.7	8.94	0.99	55.95	0.6	55.85	1.00
TiO_2	*1.06*		0.954	2.7	0.990	0.96	0.004	89.1	0.140	0.03
MnO	*0.167*		0.274	2.1	0.280	0.98	0.038	1.8	0.042	0.90
MgO	*6.37*		2.37	2.1	2.41	0.98	1.92	0.8	1.89	1.02
CaO	*10.90*		0.900	6.6	0.740	1.22	1.50	5.1	1.55	0.97
Na_2O	*2.20*		1.71	2.2	1.76	0.97	0.032	39.1	0.032	1.00
K_2O	*0.626*		3.10	7.2	3.03	1.02	0.046	89.1	0.012	3.83
P_2O_5	*0.140*		0.116	33.2	0.120	0.97	0.073	28.1	0.063	1.16

Footnotes:
a Reference values from CRPG (http://helium.crpg.cnrs-nancy.fr/SARM/pages/geostandards.html#) as of July 2016
b Reference values from USGS (http://crustal.usgs.gov/geochemical_reference_standards/pdfs/codyshale.pdf) as of July 2016
c Reference values from Kane (2004) Geostandards and Geoanalytical Research 28(1): 53-80
*IF-G is suspected to sample heterogeneities based on nugget effects explaining the somewhat lower external reproducibilities for some elements

Digestion type	Cr (µg/g)	$\delta^{53/52}Cr_{SRM979}$	2SE
Table-top 1	4.06	-0.036	0.012
		-0.032	0.013
Table-top 2	3.48	-0.028	0.012
		-0.035	0.012
Table-top 3	3.60	-0.032	0.013
		-0.037	0.014
Bomb 1	4.31	-0.050	0.012
Bomb 2	3.46	-0.031	0.015
Bomb 3	3.54	-0.011	0.019
Average	**3.74**	**-0.032**	
	0.36 (1 s.d)	**0.020 (2 s.d)**	

*IF-G: Iron formation Isua, Greenland, 3.8 Ga
**MC-ICP-MS stable Cr isotope and Cr concentration data (µg g-1) and uncertainty (2 s.d and 1 s.d respectively) for the rock standard (IF-G) determined at University of Tuebingen (UT)

Table A3. Stable Cr isotopic composition of rock reference material IF-G (above).

Mineralogical characterization of the samples from the Ijzermijn IF

X-Ray diffraction (XRD) was used on samples for mineralogical characterization in Department of Geology in University of Johannesburg. Powdered samples were hand-pressed in sample holder that caused preferred orientation of any platy components. Identification of mineral components were possible above approximately 3 wt % of mineral in the total assemblage (mineral mixture). The measurements were operated under Cu-radiation, with generator settings at 40kV/40mA and with a monochromator. For most of the samples, scan length was 5 to 80° 2θ, and few other samples had a scan length of 90° 2θ. All the minerals identified in the samples are presented in Table A4.

Table A4. Ijzermijn IF –mineral assemblages identified

Sample label	Colour of powdered sample	Major minerals (>20 wt. %)	Subordinate (minor) minerals (<20 to ~5% wt. %)	Trace components (<5 wt. %)
594	Green	Clinochlore>chamosite> quartz	—	—
530	Green	Clinochlore > quartz	Chamosite	—
450	Green	Chlorite > quartz	Chamosite	—
385	D-brown	Quartz	Magnetite > hematite	Goethite
382	Brown	Quartz > chlorite	Magnetite > hematite	Goethite
378	Brown	Quartz > chlorite	Magnetite > hematite	Goethite
358	Brown	Quartz >>	Magnetite > goethite + chlorite	Hematite
350	Brown	Quartz > chlorite	Magnetite	Hematite + goethite

335	Brown	Quartz >>	Magnetite > chlorite	Goethite
305	Pale brown	Quartz >>	Magnetite > hematite	Goethite
250	D-brown	Quartz >>	Magnetite > hematite > (todorokite?)	Goethite
192	Red-brown	Quartz >>	Hematite	Magnetite (+goethite?)
190	Brown	Quartz >>	Magnetite > hematite	—
174	Brown	Quartz	Goethite > magnetite > hematite	Chlorite
140	Brown	Quartz	Magnetite > hematite	(Goethite)
138 top	Red	Quartz	Hematite > magnetite	—
138 mid	Brown	Quartz	Hematite > magnetite	—
113	Red-brown	Quartz >>	Hematite	(Siderite ?)
105	Red	Quartz >>	Hematite	—
100	Red	Hematite > quartz	—	(Ilmenite ?)
90	Red	Quartz	Hematite	Magnetite (jacobsitic?)
80	Red	Quartz	Hematite > chlorite	—
0-base	Red	Quartz	Hematite > chlorite	—

Supplementary figures

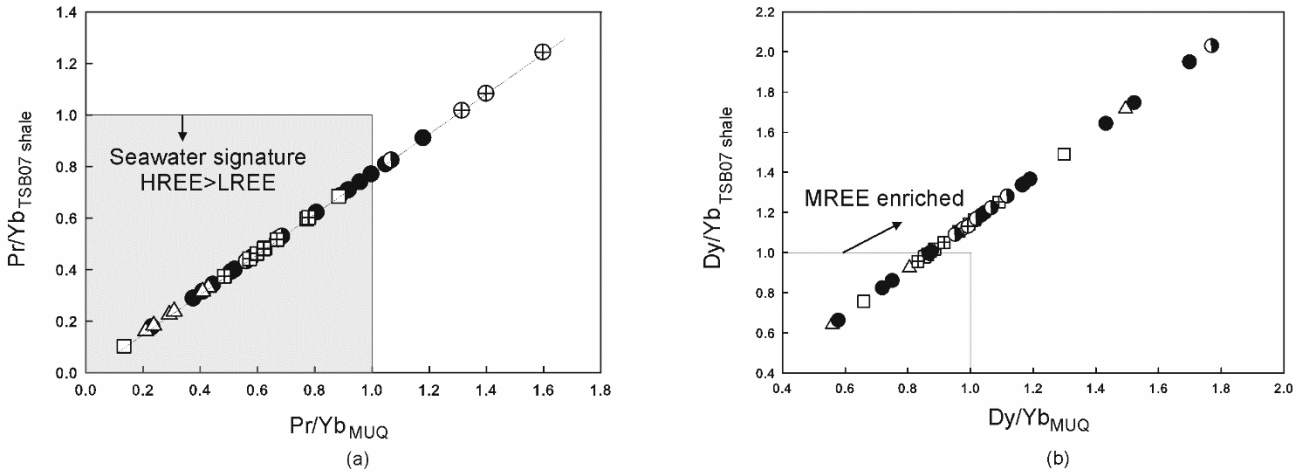

Supplementary Figure 1. Comparison of Pr/Yb **(a)** and Dy/Yb **(b)** ratios normalized to the calculated TSB07 shale average (Bolhar et al., 2015) and modern sediment average upper crustal composite known as MuQ (Kamber et al., 2005) for all IF and shale samples (symbols as per Figure 2 in the main text). Normalization to TSB07, a local shale composition, shows more LREE/HREE depleted REE patterns and better expresses the MREE enrichment of the IF, a feature that is known from the chemical sedimentary rocks of the area (Alexander et al., 2008; Bolhar et al., 2015). When normalized to the TSB07 shale, all IF samples plot to Pr/Yb ratios <1, an expected REE feature developed in marine waters relative to their source rocks during chemical weathering and hydrous transport prior to sequestration in IF. This comparison suggests that the normalization to the local shale average more accurately represents the chemical weathering flux into the Mozaan basin during its evolution.

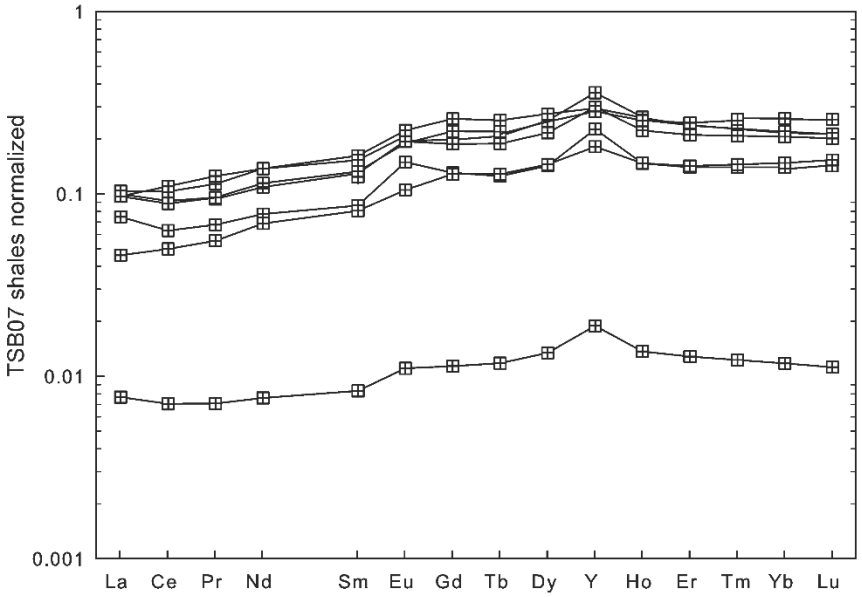

Supplementary Figure 2. REE+Y patterns of the drillcore WV006 of the Scotts Hill IF normalized to the TSB07 drillcore shale average from the Sinqeni Formation (Bolhar et al., 2015; denoted as SN). One sample, WV006-92, has a significantly higher Si content and is notably depleted in REE+Y relative to other samples from the drillcore. Six of the 9 samples contain no Ce anomaly, whereas 3 exhibit a positive Ce anomaly (see Figure 5a and 5b). The latter 3 samples are from the uppermost, hematite altered part of the IF.

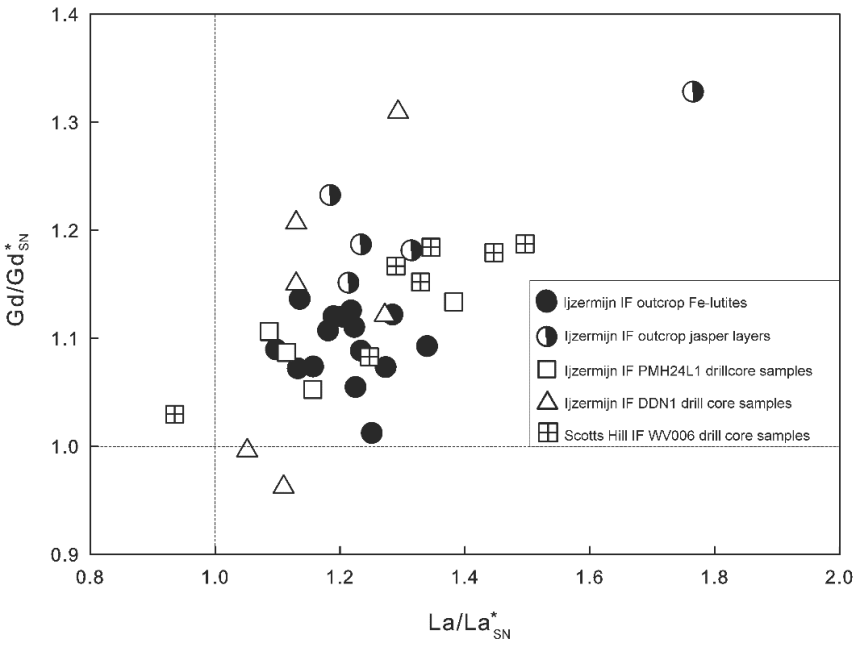

Supplementary Figure 3. All outcrop and drill core samples of Ijzermijn and Scotts Hill IF show positive La and Gd anomalies (>1), with the exception of one Scotts Hill IF drill core sample that has slightly lower $(Gd/Gd^*)_{SN}$ and two Ijzermijn IF drill core Fe-lutite samples with slightly lower $(La/La^*)_{SN}$. All elements are normalized to shale average TSB07 (Bolhar et al., 2015), denoted as SN, and anomaly calculations are according to Lawrence & Kamber (2006), whereby Gd* = [Tb x (Tb/Dy)] and La* = Pr x $(Pr/Nd)^2$

References

Alexander B.W., Bau M., Andersson P. and Dulski P. (2008) Continentally-derived solutes in shallow Archean seawater: Rare earth element and Nd isotope evidence in iron formation from the 2.9 Ga Pongola Supergroup, South Africa. *Geochimica Et Cosmochimica Acta* **72**, 378-394.

Algeo T. J., & Tribovillard N. (2009) Environmental analysis of paleoceanographic systems based on molybdenum–uranium covariation. *Chemical Geology* **268(3-4)**, 211-225.

Alibo D.S. and Nozaki Y. (1999) Rare earth elements in seawater: Particle association, shale-normalization, and Ce oxidation. *Geochimica Et Cosmochimica Acta* **63**, 363-372.

Anbar A. D. (2004) Molybdenum stable isotopes: observations, interpretations and directions. *Rev Mineral Geochem* **55**, 429–454.

Anbar A. D., Jarzecki A. A., Spiro T. G. (2005) Theoretical investigation of iron isotope fractionation between $Fe(H_2O)_6^{3+}$ and $Fe(H_2O)_6^{2+}$: Implications for iron stable isotope geochemistry. *Geochim Cosmochim Acta* **69**, 825−837.

Anbar A. D., Duan Y., Lyons T. W., Arnold G. L., Kendall B., Creaser R. A., & Buick R. (2007) A whiff of oxygen before the Great Oxidation Event. *Science* **317(5846)**, 1903-1906.

Anbar A.D., Rouxel O., (2007). Metal stable isotopes in paleoceanography. *Annu. Rev. Earth Planet. Sci*. **35**, 717-746.

Andersen M. B., Elliott T., Freymuth H., Sims K. W., Niu Y., Kelley K. A. (2015) The terrestrial uranium isotope cycle. *Nature* **517**:356–359.

Andersen M. B., Stirling C. H., & Weyer S. (2017) Uranium isotope fractionation. *Reviews in Mineralogy and Geochemistry* **82(1)**, 799-850.

Archer C., Vance D. (2008) The isotopic signature of the global riverine molybdenum flux and anoxia in the ancient oceans. *Nat Geosci* **1**, 597–600.

Aries S., Valladon M., Polve M. and Dupre B. (2000) A routine method for oxide and hydroxide interference corrections in ICP-MS chemical analysis of environmental and geological samples. *Geostandards Newsletter-the Journal of Geostandards and Geoanalysis* **24**, 19-31.

Arnold G.L., Anbar A.D., Barling J. and Lyons T.W. (2004) Molybdenum isotope evidence for widespread anoxia in mid-proterozoic oceans. *Science* **304**, 87-90.

Babechuk M.G., Kamber B.S., Greig A., Canil D. and Kodolanyi J. (2010) The behaviour of tungsten during mantle melting revisited with implications for planetary differentiation time scales. *Geochimica Et Cosmochimica Acta* **74**, 1448-1470.

Babechuk M.G., Widdowson M., Kamber B.S. (2014) Quantifying chemical weathering intensity and trace element release from two contrasting basalt profiles, Deccan Traps, India. Chemical *Geology* **363**, 56-75.

Babechuk M.G., Widdowson M., Murphy M., Kamber B.S. (2015) A combined Y/Ho, high field strength element (HFSE) and Nd isotope perspective on basalt weathering, Deccan Traps, India. *Chemical Geology* **396**, 25-41.

Babechuk M. G., Kleinhanns I. and Schoenberg R. (2017) Chromium geochemistry of the ca. 1.85 Ga Flin Flon paleosol. *Geobiology* **15**, 30-50.

Babechuk M. G., Kleinhanns I. C., Reitter E. & Schoenberg R. (2018) Kinetic stable Cr isotopic fractionation between aqueous Cr(III)-Cl-H2O complexes at 25° C: implications for Cr(III) mobility and isotopic variations in modern and ancient natural systems. *Geochimica et Cosmochimica Acta* **222,** 383-405.

Bain D. J., Bullen T. D. (2005) Chromium isotope fractionation during oxidation of Cr(III) by manganese oxides. *Geochim Cosmochim Acta* **69**: 212

Balci N., Bullen T. D., Witte-Lien K., Shanks W. C., Motelica M., & Mandernack K. W. (2006) Iron isotope fractionation during microbially stimulated Fe (II) oxidation and Fe (III) precipitation. *Geochimica et Cosmochimica Acta* **70(3)**, 622-639.

Baldwin G.J., Turner E.C. and Kamber B.S. (2012) A new depositional model for glaciogenic Neoproterozoic iron formation: insights from the chemostratigraphy and basin configuration of the Rapitan iron formation 1 1 Northwest Territories Geoscience Office Contribution 0052. *Can J Earth Sci* **49**, 455-476.

Ball J.W. and Izbicki J.A. (2004) Occurrence of hexavalent chromium in ground water in the western Mojave Desert, California. *Appl Geochem* **19**, 1123-1135.

Barbeau K., Rue E. L., Bruland K. W., & Butler A. (2001). Photochemical cycling of iron in the surface ocean mediated by microbial iron (III)-binding ligands. *Nature*, ***413*(6854)**, 409.

Bargar J. R., Reitmeyer R., Lenhart J. J. & Davis J. A. (2000) Characterization of U(VI)-carbonato ternary complexes on hematite: EXAFS and electrophoretic mobility measurements. *Geochimica et Cosmochimica Acta* **64**, 2737-2749.

Barling J., Arnold G.L. and Anbar A.D. (2001) Natural mass-dependent variations in the isotopic composition of molybdenum. *Earth Planet Sc Lett* **193**, 447-457.

Barling J. and Anbar A.D. (2004) Molybdenum isotope fractionation during adsorption by manganese oxides. *Earth Planet Sc Lett* **217**, 315-329.

Bartlett R. and James B. (1979) Behavior of Chromium in Soils .3. Oxidation. *J Environ Qual* **8**, 31-35.

Basu A., Johnson T. M. (2012) Determination of hexavalent chromium reduction using Cr stable isotopes: Isotopic fractionation factors for permeable reactive barrier materials. *Environ Sci Technol* **46,** 5353−5360.

Bau M. (1991) Rare-Earth Element Mobility during Hydrothermal and Metamorphic Fluid Rock Interaction and the Significance of the Oxidation-State of Europium. *Chem Geol* **93**, 219-230.

Bau M. (1993) Effects of Syn-Depositional and Postdepositional Processes on the Rare-Earth Element Distribution in Precambrian Iron-Formations. *Eur J Mineral* **5**, 257-267.

Bau M. (1996) Controls on the fractionation of isovalent trace elements in magmatic and aqueous systems: evidence from Y/Ho, Zr/Hf, and lanthanide tetrad effect. *Contributions to Mineralogy and Petrology* **123**, 323-333.

Bau M. (1999) Scavenging of dissolved yttrium and rare earths by precipitating iron oxyhydroxide: experimental evidence for Ce oxidation, Y-Ho fractionation, and lanthanide tetrad effect. *Geochimica et Cosmochimica Acta* **63(1)**, 67-77.

Bau M. and Alexander B.W. (2009) Distribution of high field strength elements (Y, Zr, REE, Hf, Ta, Th, U) in adjacent magnetite and chert bands and in reference standards FeR-3 and FeR-4 from the Temagami iron-formation, Canada, and the redox level of the Neoarchean ocean. *Precambrian Res* **174**, 337-346.

Bau M. and Dulski P. (1996) Distribution of yttrium and rare-earth elements in the Penge and Kuruman iron-formations, Transvaal Supergroup, South Africa. *Precambrian Res* **79**, 37-55.

Bau M., & Möller P. (1993) Rare earth element systematics of the chemically precipitated component in Early Precambrian iron formations and the evolution of the terrestrial atmosphere-hydrosphere-lithosphere system. *Geochimica et Cosmochimica Acta* **57(10)**, 2239-2249.

Beard B. L., Johnson C. M., Skulan J. L., Nealson K. H., Cox L., & Sun H. (2003). Application of Fe isotopes to tracing the geochemical and biological cycling of Fe. *Chemical Geology*, ***195*(1-4)**, 87-117.

Beard B. L., Johnson C. M., Von Damm K. L., & Poulson R. L. (2003). Iron isotope constraints on Fe cycling and mass balance in oxygenated Earth oceans. *Geology*, ***31*(7)**, 629-632.

Becquer T., Quantin C., Sicot M. and Boudot J.P. (2003) Chromium availability in ultramafic soils from New Caledonia. *Sci Total Environ* **301**, 251-261.

Bekker A., Holland H. D., Wang P. L., Rumble III D., Stein H. J., Hannah J. L., Coetzee L.L., & Beukes N. J. (2004) Dating the rise of atmospheric oxygen. *Nature* **427(6970)**, 117.

Bekker A., Slack J.F., Planavsky N., Krapez B., Hofmann A., Konhauser K.O. and Rouxel O.J. (2010) Iron Formation: The Sedimentary Product of a Complex Interplay among Mantle, Tectonic, Oceanic, and Biospheric Processes. *Econ Geol* **105**, 467-508.

Bell A., Burger P., Le L., Shearer C., Papike J., Sutton S., Newville M., Jones J. (2014) XANES measurements of cr valence in olivine and their applications to planetary basalts. *Am Mineral* **99**, 1404−1412.

Berger A. and Frei R. (2014) The fate of chromium during tropical weathering: A laterite profile from Central Madagascar. *Geoderma* **213**, 521-532.

Berglund M., Wieser M. E. (2011) Isotopic compositions of the elements 2009 (IUPAC Technical Report). *Pure Appl Chem* **83**, 397–410.

Berna E. C., Johnson T. M., Makdisi R. S., Basu A. (2010) Cr stable isotopes as indicators of Cr(VI) reduction in groundwater: a detailed time-series study of a point-source plume. *Environ Sci Technol* **44**, 1043−1048.

Bergquist B. A., Boyle E. A. (2006) Iron isotopes in the Amazon River system: Weathering and transport signatures. *Earth Planet Sci Lett* **248**, 54–68.

Berry A. J., O'Neill H. S. C. (2004) A XANES determination of the oxidation state of chromium in silicate glasses. *Am Mineral* **89**, 790−798.

Berry A. J., O'Neill H. S. C., Scott D. R., Foran G. J., Shelley J. (2006) The effect of composition on Cr^{2+}/Cr^{3+} in silicate melts. *Am Mineral* **91**, 1901−1908.

Beukes N. and Cairncross B. (1991) A lithostratigraphic-sedimentological reference profile for the Late Archean Mozaan Group, Pongola Sequence: application to sequence stratigraphy and correlation with the Witwatersrand Supergroup. *South African Journal of Geology* **94**, 44-69.

Beukes N.J. and Lowe D.R. (1989) Environmental-Control on Diverse Stromatolite Morphologies in the 3000 Myr Pongola Supergroup, South-Africa. *Sedimentology* **36**, 383-397.

Beukes N. J. & Gutzmer J. E. N. S. (2008) Origin and paleoenvironmental significance of major iron formations at the Archean-Paleoproterozoic boundary. *Reviews in Economic Geology* **15**, 5- 47.

Bigeleisen, J. (1965). Chemistry of isotopes: Isotope chemistry has opened new areas of chemical physics, geochemistry, and molecular biology. *Science **147*(3657)**, 463-471.

Bleam W. F. & McBride M. B. (1985) Cluster formation versus isolated-site adsorption. A study of Mn(II) and Mg (II) adsorption on boehmite and goethite. *Journal of colloid and interface science* **103**, 124-132.

Bolhar R., Hofmann A., Siahi M., Feng Y.X. and Delvigne C. (2015) A trace element and Pb isotopic investigation into the provenance and deposition of stromatolitic carbonates, ironstones and associated shales of the similar to 3.0 Ga Pongola Supergroup, Kaapvaal Craton. *Geochimica Et Cosmochimica Acta* **158**, 57-78.

Bolhar R., Kamber B.S., Moorbath S., Fedo C.M. and Whitehouse M.J. (2004) Characterisation of early Archean chemical sediments by trace element signatures. *Earth Planet Sc Lett* **222**, 43-60.

Bolhar R. and Van Kranendonk M.J. (2007) A non-marine depositional setting for the northern Fortescue Group, Pilbara Craton, inferred from trace element geochemistry of stromatolitic carbonates. *Precambrian Res* **155**, 229-250.

Bonnand P., James, R. H., Parkinson I. J., Connelly D. P., & Fairchild I. J. (2013). The chromium isotopic composition of seawater and marine carbonates. *Earth and Planetary Science Letters* **382**, 10-20.

Bonotto D.M., Jiménez-Rueda J.R. (2007) U-ages in soils and groundwater evidencing wet periods 400–600 kyr ago in southeast Brazil. *Applied Radiation and Isotopes* **65**, 776-783.

Brennecka G. A., Wasylenki L. E., Bargar J. R., Weyer S., Anbar A. D. (2011) Uranium isotope fractionation during adsorption to Mn-oxyhydroxides. *Environ Sci Technol* **45**, 1370–1375.

Bullen T. D., White A. F., Childs C. W., Vivit D. V., Schulz M. S. (2001) Demonstration of significant abiotic iron isotope fractionation in nature. *Geology* **29**, 699−702.

Buerge I. J., Hug S. J. (1997) Kinetics and pH dependence of chromium (VI) reduction by iron (II). *Environ Sci Technol* **31**, 1426−1432.

Burkhardt C., Kleine T., Oberli F., Pack A., Bourdon B., & Wieler R. (2011) Molybdenum isotope anomalies in meteorites: constraints on solar nebula evolution and origin of the Earth. *Earth and Planetary Science Letters* **312(3-4)**, 390-400.

Burkhardt C., Hin R. C., Kleine T., & Bourdon B. (2014) Evidence for Mo isotope fractionation in the solar nebula and during planetary differentiation. *Earth and Planetary Science Letters* **391**, 201-211.

Burns R. G. (1975) On the occurrence and stability of divalent chromium in olivines included in diamonds. *Contrib Mineral Petrol* **51**, 213−221.

Busigny V., Planavsky N. J., Jézéquel D., Crowe S., Louvat P., Moureau J., & Lyons T. W. (2014) Iron isotopes in an Archean ocean analog. *Geochimica et Cosmochimica Acta* **133**, 443-462.

Butler A. (2005). Marine siderophores and microbial iron mobilization. *Biometals* **18(4)**.

Cairns-Smith A. (1978). Precambrian solution photochemistry, inverse segregation, and banded iron formations. *Nature* **276**, 807-808.

Canfield D. E., Kristensen E., & Thamdrup B. (2005). The iron and manganese cycles. In *Advances in Marine Biology* (Vol. 48, pp. 269-312). Academic Press.

Carl C. (1987) Investigations of U series disequilibria as a means to study the transport mechanism of uranium in sandstone samples during weathering. *Uranium* **3(2-4)**, 285-305.

Chabaux F., Dequincey O., Lévčque J. J., Leprun J. C., Clauer N., Riotte J., & Paquet H. (2003) Tracing and dating recent chemical transfers in weathering profiles by trace-element geochemistry and ^{238}U- ^{234}U- ^{230}Th disequilibria: the example of the Kaya lateritic toposequence (Burkina-Faso). *Comptes Rendus Geoscience* **335(16)**, 1219-1231.

Chabaux F., Riotte J., Dequincey O., (2003) U-Th-Ra fractionation during weathering and river transport, Uranium-Series Geochemistry. *Reviews in Mineralogy & Geochemistry* **52(1)**, 533- 576.

Chabaux F., Blaes E., Stille P., di Chiara Roupert R., Pelt E., Dosseto A., Ma L., Buss H., Brantley S. (2013) Regolith formation rate from U-series nuclides: Implications from the study of a spheroidal weathering profile in the Rio Icacos watershed (Puerto Rico). *Geochimica et Cosmochimica Acta* **100**, 73-95.

Cheng H., Edwards R. L., Hoff J., Gallup C. D., Richards D. A., & Asmerom Y. (2000) The half-lives of uranium-234 and thorium-230. *Chemical Geology* **169(1-2)**, 17-33.

Cizdziel J., Farmer D., Hodge V., Lindley K., & Stetzenbach K. (2005) ^{234}U/^{238}U isotope ratios in groundwater from Southern Nevada: a comparison of alpha counting and magnetic sector ICP-MS. *Science of the total environment* **350(1-3)**, 248-260.

Claude C., Meunier J.-D., Chabaux F., Dussouillez P., Pelt E., Hamelin B., Traoré D., Colin F. (2016) Timescale of spheroidal weathering of a 293 kyr-old basaltic lava from Réunion Island, Indian Ocean. *Chemical Geology* **446**, 110-125.

Cloud P., (1973) Paleoecological significance of the banded iron-formation. *Economic Geology* **68**, 1135- 1143.

Cole E. G. (1994) Lithostratigraphy and depositional environment of the Archean Nsuze Group, Pongola Supergroup. Ph. D. thesis, University of Johannesburg.

Condie K.C. (1993) Chemical-Composition and Evolution of the Upper Continental-Crust - Contrasting Results from Surface Samples and Shales. *Chem Geol* **104**, 1-37.

Conway T. M., & John S. G. (2014) Quantification of dissolved iron sources to the North Atlantic Ocean. *Nature* **511(7508)**, 212.

Cooper G. R. C. (2002) Oxidation and toxicity of chromium in ultramafic soils in Zimbabwe. *Appl Geochem* **17**, 981-986.

Coughlin B. R. & Stone A. T. (1995) Nonreversible adsorption of divalent metal ions (Mn^{II}, Co^{II}, Ni^{II}, Cu^{II}, and Pb^{II}) onto goethite: effects of acidification, Fe^{II} addition, and picolinic acid addition. *Environmental science & technology* **29**, 2445-2455.

Croal L. R., Johnson C. M., Beard B. L., & Newman D. K. (2004) Iron isotope fractionation by Fe (II)-oxidizing photoautotrophic bacteria 1. *Geochimica et cosmochimica acta* **68(6)**, 1227-1242.

Crowe S. A., Jones C., Katsev S., Magen C., O'Neill A. H., Sturm A., Canfield D.E., Haffner G.D., Mucci A., Sundby B & Fowle D. A. (2008) Photoferrotrophs thrive in an Archean Ocean analog. *Proceedings of the National Academy of Sciences*.

Crowe S.A., Dossing L.N., Beukes N.J., Bau M., Kruger S.J., Frei R. and Canfield D.E. (2013) Atmospheric oxygenation three billion years ago. *Nature* **501**, 535-538.

Crowe S. A., Paris G., Katsev S., Jones C., Kim S. T., Zerkle A. L., Nomosatryo S., Fowle D. A., Adkins J. F., Sessions A.L. and Farquhar J., (2014) Sulfate was a trace constituent of Archean seawater. *Science* **346(6210)**, 735-739.

Czaja A. D., Johnson C. M., Roden E. E., Beard B. L., Voegelin A. R., Nägler T. F., Beukes N. J., & Wille M. (2012) Evidence for free oxygen in the Neoarchean ocean based on coupled iron–molybdenum isotope fractionation. *Geochimica et Cosmochimica Acta* **86**, 118-137.

Dahl T. W., Anbar A. D., Gordon G. W., Rosing M. T., Frei R., & Canfield D. E. (2010) The behavior of molybdenum and its isotopes across the chemocline and in the sediments of sulfidic Lake Cadagno, Switzerland. *Geochimica et Cosmochimica Acta* **74(1)**, 144-163.

Dahl T. W., Boyle R. A., Canfield D. E., Connelly J. N., Gill B. C., Lenton T. M., Bizzarro M. (2014) Uranium isotopes distinguish two geochemically distinct stages during the later Cambrian SPICE event. *Earth Planet Sci Lett* **401**, 313–326.

D'Arcy J., Babechuk M. G., Døssing L. N., Gaucher C., & Frei R. (2016) Processes controlling the chromium isotopic composition of river water: Constraints from basaltic river catchments. *Geochimica et Cosmochimica Acta* **186**, 296-315.

Dauphas N., & Rouxel O. (2006) Mass spectrometry and natural variations of iron isotopes. *Mass Spectrometry Reviews* **25(4)**, 515-550.

Davranche M., Pourret O., Gruau G., Dia A., & Le Coz-Bouhnik M. (2005) Adsorption of REE (III)-humate complexes onto MnO2: Experimental evidence for cerium anomaly and lanthanide tetrad effect suppression. *Geochimica et Cosmochimica Acta* **69(20)**, 4825-4835.

Davranche M., Pourret O., Gruau G., Dia, A., Jin D., & Gaertner D. (2008) Competitive binding of REE to humic acid and manganese oxide: impact of reaction kinetics on development of cerium anomaly and REE adsorption. *Chemical Geology* **247(1-2)**, 154-170.

De Baar H. J. W., De Jong J. T. M., Turner D. R., & Hunter K. A. (2001) The biogeochemistry of iron in seawater. In *Distributions, Sources and Sinks of Iron in Seawater* (Vol. 7). John Wiley & Sons Ltd. Chichester, UK.

De Carlo E. H., & McMurtry G. M. (1992) Rare-earth element geochemistry of ferromanganese crusts from the Hawaiian Archipelago, central Pacific. *Chemical Geology* **95(3-4)**, 235-250.

De Laeter J.R., Boehlke J.K., de Bievre P., Hidaka H., Peisler H.S., Rosman K.J.R. and Taylor P.D.P. (2003) Atomic weights of the elements: Review 2000 (IUPAC Technical Report). *Pure and Applied Chemistry* **75**, 683-800.

Delvigne C., Cardinal D., Hofmann A., & André L. (2012) Stratigraphic changes of Ge/Si, REE+ Y and silicon isotopes as insights into the deposition of a Mesoarchean banded iron formation. *Earth and Planetary Science Letters* **355**, 109-118.

Dequincey O., Chabaux F., Clauer N., Sigmarsson O., Liewig N., Leprun J.C. (2002) Chemical mobilizations in laterites: evidence from trace elements and ^{238}U-^{234}U-^{230}Th disequilibria. *Geochimica et Cosmochimica Acta* **66**, 1197-1210.

Derry L. A., & Jacobsen S. B. (1990) The chemical evolution of Precambrian seawater: evidence from REEs in banded iron formations. *Geochimica et Cosmochimica Acta* **54(11)**, 2965-2977.

Dix O. R. (1984) Early Proterozoic braided stream, shelf and tidal deposition in the Pongola Sequence, Zululand. *South African Journal of Geology* **87(1)**, 1-10.

Dosseto A., Turner S.P., Chappell J. (2008) The evolution of weathering profiles through time: New insights from uranium-series isotopes. *Earth and Planetary Science Letters* **274**, 359-371.

Dosseto A., Buss H.L., Suresh P. (2012) Rapid regolith formation over volcanic bedrock and implications for landscape evolution. *Earth and Planetary Science Letters* **337**, 47-55.

Døssing L.N., Dideriksen K., Stipp S.L.S. and Frei R. (2011) Reduction of hexavalent chromium by ferrous iron: A process of chromium isotope fractionation and its relevance to natural environments. *Chem Geol* **285**, 157-166.

Douville É., Charlou J.-L., Donval J.-P., Hureau D. and Appriou P. (1999) As and Sb behaviour in fluids from various deep-sea hydrothermal systems. Comptes Rendus de l'Academie des Sciences Series IIA *Earth and Planetary Science* **2**, 97-104.

Dunk R. M., Mills R. A., Jenkins W. J. (2002) A reevaluation of the oceanic uranium budget for the Holocene. *Chem Geol* **190**, 45–67.

Eary L. E. and Rai D. (1987) Kinetics of Chromium(Iii) Oxidation to Chromium(Vi) by Reaction with Manganese-Dioxide. *Environ Sci Technol* **21**, 1187-1193.

Economou-Eliopoulos M., Frei R., and Atsarou C. (2014) Application of chromium stable isotopes to the evaluation of Cr (VI) contamination in groundwater and rock leachates from central Euboea and the Assopos basin (Greece). *Catena* **122**, 216-228.

Eeckhout S. G., Bolfan-Casanova N., McCammon C., Klemme S., Amiguet E. (2007) XANES study of the oxidation state of Cr in lower mantle phases: Periclase and magnesium silicate perovskite. *Am Mineral* **92**, 966−972.

Eggins S.M., Woodhead J.D., Kinsley L.P.J., Mortimer G.E., Sylvester P., McCulloch M.T., Hergt J.M. and Handler M.R. (1997) A simple method for the precise determination of >=40 trace elements in geological samples by ICPMS using enriched isotope internal standardisation. *Chem Geol* **134**, 311-326.

Eickmann B., Hofmann A., Wille M., Bui T.H., Wing B.A., Schoenberg R. (2018) Isotopic evidence for oxygenated Mesoarchean shallow oceans. *Nature Geoscience* **11,** 133-138.

Elderfield H., & Greaves M. J. (1981) Negative cerium anomalies in the rare earth element patterns of oceanic ferromanganese nodules. *Earth and Planetary Science Letters* **55(1)**, 163-170.

Elderfield H. (1988) The oceanic chemistry of the rare-earth elements. *Phil. Trans. R. Soc. Lond. A* **325(1583)**, 105-126.

Elderfield H. and Schultz A. (1996) Mid-ocean ridge hydrothermal fluxes and the chemical composition of the ocean. *Annu Rev Earth Pl Sc* **24**, 191-224.

Ellis A. S., Johnson T. M. & Bullen T. D. (2002) Chromium isotopes and the fate of hexavalent chromium in the environment. *Science* **295**, 2060-2062.

Ellis A. S., Johnson T. M., & Bullen T. D. (2004) Using chromium stable isotope ratios to quantify Cr (VI) reduction: lack of sorption effects. *Environmental science & technology* **38,** 3604-3607.

Ellis A. S., Johnson T. M., Villalobos-Aragon A., Bullen T. (2008) Environmental cycling of Cr using stable isotopes: kinetic and equilibrium effects. *2008 Fall Meeting, AGU*, San Francisco, Calif 15−19 Dec, abstract #H53F−08.

Emmanuel S., Erel Y., Matthews A., & Teutsch N. (2005) A preliminary mixing model for Fe isotopes in soils. *Chemical Geology* **222(1-2)**, 23-34.

Eppich G.R., Cooper K.M., Kent A.J., Koleszar A., (2012) Constraints on crystal storage timescales in mixed magmas: Uranium-series disequilibria in plagioclase from Holocene magmas at Mount Hood, Oregon. *Earth and Planetary Science Letters* **317**, 319-330.

Erickson B. E. and Helz G. R. (2000) Molybdenum(VI) speciation in sulfidic waters: Stability and lability of thiomolybdates. *Geochim Cosmochim Ac* **64**, 1149-1158.

Eroglu S., Schoenberg R., Wille M., Beukes N., & Taubald H. (2015) Geochemical stratigraphy, sedimentology, and Mo isotope systematics of the ca. 2.58–2.50 Ga-old Transvaal Supergroup carbonate platform, South Africa. *Precambrian Research* **266**, 27-46.

Eroglu S., Schoenberg R., Pascarelli S., Beukes N. J., Kleinhanns I. C., & Swanner E. D. (2018) Open ocean vs. continentally-derived iron cycles along the Neoarchean Campbellrand-Malmani Carbonate platform, South Africa. *American Journal of Science* **318(4)**, 367-408.

Fandeur D., Juillot F., Morin G., Olivi L., Cognigni A., Webb S.M., Ambrosi J.P., Fritsch E., Guyot F. and Brown, G.E. (2009) XANES Evidence for Oxidation of Cr(III)) to Cr(VI) by Mn-Oxides in a Lateritic Regolith Developed on Serpentinized Ultramafic Rocks of New Caledonia. *Environ Sci Technol* **43**, 7384-7390.

Fantle M. S., DePaolo D. J. (2004) Iron isotopic fractionation during continental weathering. *Earth Planet Sci Lett* **228**, 547−562.

Farkaš J., Chrastný V., Novák M., Čadkova E., Pašava J., Chakrabarti R., Jacobsen S.B., Ackerman L. and Bullen T.D. (2013) Chromium isotope variations ($\delta^{53/52}$Cr) in mantle-derived sources and their weathering products: Implications for environmental studies and the evolution of $\delta^{53/52}$Cr in the Earth's mantle over geologic time. *Geochimica et Cosmochimica Acta* **123**, 74-92.

Farquhar J., Bao H.M. and Thiemens M. (2000) Atmospheric influence of Earth's earliest sulfur cycle. *Science* **289**, 756-758.

Farquhar J., Wing B.A., McKeegan K.D., Harris J.W., Cartigny P. and Thiemens M.H. (2002) Mass-independent sulfur of inclusions in diamond and sulfur recycling on early earth. *Science* **298**, 2369-2372.

Faure G. (1991) Principles and Applications of Geochemistry. Wiley, New York.

Fendorf S. E., & Zasoski R. J. (1992) Chromium (III) oxidation by δ-manganese oxide (MnO_2) Characterization. *Environmental Science & Technology* **26(1)**, 79-85.

Fendorf S.E. (1995) Surface-Reactions of Chromium in Soils and Waters. *Geoderma* **67**, 55-71.

Feng J. L. (2010) Behaviour of rare earth elements and yttrium in ferromanganese concretions, gibbsite spots, and the surrounding terra rossa over dolomite during chemical weathering. *Chemical Geology* **271(3-4)**, 112-132.

Fischer A. G. (1965) Fossils, early life, and atmospheric history. *Proceedings of the National Academy of Sciences* **53(6)**, 1205-1215.

Fleischer R. L., & Raabe O. G. (1978) Recoiling alpha-emitting nuclei. Mechanisms for uranium-series disequilibrium. *Geochimica et Cosmochimica Acta* **42(7)**, 973-978.

Frei R., Crowe S.A., Bau M., Polat A., Fowle D.A. and Dossing L.N. (2016) Oxidative elemental cycling under the low O_2 Eoarchean atmosphere. *Sci Rep* **6**, 21058.

Frei R., Gaucher C., Dossing L.N. and Sial A.N. (2011) Chromium isotopes in carbonates - A tracer for climate change and for reconstructing the redox state of ancient seawater. *Earth Planet Sc Lett* **312**, 114-125.

Frei R., Gaucher C., Poulton S.W. and Canfield D.E. (2009) Fluctuations in Precambrian atmospheric oxygenation recorded by chromium isotopes. *Nature* **461**, 250-U125.

Frei R., Poire D. and Frei K.M. (2014) Weathering on land and transport of chromium to the ocean in a subtropical region (Misiones, NW Argentina): A chromium stable isotope perspective. *Chem Geol* **381**, 110-124.

Frei R. and Polat A. (2013) Chromium isotope fractionation during oxidative weathering-Implications from the study of a Paleoproterozoic (ca. 1.9 Ga) paleosol, Schreiber Beach, Ontario, Canada. *Precambrian Res* **224**, 434-453.

French K. L., Hallmann C., Hope J. M., Schoon P. L., Zumberge J. A., Hoshino Y. & Buick R. (2015) Reappraisal of hydrocarbon biomarkers in Archean rocks. *Proceedings of the National Academy of Sciences* **112**, 5915-5920.

Froelich P.N., Klinkhammer G.P., Bender M.L., Luedtke N.A., Heath G.R., Cullen D., Dauphin P., Hammond D., Hartman B. and Maynard V. (1979) Early Oxidation of Organic-Matter in Pelagic Sediments of the Eastern Equatorial Atlantic - Suboxic Diagenesis. *Geochimica Et Cosmochimica Acta* **43**, 1075-1090.

Fryer B. (1977) Rare earth evidence in iron-formations for changing Precambrian oxidation states. *Geochimica et Cosmochimica Acta* **41**, 361-367.

Gaillard F., Scaillet B., & Arndt N. T. (2011) Atmospheric oxygenation caused by a change in volcanic degassing pressure. *Nature* **478(7368)**, 229.

Gallagher M., Turner E. C., & Kamber B. S. (2015) In situ trace metal analysis of Neoarchean – O rdovician shallow-marine microbial-carbonate-hosted pyrites. *Geobiology* **13(4)**, 316-339.

Garnier J., Quantin C., Guimaraes E.M., Vantelon D., Montarges-Pelletier E. and Becquer T. (2013) Cr(VI) genesis and dynamics in Ferralsols developed from ultramafic rocks: The case of Niquelandia, Brazil. *Geoderma* **193**, 256-264.

Gilleaudeau G.J., Frei R., Kaufman A.J., Kah L.C., Azmy K., Bartley J.K., Chernyavskiy P. and Knoll A.H. (2016) Oxygenation of the mid-Proterozoic atmosphere: clues from chromium isotopes in carbonates. *Geochem Perspect Let* **2**, 178-186.

Gold D. J. C., & Von Veh M. W. (1995) Tectonic evolution of the Late Archean Pongola-Mozaan basin, South Africa. *Journal of African Earth Sciences* **21(2)**, 203-212.

Gold D. J. C., Johnson M. R., Anhaeusser C. R., & Thomas R. J. (2006) The Pongola Supergroup. *The Geology of South Africa*, 135-148.

Goldberg T., Archer C., Vance D., & Poulton S. W. (2009) Mo isotope fractionation during adsorption to Fe (oxyhydr) oxides. *Geochimica et Cosmochimica Acta* **73(21)**, 6502-6516.

Goldberg T., Archer C., Vance D., Thamdrup B., McAnena A., & Poulton S. W. (2012) Controls on Mo isotope fractionations in a Mn-rich anoxic marine sediment, Gullmar Fjord, Sweden. *Chemical geology* **296**, 73-82.

Goldberg T., Gordon G., Izon G., Archer C., Pearce C. R., McManus J. & Rehkämper M. (2013) Resolution of inter-laboratory discrepancies in Mo isotope data: an intercalibration. *Journal of Analytical Atomic Spectrometry* **28(5)**, 724-735.

Goldmann A., Brennecka G., Noordmann J., Weyer S., & Wadhwa M. (2015) The uranium isotopic composition of the Earth and the Solar System. *Geochimica et Cosmochimica Acta* **148**, 145-158.

Gordon, R., Martin, J., Knauer, G., 1982. Iron in north-east Pacific waters.

Goto K. T., Anbar A. D., Gordon G. W., Romaniello S. J., Shimoda G., Takaya Y., Tokumaru A., Nozaki T., Suzuki K., Machida S., Hanyu T. (2014) Uranium isotope systematics of ferromanganese crusts in the Pacific Ocean: Implications for the marine $^{238}U/^{235}U$ isotope system. *Geochim Cosmochim Acta* **146**, 43–58

Govindaraju K. and Roelandts I. (1989) 1988 Compilation Report on Trace-Elements in 6 Anrt Rock Reference Samples - Diorite Dr-N, Serpentine Ub-N, Bauxite Bx-N, Disthene Dt-N, Granite Gs-N and Potash Feldspar Fk-N. *Geostandard Newslett* **13**, 5-67.

Greber N. D., Siebert C., Nägler T. F., & Pettke T. (2012) $\delta^{98/95}$Mo values and molybdenum concentration data for NIST SRM 610, 612 and 3134: Towards a common protocol for reporting Mo data. *Geostandards and Geoanalytical Research* **36(3)**, 291-300.

Greber, N.D., Maeder, U. and Naegler, T.F. (2015) Experimental dissolution of molybdenum-sulphides at low oxygen concentrations: A first-order approximation of late Archean atmospheric conditions. Earth and Space Science 2, 173-180.

Gromet L.P., Dymek R.F., Haskin L.A. and Korotev R.L. (1984) The North-American Shale Composite - Its Compilation, Major and Trace-Element Characteristics. *Geochimica Et Cosmochimica Acta* **48**, 2469-2482.

Gross G. A. (1980) A classification of iron formations based on depositional environments. *The Canadian Mineralogist* **18(2)**, 215-222.

Gueguen B., Reinhard C. T., Algeo T. J., Peterson L. C., Nielsen S. G., Wang X. L., Rowe H., Planavsky N. J. (2016) The chromium isotope composition of reducing and oxic marine sediments. *Geochim Cosmochim Acta* **184**, 1–19.

Guo Q., Strauss H., Kaufman A. J., Schröder S., Gutzmer J., Wing B., Baker M.A., Bekker A., Jin Q., Tae-Kim S., & Farquhar J. (2009) Reconstructing Earth's surface oxidation across the Archean-Proterozoic transition. *Geology* **37(5)**, 399-402.

Gutzmer J., Nhleko N., Beukes N.J., Pickard A. and Barley M.E. (1999) Geochemistry and ion microprobe (SHRIMP) age of a quartz porphyry sill in the Mozaan Group of the Pongola Supergroup: implications for the Pongola and Witwatersrand Supergroups. *South African Journal of Geology* **102**, 139-146.

Habicht K. S., Gade M., Thamdrup B., Berg P., & Canfield D. E. (2002) Calibration of sulfate levels in the Archean ocean *Science*, **298(5602)**, 2372-2374.

Halliday A. N., Lee D. C., Christensen J. N., Walder A. J., Freedman P. A., Jones C. E., Hall C. M., Yi W., Teagle D. (1995) Recent developments in inductively coupled plasma magnetic sector multiple collector mass spectrometry. *Int J Mass Spectrom Ion Processes* **146**, 21−33,

Hannah J. L., Bekker A., Stein H. J., Markey R. J., & Holland H. D. (2004) Primitive Os and 2316 Ma age for marine shale: implications for Paleoproterozoic glacial events and the rise of atmospheric oxygen. *Earth and Planetary Science Letters*, **225(1)**, 43-52.

Hansen R. O., Stout P. R. (1968) Isotopic distributions of uranium and thorium in soils. *Soil Science* **105**, 44-50.

Haqq-Misra J., Kasting J.F. and Lee S. (2011) Availability of O_2 and H_2O_2 on Pre-Photosynthetic Earth. *Astrobiology* **11**, 293-302.

Haugaard R., Ootes L., Heaman L.M., Hamilton M.A., Shaulis B.J. and Konhauser K. (2017) Depositional timing of Neoarchean turbidites of the Slave craton-recommended nomenclature and type localities. *Can J Earth Sci* **54**, 15-32.

Heimann A., Johnson C. M., Beard B. L., Valley J. W., Roden E. E., Spicuzza M. J., Beukes N. J. (2010) Fe C, O isotope compositions of banded iron formation carbonates demonstrate a major role for dissimilatory iron reduction in similar to 2.5 Ga marine environments. *Earth Planet Sci Lett* **294**, 8−18.

Helz G. R., Miller C. V., Charnock J. M., Mosselmans J. F. W., Pattrick R. A. D., Garner C. D. and Vaughan D. J. (1996) Mechanism of molybdenum removal from the sea and its concentration in black shales: EXAFS evidence. *Geochim Cosmochim Acta* **60**, 3631-3642.

Henderson G. M., Anderson R. F. (2003) The U-series toolbox for paleoceanography. *Rev Mineral Geochem* **52**, 493–531.

Herrmann A. D., Kendall B., Algeo T. J., Gordon G. W., Wasylenki L. E., Anbar A. D. (2012) Anomalous molybdenum isotope trends in Upper Pennsylvanian euxinic facies: Significance for use of δ^{98}Mo as a global marine redox proxy. *Chem Geol* **324–325**, 87–98.

Herzog R. E., Shi Q., Patil J. N., & Katz J. L. (1989) Magnetic water treatment: the effect of iron on calcium carbonate nucleation and growth. *Langmuir* **5(3)**, 861-867.

Hicks N., & Hofmann A. (2012) Stratigraphy and provenance of the auriferous-uraniferous, fluvial to shallow-marine Sinqeni Formation, Mozaan Group, northern KwaZulu-Natal, South Africa. *South African Journal of Geology* **115(3)**, 327-344.

Hinojosa J. L., Stirling C. H., Reid M. R., Moy C. M., Wilsin G. S. (2016) Trace metal cycling and $^{238}U/^{235}U$ in New Zealand's fjords: Implications for reconstructing global paleoredox conditions in organic-rich sediments. Geochim Cosmochim Acta **179**, 89–109.

Hoashi M., Bevacqua D.C., Otake T., Watanabe Y., Hickman A.H., Utsunomiya S. and Ohmoto H. (2009) Primary hematite formation in an oxygenated deep sea 3.46 billion years ago. *Geochimica Et Cosmochimica Acta* **73**, A536-A536.

Holland H. D. (1973) The oceans; a possible source of iron in iron-formations. *Economic Geology* **68(7)**, 1169-1172.

Holland H. (1994) Early Proterozoic atmospheric change, Early life on Earth. Columbia University Press New York, 237-244.

Holland H.D. (2002) Volcanic gases, black smokers, and the Great Oxidation Event. *Geochimica Et Cosmochimica Acta* **66**, 3811-3826.

Holland H.D. (2006) The oxygenation of the atmosphere and oceans. *Philos T R Soc B* **361**, 903-915.

Holland H.D. (2011) Discovering the history of atmospheric oxygen. Frontiers in geochemistry: contribution of geochemistry to the study of the earth, (eds R. S. Harmon and A. Parker), John Wiley & Sons, Ltd, Chichester, UK, 43-60.

Holmden C., Jacobson A. D., Sageman B. B. & Hurtgen M. T. (2016) Response of the Cr isotope proxy to Cretaceous Ocean Anoxic Event 2 in a pelagic carbonate succession from the Western Interior Seaway. *Geochimica et Cosmochimica Acta* **186**, 277-295.

Hopwood T. (2012) The significance of pyritic black shales in the genesis of Archean nickel sulphide deposits. *Regional and Specific Deposits* **9**, 411.

Hsi C. K. D. & Langmuir D. (1985) Adsorption of uranyl onto ferric oxyhydroxides: application of the surface complexation site-binding model. *Geochimica et Cosmochimica Acta* **49,** 1931-1941.

Huckle D., Ma L., McIntosh J., Vázquez-Ortega A., Rasmussen C., Chorover J. (2016) U-series isotopic signatures of soils and headwater streams in a semi-arid complex volcanic terrain. *Chemical Geology* **445**, 68-83.

Izbicki J. A., Ball J. W., Bullen T. D. & Sutley S. J. (2008) Chromium, chromium isotopes and selected trace elements, western Mojave Desert, USA. *Applied Geochemistry* **23**, 1325-1352.

Jamieson-Hanes J. H., Gibson B. D., Lindsay M. B., Kim Y., Ptacek C. J., Blowes D. W. (2012) Chromium isotope fractionation during reduction of Cr(VI) under saturated flow conditions. *Environ Sci Technol* **46**, 6783−6789.

Jamieson-Hanes J. H., Lentz A. M., Amos R. T., Ptacek C. J., Blowes D. W. (2014) Examination of Cr(VI) treatment by zero-valent iron using in situ, real-time X-ray absorption spectroscopy and Cr isotope measurements. *Geochim Cosmochim Acta* **142**, 299−313.

Jeandel C., & Minster J. F. (1987) Chromium behavior in the ocean: Global versus regional processes. *Global Biogeochemical Cycles* **1(2)**, 131-154.

Jemison N. E., Johnson T. M., Shiel A. E., & Lundstrom C. C. (2016) Uranium isotopic fractionation induced by U (VI) adsorption onto common aquifer minerals. *Environmental science & technology* **50(22)**, 12232-12240.

Jochum K.P., Weis U., Schwager B., Stoll B., Wilson S.A., Haug G.H., Andreae M.O. and Enzweiler J. (2016) Reference Values Following ISO Guidelines for Frequently Requested Rock Reference Materials. *Geostandards and Geoanalytical Research* **40**, 333-350.

Johnson C. M., Beard B. L., Klein C., Beukes N. J., Roden E. E. (2008) Iron isotopes constrain biologic and abiologic processes in banded iron formation genesis. *Geochim Cosmochim Acta* **72**, 151–169.

Johnson C. M., Ludois J. M., Beard B. L., Beukes N. J., Heimann A. (2013) Iron formation carbonates: Paleoceanographic proxy or recorder of microbial diagenesis? *Geology* **41**, 1147−1150.

Johnson C. M., Roden E. E., Welch S. A., Beard B. L. (2005) Experimental constraints on Fe isotope fractionation during magnetite and Fe carbonate formation coupled to dissimilatory hydrous ferric oxide reduction. *Geochim Cosmochim Acta* **69**, 963−993.

Johnson C. M., Skulan J. L., Beard B. L., Sun H., Nealson K. H., Braterman P. S. (2002) Isotopic fractionation between Fe(III) and Fe(II) in aqueous solutions. *Earth Planet Sci Lett* **195**, 141– 153.

Joubert P., & Johnson M. R. (1998) Abridged lexicon of South African stratigraphy; Council for geoscience, Geol. survey of South Africa.

Kamber B.S. (2009) Geochemical fingerprinting: 40 years of analytical development and real world applications. *Appl Geochem* **24**, 1074-1086.

Kamber B.S., Greig A. and Collerson K.D. (2005) A new estimate for the composition of weathered young upper continental crust from alluvial sediments, Queensland, Australia. *Geochimica Et Cosmochimica Acta* **69**, 1041-1058.

Kamber B. S., Whitehouse M. J., Bolhar R., & Moorbath S. (2005) Volcanic resurfacing and the early terrestrial crust: zircon U–Pb and REE constraints from the Isua Greenstone Belt, southern West Greenland. *Earth and Planetary Science Letters* **240(2)**, 276-290.

Kamber B.S., Webb G.E. and Gallagher M. (2014) The rare earth element signal in Archean microbial carbonate: information on ocean redox and biogenicity. *J Geol Soc London* **171**, 745-763.

Kane J.S. (2004) Report of the International Association of Geoanalysts on the Certification of Penrhyn Slate, OU-6. *Geostandards and Geoanalytical Research* **28**, 53-80.

Kappler A., Pasquero C., Konhauser K.O. and Newman D.K. (2005) Deposition of banded iron formations by anoxygenic phototrophic Fe(II)-oxidizing bacteria. *Geology* **33**, 865-868.

Kasting J.F., Liu S.C. and Donahue T.M. (1979) Oxygen Levels in the Prebiological Atmosphere. *J Geophys Res-Oc Atm* **84**, 3097-3107.

Kato Y., Ohta I., Tsunematsu T., Watanabe Y., Isozaki Y., Maruyama S., & Imai N. (1998) Rare earth element variations in mid-Archean banded iron formations: Implications for the chemistry of ocean and continent and plate tectonics. *Geochimica et Cosmochimica Acta* **62(21-22)**, 3475-3497.

Keech A.R., West A.J., Pett-Ridge J.C., Henderson G.M. (2013) Evaluating U-series tools for weathering rate and duration on a soil sequence of known ages. *Earth and Planetary Science Letters* **374**, 24-35.

Kendall B., Brennecka G. A., Weyer S., & Anbar A. D. (2013) Uranium isotope fractionation suggests oxidative uranium mobilization at 2.50 Ga. *Chemical Geology* **362**, 105-114.

Kendall B., Dahl T. W., & Anbar A. D. (2017) The stable isotope geochemistry of molybdenum. *Reviews in Mineralogy and Geochemistry* **82(1)**, 683-732.

Kendall B., Komiya T., Lyons T. W., Bates S. M., Gordon G. W., Romaniello S. J., Jiang G., Creaser R. A., Xiao S., McFadden K., & Sawaki, Y. (2015) Uranium and molybdenum isotope evidence for an episode of widespread ocean oxygenation during the late Ediacaran Period. *Geochimica et Cosmochimica Acta* **156**, 173-193.

Kigoshi K. (1971) Alpha-recoil thorium-234: dissolution into water and the uranium-234/uranium-238 disequilibrium in nature. *Science* **173(3991)**, 47-48.

King E. K., Perakis S. S., & Pett-Ridge J. C. (2018) Molybdenum isotope fractionation during adsorption to organic matter. *Geochimica et Cosmochimica Acta* **222**, 584-598.

Kitchen J. W., Johnson T. M., Bullen T. D., Zhu J., Raddatz A. (2012) Chromium isotope fractionation factors for reduction of Cr(VI) by aqueous Fe(II) and organic molecules. *Geochim Cosmochim Acta* **89**, 190−201.

Koeksoy E., Halama M., Hagemann N., Weigold P. R., Laufer K., Kleindienst S., Byrne J. M., Sundman A., Hanselman K., Halevy I., Schoenberg R. (2018) A case study for late Archean and Proterozoic biogeochemical iron-and sulphur cycling in a modern habitat—the Arvadi Spring. *Geobiology* **16,** 353-368.

Konhauser K. O., Hamade T., Raiswell R., Morris R. C., Ferris F. G., Southam G., & Canfield D. E. (2002) Could bacteria have formed the Precambrian banded iron formations. *Geology* **30(12)**, 1079-1082.

Konhauser K. O., Amskold L., Lalonde S. V., Posth N. R., Kappler A., & Anbar A. (2007) Decoupling photochemical Fe (II) oxidation from shallow-water BIF deposition. *Earth and Planetary Science Letters* **258(1-2)**, 87-100.

Koppi A. J., Edis R., Field D. J., Geering H. R., Klessa D. A., & Cockayne D. J. (1996) Rare earth element trends and cerium-uranium-manganese associations in weathered rock from Koongarra, Northern Territory, Australia. *Geochimica et Cosmochimica Acta* **60(10)**, 1695-1707.

König S., Wille M., Voegelin A., & Schoenberg R. (2016) Molybdenum isotope systematics in subduction zones. *Earth and Planetary Science Letters* **447**, 95-102.

Kraemer T. F., & Genereux D. P. (1998) Applications of uranium-and thorium-series radionuclides in catchment hydrology studies. *Isotope Tracers in Catchment Hydrology*, (eds. C. Kendall and J. J. McDonnell). Elsevier, Netherlands. pp. 679-722.

Ku T. L., Knauss K. G., Mathieu G. G. (1977) Uranium in open ocean—concentration and isotopic composition. *Deep- Sea Res* **24**, 1005–1017.

Kump L. R., & Barley M. E. (2007) Increased subaerial volcanism and the rise of atmospheric oxygen 2.5 billion years ago. *Nature* **448(7157)**, 1033.

Kurzweil F., Wille M., Schoenberg R., Taubald H., & Van Kranendonk M. J. (2015) Continuously increasing δ^{98}Mo values in Neoarchean black shales and iron formations from the Hamersley Basin. *Geochimica et Cosmochimica Acta* **164**, 523-542.

Kurzweil F., Wille M., Gantert N., Beukes N. J., & Schoenberg R. (2016) Manganese oxide shuttling in pre-GOE oceans–evidence from molybdenum and iron isotopes. *Earth and Planetary Science Letters* **452**, 69-78.

Lalonde S. V., & Konhauser K. O. (2015) Benthic perspective on Earth's oldest evidence for oxygenic photosynthesis. *Proceedings of the National Academy of Sciences* **112(4)**, 995-1000.

Landing W. M., & Bruland K. W. (1987) The contrasting biogeochemistry of iron and manganese in the Pacific Ocean. *Geochimica et Cosmochimica Acta* **51(1)**, 29-43.

Langmuir D. (1978) Uranium solution-mineral equilibria at low temperatures with applications to sedimentary ore deposits. *Geochimica et Cosmochimica Acta* **42(6)**, 547-569.

Larsen K., Wielandt D., Schiller M., Bizzarro M. (2016) Chromatographic speciation of Cr (III)-species, inter-species equilibrium isotope fractionation and improved chemical purification strategies for high-precision isotope analysis. *J Chromatogr A* **1443**, 162−174.

Latta D. E., Mishra B., Cook R. E., Kemner K. M. & Boyanov M. I. (2014) Stable U(IV) complexes form at high-affinity mineral surface sites. *Environmental science & technology* **48**, 1683-1691.

Lau K. V., Maher K., Altiner D., Kelley B. M., Kump L. R., Lehrmann D. J., Silva-Tamayo J. C., Weaver K. L., Yu M., Payne J. L. (2016) Marine anoxia and delayed Earth system recovery after the end-Permian extinction. *PNAS* **113**, 2360–2365.

Lawrence M.G. and Kamber B.S. (2006) The behaviour of the rare earth elements during estuarine mixing—revisited. *Marine Chemistry* **100**, 147-161.

Lin S.L., He M., Hu S.H., Yuan H.L. and Gao S. (2000) Precise determination of trace elements in geological samples by ICP-MS using compromise conditions and fine matrix-matching strategy. *Anal Sci* **16**, 1291-1296.

Lohmayer R., Kappler A., Lösekann-Behrens T., & Planer-Friedrich B. (2014) Role of sulfur species as redox partners and electron shuttles for ferrihydrite reduction by Sulfurospirillum deleyianum. *Applied and environmental microbiology* AEM-04220.

Lu X., Kendall B., Stein H. J., Li C., Hannah J. L., Gordon G. W., & Ebbestad J. O. R. (2017) Marine redox conditions during deposition of Late Ordovician and Early Silurian organic-rich mudrocks in the Siljan ring district, central Sweden. *Chemical Geology* **457**, 75-94.

Luo G., Ono S., Beukes N. J., Wang D. T., Xie S., & Summons R. E. (2016) Rapid oxygenation of Earth's atmosphere 2.33 billion years ago. *Science Advances* **2(5)**, e1600134.

Lyons T. W., Reinhard C. T., & Planavsky N. J. (2014) The rise of oxygen in Earth's early ocean and atmosphere. *Nature* **506(7488)**, 307.

Ma L., Chabaux F., Pelt E., Blaes E., Jin L., Brantley S. (2010) Regolith production rates calculated with uranium-series isotopes at Susquehanna/Shale Hills Critical Zone Observatory. *Earth and Planetary Science Letters* **297**, 211-225.

Ma L., Chabaux F., Pelt E., Granet M., Sak P.B., Gaillardet J., Lebedeva M., Brantley S.L. (2012) The effect of curvature on weathering rind formation: Evidence from Uranium-series isotopes in

basaltic andesite weathering clasts in Guadeloupe. *Geochimica et Cosmochimica Acta* **80**, 92-107.

Ma L., Chabaux F., West N., Kirby E., Jin L., Brantley S. (2013) Regolith production and transport in the Susquehanna Shale Hills Critical Zone Observatory, Part 1: Insights from U-series isotopes. *Journal of Geophysical Research: Earth Surface* **118**, 722-740.

Malinovsky D., Hammarlund D., Ilyashuk B., Martinsson O., & Gelting J. (2007) Variations in the isotopic composition of molybdenum in freshwater lake systems. *Chemical Geology* **236(3-4)**, 181-198.

Malinovsky D., & Kashulin N. A. (2018) Molybdenum isotope fractionation in plants measured by MC-ICPMS. *Analytical Methods* **10(1)**, 131-137.

Maréchal C., Télouk P., Albarède F. (1999) Precise analysis of copper and zinc isotopic compositions by plasma-source mass spectrometry. *Chem Geol* **156**, 251−273.

Marshall T. A., Morris K., Law G. T., Livens F. R., Mosselmans J. F. W., Bots P., & Shaw S. (2014) Incorporation of uranium into hematite during crystallization from ferrihydrite. *Environmental science & technology*, **48**, 3724-3731.

Martin J. H. (1990) Glacial-interglacial CO2 change: The iron hypothesis. *Paleoceanography* **5(1)**, 1-13.

Martin J. H., & Fitzwater S. E. (1988) Iron deficiency limits phytoplankton growth in the north-east Pacific subarctic. *Nature* **331(6154)**, 341.

Matthews R. (1967) Diagenetic fabrics in biosparites from the Pleistocene of Barbados, West Indies. *Journal of Sedimentary Research* **37,** 1147-1153.

Matthews A., Morgans-Bell H. S., Emmanuel S., Jenkyns H. C., Erel Y., Halicz L. (2004) Controls on iron-isotope fractionation in organic-rich sediments (Kimmeridge Clay, Upper Jurassic, southern England). *Geochim Cosmochim Acta* **68**, 3107−3123.

McClain C., Maher K. (2016) Chromium fluxes and speciation in ultramafic catchments and global rivers. *Chem Geol* **426**, 135−157.

McLennan S. M., Taylor S. and Kröner A. (1983) Geochemical evolution of Archean shales from South Africa. I. The Swaziland and Pongola Supergroups. *Precambrian Res* **22**, 93-124.

McManus J., Berelson W. M., Severmann S., Poulson R. L., Hammond D. E., Klinkhammer G. P., & Holm C. (2006) Molybdenum and uranium geochemistry in continental margin sediments: paleoproxy potential. *Geochimica et Cosmochimica Acta* **70(18)**, 4643-4662.

Menozzi D., Dosseto A., Kinsley L.P.J. (2016) Assessing the effect of sequential extraction on the uranium-series isotopic composition of a basaltic weathering profile. *Chemical Geology* **446**, 126-137.

Miller C. A., Peucker-Ehrenbrink B., Walker B. D. and Marcantonio, F. (2011) Re-assessing the surface cycling of molybdenum and rhenium. *Geochim Cosmochim Acta* **75**, 7146-7179.

Millero, F. J. (1985) The effect of ionic interactions on the oxidation of metals in natural waters. *Geochimica et Cosmochimica Acta* **49(2)**, 547-553.

Mills C. T., Morrison J. M., Goldhaber M. B. and Ellefsen K. J. (2011) Chromium(VI) generation in vadose zone soils and alluvial sediments of the southwestern Sacramento Valley, California: A potential source of geogenic Cr(VI) to groundwater. *Appl Geochem* **26**, 1488-1501.

Moeller K., Schoenberg R., Grenne T., Thorseth I. H., Drost K., & Pedersen R. B. (2014) Comparison of iron isotope variations in modern and Ordovician siliceous Fe oxyhydroxide deposits. *Geochimica et cosmochimica acta* **126**, 422-440.

Montoya-Pino C., Weyer S., Anbar A. D., Pross J., Oschmann W., van de Schootbrugge B., Arz H. W. (2010) Global enhancement of ocean anoxia during Oceanic Anoxic Event 2: A quantitative approach using U isotopes. *Geology* **38**, 315–318.

Moorbath S., O'Nions R. K., Pankhurst R. J., Gale N. H. and McGregor V. R. (1972) Further rubidium–strontium age determinations of the very early Precambrian rocks of the Godthaab district, West Greenland. *Nature Phys. Sci.* **240**, 78–82.

Moorbath S., O'Nions R. K., Pankhurst R. J. (1973) Early Archean age for the Isua iron formation, West Greenland. *Nature* **245**, 138–139.

Moorbath S., O'Nions R. K., Pankhurst R. J. (1975) The evolution of early Precambrian crustal rocks at Isua, West Greenland—geochemical and isotopic evidence. *Earth Planet. Sci. Lett.* **27**, 229–239.

Moorbath S., & Kamber B. S. (1998) Re-appraisal of the age of the oldest water-lain sediments, West Greenland. In *Exobiology: Matter, Energy, and Information in the Origin and Evolution of Life in the Universe.* Springer, Dordrecht, 81-86.

Moore J. K., Doney S. C., Glover D. M., Fung I. Y. (2002) Iron cycling and nutrient-limitation patterns in surface waters of the World Ocean. *Deep Sea Res Part II* **49**, 463–507.

Moragues-Quiroga C., Juilleret J., Gourdol L., Pelt E., Perrone T., Aubert A., Morvan G., Chabaux F., Legout A., Stille P., Hissler C. (2017) Genesis and evolution of regoliths: Evidence from trace and major elements and Sr-Nd-Pb-U isotopes. *Catena* **149(1)**, 185-198.

Moreira-Nordemann L. M. (1980) Use of $^{234}U/^{238}U$ disequilibrium in measuring chemical weathering rate of rocks. *Geochimica et Cosmochimica Acta* **44(1)**, 103-108.

Morford J. L. and Emerson S. (1999) The geochemistry of redox sensitive trace metals in sediments. *Geochim Cosmochim Acta* **63**, 1735-1750.

Morris R. C. (1993) Genetic modelling for banded iron-formation of the Hamersley Group, Pilbara Craton, Western Australia. *Precambrian Research* **60(1-4)**, 243-286.

Moynier F., Yin Q. Z., Schauble E. (2011) Isotopic evidence of Cr partitioning into Earth's core. *Science* **331**, 1417−1420.

Mukasa S.B., Wilson A.H. and Young K.R. (2013) Geochronological constraints on the magmatic and tectonic development of the Pongola Supergroup (Central Region), South Africa. *Precambrian Res* **224**, 268-286.

Nägler T. F., Anbar A. D., Archer C., Goldberg T., Gordon G. W., Greber N. D., & Vance D. (2014) Proposal for an international molybdenum isotope measurement standard and data representation. *Geostandards and Geoanalytical Research* **38(2)**, 149-151.

Nägler T. F., Neubert N., Bottcher M. E., Dellwig O. and Schnetger B. (2011) Molybdenum isotope fractionation in pelagic euxinia: Evidence from the modern Black and Baltic Seas. *Chem Geol* **289**, 1-11.

Nakagawa Y., Takano S., Firdaus M. L., Norisuye K., Hirata T., Vance D., Sohrin Y. (2012) The molybdenum isotopic composition of the modern ocean. *Geochem J* **46**, 131–141.

Nelson J. P., Beukes N. J., & Cairncross B. (1995) Tectono-stratigraphic setting of the∼ 2.9 Ga Mozaan Group of the Pongola Supergroup and correlation with the Witwatersrand Supergroup. *Ext. Abstr. Centennial Geocongress,* Geol. Soc. S. Afr.*,* Rand Afrikaans University **1**, 838-840.

Neubert N., Nägler T. F., Böttcher M. E. (2008) Sulfidity controls molybdenum isotope fractionation onto euxinic sediments: Evidence from the modern Black Sea. *Geology* **36**, 775–778.

Nhleko, N. (2003). *The Pongola Supergroup in Swaziland*. Ph. D. thesis, University of Johannesburg.

Nico P. S., Stewart B. D. & Fendorf S. (2009) Incorporation of oxidized uranium into Fe (hydr) oxides during Fe(II) catalyzed remineralization. *Environmental science & technology* **43**, 7391-7396.

Nielsen S. G., Rehkamper M., Teagle D. A. H., Butterfield D. A., Alt J. C. and Halliday A. N. (2006) Hydrothermal fluid fluxes calculated from the isotopic mass balance of thallium in the ocean crust. *Earth Planet Sc Lett* **251**, 120-133.

Noffke N., Beukes N., Bower D., Hazen R. M., & Swift D. J. P. (2008) An actualistic perspective into Archean worlds–(cyano-) bacterially induced sedimentary structures in the siliciclastic Nhlazatse Section, 2.9 Ga Pongola Supergroup, South Africa. *Geobiology* **6(1)**, 5-20.

Noordmann J., Weyer S., Montoya-Pino C., Dellwig O., Neubert N., Eckert S., Paetzel M., Böttcher M. E. (2015) Uranium and molybdenum isotope systematics in modern euxinic basins: Case studies from the central Baltic Sea and the Kyllaren fjord (Norway). *Chem Geol* **396**, 182–195.

Noordmann J., Weyer S., Georg R. B., Jöns S., & Sharma M. (2016) $^{238}U/^{235}U$ isotope ratios of crustal material, rivers and products of hydrothermal alteration: new insights on the oceanic U isotope mass balance. *Isotopes in environmental and health studies* **52(1-2)**, 141-163.

Novak M., Chrastny V., Cadkova E., Farkas J., Bullen T. D., Tylcer J. & Stepanova M. (2014) Common occurrence of a positive δ53Cr shift in Central European waters contaminated by geogenic/industrial chromium relative to source values. *Environmental science & technology* **48**, 6089-6096.

Ohnuki T., Ozaki T., Kozai N., Nankawa T., Sakamoto F., Sakai T., & Francis A. J. (2008) Concurrent transformation of Ce (III) and formation of biogenic manganese oxides. *Chemical Geology* **253(1-2)**, 23-29.

Ohta A., & Kawabe I. (2001) REE (III) adsorption onto Mn dioxide (δ-MnO_2) and Fe oxyhydroxide: Ce (III) oxidation by δ-MnO_2. *Geochimica et Cosmochimica Acta* **65(5)**, 695-703.

Olson S. L., Kump L. R., & Kasting J. F. (2013) Quantifying the areal extent and dissolved oxygen concentrations of Archean oxygen oases. *Chemical Geology* **362**, 35-43.

Osmond J. K., & Cowart J. B. (1976) The theory and uses of natural uranium isotopic variations in hydrology. *Atomic Energy Review* **14(4)**, 621-679.

Ossa F. O., Hofmann A., Vidal O., Kramers J. D., Belyanin G., & Cavalazzi B. (2016) Unusual manganese enrichment in the Mesoarchean Mozaan Group, Pongola Supergroup, South Africa. *Precambrian Research* **281**, 414-433.

Ossa F. O., Hofmann A, Wille M., Spangenberg J. E., Bekker A., Poulton S. W., Eickmann, B., and Schoenberg R. (2018) Aerobic iron and manganese cycling in a redox-stratified Mesoarchean epicontinental sea. *Earth and Planetary Science Letters* **500**, 28-40.

Oze C., Bird D.K. and Fendorf S. (2007) Genesis of hexavalent chromium from natural sources in soil and groundwater. *P Natl Acad Sci USA* **104**, 6544-6549.

Paces J. B., Ludwig K. R., Peterman Z. E., & Neymark L. A. (2002) $^{234}U/^{238}U$ evidence for local recharge and patterns of ground-water flow in the vicinity of Yucca Mountain, Nevada, USA. *Applied Geochemistry* **17(6)**, 751-779.

Pack A., Russell S. S., Shelley J. M. G. & Van Zuilen M. (2007) Geo-and cosmochemistry of the twin elements yttrium and holmium. *Geochimica et Cosmochimica Acta* **71**, 4592-4608.

Partin C. A., Lalonde S. V., Planavsky N. J., Bekker A., Rouxel O. J., Lyons T. W., & Konhauser K. O. (2013). Uranium in iron formations and the rise of atmospheric oxygen. *Chemical Geology* **362**, 82-90.

Paulukat C., Døssing L. N., Mondal S. K., Voegelin A. R. & Frei R. (2015) Oxidative release of chromium from Archean ultramafic rocks, its transport and environmental impact–A Cr isotope perspective on the Sukinda valley ore district (Orissa, India). *Applied Geochemistry* **59**, 125-138.

Pavlov A.A. and Kasting J.F. (2002) Mass-independent fractionation of sulfur isotopes in Archean sediments: Strong evidence for an anoxic Archean atmosphere. *Astrobiology* **2**, 27-41.

Pelt E., Chabaux F., Innocent C., Navarre-Sitchler A.K., Sak P.B., Brantley S.L. (2008) Uranium–thorium chronometry of weathering rinds: Rock alteration rate and paleo-isotopic record of weathering fluids. *Earth and Planetary Science Letters* **276**, 98-105.

Pereira N. S., Vögelin A. R., Paulukat C., Sial A. N., Ferreira V. P., Frei R. (2015) Chromium-isotope signatures in scleractinian corals from the Rocas Atoll, Tropical South Atlantic. *Geobiology* **4**, 1–13.

Piper D. Z. (1974) Rare earth elements in ferromanganese nodules and other marine phases. *Geochimica et Cosmochimica Acta* **38(7)**, 1007-1022.

Planavsky N. J., Asael D., Hofmann A., Reinhard C. T., Lalonde S. V., Knudsen A., & Beukes N. J. (2014a) Evidence for oxygenic photosynthesis half a billion years before the Great Oxidation Event. *Nature Geoscience* **7(4)**, 283.

Planavsky N., Bekker A., Rouxel O. J., Kamber B., Hofmann A., Knudsen A., & Lyons T. W. (2010) Rare earth element and yttrium compositions of Archean and Paleoproterozoic Fe formations revisited: new perspectives on the significance and mechanisms of deposition. *Geochimica et Cosmochimica Acta* **74(22)**, 6387-6405.

Planavsky N. J., Reinhard C. T., Wang X., Thomson D., McGoldrick P., Rainbird R. H., & Lyons T. W. (2014b) Low Mid-Proterozoic atmospheric oxygen levels and the delayed rise of animals. *Science* **346(6209)**, 635-638.

Potts P.J. and Kane J.S. (2005) International Association of Geoanalysts Certificate of Analysis: Certified Reference Material OU-6 (Penrhyn Slate). *Geostandards and Geoanalytical Research* **29**, 233-236.

Potts P.J., Thompson H., Chenery S., Webb P.C. and Batjargal B. (2003) GeoPT12-An international proficiency test for analytical geochemistry laboratories-report on round 12/January 2003 (GAS serpentinite). International Association of Geoanalysts.

Prytulak J., Elliott T., Hoffmann D.L., Coath C.D., (2008) Assessment of USGS BCR-2 as a reference material for silicate rock u-pa disequilibrium measurements. *Geostandards and Geoanalytical Research* **32(1)**. 55-63.

Radic A., Lacan F., Murray J. W. (2011) Iron isotopes in the seawater of the equatorial Pacific Ocean: New constraints for the oceanic iron cycle. *Earth Planet Sci Lett* **306**, 1–10.

Raiswell R., & Canfield D. E. (1996) Rates of reaction between silicate iron and dissolved sulfide in Peru Margin sediments. *Geochimica et Cosmochimica Acta* **60(15)**, 2777-2787.

Rasmussen B., Fletcher I.R., Brocks J.J. and Kilburn M.R. (2008) Reassessing the first appearance of eukaryotes and cyanobacteria. *Nature* **455**, 1101-U1109.

Reinhard C. T., Planavsky N. J., Robbins L. J., Partin C. A., Gill B. C., Lalonde S. V., Bekker A., Konhauser K. O. and Lyons T. W. (2013) Proterozoic ocean redox and biogeochemical stasis. *P Natl Acad Sci USA* **110**, 5357-5362.

Reinhard C.T., Raiswell R., Scott C., Anbar A.D. and Lyons T.W. (2009) A Late Archean Sulfidic Sea Stimulated by Early Oxidative Weathering of the Continents. *Science* **326**, 713-716.

Reinhard CT, Planavsky NJ, Wang X, Fischer WW, Johnson TM, Lyons TW (2014) The isotopic composition of authigenic chromium in anoxic marine sediments: A case study from the Cariaco Basin. Earth Planet Sci Lett 407:9–18.

Rezzoug S., Fernex F., Michel H., Barci-Funel G., Barci V. (2009) Behavior of uranium and thorium isotopes in soils of the Boréon area, Mercantour Massif (S.E. France): Leaching and weathering rate modeling. *Journal of Radioanalytical and Nuclear Chemistry* **279**, 801-809.

Richter S., Alonso A., De Bolle W., Kühn H., Verbruggen A., Wellum R., & Taylor P. D. P. (2005) Re-certification of a series of uranium isotope reference materials: IRMM-183, IRMM-184, IRMM-185, IRMM-186 and IRMM-187. *International Journal of Mass Spectrometry* **247(1-3)**, 37-39.

Richter S., Alonso-Munoz A., Eykens R., Jacobsson U., Kuehn H., Verbruggen, A., Aregbe Y., Wellum R., & Keegan, E. (2008) The isotopic composition of natural uranium samples—

Measurements using the new n (^{233}U)/n (^{236}U) double spike IRMM-3636. *International Journal of Mass Spectrometry* **269(1-2)**, 145-148.

Richter S., Eykens R., Kühn H., Aregbe Y., Verbruggen A., & Weyer S. (2010) New average values for the n (^{238}U)/n (^{235}U) isotope ratios of natural uranium standards. *International Journal of Mass Spectrometry* **295(1-2)**, 94-97.

Riding R., Fralick P., & Liang L. (2014) Identification of an Archean marine oxygen oasis. *Precambrian Research* **251**, 232-237.

Riotte J., & Chabaux F. (1999) (^{234}U/^{238}U) activity ratios in freshwaters as tracers of hydrological processes: the Strengbach watershed (Vosges, France). *Geochimica et Cosmochimica Acta* **63(9)**, 1263-1275.

Robbins L. J., Lalonde S. V., Planavsky N. J., Partin C. A., Reinhard C. T., Kendall B. & Dupont C. L. (2016) Trace elements at the intersection of marine biological and geochemical evolution. *Earth-Science Reviews* **163**, 323-348.

Romaniello S. J., Herrmann A. D., Anbar A. D. (2013) Uranium concentrations and ^{238}U/^{235}U isotope ratios in modern carbonates from the Bahamas: assessing a novel paleoredox proxy. *Chem Geol* **362**, 305–316.

Roscoe S. M. (1973) The Huronian Supergroup, a Paleoaphebian succession showing evidence of atmospheric evolution. *Geological Association of Canada, Special Paper* **12**, 31-47.

Rosholt J. N., Doe B. R., & Tatsumoto M. (1966) Evolution of the isotopic composition of uranium and thorium in soil profiles. *Geological Society of America Bulletin* **77(9)**, 987-1004.

Rossman K. J. R., Taylor P. D. P. (1998) Isotopic composition of the elements. Pure Appl Geophys **70**, 217−236.

Rouxel O. J., Bekker A., Edward K. J. (2006) Response to comment on “Iron isotope constraints on the archean and paleoproterozoic ocean redox state”. *Science* **311**.

Rouxel O., Fouquet Y., & Ludden J. N. (2004). Subsurface processes at the lucky strike hydrothermal field, Mid-Atlantic ridge: evidence from sulfur, selenium, and iron isotopes 1. *Geochimica et Cosmochimica Acta* **68(10)**, 2295-2311.

Rouxel O., Shanks W. C., Bach W., & Edwards K. J. (2008) Integrated Fe-and S-isotope study of seafloor hydrothermal vents at East Pacific Rise 9–10 N. *Chemical Geology* **252(3)**, 214-227.

Rouxel O., Toner B. M., Manganini S. J., & German C. R. (2016) Geochemistry and iron isotope systematics of hydrothermal plume fall-out at East Pacific Rise 9 50’ N. *Chemical Geology* **441**, 212-234.

Roy S. (2000) Late Archean initiation of manganese metallogenesis: its significance and environmental controls. *Ore Geology Reviews* **17(3)**, 179-198.

Roy S. (2006) Sedimentary manganese metallogenesis in response to the evolution of the Earth system. *Earth-Science Reviews* **77(4)**, 273-305.

Rudge J. F., Reynolds B. C., & Bourdon B. (2009) The double spike toolbox. *Chemical Geology* **265(3- 4)**, 420-431.

Rudnick R. L. & Gao S. (2003) Composition of the continental crust. *Treatise on geochemistry* **3**, 659.

Rudnick R. and Gao S. (2003) The role of lower crustal recycling in continent formation. *Geochimica Et Cosmochimica Acta* **67**, A403-A403.

Rush J. D., & Bielski B. H. (1985) Pulse radiolytic studies of the reaction of perhydroxyl/superoxide O2-with iron (II)/iron (III) ions. The reactivity of HO2/O2-with ferric ions and its implication on the occurrence of the Haber-Weiss reaction. *The Journal of Physical Chemistry* **89(23)**, 5062-5066.

Saad E. M., Wang X., Planavsky N. J., Reinhard C. T. & Tang Y. (2017) Redox-independent chromium isotope fractionation induced by ligand-promoted dissolution. *Nature Communications* **8**, 1590.

SACS. (1980) Stratigraphy of South Africa, Part 1: Lithostratigraphy of the Republic of South Africa, South West Africa/Namibia and the Republics of Bophuthatswana, Transkei and Venda. *Geological Survey of South Africa Handbook*. (ed. L. E Kent). pp. 1-690.

Satkoski A.M., Beukes N.J., Li W.Q., Beard B.L. and Johnson C.M. (2015) A redox-stratified ocean 3.2 billion years ago. *Earth Planet Sc Lett* **430**, 43-53.

Schauble E. (2004) Applying stable isotope fractionation theory to new systems. *Rev Mineral Geochem* **55**, 65−111.

Scheiderich K., Amini M., Holmden C. & Francois R. (2015) Global variability of chromium isotopes in seawater demonstrated by Pacific, Atlantic, and Arctic Ocean samples. *Earth and Planetary Science Letters* **423**, 87-97.

Schidlowski M. (1983) Evolution of photoautotrophy and early atmospheric oxygen levels. *Precambrian Research* **20(2-4)**, 319-335.

Schoenberg R., & von Blanckenburg F. (2005) An assessment of the accuracy of stable Fe isotope ratio measurements on samples with organic and inorganic matrices by high-resolution multicollector ICP-MS. *International Journal of Mass Spectrometry* **242(2-3)**, 257-272.

Schoenberg R., Zink S., Staubwasser M. and von Blanckenburg F. (2008) The stable Cr isotope inventory of solid Earth reservoirs determined by double spike MC-ICP-MS. *Chem Geol* **249**, 294-306.

Schoenberg R., Merdian A., Holmden C., Kleinhanns I.C., Hassler K., Wille M. and Reitter E. (2016) The stable Cr isotopic compositions of chondrites and silicate planetary reservoirs. *Geochimica Et Cosmochimica Acta* **183**, 14-30.

Scholz F., McManus J., & Sommer S. (2013) The manganese and iron shuttle in a modern euxinic basin and implications for molybdenum cycling at euxinic ocean margins. *Chemical Geology* **355**, 56-68.

Scott C., Lyons T. W., Bekker A., Shen Y., Poulton S. W., Chu X., Anbar A. D. (2008) Tracing the stepwise oxygenation of the Proterozoic ocean. *Nature* **452**, 456–459.

Severmann S., Johnson C. M., Beard B. L., German C. R., Edmonds H. N., Chiba H., & Green D. R. H. (2004) The effect of plume processes on the Fe isotope composition of hydrothermally derived Fe in the deep ocean as inferred from the Rainbow vent site, Mid-Atlantic Ridge, 36 14′ N. *Earth and Planetary Science Letters* **225(1-2)**, 63-76.

Severmann S., Johnson C. M., Beard B. L., McManus, J. (2006) The effect of early diagenesis on the Fe isotope compositions of porewaters and authigenic minerals in continental margin sediments. *Geochim Cosmochim Acta* **70**, 2006–2022.

Sharma M., Polizzotto M., & Anbar A. D. (2001) Iron isotopes in hot springs along the Juan de Fuca Ridge. *Earth and Planetary Science Letters* **194(1-2)**, 39-51.

Shih P. M., Hemp J., Ward L. M., Matzke N. J. and Fischer W. W. (2017) Crown group Oxyphotobacteria postdate the rise of oxygen. *Geobiology* **15**, 19-29.

Sholkovitz E.R., Landing W.M. and Lewis B.L. (1994) Ocean Particle Chemistry - the Fractionation of Rare-Earth Elements between Suspended Particles and Seawater. *Geochimica Et Cosmochimica Acta* **58**, 1567-1579.

Siebert C., Nägler T. F., & Kramers J. D. (2001) Determination of molybdenum isotope fractionation by double-spike multicollector inductively coupled plasma mass spectrometry. *Geochemistry, Geophysics, Geosystems* **2(7)**.

Siebert C., Nägler T. F., von Blanckenburg F., & Kramers, J. D. (2003) Molybdenum isotope records as a potential new proxy for paleoceanography. *Earth and Planetary Science Letters* **211(1-2)**, 159-171.

Sikora E. R., Johnson T. M., Bullen T. D. (2008) Microbial mass-dependent fractionation of chromium isotopes. *Geochim Cosmochim Acta* **72**, 3631−3641.

Skulan J. L., Beard B. L., Johnson C. M. (2002) Kinetic and equilibrium Fe isotope fractionation between aqueous Fe (III) and hematite. *Geochim Cosmochim Acta* **66**, 2995−3015.

Smith A. J. B. (2007) The paleo-environmental significance of the iron-formations and iron-rich mudstones of the Mesoarchean Witwatersrand-Mozaan Basin, South Africa. Ph. D. thesis. University of Johannesburg.

Staton S., Amskold L., Gordon G., Anbar A., & Konhauser K. (2006) Iron isotope fractionation during photo-oxidation of aqueous ferrous iron. In *AGU Spring Meeting Abstracts*.

Staubwasser M., Von Blanckenburg F., & Schoenberg R. (2006) Iron isotopes in the early marine diagenetic iron cycle. *Geology* **34(8)**, 629-632.

Steinhoefel G., Horn I., & von Blanckenburg F. (2009) Micro-scale tracing of Fe and Si isotope signatures in banded iron formation using femtosecond laser ablation. *Geochimica et Cosmochimica Acta* **73(18)**, 5343-5360.

Stirling C. H., Andersen M. B., Potter E. K., & Halliday A. N. (2007) Low-temperature isotopic fractionation of uranium. *Earth and Planetary Science Letters* **264(1-2)**, 208-225.

Strauss H., Chmiel H., Christ A., Fugmann A., Hanselmann K., Kappler A., Königer P., Lutter A., Siedenberg K. and Teichert B. M. (2016). Multiple sulphur and oxygen isotopes reveal microbial sulphur cycling in spring waters in the Lower Engadin, Switzerland. *Isotopes in environmental and health studies* **52(1-2)**, 75-93.

Stylo M., Neubert N., Wang Y., Monga N., Romaniello S. J., Weyer S., & Bernier-Latmani R. (2015) Uranium isotopes fingerprint biotic reduction. *Proceedings of the National Academy of Sciences* **112(18)**, 5619-5624.

Suhr N., Widdowson M., McDermott F., & Kamber B. S. (2018) Th/U and U series systematics of saprolite: importance for the oceanic ^{234}U excess. *Geochemical Perspectives Letters* **6**, 17-22.

Suksi J., Rasilainen K., & Pitkänen P. (2006) Variations in $^{234}U/^{238}U$ activity ratios in groundwater—A key to flow system characterisation. *Physics and Chemistry of the Earth, Parts A/B/C*, **31(10-14)**, 556-571.

Suresh P.O., Dosseto A., Hesse P.P., Handley H.K. (2013) Soil formation rates determined from Uranium-series isotope disequilibria in soil profiles from the southeastern Australian highlands. *Earth and Planetary Science Letters* **379**, 26-37.

Swanner E. D., Mloszewska A. M., Cirpka O. A., Schoenberg R., Konhauser K. O., & Kappler A. (2015) Modulation of oxygen production in Archean oceans by episodes of Fe (II) toxicity. *Nature Geoscience* **8(2)**, 126-130.

Swanner E. D., Bayer T., Wu W., Hao L., Obst M., Sundman A., & Schoenberg R. (2017) Iron Isotope Fractionation during Fe (II) Oxidation Mediated by the Oxygen-Producing Marine Cyanobacterium Synechococcus PCC 7002. *Environmental Science & Technology* **51(9)**, 4897-4906.

Takahashi Y., Manceau A., Geoffroy N., Marcus M. A., & Usui A. (2007) Chemical and structural control of the partitioning of Co, Ce, and Pb in marine ferromanganese oxides. *Geochimica et Cosmochimica Acta* **71(4)**, 984-1008.

Takahashi Y., Shimizu H., Usui A., Kagi H., & Nomura M. (2000) Direct observation of tetravalent cerium in ferromanganese nodules and crusts by X-ray-absorption near-edge structure (XANES). *Geochimica et Cosmochimica Acta* **64(17)**, 2929-2935.

Tankard A.J. and Barwis J.H. (1982) Wave-Dominated Deltaic Sedimentation in the Devonian Bokkeveld Basin of South-Africa. *J Sediment Petrol* **52**, 959-974.

Taylor S. and McLennan S. (1985) The continental crust: its evolution and composition. London: Blackwell Science Publishers.

Taylor P. D. P., Maeck R. and De Bievre P. (1992) Determination of the Absolute Isotopic Composition and Atomic-Weight of a Reference Sample of Natural Iron. *International Journal of Mass Spectrometry and Ion Processes* **121**, 111-125.

Teng F. Z., Dauphas N., & Watkins J. M. (2017) Non-traditional stable isotopes: retrospective and prospective. *Reviews in Mineralogy and Geochemistry* **82(1)**, 1-26.

Tissot F. L. H., Dauphas N. (2015) Uranium isotopic compositions of the crust and ocean: age corrections, U budget and global extent of modern anoxia. *Geochim Cosmochim Acta* **167**, 113–143.

Tosca N. J., Guggenheim S., & Pufahl P. K. (2016) An authigenic origin for Precambrian greenalite: Implications for iron formation and the chemistry of ancient seawater. *Bulletin* **128(3-4)**, 511-530.

Tossell J. A. (2005) Calculating the partitioning of the isotopes of Mo between oxidic and sulfidic species in aqueous solution. *Geochim Cosmochim Ac* **69**, A210-A210.

Trendall A. F., Altermann W., & Corcoran P. L. (2002) The significance of iron-formation in the Precambrian stratigraphic record. *Precambrian sedimentary environments: a modern approach to depositional systems. IAS Spec Publ* **44**, 33-66.

Tribovillard N., Algeo T. J., Lyons T. and Riboulleau A. (2006) Trace metals as paleoredox and paleoproductivity proxies: An update. *Chem Geol* **232**, 12-32.

Towe K. M. (1990) Aerobic respiration in the Archean. *Nature* **348(6296)**, 54.

Tsikos H., Matthews A., Erel Y., & Moore J. M. (2010) Iron isotopes constrain biogeochemical redox cycling of iron and manganese in a Palaeoproterozoic stratified basin. *Earth and Planetary Science Letters* **298(1-2)**, 125-134.

Ulrich T., Kamber B.S., Woodhead J.D. and Spencer L.A. (2010) Long-Term Observations of Isotope Ratio Accuracy and Reproducibility Using Quadrupole ICP-MS. *Geostandards and Geoanalytical Research* **34**, 161-174.

Urey H. C. (1947) The thermodynamic properties of isotopic substances. *Journal of the Chemical Society (Resumed)* 562-581.

Valley J. W., Cole D. R. E. (Eds.) (2001) Stable Isotope Geochemistry. Rev Mineral Geochem 43, Mineralogical Society of America and the Geochemical Society, Washington DC.

Valley J. W., Taylor H. P., O'Neil J. R. (1986) Stable Isotopes in High-Temperature Geological Processes. Rev Mineral 16. The Mineralogical Society of America, Washington DC.

Van Cappellen P. and Wang Y. (1996) Cycling of iron and manganese in surface sediments; a general theory for the coupled transport and reaction of carbon, oxygen, nitrogen, sulfur, iron, and manganese. *American Journal of Science* **296**, 197-243.

Viehmann S., Hoffmann J.E., Munker C. and Bau M. (2014) Decoupled Hf-Nd isotopes in Neoarchean seawater reveal weathering of emerged continents. *Geology* **42**, 115-118.

Voegelin A. R., Nägler T. F., Beukes N. J., & Lacassie J. P. (2010) Molybdenum isotopes in late Archean carbonate rocks: implications for early Earth oxygenation. *Precambrian Research* **182(1-2)**, 70-82.

Von Brunn V. and Hobday D.K. (1976) Early precambrian tidal sedimentation in the Pongola supergroup of South Africa. *Journal of Sedimentary Research* **46**, 670-679.

Von Brunn V. and Mason T. (1977) Siliciclastic—carbonate tidal deposits from the 3000 MY Pongola Supergroup, South Africa. *Sedimentary Geology* **18**, 245-255.

Vorlicek T. P., Kahn M. D., Kasuya Y., Helz G. R. (2004) Capture of molybdenum in pyrite-forming sediments: role of ligand-induced reduction by polysulfides. *Geochim Cosmochim Acta* **68**, 547–556.

Wang D. T., Fregoso D. C., Ellis A. S., Johnson T. M., Bullen T. D. (2010) Stable isotope fractionation during chromium(III) oxidation by δ-MnO_2. Abstract H53F−1109 Fall Meeting, AGU, San Francisco.

Wang X. L., Johnson T. M., Ellis A. S. (2015) Equilibrium isotopic fractionation and isotopic exchange kinetics between Cr(III) and Cr(VI). *Geochim Cosmochim Acta* **153**, 72–90.

Wang X. L., Planavsky N. J., Reinhard C. T., Zou H. J., Ague J. J., Wu Y. B., Gill B. C., Schwarzenbach E. M., Peucker- Ehrenbrink B. (2016) Chromium isotope fractionation during subduction-related metamorphism, black shale weathering, and hydrothermal alteration. *Chem Geol* **423**, 19–33.

Wang Z., Ulrich K. U., Pan C., & Giammar D. E. (2015) Measurement and modeling of U(IV) adsorption to metal oxide minerals. *Environmental Science & Technology Letters* **2**, 227-232.

Wasylenki L.E., Rolfe B.A., Weeks C.L., Spiro T.G. and Anbar A.D. (2008) Experimental investigation of the effects of temperature and ionic strength on Mo isotope fractionation during adsorption to manganese oxides. *Geochimica Et Cosmochimica Acta* **72**, 5997-6005.

Weilers B. F. (1990) *A review of the Pongola Supergroup and its setting on the Kaapvaal Craton*. University of the Witwatersrand, Johannesburg.

Welch S. A., Beard B. L., Johnson C. M., Braterman P. S. (2003) Kinetic and equilibrium Fe isotope fractionation between aqueous Fe(II) and Fe(III). *Geochim Cosmochim Acta* **67**, 4231−4250.

Weyer S., Anbar A. D., Gerdes A., Gordon G. W., Algeo T. J., & Boyle E. A. (2008) Natural fractionation of $^{238}U/^{235}U$. *Geochimica et Cosmochimica Acta* **72(2)**, 345-359.

Weyer S., & Schwieters J. B. (2003) High precision Fe isotope measurements with high mass resolution MC-ICPMS. *International Journal of Mass Spectrometry* **226(3)**, 355-368.

Wheat C. G., Mottl M. J., Rudnicki M. (2002) Trace element and REE composition of a low-temperature ridge-flank hydrothermal spring. *Geochim Cosmochim Acta* **66**, 3693–3705.

Whitehouse M. J., & Fedo C. M. (2003) Deformation features and critical field relationships of early Archean rocks, Akilia, southwest Greenland. *Precambrian Research* **126(3-4)**, 259-271.

Whitehouse M. J., & Fedo C. M. (2007) Searching for Earth's Earliest Life in Southern West Greenland–History, Current Status, and Future Prospects. *Developments in Precambrian Geology* **15**, 841-853.

Whitehouse M. J., & Kamber B. S. (2004) Assigning dates to thin gneissic veins in high-grade metamorphic terranes: a cautionary tale from Akilia, southwest Greenland. *Journal of Petrology* **46(2)**, 291-318.

Widdel F., Schnell S., Heising S., Ehrenreich A., Assmus B., & Schink B. (1993) Ferrous iron oxidation by anoxygenic phototrophic bacteria. *Nature* **362(6423)**, 834.

Wieser M. E., Holden N., Coplen T. B., Böhlke J. K., Berglund M., Brand W. A., & Hirata T. (2013) Atomic weights of the elements 2011 (IUPAC Technical Report). *Pure and Applied Chemistry* **85(5)**, 1047-1078.

Willbold M., & Elliott T. (2017) Molybdenum isotope variations in magmatic rocks. *Chemical Geology* **449**, 253-268.

Wille M., Babechuk M.G., Kleinhanns I.C., Stegmaier J., Suhr N., Widdowson M., Kamber B.S., Schoenberg R. (2018) Silicon and chromium stable isotopic systematics during basalt weathering and lateritisation: A comparison of variably weathered basalt profiles in the Deccan Traps, India. *Geoderma* **314**, 190-204.

Wille M., Kramers J. D., Nägler T. F., Beukes N. J., Schröder S., Meisel T., Lacassie J. P. & Voegelin, A. R. (2007) Evidence for a gradual rise of oxygen between 2.6 and 2.5 Ga from Mo isotopes and Re-PGE signatures in shales. *Geochimica et Cosmochimica Acta* **71(10)**, 2417-2435.

Wille M., Nebel O., Pettke T., Vroon P. Z., König S., & Schoenberg R. (2018) Molybdenum isotope variations in calc-alkaline lavas from the Banda arc, Indonesia: Assessing the effect of crystal fractionation in creating isotopically heavy continental crust. *Chemical Geology* **485**, 1-13.

Wille M., Nebel O., Van Kranendonk M. J., Schoenberg R., Kleinhanns I. C., & Ellwood M. J. (2013) Mo–Cr isotope evidence for a reducing Archean atmosphere in 3.46–2.76 Ga black shales from the Pilbara, Western Australia. *Chemical Geology* **340**, 68-76.

Wilson A., Groenewald B., & Palmer C. (2013) Volcanic and volcaniclastic rocks of the Mesoarchean Pongola Supergroup in South Africa and Swaziland: distribution, physical characteristics, stratigraphy and correlations. *South African Journal of Geology* **116(1)**, 119-168.

Wronkiewicz D. J. (1989) Geochemistry and provenance of sediments from the Pongola Supergroup, South Africa: evidence for a 3.0-Ga-old continental craton. *Geochimica et Cosmochimica Acta* **53**, 1537-1549.

Wu L., Beard B. L., Roden E. E., Johnson C. M. (2011) Stable iron isotope fractionation between aqueous Fe (II) and hydrous ferric oxide. *Environ Sci Technol* **45**, 1847−1852.

Wu W., Swanner E. D., Kleinhanns I. C., Schoenberg R., Pan Y., & Kappler A. (2017) Fe isotope fractionation during Fe (II) oxidation by the marine photoferrotroph Rhodovulum iodosum in the presence of Si–Implications for Precambrian iron formation deposition. *Geochimica et Cosmochimica Acta* **211**, 307-321.

Yamaguchi K. E., Johnson C. M., Beard B. L., Ohmoto H. (2005) Biogeochemical cycling of iron in the Archean- Paleoproterozoic Earth: Constraints from iron isotope variations in sedimentary rocks from the Kaapvaal and Pilbara Cratons. *Chem Geol* **218**, 135−169.

Yao W., & Millero F. J. (1996) Oxidation of hydrogen sulfide by hydrous Fe (III) oxides in seawater. *Marine Chemistry* **52(1)**, 1-16.

Zink S., Schoenberg R. and Staubwasser M. (2010) Isotopic fractionation and reaction kinetics between Cr(III) and Cr(VI) in aqueous media. *Geochimica Et Cosmochimica Acta* **74**, 5729-5745